Investigation of Synchronization in a Ring of Coupled MEMS Resonators

Suketu Dilipkumar Naik

2011

Abstract

MEMS resonators are becoming ubiquitous in modern signal processing systems. They are increasingly being used as sensors, reference clocks, memory elements, and filters. A MEMS resonator is limited to a maximum usable amplitude at its resonant frequency. The frequency peak shifts from the linear resonance to the nonlinear resonance with large excitation voltage. At large vibration amplitude, the device may exhibit hysteresis during the upsweep and the downsweep of the frequency. Along with the ac excitation voltage and the bias, the actuation mechanisms such as parallel plate comb-drive or laterally driven comb-drive determine whether the soft-spring or the hard-spring behavior is exhibited. These topics insinuate an investigation of the nonlinear resonance of MEMS devices so that they can be ultimately used in the aforementioned applications. Operation of the device in a usable frequency range at large amplitude in the linear regime requires strenuous design efforts. Instead it would be beneficial to utilize the nonlinear behavior. Intriguing dynamics arise when nonlinear MEMS devices are coupled together. Coupled dynamics can be utilized in the design of sensors.

In this study a synthesis of design, analysis, and characterization of the nonlinear MEMS resonators is presented. The nonlinear resonator in this study exhibits the hard-spring response. Under specific excitation conditions, it shows an extension of the hysteresis during upsweep and downsweep of the excitation frequency. The extension of the hysteresis can be tuned by changing the excitation voltage. Furthermore a unidirectionally coupled system consisting of the above nonlinear resonators is characterized. It is shown that the coupled system can oscillate at a certain value of the coupling strength. The autonomous system can exhibit in-phase vibrations and out-of-phase vibrations depending on the coupling circuit and the combination of the coupling strengths. In the presence of the excitation force the coupled system shows full synchronization to the excitation frequency in a priori in-phase and out-of-phase oscillatory state. A priori quasiperiodic oscillations can also be synchronized to the excitation frequency. Sensitivity in regards to coupling strength, excitation frequency, excitation amplitude, and pressure is demonstrated. It is concluded from this study that the coupled system has a strong potential as a sensor depending on the application.
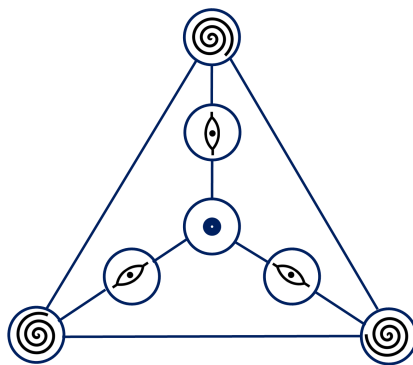
Keywords: MEMS, Nonlinear MEMS Resonator, Coupled Resonators, Synchronization, Unidirectional Coupling.

Dedication

To my dear wife Poonam...

To the Goddess–the mother of all...

To the endless beginning...

Acknowledgements

I would like to express my sincerest gratitude to Dr. Takashi Hikihara without whom none of this would have transpired, beginning with an opportunity to come to Japan and conduct the research under his supervision. I am humbled by his overwhelming support during my stay in Japan and his guidance in the research. I would like to thank him for instilling in me patience, perseverance and willingness to make things work–the most valuable lessons one can imbibe. I am truly grateful for his guidance and counsel on all matters related and unrelated to the research. He provided invaluable observations, constructive opinions and encouragement. He guided me through the gruesome process of PhD research and never accepted anything less than my best effort.

I'd like to thank Dr. Osamu Tabata and Dr. Hirofumi Yamada for being part of my dissertation committee. I am grateful to Dr. Tabata for allowing an excess to his lab and his field of knowledge in MEMS. I would have not made any headway without his guidance; I had many treasured discussions on the MEMS design and related topics with him. I would like to thank Dr. Yamada for providing me with valuable suggestions and insights during our discussions. I'd like to thank Dr. Shinji Doi for being part of my pre-defense committee and for making important suggestions.

I would like to extend my gratitude to Dr. Visarath In (SSC-Pacific, San Diego) and Dr. Antonio Palacios (San Diego State University) for collaborating on the research as well as providing valuable suggestions to improve the research. Their insights into the coupled systems turned out to be crucial for this research. I also want to thank Dr. Huy Vu and Dr. Patrick Longhini (SSC-Pacific, San Diego) for their advice, discussions and suggestions. I want to thank the rest of folks in Nonlinear Dynamical Systems group at SDSU. I'd like to thank Dr. Visarath In and Dr. Adi Bulsara (SSC-Pacific, San Diego) for the encouragement and the support to engage in the PhD research. I want to thank Dr. Joseph Neff (SSC-Pacific, San Diego) and Mr. David Pacifico, whose suggestions and comments got me interested in MEMS research. I'd also like to thank the rest of the SSC-Pacific team from whom I have learned important lessons during various projects. I really appreciate that Dr. Sam Kassegne (San Diego State University) took an interest in my work and discussed various topics regarding the MEMS design during my visit to San Diego.

I also wish to thank Mr. Hiroyuki Tokusaki, Dr. Toshiyuki Tsuchiya, Mr. Praveen Singh and the rest of the members of Tabata Laboratory (Dept. of Microengineering, Kyoto University) for their help and discussions in the design and the experiments. I'd like to thank Dr. Nobuo Satoh for the awesome jokes and the advice in the experiments. I want to thank Mr. Jimin Oh for helping me get my footing in Japan and for discussing various research topics.

Contents

Glossary

Acronyms

In alphabetical order:

BAW	Bulk Acoustic Wave
CMOS	Complementary Metal Oxide Semiconductor
DOF	Degree Of Freedom
DUT	Device Under Test
FEA	Finite Element Analysis
IC	Integrated Circuit
LHS	Left Hand Side
MEMS	Micro Electro Mechanical Systems
ODE	Ordinary Differential Equation
Opamp	Operational Amplifier
PCB	Printed Circuit Board
RHS	Right Hand Side
SOIMUMPs	Silicon On Insulator Multi User MEMS Processes
SNR	Signal to Noise Ratio
UV	Ultra Violet (light)

Chapter 1

Introduction

Nature, the complex system which we are part of, or any large coupled system that is under investigation, can be assessed from the standpoint of self-organizing components. In particular, these components often oscillate and share a common time which allows them to be 'aligned' to each other or to be *synchronized* to each other. The observation and study of the oscillatory behaviors can give us an important clue as to the interdependence of these behaviors in relation to their environment. In fact their interaction with other oscillatory systems/components are at the heart of the phenomena of synchronization. Drawing from the study of such type of interactions, we can realize that astounding symmetries and self-organization exists in nature which can be nearly perfect or are under their evolutionary march towards perfection. Based on these observations we can not only improve the quality of human life but also become more adapt at learning how and why the human species is wholly integrated part of nature. To be specific the field of MEMS, micromechanical devices, and their interactions at micro scale provides ample opportunities to explore rich dynamical behaviors including synchronization. Nonlinear dynamics of resonant micro and nanoelectromechanical systems involves a methodical study of nonlinear behaviors arising in small scale, vibratory, mechanical devices that are typically integrated with electronics for the signal processing, actuation, and sensing applications. In modern signal processing systems MEMS devices are becoming ubiquitous and are increasingly being used as parts of sensor systems, as reference clocks, as memory elements, and as filters [1] [2]. MEMS devices can exhibit many nonlinear behaviors including the hard-spring effect and the soft-spring effect. Along with ac excitation voltage and bias, actuation mechanisms such as parallel plate combdrive or laterally driven comb-drive determine whether soft-spring or hard-spring behavior is exhibited. Furthermore a closed-loop coupled nonlinear system can offer additional advantages including self-excited oscillations and synchronization to an excitation signal. These factors insinuate an investigation of the nonlinear resonance in coupled MEMS devices so that they can be used ultimately in aforementioned applications and other sensing applications.

1.1 Coupled Systems

The study of the dynamical behavior in the coupled systems and their synchronization properties can greatly enhance our understanding of the various fundamental processes in physical, biological, engineering, and economic systems [3]. Learning about the specific properties of the individual behavior and understanding the coupling architectures that give rise to various types of collective behavior can help us comprehend the fundamental nature of vibrations and all things effected by them. It is known that the coupled dynamics of a system consisting of nonlinear oscillators can generate complex spatio-temporal patterns. By exploring these patterns and analyzing the nature of complex interaction between the individual elements, the coupled systems can be used as sensors in a wide range of application areas such as magnetic field sensing, electric field sensing, and multi-frequency generation because of high sensitivity and output signal in the presence of noise. Indeed the coupled systems have tremendous potential in a large amount of application areas as the research in past few decades has shown. For example, the field of Coupled Map Lattice (CML) has revealed a qualitative universality in a variety of areas including pattern selection, spatio-temporal intermittency, and soliton turbulence to name a few [4, 5].

In particular, rings of coupled analog oscillators have been reported which show the appearance of periodic rotating waves in the chaotic Lorenz oscillators [6] and a route to chaotic oscillations through quasiperiodicity [7]. Coupling induced oscillations have been shown to be very sensitive when a target signal is present [8] [9] and mutual coupling between two coupled arrays can even lead to multiple frequencies [10]. The emergent oscillations can be carefully controlled by adjusting the control parameters and they can be used in a milieu of applications including reference clocks and enhanced sensors [9].

1.2 Nonlinear MEMS Resonator

MEMS devices are normally targeted to achieve a specific range within its linear mode of operation. At a higher vibration amplitude, the devices may exhibit nonlinear response [11]. The causes of nonlinearity in MEMS include material anisotropicity in a nonuniform material, large vibrations, variation in individual structure elements during fabrication, circuit elements, and/or a combination of all of the above. In particular hard spring effect in electrostatically excited fixed-fixed beam resonator and comb-drive resonator has already been reported in MEMS research [12] [13] [14]. Nonlinear oscillations in MEMS devices have been demonstrated for many potential applications. In [15] chaotic vibrations were investigated in a nonlinear MEMS oscillator by using two actuators and the device was demonstrated in a secure communication experiment. In [16] a MEMS oscillator with two sets of noninterdigitated comb-drives were shown to exhibit chaos through the parametric resonance. The above research also denoted the effects of tuning linear and nonlinear stiffnesses through restoring force that was governed by Nonlinear Mathieu's Equation. In [17] a micro gyroscope was shown to be robust when actuated by parametric resonance.

MEMS resonators that exhibit the hard-spring behavior shown in Fig. 1.1, are the focus

(a) Normal hysteresis   (b) Extended hysteresis
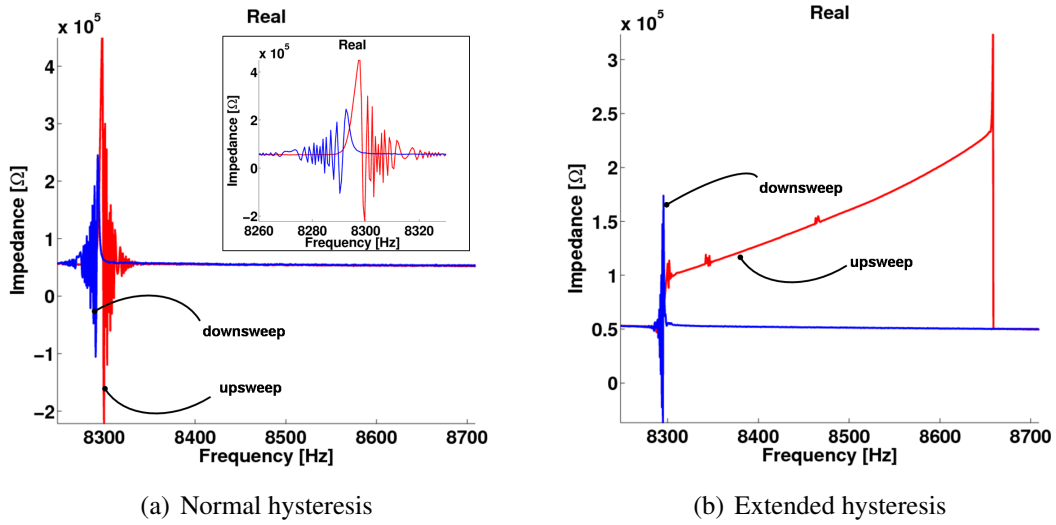
Figure 1.1: Real part of the impedance of the fabricated MEMS resonator: (a) normal hys-terectic behavior during the upsweep and the downsweep of frequency with the inset showing the zommed view of the hysteresis and (b) extended hysteresis. Test conditions are pressure = 30 Pa, bias = 20 V, ac amplitude = 105 mV and 305 mV in (a) and (b) respectively.

of this thesis. The resonators exhibit an extended hysteresis after increasing the ac excitation voltage as shown in Fig. 1.1(b). This behavior is also observed while changing other test conditions such as dc bias and pressure.

1.3 Coupled MEMS Resonators

Coupled MEMS resonators and oscillators can offer additional advantages such as pat-tern forming and signal processing by the virtue of nonlinear phase-locking as was shown in [18]. Mechanically coupled multiple comb-drives were utilized in [19] to provide wider drive-mode bandwidth and robustness of the gyroscopes was increased while operating the system in the linear regime. In [20] a mechanically coupled system of three high-Q MEMS resonators was configured in open loop as a bandpass filter at the center frequency of 340 kHz with very low insertion loss. In [21] open loop and closed loop chains of beam res-onators were compared in a detailed simulation study and it was observed that the closed loop chains offered excellent passband rejection, symmetric frequency response and robust-ness to process-induced variations. In the experimental study shown in [22], synchronization in two beam resonators coupled via a beam was realized and the coupled system demon-strated rich dynamical behavior leading to a number of synchronization regions. In [23] an opto-mechanical system of a grating array with a large number of doubly clamped beams was electrostatically actuated which induced mechanical coupling and a wide range of vibra-tional modes. The plethora of the devices and results reported above indicate that the coupled MEMS can exhibit many intriguing behaviors. Furthermore in [24] a rigorous theoretical study was presented which showed that a ring of coupled nonlinear gyroscopes exhibits an

increase in sensitivity and robustness against noise. Hence it is necessary to provide a comprehensive perspective by experimental verification of the aforementioned concepts in a ring of coupled nonlinear MEMS devices. This thesis is devoted to the study of synchronization in a ring of unidirectionally coupled nonlinear MEMS resonators that exhibit the nonlinear behavior such as the one shown previously in Fig. 1.1. The benefits of the coupled system of nonlinear MEMS resonators are as follows: the MEMS resonator has simpler components than its electronic counterpart, the coupled system can be utilized in both electrical and mechanical signal domains, the coupled system has high sensitivity near the bifurcation points to small perturbations which can be useful for signal detection and amplification. This study also offers an insight into the coupled dynamics and pattern formation that leads to self-organization based on an interplay between between different governing forces.

1.4 Purpose and Outline of the Thesis

This thesis is aimed at the synthesis of design, analysis, and characterization of nonlinear MEMS resonators in the coupled system. The focus of this thesis is on the investigation of the nonlinear resonance of MEMS resonator as well as the discovery of any intriguing phase-locked or frequency-locked state produced by nonlinear MEMS resonators when they are coupled by discrete electronics in a ring formation. Both the self-excited oscillations and the forced oscillations of the coupled system are investigated. Firstly simulations are carried out to understand the dynamics of a nonlinear MEMS resonator and a coupled system based on the design of the resonator. The width of the hysteresis, which is determined from the two jump points during upsweep and downsweep of excitation frequency, is the key to understanding the synchronized behavior of coupled resonators. To this end, linear and nonlinear resonance characteristics different resonators are shown by entailing the experimental results. Finally the usage of the individual resonators in a unidirectionally coupled system is demonstrated. The coupling parameter and the frequency of the excitation force also play a major role in the type of behavior that is exhibited; thus the coupled system can be used as a sensor depending on the target application.

In chapter 2, an overview of synchronization in coupled systems is presented. To begin with, synchronization is presented as an omnipresent phenomenon in relation to self-organization. Next, the specifics of synchronization the coupled systems are presented from the perspectives of the mutual coupling and the excitation force. The region of synchronization is discussed. The phase dynamics of the forced system are also entailed.

In chapter 3, MEMS resonator with harmonic excitation is presented in detail. First the electrostatic actuation is explained from the perspective of the electrostatic potential energy. Electrostatic model of the comb-drive resonator is discussed in detail. Next the analytical solution of the dynamical equation by averaging method is presented and related parameters are discussed. The frequency response curves are also shown.

Chapter 4 entails the design process of the nonlinear MEMS resonator and related simulation results. First the basics of microfabrication are discussed and the major steps of SOIMUMPs process are summarized. Next an in-depth analysis and simulation of MEMS

resonator using FEA is presented while emphasizing the nonlinearity in this device.

In chapter 5, the simulation study of a unidirectional coupled system of resonators is presented. An autonomous system of coupled resonators is described and various periodic states are discussed. Then the non-autonomous system is simulated and regions of synchronization are shown. Here the effects of damping, nonlinearity, excitation force and coupling are discussed. These simulations show that the coupled system under study consisting of the nonlinear MEMS resonators can indeed show self-excited oscillations at a critical coupling strength and it can synchronize to an excitation signal. The coupled system exhibits a rich dynamical behavior based on the design parameters.

In chapter 6, the characterization results of the fabricated MEMS resonators are shown. Frequency response curves of various resonators selected from separate dies and from a single die are shown. First the resonance characteristics are shown. Next the hysteresis characteristics of different resonators are shown under varying excitation conditions including bias, ac amplitude, and pressure. Finally the experimental results of the coupled system are presented. Self-excited and forced modes of the coupled system are shown. Both in-phase and out-of phase vibrations of the coupled system are presented and the regions of synchronization are shown.

In chapter 7, important conclusions are drawn from the simulation and experimental studies of the single nonlinear MEMS resonator and the coupled system. The course of future work based on the improvements in the design on the single resonator and the coupled system shown in this thesis is laid out. It is shown that the coupled nonlinear MEMS resonators can be used in a milieu of application areas.

Chapter 2

Synchronization in Coupled Systems

In this chapter, the general concept of synchronization related to coupled system is explicated.

2.1   Introduction to Synchronization

It has been said that the premise of human endeavor to understand the universe involves an acute observation and objective assessment of the observations. The objective assessment is nearly impossible due the fact that we *are* part of nature, the dynamical flow of the planet, and the universe at large. Hence the efficacy of scientific method has more to do with a subjective interpretation of observations no matter how much repeatable they are. The geriatric notion of 'inconscience' of nature dictates the outlines of the observational and conjectural scientific practices and it appears in every aspect of humanity and our interaction with nature. This older direction and outdated model that bears the stamp of good scientific understanding can be subverted by involving a better perspective to advance the subjectivity of human interaction with the 'external' reality that we call nature. Without a binding and guiding principle that can tie the loose ends, it seems that the concept of *synchronization* can been applied to understand the order in nonlinear dynamical systems that are abundant in nature from the perspective of self-organization.

2.1.1   Self-organization

Synchronization can only be explained in relation to the concept of self-organization. While advancing our efforts to understand and work with the nature, it is important to understand the natural processes involved in synchronization which lead to self-organization. For example, the concept of synchronization is applicable to the reformulation of the theoretical models that describe organization at both at the universal scale and at the nano scale. The observation of synchronization and self-organization in the plasma, the gases, and the spin of atoms can help improve the existing models. Our expanded understanding based on such models can then filter into the manipulation of the matter and the energy that forms the matter as we attempt to miniaturize our instruments, robots, equipment etc. For example

if the inherent nature of what we perceive as reality is chaotic and dynamic then learning how life around us including our DNA self-organizes from molecules to organs to bodies to a conscious human being can provide us clues as to how structures at nano-scale can be a) fabricated and b) self-assembled to whatever shape and structure that we choose to apply [25] [26]. In this way, the study of the self-organization of bio-molecules such as DNA can help us create nano-structures, manufacture materials through automated machines, self-heal and assemble informational web of sensors and networks. Moreover this knowledge can bridge the patterns that govern complex systems with multiple dynamical and interactive yet individual components including the biological cells as well as formation of ordered and stable structures such as molecular crystals [27] [26] [28].

Self-organizing systems are adaptive and robust in that they can reconfigure themselves to changing demands and thus keep on functioning in spite of perturbations. Because of this, self-organization has been used as a paradigm to design adaptive and robust artificial systems [29]. The researches conducted so far have shown that there are four types of self-organization: a) static, b) dynamic, c) templated self-organization, d) biological self-organization [26]. Static self-organization would involve systems that are at equilibrium (e.g. stable) and do not emit energy. In other words, in static organization, after some form of energy is externally applied, the system reaches global or local equilibrium and it does not dissipate energy. Majority of research has focused on this type of self-organization [29]. An example of this type of organization is folded proteins that normally do not change the shape. Dynamic self-organization involves reactive and diffusive interactions between components such that a desired pattern is created. In this way, the system constantly dissipates energy much like the human cells. This field in terms of the study and the application of this type of organization is nascent due to the complexity involved. Templated self-organization involves not only dynamics and interactions between the components but the exchange of the information between the surrounding environment. For an example, the diseased human cells quickly heal if the environs (other cells surrounding the approximate boundary of the sick cells) are conducive to such healing. In templated self-organization an organic and ordered structure grows out of the conditions that are more favorable to such structure. An example of this type of organization is the crystallization of colloids[1] which can be observed in 3-d optical field created by techniques such as Atomic Force Microscopy (AFM) or Scanning Tunneling Microscopy (STM). On the other hand, biological self-organization is the holy grail of self-structuring patterns [30]. Most prominent example is the human DNA. The important characteristic of this type of organization is the inexhaustible variety and complexity of functions created from it. It is also the least understood type of organization. The design of components that form themselves into desired patterns (which define the functions) and functions (which define pattens) that DNA represents within human cells, is the key to self-organization [26]. At a holistic level, this type of organization would involve all of the previously mentioned types of organization. For an example, the components of a cell (e.g. various proteins, mitochondrial and nucleic DNA, peptide bonds, cytoplasm etc) achieve a superb balance between organizing in aggregate (e.g. resistance to compression) and non-

---

[1] A colloidal system has even distribution of one substance, e.g. milk and cheese

aggregate states as well as performing myriad of actions. Another characteristic of the cell is that the components replicate and assemble yet another cell that behaves similarly to the source cell. The cell components also move and obtain steady state such that an incredible balance is achieved between attraction and repulsion in a feedback loop for the overall health of the cell [26] [30]. The cytoplasm and other components contain thousands of sensors to sense heat, pressure, presence of harmful bacteria etc. In other words, a cell is a fine example of self-organization that is a) adaptive, b) dissipates energy, c) self replicates d) enclosed with an interactive boundary, and e) allows for a constant in-flux and out-flux of energy within its own structure as well as within the group of cells. The cell exhibits amazing balance in form of self-organization between a) simplicity of molecular reactions and b) complexity of division [28].

2.2   Synchronization in Coupled Systems

Inspired by the above examples, any given body can be assessed from the standpoint of self-organizing components. In particular, these components often oscillate and share a common time which allows them to be 'aligned' to each other or to be synchronized to each other. Examples include synchronous variation of cell nuclei, synchronous firing of neurons, adjustment of heart rate to bodily rhythms, cooperative behavior of insects, animals and humans [31]. Examples of oscillations are also abundant: an orchestra full of instruments, fireflies emitting light pulses, crickets making chirps, birds flapping wings, chemical systems that exhibit oscillation of the concentration of reagents [3] [32] [33]. The observation and study of these oscillatory behaviors give us an important clue that these behaviors are not independent of their environment. In fact their interaction with other oscillatory systems/components are at the heart of the phenomena of synchronization. Albeit of being weak or strong, the coupling/interaction between the oscillatory objects causes objects to adjust their spatial and spatio-temporal rhythms to each other [31]. To be specific, *synchronization is an adjustment to rhythms of oscillatory objects because of their weak interaction.*

To begin with, in self-sustained oscillations, the source of energy is internal and is transformed into some sort of oscillatory movement. Given a low amount of damping, the oscillations continue until the source of energy is exhausted. The amplitude of the vibrations of such a system depends on the supplied energy and dissipated energy. Moreover this system has to be inherently nonlinear in order to sustain the vibrations at this amplitude value. This type of system is known as the autonomous dynamical system and it has no explicit dependence on time. After small perturbations, the autonomous system returns to its original state and continues the oscillations. Beginning with historical experiments of Huygens, it has been observed that a weak interaction between two autonomous systems can lead to synchronization [31]. The adjustment of their frequencies to a common (shared) frequency is known as *frequency entrainment or frequency locking*. Moreover the experiments have shown that synchronized state and therefore the emergent oscillations/patterns depend on the interplay between attractive and repulsive forces [34]. The synchronization in a mutually coupled system primarily depends on the coupling strength (e.g. strong or weak) and
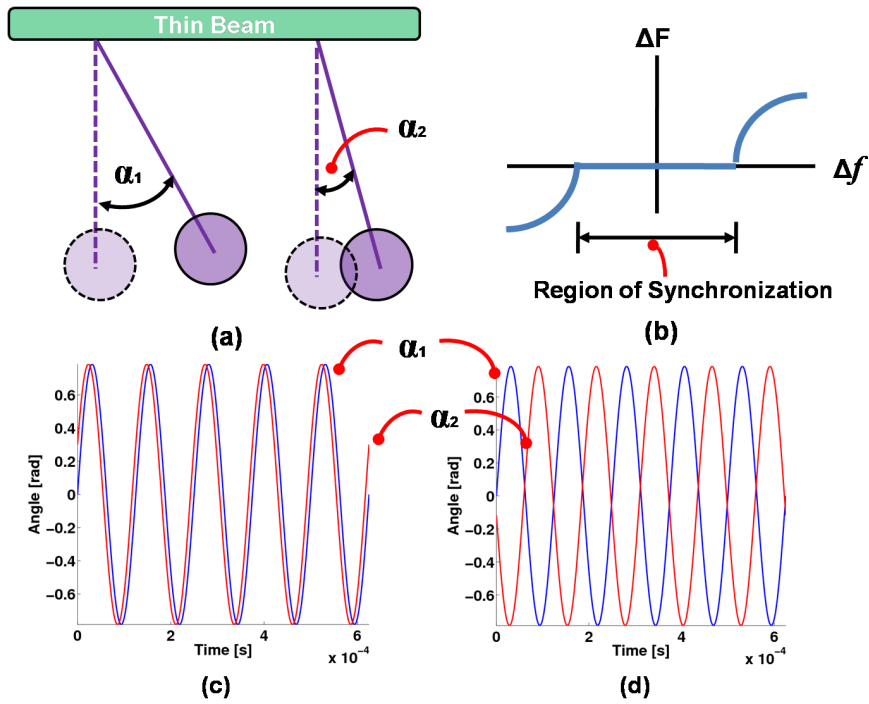
Figure 2.1: Synchronization of pendulums: (a) Two pendulums are coupled together by a thin beam (weak coupling) and they have different angular displacements, α_1 and α_2. (b) Frequency vs. detuning plot: let f_1 and f_2 be the uncoupled frequencies, and let F_1 and F_2 the coupled frequencies then $\Delta f = f_1 - f_2$ and $\Delta F = F_1 - F_2$. In the region of synchronization $\Delta F = 0$. (c) Nearly in-phase oscillations.(d) Nearly out-of-phase oscillations.

the frequency detuning between the individual autonomous systems' frequencies. Another type of synchronization depends on the excitation amplitude and the frequency detuning between the excitation frequency and the frequency of the forced system. These two cases are explained in the subsequent sections.

2.2.1 Mutual Coupling

Figure 2.1 shows the synchronization in two pendulums which are autonomous systems if they are not coupled together. The thin beam shown in Fig. 2.1(a) illustrates weak coupling. Two forms of synchronization of frequencies shown in Fig. 2.1(b) can appear: (1) in-phase with phase difference ≈ 0 as shown in Fig. 2.1(c) and (2) out-of-phase with phase-difference $\approx \pi$ as shown in Fig. 2.1(d). Generally the width of synchronization region depends on the coupling strength. It is important to note that compliance in the thin beam allows synchronization to take place. Otherwise a very rigid beam, which provides strong coupling, would absorb the individual motions and no interaction takes place between the two pendulums.

10

2.2.2 Weakly Forced Oscillator

Some movable objects exhibit resonance in the presence of an excitation force. Specifically when the excitation force is applied, the oscillating object resonates at some amplitude depending on the damping and the composition of the object. The frequency of the oscillation is governed by the excitation force. All resonators exhibit a peak amplitude at a specific value of the excitation frequency. This frequency point is referred to as the natural frequency of the object. At this frequency, we would expect the object to exhibit the largest oscillation amplitude. In other words, at the natural frequency the resonating object is able to overcome damping effect and other noise sources and will show a clear oscillatory behavior. Note that in resonance the excitation force governs both the amplitude and the frequency.

In comparison to a resonator, an oscillator generates periodic oscillations without periodic forces. As noted before an oscillator is a dissipative nonlinear system described by an autonomous ODE and possesses a limit cycle in the phase space. An autonomous system with the self-sustained oscillations, which are governed by an internal source of energy, oscillates at a natural frequency. Figs. 2.2, 2.3, and 2.4 show different states of the perturbed autonomous system. Let the natural frequency of the system be denoted as ω_o, the initial phase as ϕ_o, and the amplitude of oscillations as A. In the case of a quasilinear oscillator, the oscillations can be described as $x(t) = A \sin(\omega_o t + \phi_o)$. Fig. 2.2(a) shows a limit cycle of such oscillations as a circle in a phase space comprising of displacement and velocity. If we denote $\phi(t) = \omega_o t + \phi_o$ and view the phase point in a rotating coordinate frame with frequency ω_o in the same direction as the oscillation, then it can be seen as a fixed point on this limit cycle as shown in Fig. 2.2(b). Suppose a small perturbation induced by a weak force is
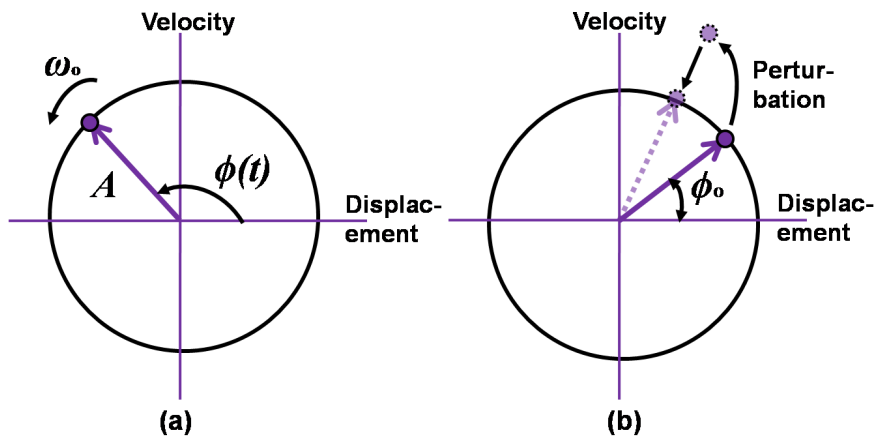
Figure 2.2: Limit cycle of an oscillator: (a) the amplitude A and the phase $\phi(t) = \omega_o + \phi_o$ of the oscillator are shown within the circular phase-space. (b) Given any phase-point in (a) of an oscillatory motion, the initial phase can be seen as a fixed point. If the oscillator is perturbed by a weak force, this point will leave the original limit cycle and will come back after the perturbed amplitude decays. Note that the amplitude remains unchanged after perturbation but the phase is changed.
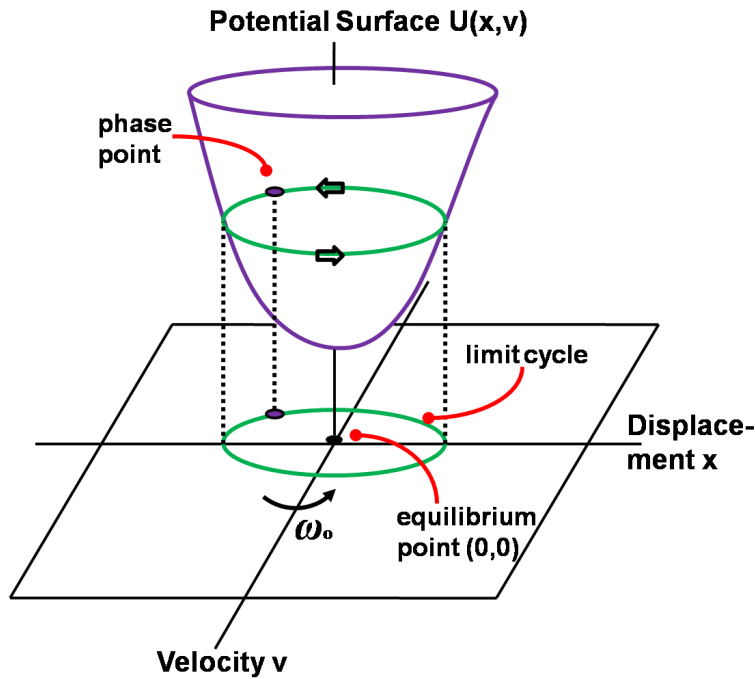
Figure 2.3: Potential surface and the limit cycle: the phase space of an autonomous system can be visualized as a projection of the potential surface on which the phase point rotates with a uniform frequency ω_o.

applied to the oscillator. Then the fixed point shown in Fig. 2.2(b) will leave the limit cycle. After the perturbed amplitude has decayed and the original amplitude is restored, the initial phase $\phi_o = \phi(t) - \omega_o t$ would have changed [3] [35]. This phase value will not be changed until another perturbation is applied. This figure illustrates the essence of synchronization. It should be clear from this figure that the phase is free and can be adjusted by an excitation force leaving the amplitude the same as before. And as a result the oscillator can be *synchronized* to the excitation force.

Figure 2.3 shows the potential surface based on the potential function of an autonomous system with frequency ω_o. Here the phase point rotates on the potential surface when a stable limit cycle has been generated. When a small perturbation has been applied to the system as shown in Fig. 2.4(a), the phase point, which can be visualized in a rotating frame of (A, ϕ) as a fixed point, rotates until the amplitude of the perturbation is decayed and reaches a steady state as shown in Fig. 2.4(b). Following the motion of the fixed point, we can see that in the gradient system consisting of the fixed phase point it resembles a particle sliding down a tilted plane.
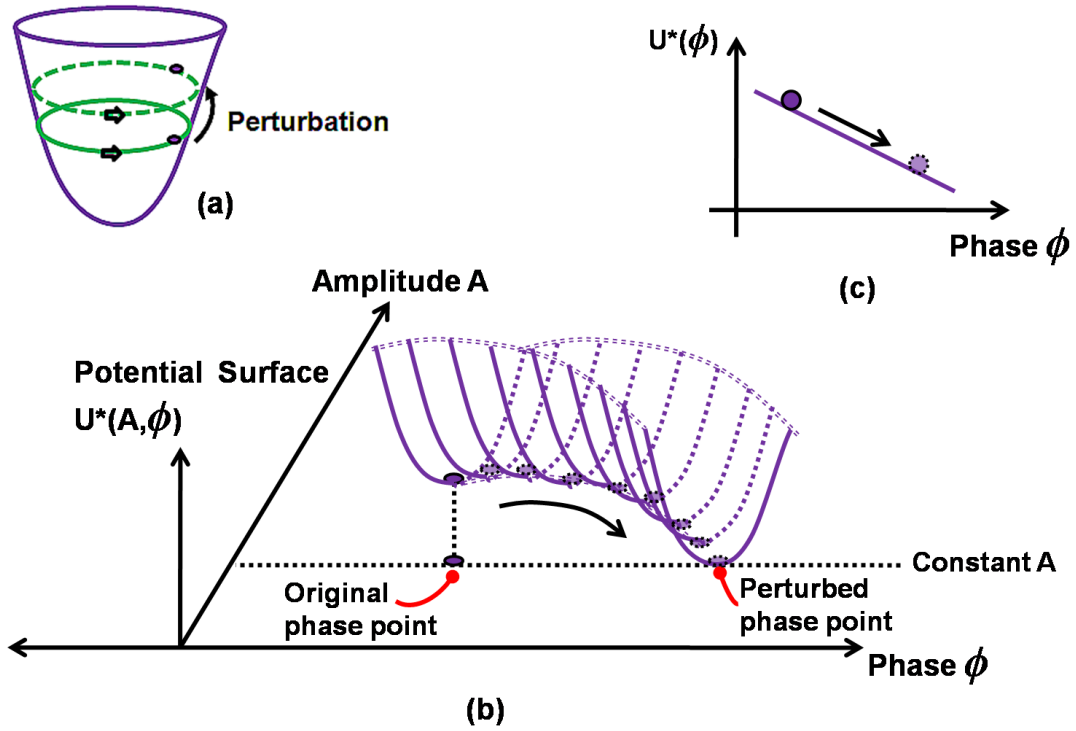
Figure 2.4: Potential surface $U^*(A, \phi)$ and the perturbed phase point: (a) potential surface $U(x, v)$ similar to the one shown in Fig. 2.3, where the perturbation creates a bigger limit cycle in the vicinity of the original limit cycle. (b) After being perturbed, the original potential surface can now be viewed in a rotating reference frame of (A, ϕ) with frequency $= \omega_o$. Here the fixed phase point shown previous in Fig. 2.2(b) rotates until the amplitude of the perturbation is decayed and reaches a steady state. Thus the perturbed response of the phase point can be observed as (c) which is a gradient system, i.e. the phase point on an inclined plane.

2.2.3   Phase and Frequency Locking

In the presence of an excitation force $F(t)$ with frequency ω, initial phase ϕ'_e and amplitude ϵ as $F(t) = \cos(\omega t + \phi'_e)$, the detuning can be assigned as $\omega_o - \omega$. Let the phase of the excitation force be denoted as $\phi_e(t) = \omega t + \phi'_e$. There are three scenarios in which synchronization can take place: (1) $\omega_o > \omega$, (2) $\omega_o = \omega$, and (3) $\omega_o < \omega$. Let's assume that the forced system can be presented in the new reference frame which rotates counterclockwise (same direction as the autonomous system as was shown in Fig. 2.2(a)), with the rotational frequency $\omega_o - \omega$. Note that the phase point of the forced system can rotate counterclockwise for $\omega_o > \omega$, stay fixed at $\omega_o = \omega$, or rotate clockwise for $\omega_o < \omega$.
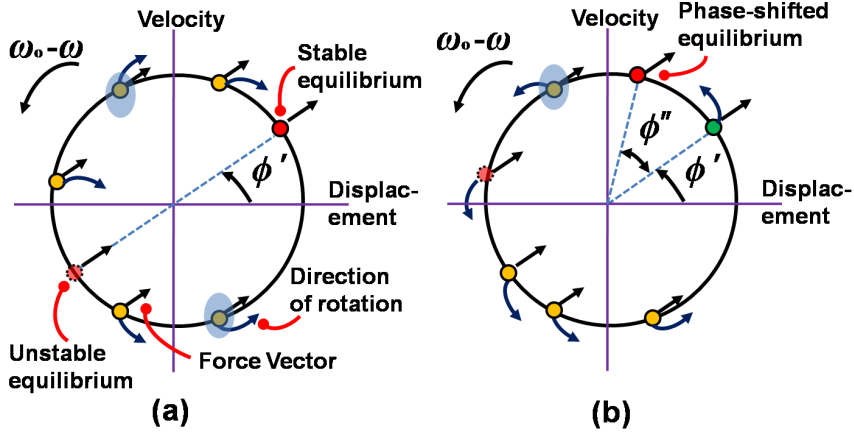
Figure 2.5: Phase transitions of the forced system [31]: (a) force acting at some angle ϕ', creates stable (unstable) equilibrium minima which attracts (repels) the phase point, denoted by $\phi - \phi_e$ in a rotating frame with excitation frequency $\omega_o - \omega$. Here the constant force vector based on its rotating frame at ω frequency on each of the phase point is shown by a straight arrow. This force vector dictates the rotation of the phase point as shown by curved arrows which indicate the direction of the rotation. Note that the strength of the force vector depends strongly on the phase difference $\phi - \phi_e$ and is maximum at the points shown by the ovals. (b) The phase point now rotates towards the equilibrium created by the force and is pulled apart by frequency detuning in the counterclockwise direction if $\omega_o > \omega$. For $\omega_o < \omega$ this rotation would be clockwise. Eventually the effect of the force and the effect of detuning balance out and the original equilibrium point is phase-shifted by ϕ'' at which the phase point becomes stable.

$\omega_o = \omega$

As the force impinges on the autonomous system, it acts on the system at some initial angle ϕ' as shown in Fig. 2.5(a)[2]. Depending on the the phase difference, the phase point of the forced system *rotates* towards ϕ', where the phase difference is constant, e.g. $\phi - \phi_e = \phi'$. This is known as the *phase-locked* state. Note that in the presence of an infinitesimally small force the synchronization can take place this way after an infinitely long time. Obviously as the force is increased, the synchronization time is decreased. Here the effect of the force on the phase point depends strongly on the phase difference $\phi - \phi_e$. For example, the force is maximum at the points show by ovals in Fig. 2.5(a).

For $\omega_o \neq \omega$ there are two factors interact with each other leading to the final synchronized state: (a) the detuning of the frequency and (b) the amplitude of the excitation force. Detuning drags ϕ and ϕ_e apart from each other whereas the force acts on the system to make the phase difference constant, i.e. brings them closer to each other.

---

[2] Note that this angle is different from the initial phase of the force ϕ'_e because of the rotating frame.
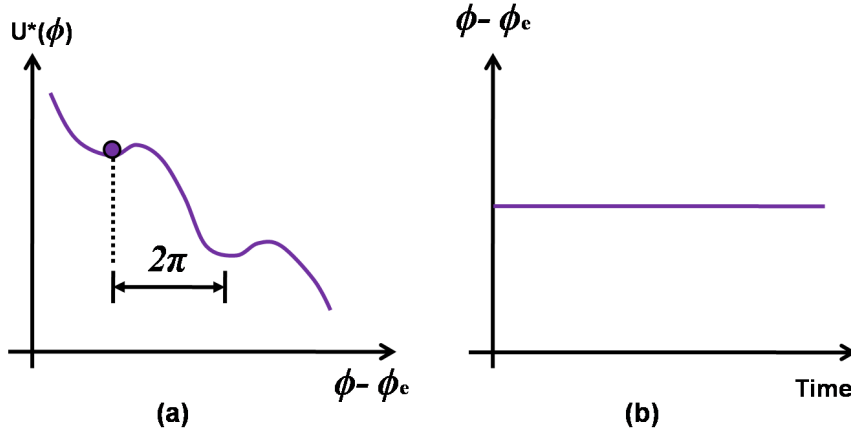
Figure 2.6: Effect of small detuning $\omega_o - \omega$ for $\omega_o > \omega$ at a constant ϵ [31]: (a) the synchronization takes place mainly due to the minima created by the force in the tilted potential, as was shown in Fig. 2.4(c), where the phase point can rest and hence (b) the external force can synchronize the autonomous system by making the phase difference $\phi - \phi_e$ constant. Note that for $\omega_o < \omega$, the potential is tilted the other way.

Small Detuning

In the case of small detuning the system behaves as shown in Fig. 2.5(b) and a fixed point emerges after a transient. Depending on the phase difference, the force will appropriately accelerate or decelerate the rotation of the phase point such that the phase difference eventually becomes constant. Note that Fig. 2.5(b) shows the counterclockwise rotation due to detuning effect due for $\omega_o > \omega$. For $\omega_o < \omega$ this rotation would be clockwise. As noted before the interaction of detuning and the amplitude of force determine where the new equilibrium point appears which can be phase-shifted by ϕ'' as shown in Fig. 2.5(b) where $\phi - \phi_e = \phi' + \phi''$. The frequency of the driven autonomous system can be denoted as Ω in the phase-locked state. It is obvious that the synchronized state corresponds to $\Omega = \omega$. The presence of excitation force creates ripples in the potential $U^*(\phi)$, which was shown in Fig. 2.4(c), such that the phase point becomes trapped in the minima created by the force. This is represented pictorially in Fig. 2.6(a). After the transient is over, the phase difference $\phi - \phi_e$ becomes constant as shown in Fig. 2.6(b). Note that at this point the frequency of rotation Ω remains constant.

Large Detuning

In the case of large detuning, the force can not influence the phase point to an extent at which it can stop rotation of the phase point for either $\omega_o > \omega$ or $\omega_o < \omega$. Indeed the equilibrium point is shifted to the point shown by the oval in Fig. 2.5(b) where the effect of the force is maximum. Eventually the stable and unstable equilibrium points collide and disappear [31] and the phase point now begins to rotate at some frequency. Let this frequency
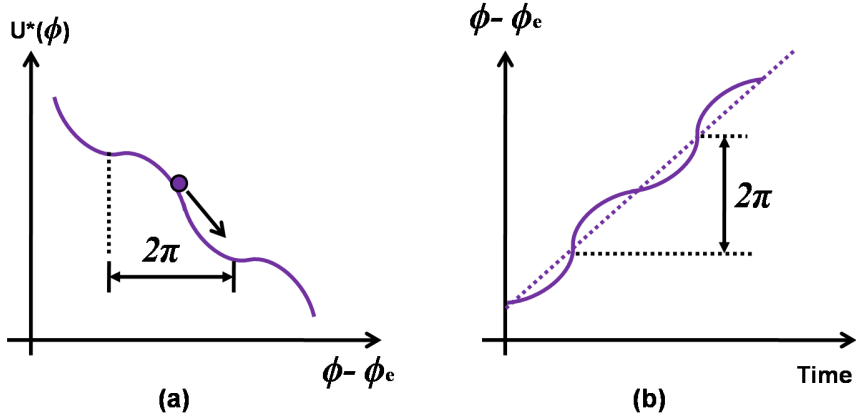
15

Figure 2.7: Effect of large detuning $\omega_o - \omega$ for $\omega_o > \omega$ at a constant ϵ [31]: (a) for large detuning, there no local minima present in the tilted potential and the phase point slides down. (b) The phase grows at some average value shown as the dotted line which determines the beat frequency. Note that for $\omega_o < \omega$, the potential is tilted the other way.

be denoted as Ω_b which is commonly referred to as *the beat frequency* [31].

Quasiperiodicity

As shown in Fig. 2.7(a), the force creates ripples in the titled potential but it can not overcome the effect of detuning to induce a minimum. As a result the phase difference does not stay constant and it grows in time with fluctuations as shown in Fig. 2.7(b). Here the slope of the curve shown by the dotted line is the beat frequency Ω_b. As noted before the phase point rotates counterclockwise in the case of $\omega_o > \omega$. The rotation of the phase point with the beat frequency appears such that $\Omega_b < \omega_o - \omega$. This is because the fixed point sliding down the potential nearly stops at the original location of minima where the slope is minimum. Now we have a fast rotation based on $\Omega_b + \omega$ and a slow rotation based on Ω_b which modulates the growth of the phase and hence the amplitude of the vibrations. The combined frequency of the system is now $\Omega_b + \omega < \omega_o$. This motion is known as *quasiperiodic* if the ratio $\dfrac{\Omega_b + \omega}{\Omega_b}$ is irrational [31]. In the quasiperiodic flow all trajectories of the system wind around endlessly, never intersect each other, and come arbitrarily close to each other on a torus with coordinates ϕ and ϕ_e [3]. Quasiperiodicity is related to incommensurate (irrational) ratio such that the fast periodic orbit does not go through the same initial conditions; it rotates around in a loop with a smaller periodic orbit as shown in Fig. 2.8(a). Therefore the quasiperiodic behavior can be determined by a closed loop, e.g. the points rotate around in a loop on the Poincaré section taken at every period as shown in Fig. 2.8(b). On the other hand, a commensurate (rational) ratio of frequencies results in the periodic orbits with two different frequencies that eventually go through the same initial conditions as shown in Fig. 2.8(b). Hence the nonquasiperiodic behavior (i.e. commensurate ratio of the frequencies) can be
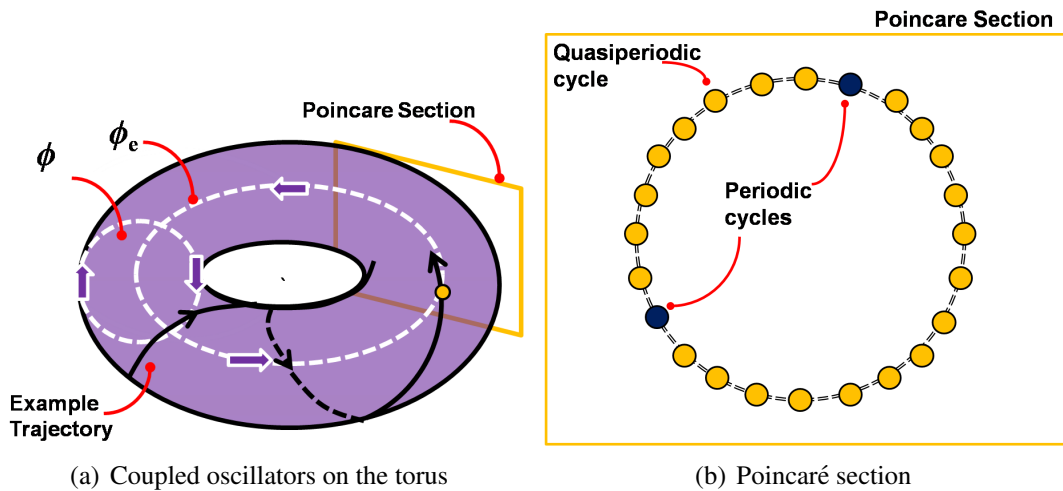
16

(a) Coupled oscillators on the torus   (b) Poincaré section

Figure 2.8: Coupled phase dynamics on a torus: (a) here the two oscillators denoted by ϕ_e and ϕ chart two frequency loops at different frequencies, the combination of which describes the torus surface. An example trajectory of the driven autonomous system is shown for large detuning in which $\omega_o > \omega$. For any given initial condition, the trajectory never passes through the same point again on the Pointcaré section taken at every period; it only comes infinitely close. The result of this is (b) Pointcaré section with many fixed points that enclose a circle. Note that this happens only if the ratio of the frequency is irrational. However for a commensurate ratio there are two distinct fixed points where the driven system crosses and returns.

distinguished by observing whether the points on the section would fill in the loop or not. In this case, the Poincaré section has a finite number of closely placed points. Based on the above, we can note that quasiperiodic motion exhibits distinctive harmonics and interlacing of harmonics.

It follows from the above discussion that for large detuning a large force is needed to synchronize the system. Also note that quasiperiodic behavior can also occur naturally when two autonomous systems are connected together by weak coupling. Here we only have to replace the excitation force with an another autonomous system. The rest of the concepts are applicable to the coupled system.

2.2.4 Region of Synchronization

As noted before, when the amplitude of the excitation force ϵ is able to entrain the autonomous system and create the phase-locked state depending on the detuning $\omega_o - \omega$, the frequency of the entrained system Ω becomes equal to ω as shown in Fig. 2.9(a). This is known as as *frequency-locking*. We can expect that for increasing values of ϵ, the frequency range of ω, in which $\Omega = \omega$ occurs, also increases as shown in Fig. 2.9(b). When plotted strictly as the excitation amplitude versus the excitation frequency, the curve captures the
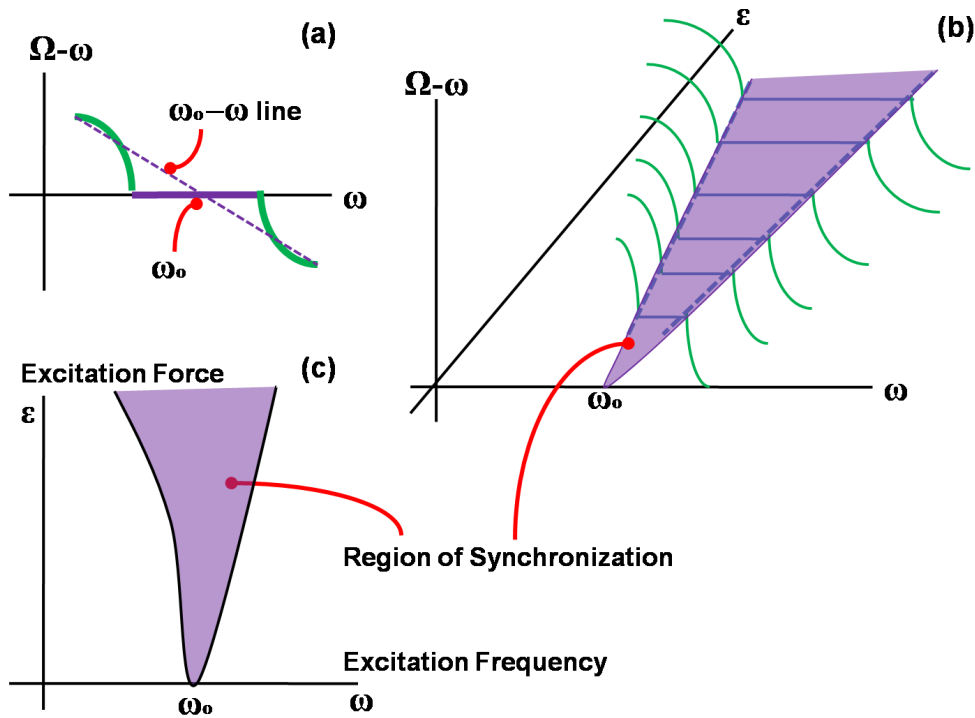
Figure 2.9: Region of synchronization and effects of detuning [31]: (a) difference of the entrained frequency vs the excitation frequency for a fixed ϵ is shown. Here the frequency-locking region is where the difference $\Omega - \omega$ is zero. The dashed line represents $\omega_o - \omega$ vs ω. Outside of the entrained region the force is too weak to entrain the system and curve eventually meets the dashed line. (b) For increasing values of ϵ the curves would show an increase in the range of synchronization. (c) The family of ϵ curves can now be reduced to a simpler form where the relationship between the excitation force and excitation frequency can aptly describe the synchronized state of the driven system. This curve is called the *Region of Synchronization* or Arnold Tongue. Note that close to the boundary the force can still pull Ω to ω. These are the sensitive regions where the governing bifurcations create an abrupt change in behavior of the system.

synchronized behavior of the driven system as shown in Fig. 2.9(c). Note that in the experiments the region of synchronization may not extend all the way to ω_o for very small ϵ. Depending on the damping and the dynamics of the system, the synchronization can be lost or the region for small ϵ can be open or closed (see Chapter 5 and 6). Other sensitive areas are the boundaries of the synchronization region where the bifurcations can change in behavior of the system making the system highly sensitive to a sudden change. The example curves shown in these figures chart the behavior of synchronization region close to and at $\Omega = \omega$. However other regions of synchronization may be observed depending on the nonlinearity present in the autonomous system and the excitation force. For example, in parametrically
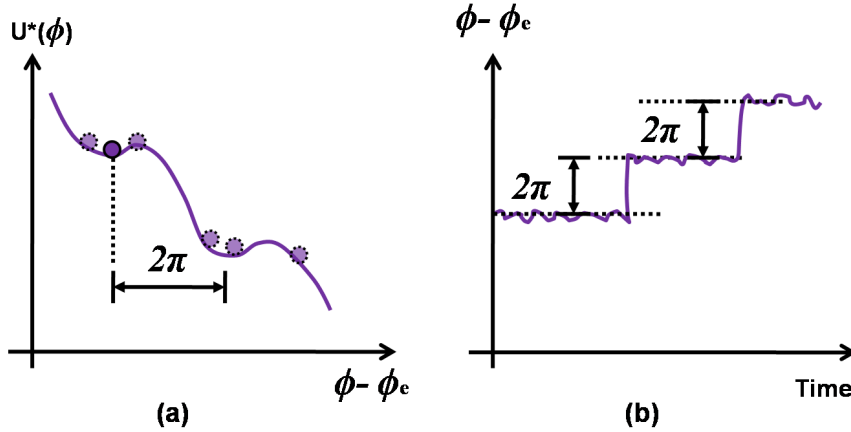
Figure 2.10: Effect of noise in small detuning $\omega_o - \omega$ for $\omega_o > \omega$ at constant ϵ [31]: (a) Gaussian noise can make the stable equilibrium point oscillate in the potential well $U^*(\phi)$ and can make it jump over the barrier. (b) Phase slips can occur in the presence of strong noise. This is similar to the transitions at the boundaries of the synchronization region however noise creates random phase-slips.

excited nonlinear MEMs devices, $\Omega : \omega = 1 : 2$ region can be observed [12, 36]. Following the behavior of system around the fundamental frequency and its harmonics, the regions of synchronization may exist for $\Omega : \omega = 3 : 1$, $\Omega : \omega = 2 : 1$, $\Omega : \omega = 1 : 2$, $\Omega : \omega = 1 : 3$, and so on. Note that for these specific ratios, the regions of synchronization are usually narrow. Additionally for higher values of ϵ the regions of synchronization may overlap with each other.

Finally, it is important to note that the effect of the synchronization, the criteria for synchronization, and the region of synchronization can be viewed in different ways as mentioned in this chapter; however the basis of any such phenomena is strictly the experimental data. As it often happens, the experimental data is often obscured with noise and it has an effect on synchronization such that the boundaries that define synchronized behavior can be skewed. In some cases they may be very obscure in the presence of the unbounded noise (e.g. Gaussian) which can cause phase-slips [31] and as a result the phase point can jump over the barrier and can travel between the minima at random as shown in Fig. 2.10(a). The phase-slips can make the phase difference jump at random and make the phase grow at an average rate as shown in Fig.2.10(b). Thus the phase slips can eventually destroy both the phase-locked and frequency-locked states if the noise is strong.

2.3 Phase Dynamics

In this section, the forced system mentioned the previous section is modeled by Adler equation and the stability of the forced system based on this equation is discussed [3] [31].

Since the phase of the forced system is affected by the excitation force, it is useful to

examine the dynamics of phase of the autonomous system [37]. Let the phase of the forced system be defined as ϕ and define the phase dynamics as [3] [31],

$$\dot{\phi} = \omega_\text{o} + \epsilon G(\phi, \phi_\text{e}) \tag{2.1a}$$

$$\dot{\phi}_\text{e} = \omega. \tag{2.1b}$$

Where $\phi_\text{e} = \omega t$ and it denotes the phase of the excitation force, ω_o and ω denote the frequency of the autonomous system and the excitation force, respectively. ϵ is the amplitude of the excitation force, and $G(\phi, \phi_\text{e})$ is the 2π periodic phase function that depends on the form of the limit cycle of the autonomous system and the type of the excitation force. After expanding it into a Fourier series, $G(\phi, \phi_\text{e})$ contains fast varying and slowly varying [37] [31]. The slowly varying terms can be gathered as $g(\phi - \phi_\text{e}) = \epsilon \sin(\phi - \phi_\text{e})$. After averaging over the fast varying terms, the dynamics of the phase difference, $\varphi = \phi - \phi_\text{e}$, can be described by the Adler Equation as [31] [38],

$$\dot{\varphi} = \Delta\omega + \epsilon \sin \varphi. \tag{2.2}$$

Where $\Delta\omega = \omega_\text{o} - \omega$ and it denotes the detuning effect. Now we have two parameters ϵ and $\Delta\omega$; the interplay of these two parameters dictate the synchronization properties.

2.3.1 $|\Delta\omega| < \epsilon$

Figure 2.11 shows the periodic phase dynamics for $|\Delta\omega| < \epsilon$ and depicts frequency-locking and phase-locking of the forced system. Here Figs. 2.11(a) and 2.11(b) show the time-series for $\omega_\text{o} > \omega$ and $\omega_\text{o} < \omega$, respectively. It can be seen that the solution for φ involves unstable and stable equilibria and the phase tends to the stable equilibrium as the time progresses. The constant phase values indicate that the system reaches a stable periodic limit cycle. Similarly Figs. 2.11(c) and 2.11(d) show the phase-space for $\omega_\text{o} > \omega$ and $\omega_\text{o} < \omega$, respectively. To determine the stability of the equilibrium, first we set L.H.S of Eq. 2.2 to zero. Then from the R.HS. we obtain the equilibrium points. Examining the second derivatives at these points provide us with the stability criteria, e.g. if $\ddot{\varphi} < 0$ then it is stable and if $\ddot{\varphi} > 0$ then it is unstable. These points are marked in the figures for $\varphi \in [-2\pi, 2\pi]$. Now the time evolution of an overdamped stable phase point is equivalent to its motion on an inclined potential plane, which can be described as, $\dfrac{\mathrm{d}\varphi}{\mathrm{d}t} = -\dfrac{\mathrm{d}U(\varphi)}{\mathrm{d}\varphi}$. From Eq. 2.2, it follows that $U(\varphi) = -\Delta\omega\varphi + \epsilon \cos \varphi$. The potential function is depicted in Figs. 2.11(e) and 2.11(f) for $\omega_\text{o} > \omega$ and $\omega_\text{o} < \omega$, respectively. By examining the potential function we can see that the excitation force creates valleys and peaks as the phase evolves over time. The peaks or barriers are harder to overcome for $|\Delta\omega| < \epsilon$ and the phase-points stays *trapped* at the stable equilibrium point (see Fig. 2.6(a)). Also note that the direction of motion and hence the slope of the potential function is in opposite directions for $\omega_\text{o} > \omega$ and $\omega_\text{o} < \omega$. Consequently $\omega_\text{o} > \omega$ and $\omega_\text{o} < \omega$ relate to the left and right boundaries in Fig. 2.9, respectively.
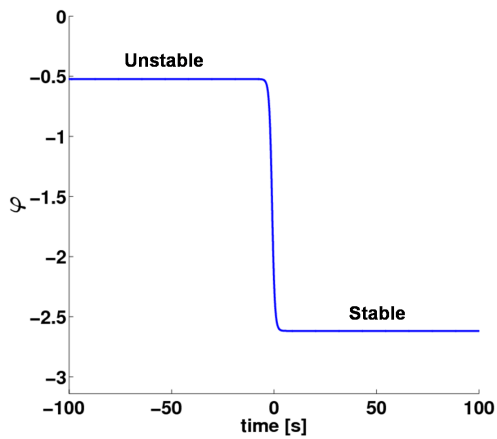
(a) Time-series: $\Delta\omega = 0.786$ and $\epsilon = 1.571$
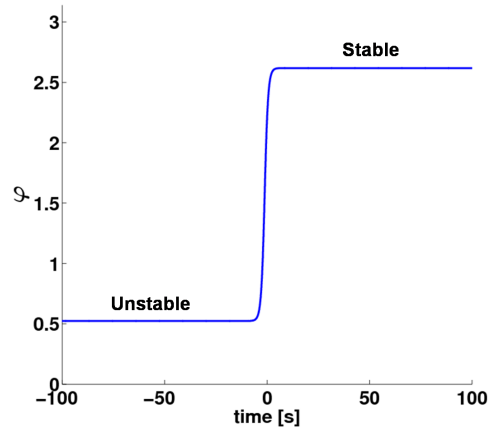
(b) Time-series: $\Delta\omega = -0.628$ and $\epsilon = 1.257$
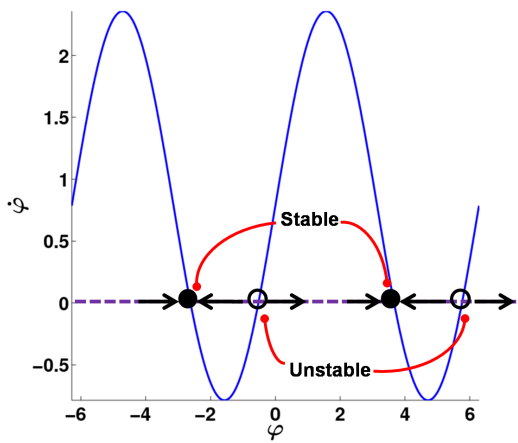
(c) Phase-space: $\Delta\omega = 0.786$ and $\epsilon = 1.571$
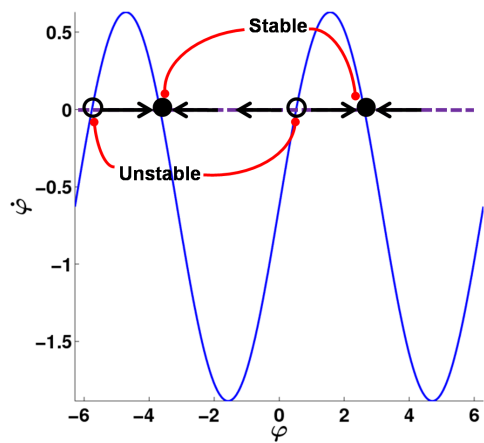
(d) Phase-space: $\Delta\omega = -0.628$ and $\epsilon = 1.257$
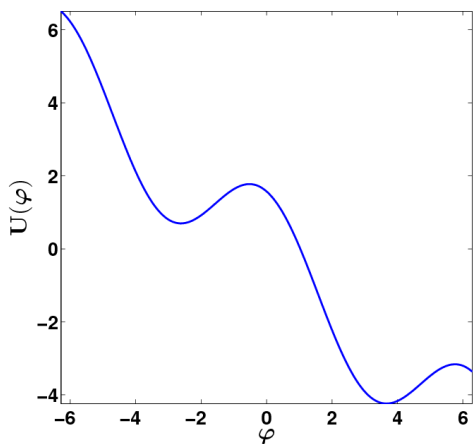
(e) Potential: $\Delta\omega = 0.786$ and $\epsilon = 1.571$
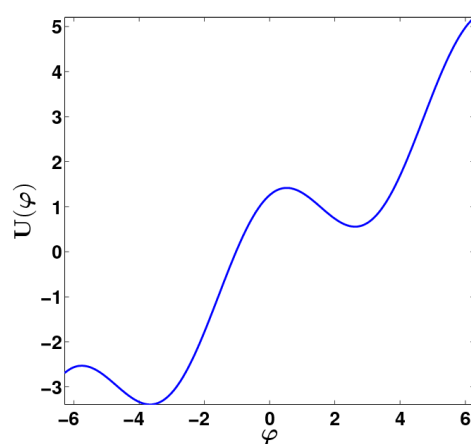
(f) Potential: $\Delta\omega = -0.628$ and $\epsilon = 1.257$

Figure 2.11: Periodic cycles with $|\Delta\omega| < \epsilon$: (a), (c), and (e) depict the states of the system for $\omega_\mathrm{o} > \omega$ whereas (b), (d), and (f) show the system for $\omega_\mathrm{o} < \omega$. (c) and (d) show the equilibrium points and their stability properties. (e) and (f) show the potential function to see how the excitation force creates shallow valleys where the phase points can be trapped.

2.3.2 $|\Delta\omega| > \epsilon$

Figure 2.12 shows the phase dynamics for $|\Delta\omega| > \epsilon$ and depicts the asynchronous or the quasiperiodic motion of the forced system. Here the top parts of Figs. 2.12(a) and 2.12(b) show the time-series for $\omega_o > \omega$ and $\omega_o < \omega$, respectively. It can be seen that the time-series for φ shows no stable state and the phase oscillates as the time progresses. The middle parts in Figs. 2.12(a) and 2.12(b) show the unwrapped phase, where the jumps between π and $-\pi$ have been removed. Here we see that the phase does not stay constant and it exhibits ripples as it grows. The growth of phase with such oscillations can be identified as the beat frequency of the quasiperiodic limit cycles. Figs. 2.12(c) and 2.12(d) show the phase-space for $\omega_o > \omega$ and $\omega_o < \omega$, respectively. We can see that the system no longer contains any equilibria and as a result the phase point rotates (see Fig. 2.8). The potential function is depicted in Figs. 2.12(e) and 2.12(f) for $\omega_o > \omega$ and $\omega_o < \omega$, respectively. Here we can see that the barriers created by the excitation force barriers are shallow and as a result the phase-point is free to travel. Note that the slopes of the potential functions in Figs. 2.12(e) and 2.12(f) are steeper in the shallow regions than the barrier regions, which determine the fast varying and slow varying time cycles.

2.4 Summary

In this chapter, the basics of synchronization were presented. To begin with synchronization was shown as an essential phenomena associated with self-organization which occurs naturally. Next, the specifics of synchronization the coupled systems were presented from the perspectives of the mutual coupling and the excitation force. This entailed the concepts of phase-locking and frequency-locking. Region of synchronization was also discussed. Phase dynamics of the forced system and the governing parameters, e.g. excitation amplitude and frequency detuning, were discussed.

(a) Time-series: $\Delta\omega = 0.786$ and $\epsilon = 0.628$

(b) Time-series: $\Delta\omega = -0.628$ and $\epsilon = 0.503$
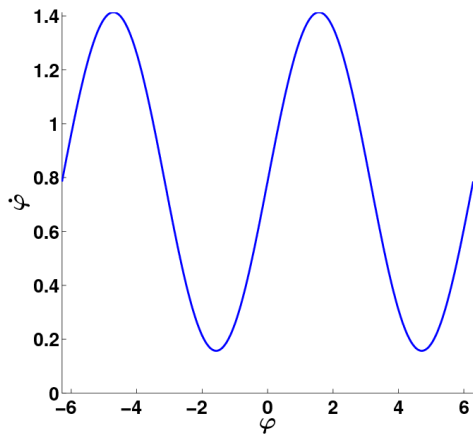
(c) Phase-space: $\Delta\omega = 0.786$ and $\epsilon = 0.628$
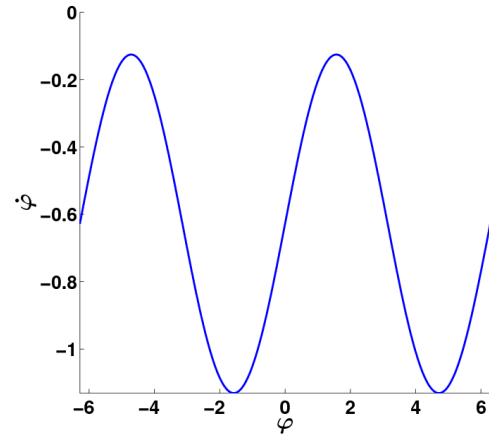
(d) Phase-space: $\Delta\omega = -0.628$ and $\epsilon = 0.503$
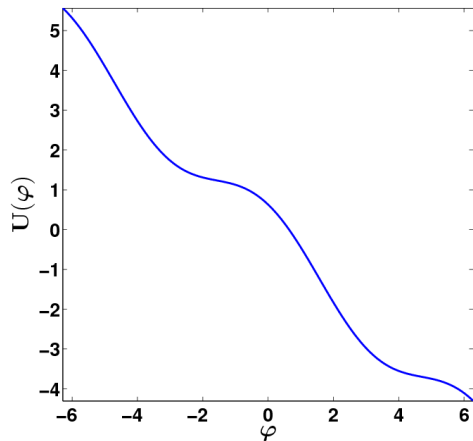
(e) Potential: $\Delta\omega = 0.786$ and $\epsilon = 0.628$
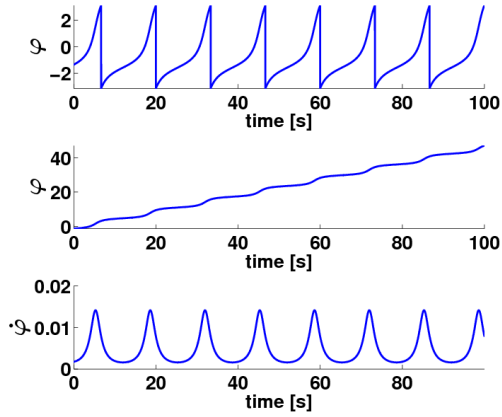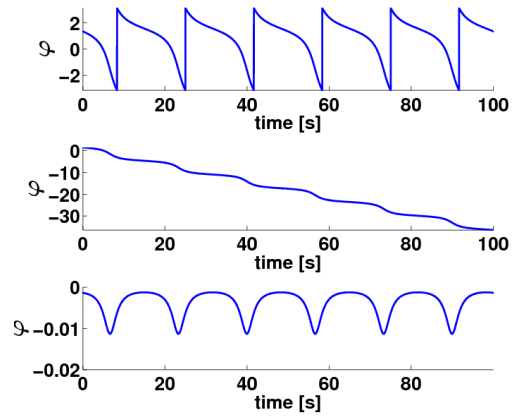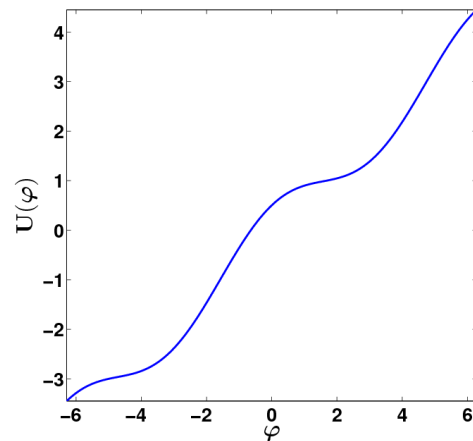
(f) Potential: $\Delta\omega = -0.628$ and $\epsilon = 0.503$

Figure 2.12: Quasiperiodic cycles with $|\Delta\omega| > \epsilon$: (a), (c), and (e) depict the system for $\omega_o > \omega$ and (b), (d), and (f) depict the system for $\omega_o < \omega$. (a) and (b) also show the beat frequency from the unwrapped phase. The equilibrium points have vanished in (c) and (d). (e) and (f) show that barriers created by the excitation force in the potential function can not retain the phase point.

23

Chapter 3

Harmonically Excited MEMS Resonator

3.1 Introduction

Today the MEMS research is rich with many different types of resonators. Resonant MEMS devices can be viewed as miniature machines designed for very specific purposes. They are fabricated using typical methods adopted from traditional IC fabrication technologies. They are simple devices in that there are few elements such as beams, lumped masses, and electrodes. The forces acting on these devices at microscale are the same as those encountered at the macroscale. These forces stem from elastic, magnetic, electromagnetic, and aerodynamic sources. However at microscale, additional forces including van der Waals, adhesion, Casimir, and electrostatic forces also play major role [39]. The combination of these effects and the interface of MEMS devices with electronics provide ample opportunities as well as challenges. Typically MEMS resonators are at the scale of about 10^1 to 10^4 μm, can be designed with natural frequencies in the range between 10^4 to 10^9 Hz, and can exhibit Q factors in the range of 10 to 10^5 [39].

A variety of actuation, excitation, and detection techniques exist that utilize mechanical, opto-mechanical, and electrostatic excitation. Most of the design effort is spent on creating viable flexures and meeting the specifications of the design after choosing a specific excitation method. Fig. 3.1 shows the major types of resonators that can be readily found in MEMS. Disk resonator and lame-mode resonators, which are shown in Fig. 3.1(a) and Fig. 3.1(b) respectively, provide multiple degrees of freedom depending the method of excitation, detection, and the deformation of the springs. Beam resonators, as shown in Fig. 3.1(c), are used to restrict the movement and layout area on the chip. The resonators shown in Figs. 3.1(a)–(c) are usually classified as *parametrically excited* resonators. Fig. 3.1(d) shows a typical comb-drive resonator that exhibits lateral motion and is classified as *harmonically excited* resonator. This classification is primarily based on the effect of the excitation force on the displacement and hence the resonant behavior of the device.

(a) Disk resonator

(b) Lame-mode resonator

(c) Beam resonator

(d) Comb-drive resonator
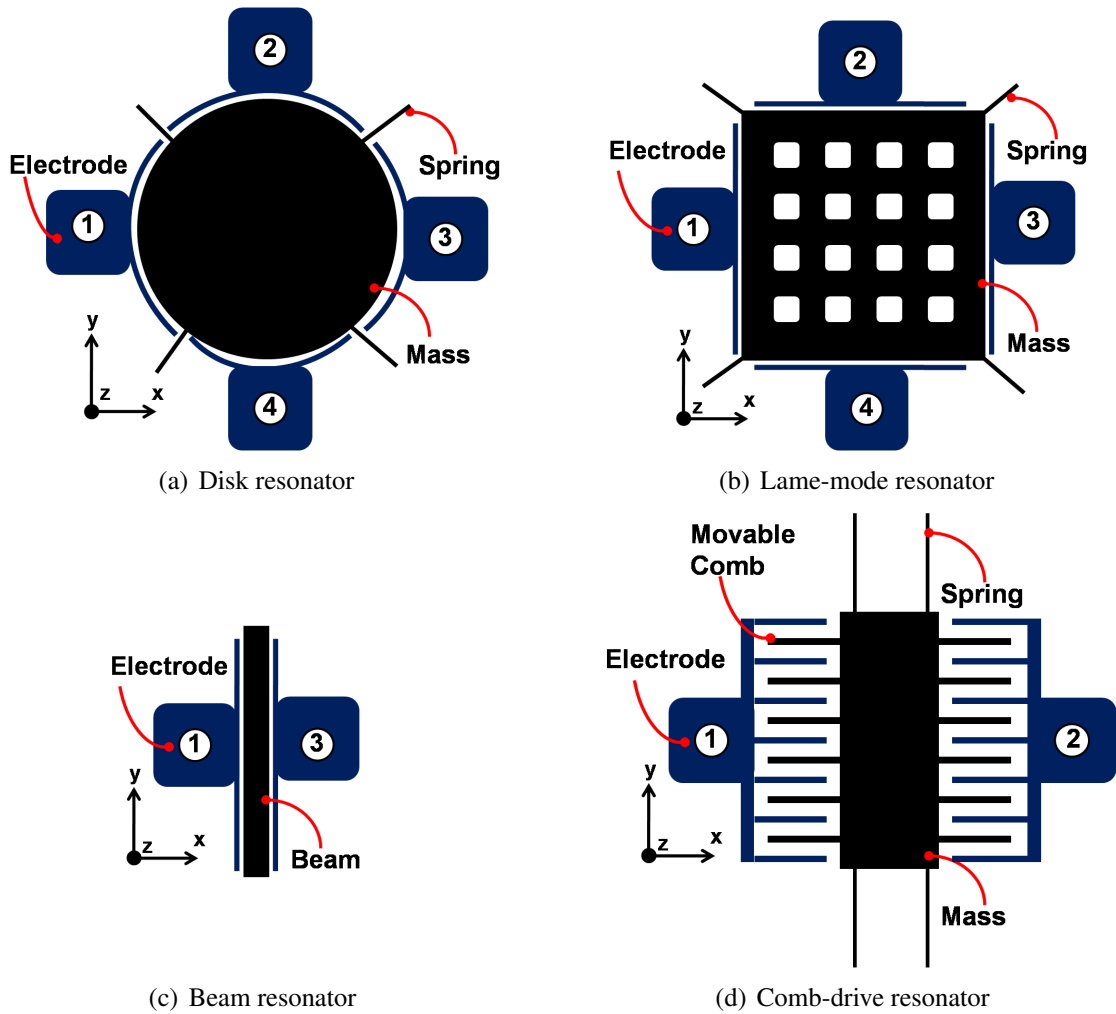
Figure 3.1: Major resonator types are shown. (a) Disk resonator where multiple modes of vibrations can be induced. (b) Lame-mode resonator which are commonly found in BAW resonators that utilize normal and translational modes. (c) Beam resonator is the simplest. (d) Comb-drive resonator. Note that parametric excitation is used in (a)–(c) whereas (d) is excited harmonically. In the figures, numbers represent different electrodes which can be utilized for different excitation and/or detection schemes, which in turn create interesting dynamics.

3.2 Electrostatic Actuation

Figure 3.2 shows the diagram of a comb-drive under study that can be used in the prototype design. The various parameters listed in the figure are as follows: L_s is the length of spring along y-axis, L_1 is the length of spring along x-axis, s is the overlap between the fingers, L is the length of the fingers, g is the gap between the fingers, W is the width of the fingers, T_{th} is the thickness of the fingers (the thickness of the layer on which the mass is
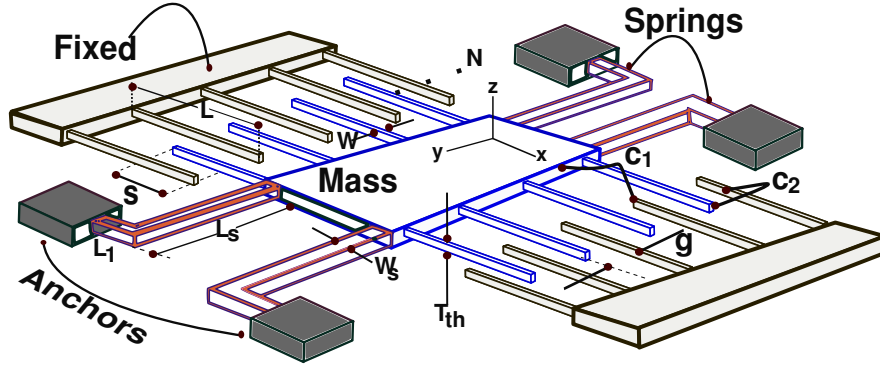
Figure 3.2: Diagram of a laterally driven comb-drive resonator: important dimensions and parameters, and their corresponding locations are indicated.

fabricated), C_1, C_2 are the capacitances between the cavity of fixed fingers and the movable fingers of the shuttle mass along x-axis and y-axis respectively, and N is the total number of movable fingers on both sides. When a voltage is applied between the fixed combs and the movable combs, it generates an electric field E. This field results in the electrostatic potential energy U_e. The movement of the mass along x-axis is a result of the electrostatic force exerted on the mass in this field. Here we can ignore C_1 since $C_2 \gg C_1$ due to the proximity of the fixed comb to the movable comb, i.e. $(L - s) \gg g$. The electrostatic force depends on the change in capacitance with respect to distance traveled in x direction and the voltage between the electrodes. This dependence is shown by deriving of the electrostatic potential energy in the next section.

3.2.1 Electrostatic Potential Energy

Figure 3.3 shows the principles of stored energy in a cavity consisting of a dielectric with nonlinear capacitive response and co-energy associated with it. There are two ways of generating electrostatic force, F_e, in a parallel plate capacitor as shown in Fig. 3.3(a). Co-energy, W^*, is the resultant energy based on the voltage control whereas the stored energy is dependent on the amount of charge present on the two parallel plates as shown in Fig. 3.3(b). Hence there are two ways to change the energy that is stored between the two parallel plates: (1) change the charge q or (2) change the separation g. If the stored energy can be converted into work, W, then let dW be defined as,

$$dW(q, g) = V dq + F_e dg \qquad (3.1)$$

Stored energy can be converted into work by increasing/decreasing gap after charging the capacitor at a zero gap. This task can be extremely difficult and therefore controlling the energy by charge is a major challenge given the small capacitance ($\sim$pF) of a MEMS capacitor fabricated in the current MEMs and IC fabrication technologies. However controlling the energy by changing the voltage is easier in a MEMS capacitor. As shown in Fig. 3.3(a), with
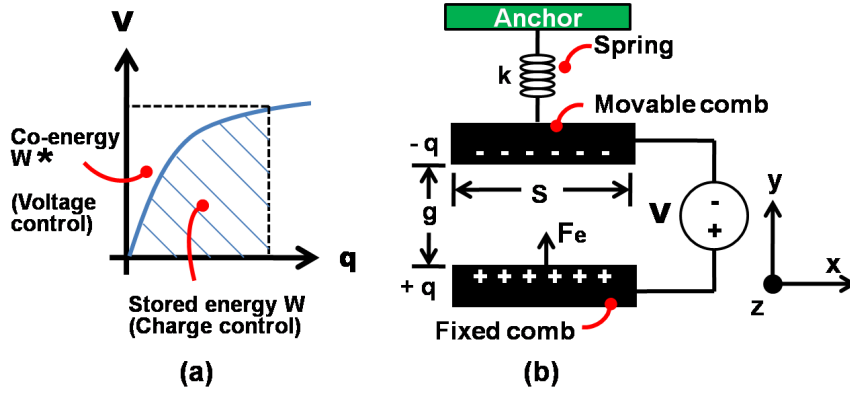
Figure 3.3: Principles of electrostatic actuation based on co-energy: (a) voltage versus charge curve, which shows nonlinear capacitive profile, can be controlled with either voltage or charge. Voltage controlled part of the integrated area is called co-energy and is easier to implement in a MEMS device. (b) By connecting a parallel plate capacitor suspended by a spring with spring constant k to a voltage source, the electrostatic force F_e is generated and it depends on the gap g.

voltage as the control parameter, the energy in a parallel plate capacitors can be defined by co-energy W^* and the energy change dW^* due to dV can be defined as,

$$W^*(V, g) = qV - W, \tag{3.2a}$$

$$dW^*(V, g) = qdV + Vdq - dW, \tag{3.2b}$$

$$= qdV + F_e dg. \tag{3.2c}$$

Where dW was substituted from Eq. 3.1. Note that qV is the total energy in the voltage versus charge curve shown in Fig. 3.3(a). Here Vdq is the electrical work and $F_e dg$ is the mechanical work done due to electrostatic force F_e. The capacitance between two parallel plates can be described as $C = \epsilon A/g$; where A = parallel plate area, g = gap between the plates, and ϵ = permittivity = $\epsilon_o \epsilon_r$. In air, $\epsilon = \epsilon_o$. Therefore, the total capacitance between the movable fingers and the fixed fingers on either side (shown as C_2 in Fig. 3.2) can be defined as,

$$C(x) = \frac{2N\epsilon_o(s + x)T_{th}}{g}, \tag{3.3}$$

where, x = displacement in x direction, s = overlap, and T_{th} = thickness of the structural layer (see Fig. 3.2). If we assume that the gap is fixed, the capacitor is charged, and it is in steady-state then the second term in the expression of $dW^*(V, g)$ in Eq. 3.2c drops out. Then for a charge at fixed gap, we can evaluate the co-energy as a function of gap and voltage by first finding the associated voltage as a function of gap and charge as a function of gap and

voltage as,

$$V' = - \int_0^g E \, dg' = \left(\frac{q}{\epsilon A} \right) g,$$

$$q(g, V') = \frac{\epsilon A}{g} V' = C(x) V'.$$

(3.4)

Substituting the above into Eq. 3.2 and integrating it gives us the co-energy expression,

$$W^* = \int_0^V q(g, V') \, dV' = \int_0^V C(x) V' \, dV' = \frac{1}{2} C(x) V^2.$$

(3.5)

From Eq. 3.5, we can see that the capacity to do work due to the change in potential dV is same as the electrostatic potential energy. Let us assume that the suspension beams exert a linear restoring force (as first approximation) as the mass moves between the fixed combs. Let the restoring force result from the mechanical potential energy U_m. Assuming voltage-controlled electrostatic actuation as above, we can define the total energy present between the fixed and movable combs in x direction as,

$$U_T(x, V) = \underbrace{\frac{1}{2} k x^2}_{U_m} - \underbrace{\frac{1}{2} C(x) V^2}_{U_e},$$

(3.6)

where k = spring constant in x direction and x = the displacement in x direction. Taking partial derivative of $U_T(x, V)$ with respect to x gives us the total force in x direction,

$$F_T(x, V) = kx - \frac{1}{2} \frac{\partial C(x)}{\partial x} V^2.$$

(3.7)

Now considering the second term in the above equation and taking the derivative of $C(x)$ with respect to x gives us the electrostatic force in *x direction* as,

$$F_e = \frac{N \epsilon_o T_{th} V^2}{g}.$$

(3.8)

Note that the electrostatic force exerted on the mass in x direction in a laterally driven comb-drive does not depend on displacement in x direction. This conclusion is based on the assumption that there is no movement in y direction which can offset the movement in x direction. Also, we have ignored the capacitance between the movable fingers and cavity of the fixed fingers in x direction (denoted as C_1 in Fig. 3.2). Let the excitation voltage $V = V_{dc} + V_{ac} \cos(\omega t)$, where V_{dc} is the bias and V_{ac} is the ac amplitude. Then F_e becomes,

$$F_e = \frac{N \epsilon_o T_{th}}{g} \left(V_{dc}^2 + 2 V_{dc} V_{ac} \cos(\omega t) + V_{ac}^2 \cos(\omega t)^2 \right),$$

(3.9a)

$$= \frac{N \epsilon_o T_{th}}{g} \left(V_{dc}^2 + \frac{1}{2} V_{ac}^2 + 2 V_{dc} V_{ac} \cos(\omega t) + \frac{1}{2} V_{ac}^2 \cos(2\omega t) \right)$$

(3.9b)

The above expression contains dc terms, fundamental excitation frequency and the second harmonic of the excitation frequency hence the name *harmonically excited* resonator.

3.2.2 Dynamics

The dynamics of laterally driven comb-drive with one degree of freedom can be represented as,

$$\underbrace{m\ddot{x}}_{F_a} + \underbrace{c\dot{x}}_{F_d} + \underbrace{k_1 x}_{F_k} = F_e, \tag{3.10}$$

where, x = the displacement along the x-axis, m = the total mass including the fingers, c = damping coefficient, and k_1 = linear spring constant of the suspension beams in x direction. Here it is assumed that as F_e changes direction (due to the change in polarity of V), the restoring force F_k and the damping force F_d also change their directions to oppose F_e.

Damping

Viscous damping, which is also known as slide-film damping, is the dominant source of energy dissipation in laterally driven comb-drives. As the movable finger slides in the cavity of the fixed fingers, it experiences the slide-film damping on each side. Additionally, the mass experiences damping in z direction, known as squeeze-film damping, between the bottom surface of the mass and the top surface of the surface. Thus the total damping in x direction can be modeled by (1) the flow between the shuttle and the ground plate and (2) Couette flow between the fingers [40] as,

$$c = \underbrace{\mu_e \frac{A}{z_o}}_{\text{squeeze-film damping}} + \underbrace{\mu_e \frac{2NLT_{th}}{g}}_{\text{slide-film damping}}. \tag{3.11}$$

Where, μ_e = effective viscosity constant = 1.66×10^{-5} N s/m^2 [41], A = area of the shuttle including the fingers, and z_o = distance between the bottom of the mass and substrate. Given high aspect ratio between thickness and width, we can ignore squeeze-film damping assuming that the springs do not allow any oscillation in z direction. See Appendix B for a pictorial representation of the damping.

Spring Constant

To begin with, the spring can be modeled as a straight cantilever beam. Using Euler-Bernoulli beam theory the linear spring constant in the x direction, due to load at the tip of the beam, can be defined as,

$$k_1 = \frac{12 I_x E}{L_s^3} = \frac{E T_{th} W_s^3}{L_s^3}, \tag{3.12}$$

where, I_x = area moment of inertia (second moment of area) in x direction = $\dfrac{T_{th} W_s^3}{12}$, E = Young's modulus, T_{th} = thickness of the structure, W_s = width of the spring, and L_s = length of the spring.

Under large deformation the spring can harden and can exhibit nonlinear stiffness k_3. If we assume that the nonlinearity in the comb-drive is only due to the springs, then we
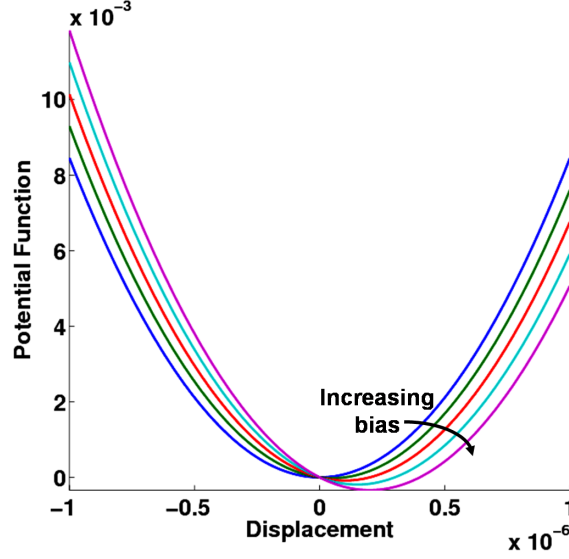
Figure 3.4: Effect of increasing the bias voltage: as the bias is swept, the equilibrium point shifts to the right when the energy in the MEMS spring, described by a single well potential function, reaches steady state after a small ac perturbation.

can approximate it by using the Duffing equation. Assuming that no even order terms are present, the nonlinear restoring force can be more accurately represented as, $F_k = k_1 x + k_3 x^3$. Depending on the sign of k_1, the spring can be modeled as hard if $k_1 > 0$ or soft if $k_1 < 0$. As displacement increases, a hard spring exhibits an increment in restoring force whereas a soft spring exhibits a decrement in restoring force. The following equation represents a nonlinear MEMS resonator with a cubic spring constant term [12].

$$m\ddot{x} + c\dot{x} + k_1 x + k_3 x^3 = A_d \cos(\omega_d t), \tag{3.13}$$

where, ω_d is the angular excitation frequency and A_d is the excitation amplitude. As noted before the potential function is based on the hard-spring and is uniwell. Note that the electrostatic force expression is simplified as sinusoidal excitation with fundamental excitation frequency by ignoring higher order terms. Typically in a MEMS resonator the voltage is applied as ac excitation + dc bias. This is evident from Eq. 3.9, where the R.H.S. contains a constant plus a sum of two harmonic functions[1]. If $V_{dc} >> V_{ac}$ then the second harmonic terms can be neglected. However the effect of bias can also be ignored as it simply tilts the potential well as shown in Fig. 3.4 and changes the equilibrium point. The following equation represents the MEMS resonator with nonlinearity in dimensionless form by substituting $\tau = \omega_0 t$ in Eq. 3.13.

$$x'' + \delta x' + x + \beta x^3 = \epsilon \cos(\omega \tau), \tag{3.14}$$

---

[1] If a push-pull (differential) excitation scheme is used then the constant dc terms cancel out completely because $F_e = (1/2)(\partial C/\partial x)(V_+^2 - V_-^2) = 2(\partial C/\partial x)(V_{dc} V_{ac} \cos(\omega t))$.

where ($'$) and ($''$) represent first and second order derivatives with respect to the normalized time τ. ω_0 denotes the natural frequency used in the normalization. Then it follows that $\delta = c/(m\omega_0)$, $\beta = k_3/(m\omega_0^2)$, $\epsilon = A_d/(m\omega_0^2)$, and $\omega = \omega_d/\omega_0$.

3.2.3 Analytical Solution

Equation 3.14 can be represented as a system of one dimensional set of nonlinear equations as follows:

$$x_1' = x_2 \tag{3.15a}$$

$$x_2' = -\delta x_2 - x_1 - \beta x_1^3 + \epsilon \cos(\omega\tau) \tag{3.15b}$$

Using van der Pol transformation, let x_1 and x_2 be presented as,

$$x_1 = u_1 \cos(\omega\tau) - u_2 \sin(\omega\tau) \tag{3.16a}$$

$$x_2 = -\omega(u_1 \sin(\omega\tau) + u_2 \cos(\omega\tau)). \tag{3.16b}$$

After substituting Eq. 3.16 in Eq. 3.15, multiplying the corresponding equations with $\sin(\omega\tau)$ and $\cos(\omega\tau)$, rearranging terms, and averaging over $\left[0, \dfrac{2\pi}{\omega}\right]$ we obtain,

$$u_1' = \frac{1}{2\omega}\left[-\delta\omega u_1 + (\omega^2 - 1)u_2 - \frac{3\beta}{4}(u_1^2 + u_2^2)u_2\right] \tag{3.17a}$$

$$u_2' = \frac{1}{2\omega}\left[-\delta\omega u_2 - (\omega^2 - 1)u_1 + \frac{3\beta}{4}(u_1^2 + u_2^2)u_1 - \epsilon\right]. \tag{3.17b}$$

Substituting $u_1 = r\cos\theta$ and $u_2 = r\sin\theta$ in Eq. 3.17, multiplying the corresponding equations with $\cos\theta$ and $\sin\theta$ and rearranging the terms, we obtain the amplitude and the phase as follows,

$$r' = \frac{1}{2\omega}\left[-\delta\omega r - \epsilon\sin\theta\right] \tag{3.18a}$$

$$\theta' r = \frac{1}{2\omega}\left[-(\omega^2 - 1)r + \frac{3\beta}{4}\beta r^3 - \epsilon\cos\theta\right]. \tag{3.18b}$$

Parameter Values

In this section, the estimation of parameter values in Eq. 3.13 is presented.

Mass   The value of the mass m is the least affected parameter during MEMS fabrication [19]. This value is calculated from $m = Ah\rho = 5.92 \times 10^{-9}$ kg, where A is the total area obtained from the layout, h is the structural thickness, and ρ is the density of Silicon (about 2.33×10^3 kg/m^3).

Spring Constants From the spring design equations for the folded fixed-guided beams, the spring constant k_1 is approximated as 30.97 N/m. This value is verified in Comsol by plotting an applied force versus displacement for a range of applied force magnitudes and by estimating the slope. For simulation purposes, the nonlinear spring constant k_3 is estimated as 100 N/m^3.

Natural Frequency Using these values the natural frequency of the device is approximated as 11512 Hz from $f_0 = \omega_0/2\pi$, where $\omega_0 = \sqrt{k_1/m}$. The value of f_0 can also verified by running modal analysis (see Chapter 4) and frequency sweep analysis in Comsol.

Damping In thin-film MEMS processes, the substrate underneath the structure is one of the major sources of energy loss due to the effect known as squeeze-film damping [19]. In SOIMUMPs, which was the process used for the fabrication of the resonators, the substrate under the spring-mass structure is completely removed (see Chapter 4). This etching step lowers the energy loss in the structure. Therefore it is anticipated that the loss of energy and lowering of the Q factor would be mostly due to the slide-film damping between the comb fingers [19], the parasitic capacitances of the bond-pads, and the electronics. Additionally the energy loss can also occur due to the structure instability during oscillations, viscous damping, and a finite volume of the anchor. Moreover the damping effect is even higher at atmospheric pressure where $Q < 100$. After considering all of the above issues, the quality factor Q of the resonator is estimated as 282. With this value of Q, the resonator can be categorized between the resonators with high energy loss in the air and the resonators with high Q in the vacuum [13]. From $Q = \omega_0 m/c$, the damping constant c is estimated to be 1.5×10^{-6} N s/m. Note that this value of c is overestimated than the one that was obtained by Eq. 3.11.

Based on the above values, δ is estimated as 0.0035, and β is estimated as 3.23 in Eq. 3.18. After fixing all other parameters, the tunable parameters in the dimensionless form are ϵ and ω.

3.2.4 Frequency Response Curves

Fig. 3.5 shows the amplitude response and the phase response curves for $\epsilon = 0.001$ as ω is swept. Expectedly during up-sweep and down-sweep of the frequency, the linear resonance appears with $\beta = 0$. The resonator shows the hard-spring effect resulting in the hysteresis with $\beta = 3.23$. The width of the hysteretic region is defined by the end-points of the up-sweep and the down-sweep where the jump phenomenon occurs. The end-points depend on the excitation amplitude, the nonlinear spring constant, and the damping constant. For example, the amplitude and the width of the hysteretic region significantly increase at $\epsilon = 0.01$, as was observed in the simulation. Similarly the curves bend to the right after increasing β to 5, thereby enlarging the width as shown in Fig. 3.5. Control of the width of hysteresis is an important design feature as this characteristic is crucial in understanding the synchronized behavior of coupled resonators. Additionally it is worth nothing that the damping constant
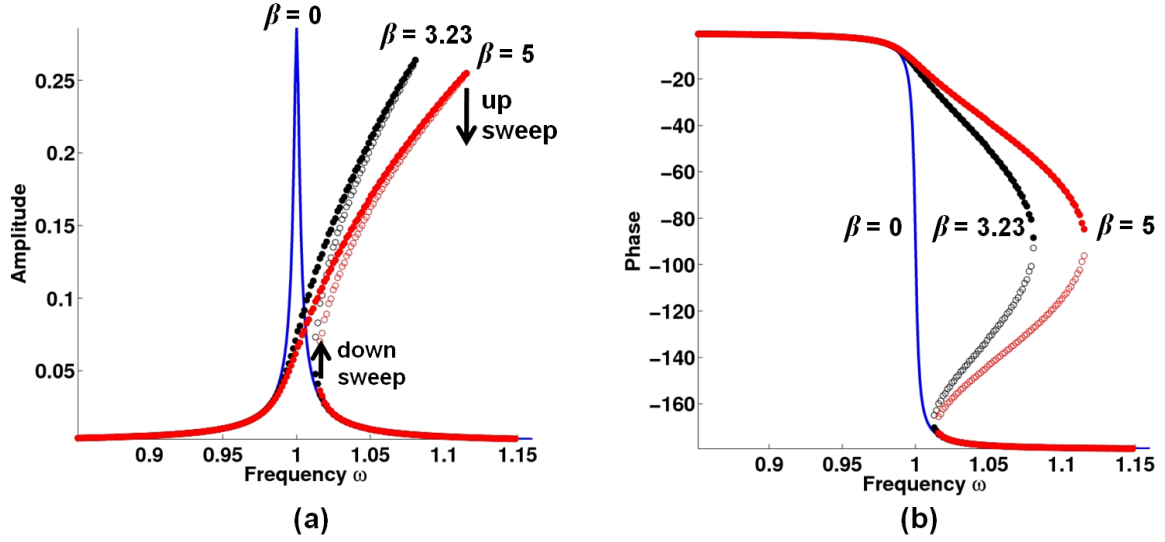
Figure 3.5: Frequency response curves for $\epsilon = 0.001$ with upsweep and downsweep of frequency: (a) amplitude response with $\beta = 0$, $\beta = 3.23$, and $\beta = 5$ (b) phase response with $\beta = 0$, $\beta = 3.23$, and $\beta = 5$. Dots represent stable points and circles represent unstable points.

determines the tip of the amplitude response curve during the up-sweep. The single resonator in Eq. 3.14 has a single well potential function with $x = 0$ as the equilibrium point. By applying a sinusoidal external force, the equilibrium point becomes unstable and a stable periodic cycle appears at the excitation frequency. At a frequency value within the hysteretic region, two stable periodic cycles and an unstable periodic cycle exist indicating that the resonator has gone through a Saddle-Node (SN) bifurcation. The stability of the limit cycles in the hysteretic region was verified by checking the eigenvalues on the corresponding Poincaré sections by the numerical method described in [42]. If the largest eigenvalue corresponding to the unstable solution leaves unit-circle from the real axis (e.g. > 1), the bifurcation can be classified as SN [43]. Outside the hysteretic region one periodic cycle appears at higher frequencies.

Figure 3.6 shows the amplitude response curves by varying ϵ at constant β. Sweeping the excitation amplitude ϵ reveals that the resonator would exhibit an enlargement in the hysteresis width as well as the vibrational amplitude. In comparison the responses shown in Fig. 3.5(a) indicate that changing β at constant ϵ enlarges the bandwidth in which two stable vibrational amplitudes co-exist but does not necessarily enlarge the amplitude.

3.3 Summary

In this chapter the basics of harmonically excited MEMS resonator were presented. First the electrostatic actuation was explained from the perspective of the electrostatic potential energy. An expression of the electrostatic force in laterally driven and harmonically excited
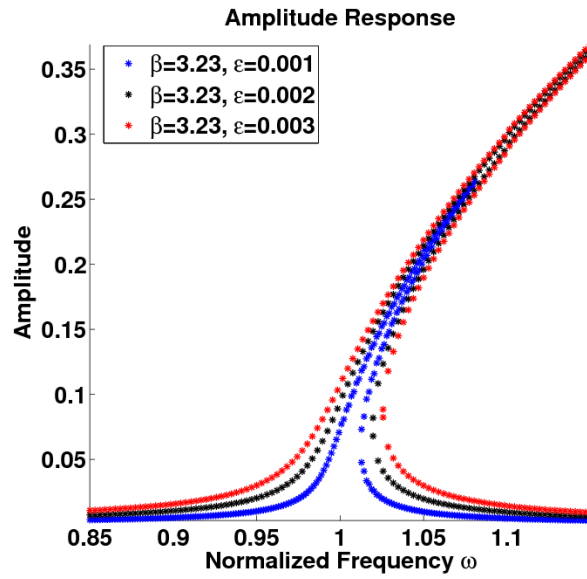
Figure 3.6: Amplitude response curves by varying ϵ with constant $\beta = 3.23$: the behavior is similar to the amplitude response curves shown in Fig. 3.5(a). Note that the amplitude increases and the bandwidth also increases in which two stable periodic orbits at a single frequency co-exist.

comb-drive was derived. Next, the dynamics of the comb-drive and the pertinent parameters were discussed. The effect of dc bias on the potential well was explained. Next the analytical solution of the dynamical equation by using averaging method was presented and the appropriate parameters were discussed. Next the frequency response curves were presented. The effects of changing the nonlinearity and the amplitude of excitation force were shown.

Chapter 4

Design of Nonlinear MEMS Resonator

In this chapter the design process of the MEMS resonator is described in detail.

4.1   Fabrication

The MEMS device is highly dependent on the fabrication process by which it is made.

4.1.1   Basics of Microfabrication

MEMS fabrication has been primarily derived from IC microfabrication technologies. Semiconductor fabrication has paved way for novel MEMS processes and techniques that are available today. The fundamental technology of microfabrication is based on photolithography [19].

Photolithography

Photolithography is used to transfer the desired patten into the structural layers consisting of the materials used in the process. Most processes involve multiple layers. The following are the common principles of photolithography. The fabrication begins with spin-coating a wafer with photoresist. Photoresist is a photosensitive material that is deposited on the wafers to define the patterns to be deposited, removed or doped. Firstly the design is created by the designer given that the necessary layer definitions and design rules are provided by the foundry in a design kit. The photolithography masks based on the design are then precisely aligned to the wafer to develop multiple layers (or single layer depending the process). Then the wafer, which was coated with the photoresist, is exposed to the UV light using the mask as shown in Fig. 4.1(a). The exposed photoresist areas are altered through the restructuring of the polymers in the material by the UV light. The areas underneath the dark shades of the mask (i.e. the intended pattern) are not exposed. The wafer is then developed in a solution. For a positive photoresist coated wafer, the exposed areas are dissolved in the solution (for a negative photoresist coated wafer, the exposed areas are insoluble in the solution and the unexposed areas are dissolved). The remaining photoresist pattern mimics the original

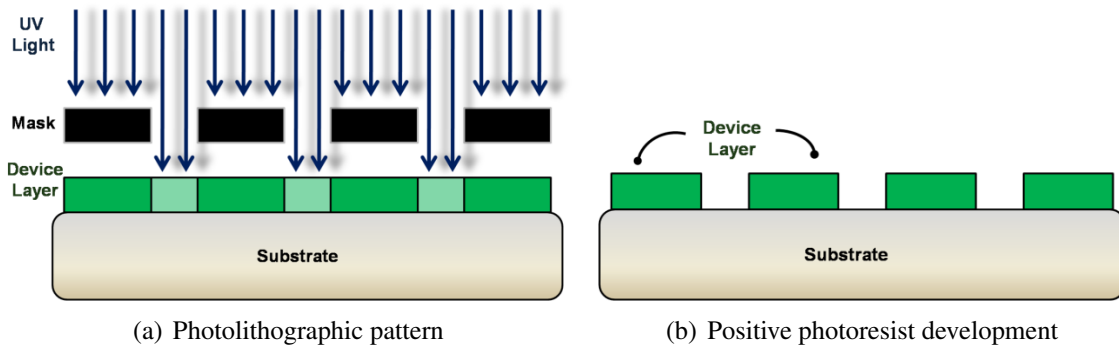(a) Photolithographic pattern   (b) Positive photoresist development

Figure 4.1: Basics of photolithography using a *positive* photoresist [19]: (a) the photolithography mask is aligned to the wafer (substrate) that is exposed to the UV light and (b) the wafer is developed to remove the exposed photoresist leaving the intended pattern as the device.

mask pattern as shown in Fig. 4.1(b). The spot size of the UV light exposure determines the minimum feature and the accuracy by which the processed material is transformed into the device. Typical MEMS processes feature one or multiple thin film layers which are deposited and developed depending on the foundry. Different layers can be used for the moving structures, interconnect, electrodes, or dielectric layer to provide isolation [19].

Etching

The photoresist pattern is developed into the structural layer by etching. Etching defines the geometry of the device by a selective removal of the material [19]. Two major categories of etching are available today: (1) wet etching and (2) dry etching. In wet etching the wafers are dipped into an etchant solution. Depending the etching technique and crystallographic orientation of the material in the wafers (e.g. <111> or <100>), the etch rate can be the same in all directions providing the isotropic etching or it can be directed and different providing the anisotropic etching as shown in Fig. 4.2. Single crystal materials like Silicon can exhibit anisotropic etching in certain chemicals such as Potassium Hydrooxide (KOH). In the anisotropic etching different etch rates in different directions in the material create the <111> crystal plane sidewalls when etching a hole in a <100> silicon wafer as shown in Fig. 4.2(b). In dry etching, an RF pulsed power source ejects plasma which is bombarded as ions onto the target material. Dry etching has now matured into sophisticated technologies such as Reactive Ion Etching (RIE) and Deep Reactive Ion Etching (DRIE) in which the reaction of the material with the ions and the directed source of energy allows incredibly selective etching that can provide almost vertical sidewalls.

The process steps and the etching steps determine the material properties that govern the geometry, the matching of devices on different dies and on the same die, and the movement of the intended structure. There are many major commercial foundries that offer versatile MEMS processes [44] [45]. For the purposes of the research conducted in this thesis, SOI-

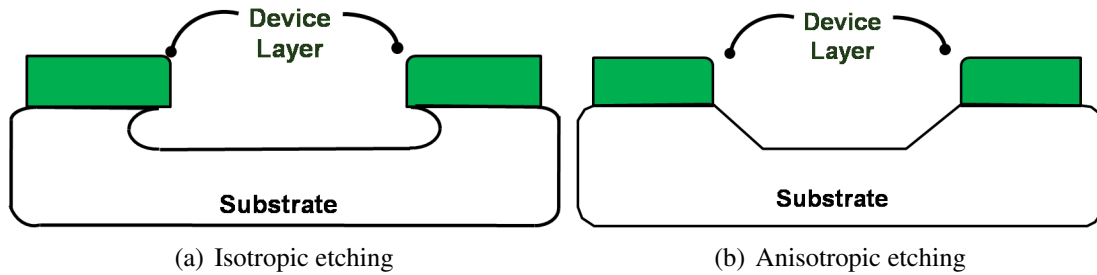(a) Isotropic etching   (b) Anisotropic etching

Figure 4.2: Two types of etching: (a) isotropic etching where the etch rate is identical in all directions and (b) anisotropic etching where the sidewalls can be angled and bounded by <111> planes controlling the etch rate in different directions.

MUMPs offered by Memscap Inc [46] was used.

4.1.2 SOIMUMPs

SOIMUMPs is a Silicon-On-Insulator (SOI) patterning and etching process offered by Memscap, Inc. Fig. 4.3 illustrates a summary of the major fabrication steps used in SOI-MUMPs [46]. The process begins with the 150 mm SOI wafers. The top surface of the Silicon layer is doped by depositing a phosphosilicate glass (PSG) layer and annealing at a high temperature (Fig 4.3(a)). Then a metal stack of 20 nm of chrome and 500 nm of gold is deposited by patterning the Pad Metal mask (Fig 4.3(b)). Then the Silicon layer is lithographically patterned by SOI mask and etched using DRIE (Fig 4.3(c)). Next, a protective material is applied to the top surface of the Silicon layer, the Substrate layer is lithographically patterned from the bottom surface using the Trench mask, the Bottom Oxide layer is removed using RIE, a DRIE etch is used to remove the substrate completely in this area, and the buried Oxide in the Trench mask area is removed using a wet etch (Fig 4.3(d)). Next the protective material is stripped in a dry etch process. In this step the mechanical structures in the Silicon layer are released. The remaining Oxide layer is removed using a vapor HF process (Fig 4.3(e)). More details are provided in [46]. Here the end result is a 25 μm thick doped Silicon as the structure layer followed by a 2 μm thick Oxide layer patterned and etched on a 400 μm thick Silicon substrate [46]. The substrate is completely removed in the back-etch step as shown in Fig. 4.3(d) which reduces parasitic capacitances and damping. The Pad Metal layer is used in the bond-pads for excitation and detection.

(a) Step 1: Silicon Doping

(b) Step 2: Pad Metal Liftoff

(c) Step 3: Silicon Patterning

(d) Step 4: Substrate Patterning
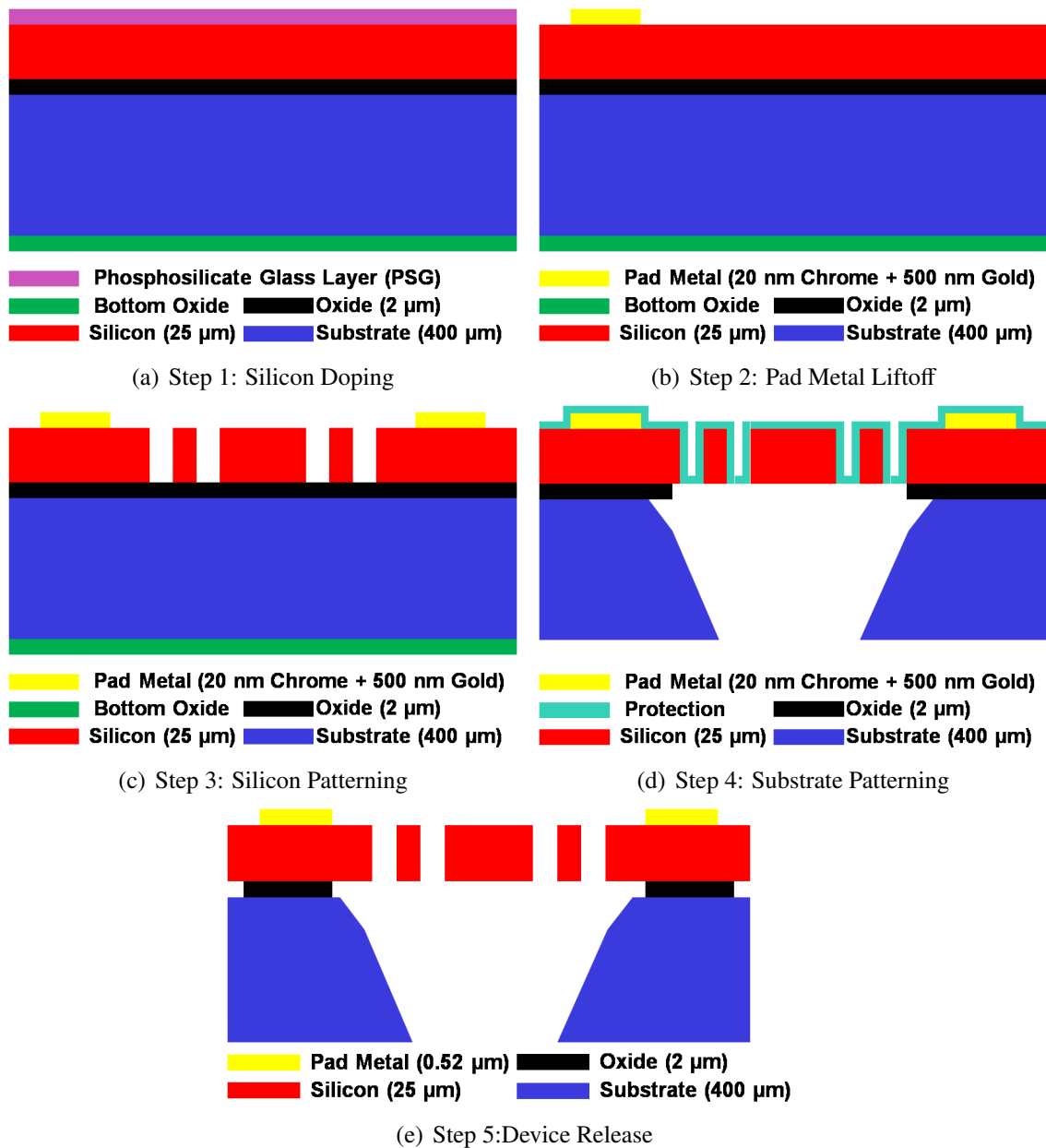
(e) Step 5:Device Release

Figure 4.3: Major fabrication steps in SOIMUMPs [46]:(a) Step 1: PSG is deposited, phosphorus is pushed into Silicon by annealing, and PSG is removed by wet chemical etching. (b) Step 2: negative photoresist is coated, PadMetal mask is lithographically patterned and developed, a metal stack of chrome and gold is deposited, and then the photoresist is dissolved. (c) Step 3: positive photoresist is coated, SOI mask is lithographically patterned and developed, DRIE is used to etch Si down to Oxide, and the photoresist is dissolved. (d) Step 4: protective material is applied on the top surface, the bottoms surface is coated with positive photoresist, Trench mask is lithographically patterned, RIE is used to remove the bottom oxide, DRIE is used to etch completely through the substrate stopping at the Oxide (black), photoresist is removed, and wet etch is used to remove the Oxide in the Trench area. (e) Step 5: protective material is removed from the top surface using dry etch, Oxide underneath the device is undercut, and removed by a vapor HF process.
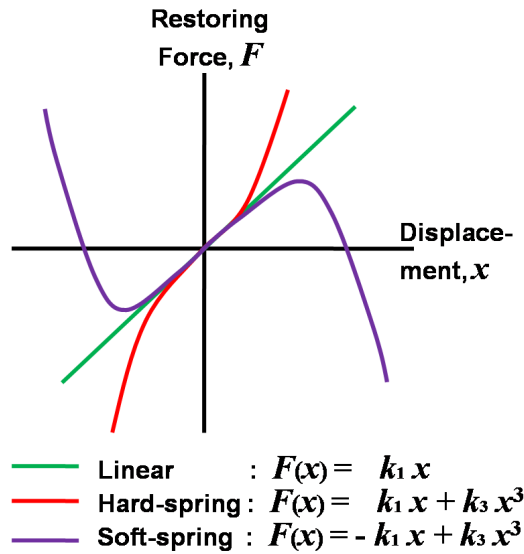
40

Figure 4.4: Nonlinearity in MEMS: soft-spring effect where the restoring force decreases with increasing displacement and hard-spring effect where the restoring force increases with increasing displacement. Here k_1 = linear spring constant and k_3 = nonlinear spring constant.

4.2 Nonlinearity in MEMS

In this section the nonlinear behavior that occurs in MEMS devices is discussed. Typically the nonlinearity in MEMS is categorized as soft-spring effect and hard-spring effect. In the soft-spring effect the springs soften, that is the restoring force decreases as the displacement increases. On the other hand the hard-spring effect is characterized by an increase in the restoring force with increasing displacement. The two scenarios are shown in Fig. 4.4. This type of effect can often be seen in the frequency response curves (amplitude versus frequency) as discussed in the previous chapter. The actuation mechanism plays a major role in which type of behavior is exhibited. For example, parallel plate actuation generates a strong dependence on the bias in the applied force value; it effects the linear spring constant term by reducing it. At high dc bias the effective linear spring constant term becomes negative and the device exhibits soft-spring effect. On the other hand if driven hard by laterally driven comb-drive, device can show the hard-spring behavior. Generally a MEMS device is driven symmetrically by an ac excitation force which cancels out even-order nonlinear terms. The primary cause of the nonlinearity is the material deformation in the device.

4.2.1 Material Deformation

Several tensile (or compressive), shear, and/or volumetric forces are present during and after the fabrication of the MEMS device as shown in Fig. 4.5(a). The material strength is measured by various moduli such as Young's modulus, Shear modulus, and Bulk modulus
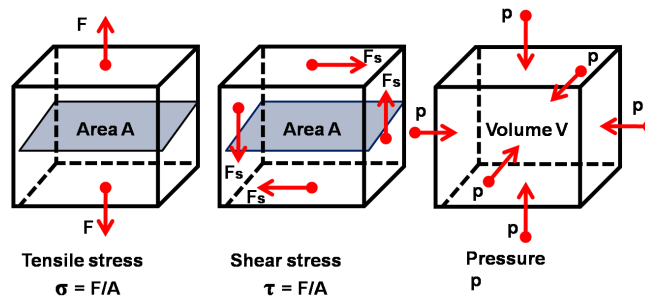
(a) Various tensile and compressive forces
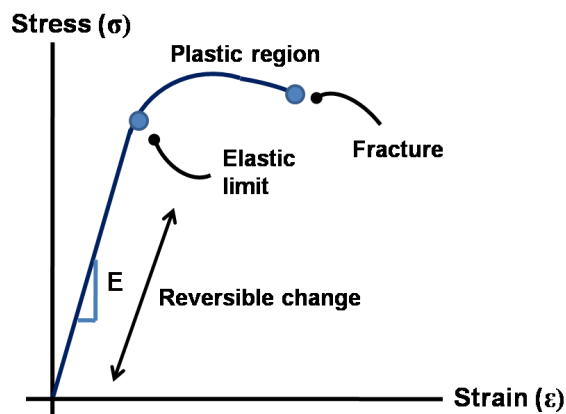
(b) Stress versus strain curve

Figure 4.5: Material deformation: (a) axial stress, shear stress and pressure can stretch or compress the material in the axial direction, sideways or as a volume respectively and (b) typical curve showing stress vs. strain relationship where the material change is reversible up to the elastic limit after which it enters plastic region, and finally reaches the fracture point. The slope of curve in the elastic region defines Young's modulus E.

depending on the type of force. Fig. 4.5(b) shows Young's modulus E, which is the most commonly used measure for a given material. It is the ratio of tensile stress vs. tensile strain where strain is a measure of change in the length divided by the original length. Beyond the elastic region where a reversible change in the material is possible, the material can enter plastic region and a permanent change exists in the presence of a large tensile stress. At even larger stress the material can eventually break as shown in Fig. 4.5(b).

Another important measure is Poisson's ratio, v, which defined as the lateral strain vs longitudinal strain ratio [47]. Lateral strain occurs at the right angle to the direction of the applied tensile (compressive) stress. Hence the lateral strain is defined as the ratio of the change in the height (or the width) of the material to the original height (or the width) as shown in Fig. 4.6. The longitudinal strain occurs when the material is subjected to an axial tensile (compressive) stress producing an axial deformation. Hence the longitudinal strain is defined as the ratio of the axial deformation to the original length as shown in Fig. 4.6. Note
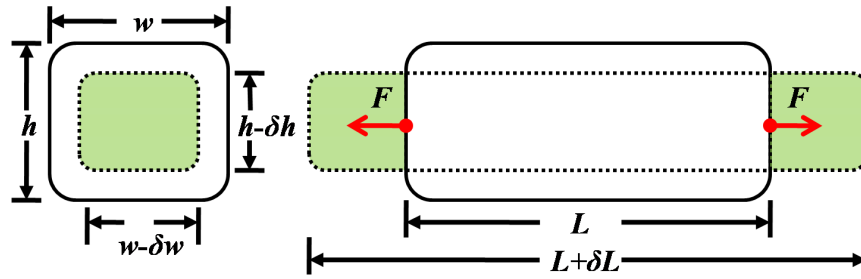
Figure 4.6: A simple definition of Poisson's ratio, v, for a beam under lateral strain ϵ_1 and longitudinal strain ϵ_2 [47]. Let F = the applied stress, L and δL = the original length and the change in length respectively, w and δw = the original width and the change in width respectively, h and δh = the original height and the change in height respectively. Here $\epsilon_1 = \dfrac{\delta w}{w}$ or $\dfrac{\delta h}{h}$ and $\epsilon_2 = \dfrac{\delta L}{L}$, then $v = \dfrac{\epsilon_1}{\epsilon_2}$.

that when the longitudinal strain is tensile, the lateral strain is compressive. Consequently Poisson's ratio is the ratio of the lateral strain to the longitudinal strain.

Silicon

Typically in a stable, isotropic and linear elastic material, the Poisson's ratio appears in the range $-1.0 < v < 0.5$ [48]. Most MEMS processes use Silicon as the structural material because of its excellent electrical and material properties. Normally Silicon in MEMS is used in its in polycrystalline or single crystal form [19] [46] [49]. For single crystal Silicon, $v = 0.28$ [19]. Silicon is very brittle material and hence it experiences no plastic deformation. It provides superior mechanical stability with no hysteresis, exhibits negligible energy loss, and minimal fatigue [19]. It is important to note that Silicon is an anisotropic material [50]. In an anisotropic material the material properties are not independent of direction of the motion and it exhibits different physical properties in different directions relative to the crystallographic orientation of the material. For example, in a <100> wafer, Silicon exhibits E = 169 GPa in the <110> plane and E = 130 GPa in the <100> plane [51]. A typical MEMs device can have suspension beams with arbitrary lengths and angles in different directions. Anisotropic elasticity occurs due to fabrication imperfections which result in non-ideal geometries. Non-ideal geometries results in elastic cross-coupling in the suspension elements. Consequently between the principal axes of elasticity (e.g. x and y), the springs can have cross-coupling. Additionally the direction of movement of the springs relative to the principal axes of elasticity can also contribute to cross-coupling. Hence the anisotropicity of Silicon can play a major role in the behavior and the stability of a resonant structure when its in motion. The moduli shown before do not contain enough information to describe the dynamic behavior of the structure. However in [11] and [52] these effects were modeled using generalized Hooke's law containing the nonlinear terms and verified experimentally. In particular this research showed that a high quality factor makes resonators fabricated in
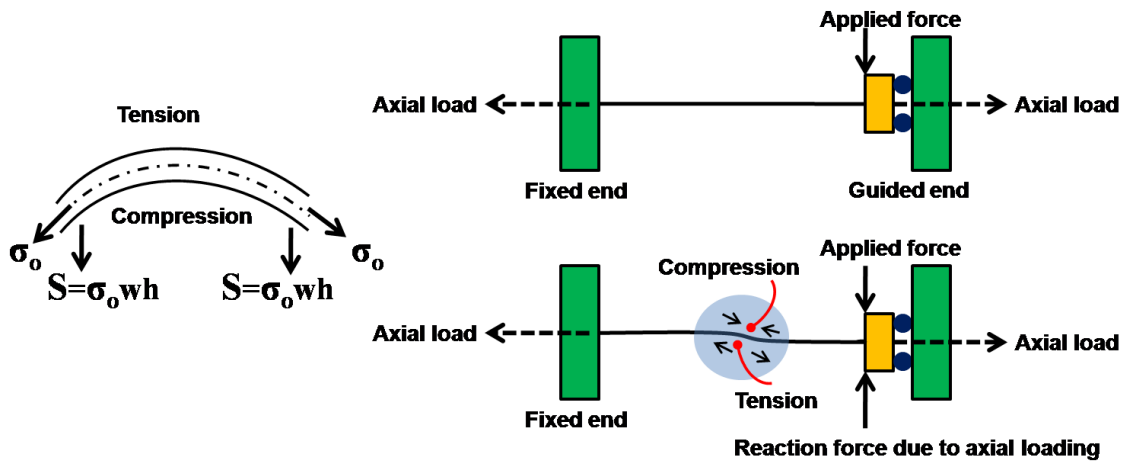
Figure 4.7: Residual stress and nonlinearity: the stress variation in the layered materials can result in average residual stress as the axial stress (σ_o). Large force can lead to large deformation and it stretches the central axis of the beam. During actuation when the beam is bent, the axial stress produces a reaction force (S) in addition to the linear elastic restoring force in the thin long beams. As a result the beams harden and exhibit nonlinear restoring force. Here w and h are the width and the thickness of the beam, respectively.

single crystal Silicon susceptible to nonlinearities and even a small material nonlinearity can become significant at high quality factor. Additionally the researchers confirmed that large deformations result in a geometrical nonlinear effect and soft-spring effect can be observed in a BAW resonator at the bias = 100 V and ac amplitude = 560 mV because of capacitive and material nonlinearities. Another cause of the nonlinearity in MEMs devices is due to the residual stress effect. Thin films of multilayered structures are subjected to the residual stresses. The resulting elastic deformation can create the phenomena such as the curling, the buckling, and even the fracture [53]. The residual stress occurs due to the varying conditions that are present during the layer development in the fabrication process which can cause the stress variation in the layered materials and as result residual stress remains after releasing the device. Average residual stress results in the axial stress which produces a reaction force in the thin long beam when it is bent during actuation in the presence of the applied force as shown in Fig. 4.7. When such a structure is actuated it can exhibit a significant nonlinearity and instability when a large force is present. Large force creates large deformation $> 0.15L$ (appx.), where L is the length of the beam [54]. When the force is applied, the energy potential is stored in the form of elastic deformation energy in the entire beam which results in the linear elastic restoring force (governed by Hooke's law) combined with the additional reaction forces due to axial loading as depicted in Fig. 4.7. Yet another cause of the nonlinearity is based on the contact where the springs would touch the other springs or parts [55]. In summary, the nonlinearity in the MEMS devices can appear due large vibrations, residual stress, variation in the individual elements, contact with other elements, circuit elements, and/or a combination of all of the above. Fig. 4.8 shows the simulation of a thin long beam
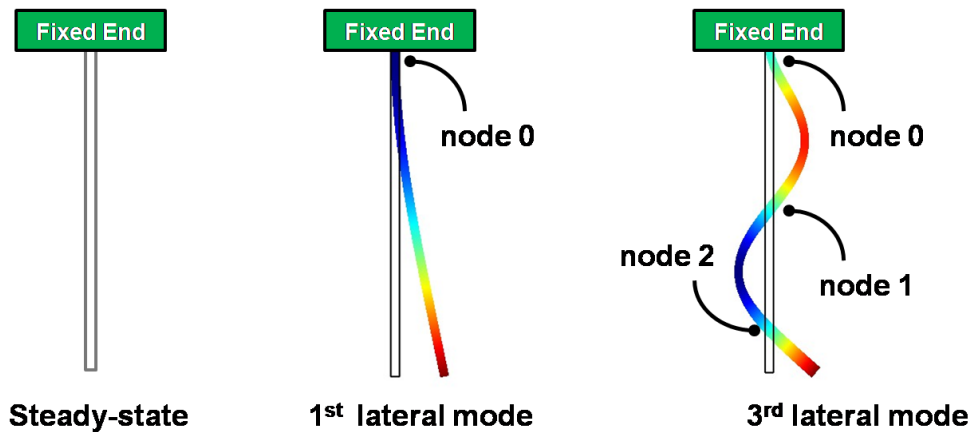
Figure 4.8: Fixed-free beam in motion when a load is applied at the tip (Comsol): the beam in the steady-state develops the first lateral mode in which the linear displacement occurs. Here the compliance in the axis of direction allows the motion to occur due to the restoring force in the beam. However given the large deformations due to a large force, the beam may harden and exhibit nonlinear restoring force. For a symmetrically driven beam, the 3rd lateral mode commonly results in unstable behavior.

in Comsol. Among the many modes that such a beam can exhibit, the first lateral mode is the most preferred mode of vibration in the presence of an applied force at the tip of the free end. Usually linear displacement occurs in this mode for small force. In this mode, the beam goes through large deformation in the presence of a large force which can result in the nonlinear restoring force. The next lateral mode is also shown on the right where two additional nodes develop during large oscillations. The mode primarily occurs so that the beam can sustain an equilibrium with the applied force while moving; the beam may become unstable in this mode.

4.2.2 Application of Nonlinearity

The soft-spring and hard-spring effects in an electro-statically excited fixed-fixed beam resonator and a comb-drive resonator have been reported in MEMS research [12] [13] [14]. Normally the nonlinearity of the device is characterized so that the device can be designed and operated with linear resonance [11] [13] or the layout of the resonator is optimized [12]. On the other hand, some research phenomenologically focuses on a MEMS device with nonlinear resonance that can show oscillations at superharmonic excitation, period-doubling bifurcations and a route to chaos [36]. In [55] a MEMS energy harvesting device excited by mechanical vibration was characterized with the hard-spring effect creating an extension of 27 Hz from the resonance frequency. In [17] the parametric resonance was exploited to show that the hard-spring effect can extend the resonance curve up to 1 kHz. In this study the nonlinear behavior is considered in order to investigate the synchronized behavior of the coupled system which can only happen when the individual resonators exhibit a tangible
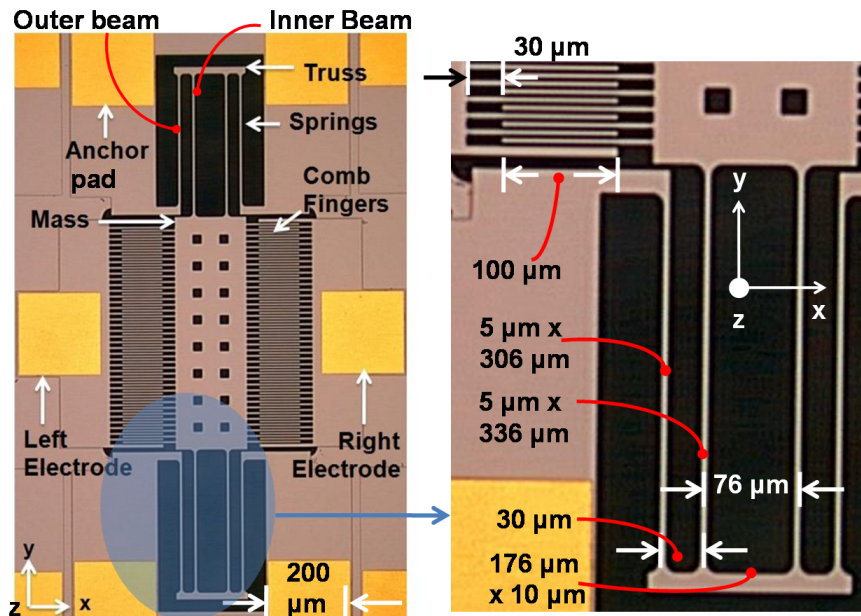
Figure 4.9: Comb-drive resonator fabricated in SOIMUMPs process: note the difference between the lengths of the inner beam and outer beam within a pair of folded beams.

nonlinear resonance.

4.3 Single Nonlinear Resonator

Many different designs were fabricated from which a workable resonator design based on the laterally driven comb-drive was finally conceived and enhanced. This section describes the details of the resonator that yielded the experimental results shown in Chapter 6.

4.3.1 Fabricated Resonator

Figure 4.9 illustrates a laterally driven comb-drive resonator that was fabricated in SOI-MUMPs process. The resonator consists of a perforated mass suspended by folded springs. The springs are attached to the truss. The device is designed to be symmetric about the x-axis and the y-axis to provide stable oscillations. Usually the device is biased at a dc voltage. By applying ac voltage between the comb fingers attached to the mass and the fixed electrode (either left or right electrode in Fig. 4.9), a time varying electrostatic force is generated which makes the mass vibrate in the x-direction. Typically the motional current, which is proportional to the change in the capacitance between the comb fingers and the excitation voltage, is measured. The vibration in this type of resonator will be only in the x-direction due to two design features: folded flexure and thickness of the structure. These features reduce the axial stress and restrict the out-of-plane movement thereby minimizing unstable

46

Table 4.1: Important dimensions of the device shown in Fig. 4.9

Part Description	Designed Value
Structure thickness (z-dir)	25 μm
Number of movable fingers (one side)	39
Gap between movable and fixed finger	3 μm
Overlap between movable and fixed finger	100 μm
Folded flexure (outer-beam): width × length	5 μm × 306 μm
Folded flexure (inner-beam): width × length	5 μm × 336 μm
Mass width × length	175 μm × 570 μm

and unwanted vibrations in the other axes [19]. Table 4.1 shows the important dimensions of the designed resonator. Here the overlap between the movable and fixed comb fingers was increased to 100 μm to increase the steady-state capacitance during a design revision. Also small dimples were placed to avoid the stiction between the long comb-fingers with small gap.

4.3.2 Comb-drive

Fig. 4.10(a) shows the potential distribution in a set of a movable comb finger and a pair of fixed comb fingers by fixing potential on the movable comb to zero and the fixed combs to 20 V. Fig. 4.10(b) shows the corresponding electric field distribution. Here it can be seen that the electric field is largest in the parallel direction for a static dc potential distribution and it is reciprocal due to the symmetrical placement of the movable comb in the fixed combs. Also note the fringe field distribution at the end of the combs on both sides. Here the electric field in the parallel region and the fringe region changes directions when an ac voltage is applied in addition to the dc voltage. The resultant force is the time varying electrostatic force in x direction, normal to the parallel region, which pushes structure to the right and pulls it to the left according to the change in the ac voltage. Fig. 4.11 shows the ac voltage and the corresponding electrostatic force. The simulations were done by increasing the static dc voltage in small increments to imitate one full period of the ac voltage. Here the applied ac voltage with frequency of 8 kHz is shown in Fig. 4.11(a) and the resultant force in the x direction is shown in Fig. 4.11(b). This force is based on the maxwell stress tensor integrated at the boundary as shown in the inset. The resultant force in the y direction, as shown in Fig. 4.11(c), is about 14 orders of magnitude smaller than the force in the x direction. Given the symmetric placement of the movable finger between the two fixed fingers the total force in y direction is nearly zero. These simulations show that an ac voltage in an inter-digitated set of comb fingers creates the time varying electrostatic force in x direction. Consequently the structure moves in the direction of the force due to the compliance in the suspension beams. The suspension beams exert the restoring force in the opposite direction to the applied force thereby sustaining the motion and ultimately creating resonance at the structure's natural vibration frequency. As discussed before, in the presence of large force the

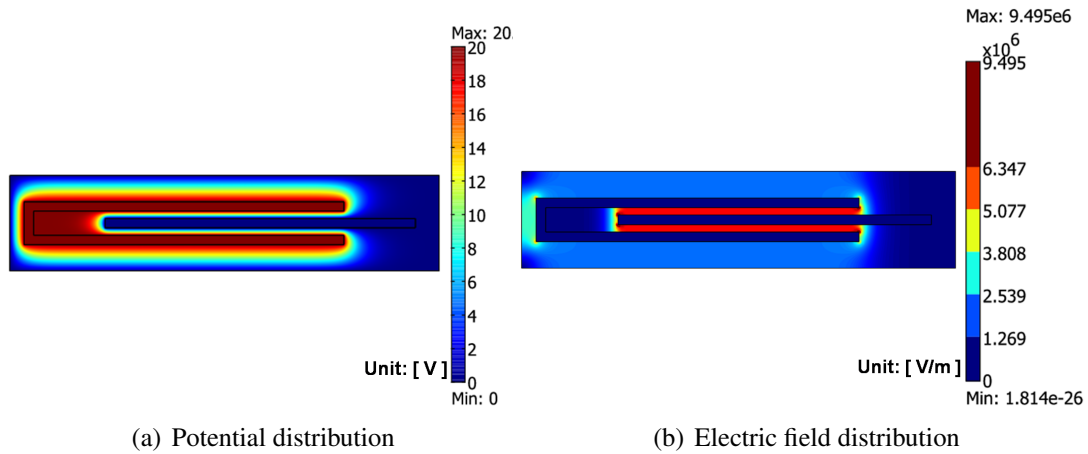(a) Potential distribution   (b) Electric field distribution

Figure 4.10: Electrostatic field in the comb fingers (Comsol): (a) potential distribution with the potential on the fixed and movable combs set to 20 V and 0 V respectively and (b) the electric field distribution in V/m. The field lines change the direction when an ac voltage is applied such that the direction of the total applied force on the movable fingers is to the right.

beams go through large deformation and the nonlinear stiffness arises due to the stretching of the beams' neutral axes.

4.3.3 Suspension

As noted before the oscillations in a resonant MEMS device depend primarily on the suspension springs as they exert the necessary restoring force. A slew of suspension springs are used in MEMs devices of which the major types are illustrated in Fig. 4.12. The suspension beams are designed to be compliant along the desired direction of motion and stiff in the other directions. Fig. 4.12(a) shows the straight beam in which the boundary conditions are commonly referred to as fixed-guided since one end is connected to the anchor (which is attached all the way to the substrate) and the other end is connected to the device. The stiffness of the fixed-guided beam along the three major axes can be found as[1] [19],

$$k_\mathrm{x} = E\frac{w^3 h}{L^3}, k_\mathrm{y} = E\frac{wh}{L}, k_\mathrm{z} = E\frac{wh^3}{L^3}. \tag{4.1}$$

Where k_x, k_y, k_z denote the stiffnesses in x, y, z directions respectively, w is the width of the beam (x-dir), h is the height of the beam (z-dir), L is the length of the beam (y-dir), and E is the Young's modulus. It can be seen from the ratio of k_z and k_x that the thicker the structure the stiffer it becomes in the z direction; this helps reduce the out of plane vibrations. By designing long and narrow beams, the ratio of the axial stiffness k_y and k_x can be increased which provides a better suppression of the vibrations in y direction. However when a large lateral force is present, the straight beam can become axially loaded. It can exhibit higher
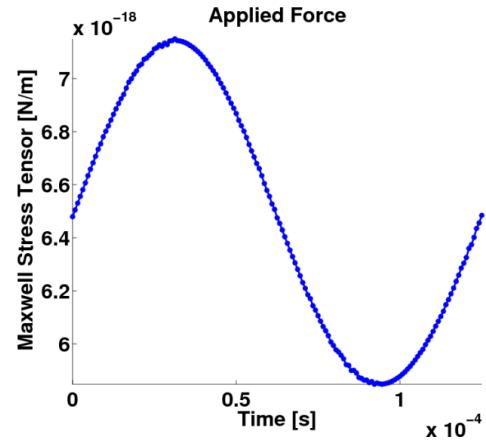
---

[1] See Appendix C for the derivation of k_x.
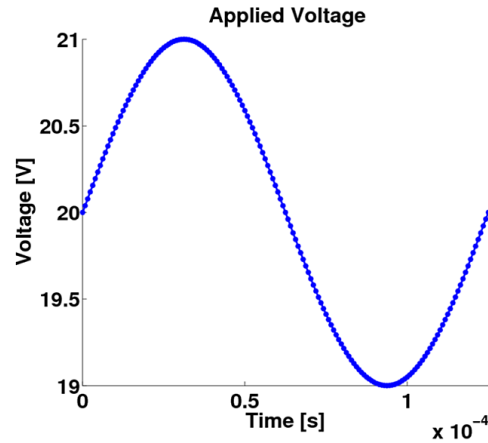
(a) Applied voltage with ac amplitude = 1V at dc = 20V
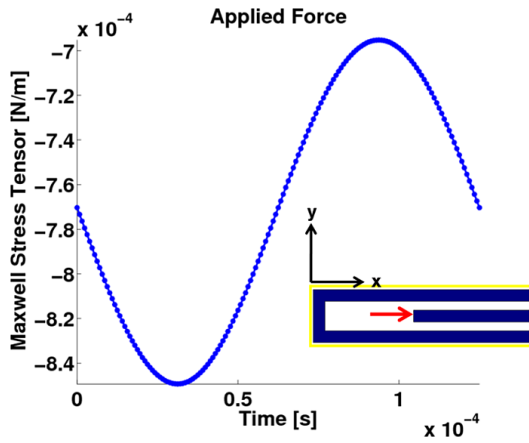
(b) Applied force in x-direction

(c) Applied force in y-direction

Figure 4.11: Time varying electrostatic force (Comsol): (a) applied voltage and resultant force in x direction (b) and in y direction (c). Inset in (b) shows the boundary at which the maxwell stress tensor was integrated. Note that the force in x direction is many orders of magnitude higher than in y direction.

order modes of vibration and as a result it can be quite unstable. As a remedy to this problem the crab-leg flexures, as shown in Fig. 4.12(b), are used which reduce the stress in x direction. However the stiffness in the y direction in the crab-leg flexure is also reduced. To create more stable vibrations, the folded beam flexures as shown in Fig. 4.12(c) and (d) are used. With the beams in series, the stiffnesses become,

$$\frac{1}{k_{\mathrm{f}}} = \frac{1}{k_{\mathrm{x}}} + \frac{1}{k_{\mathrm{x}}} \implies k_f = E\frac{w^3 h}{2L^3}, \tag{4.2}$$

$$k_{\mathrm{df}} = k_{\mathrm{f}}/2 = E\frac{w^3 h}{4L^3}. \tag{4.3}$$
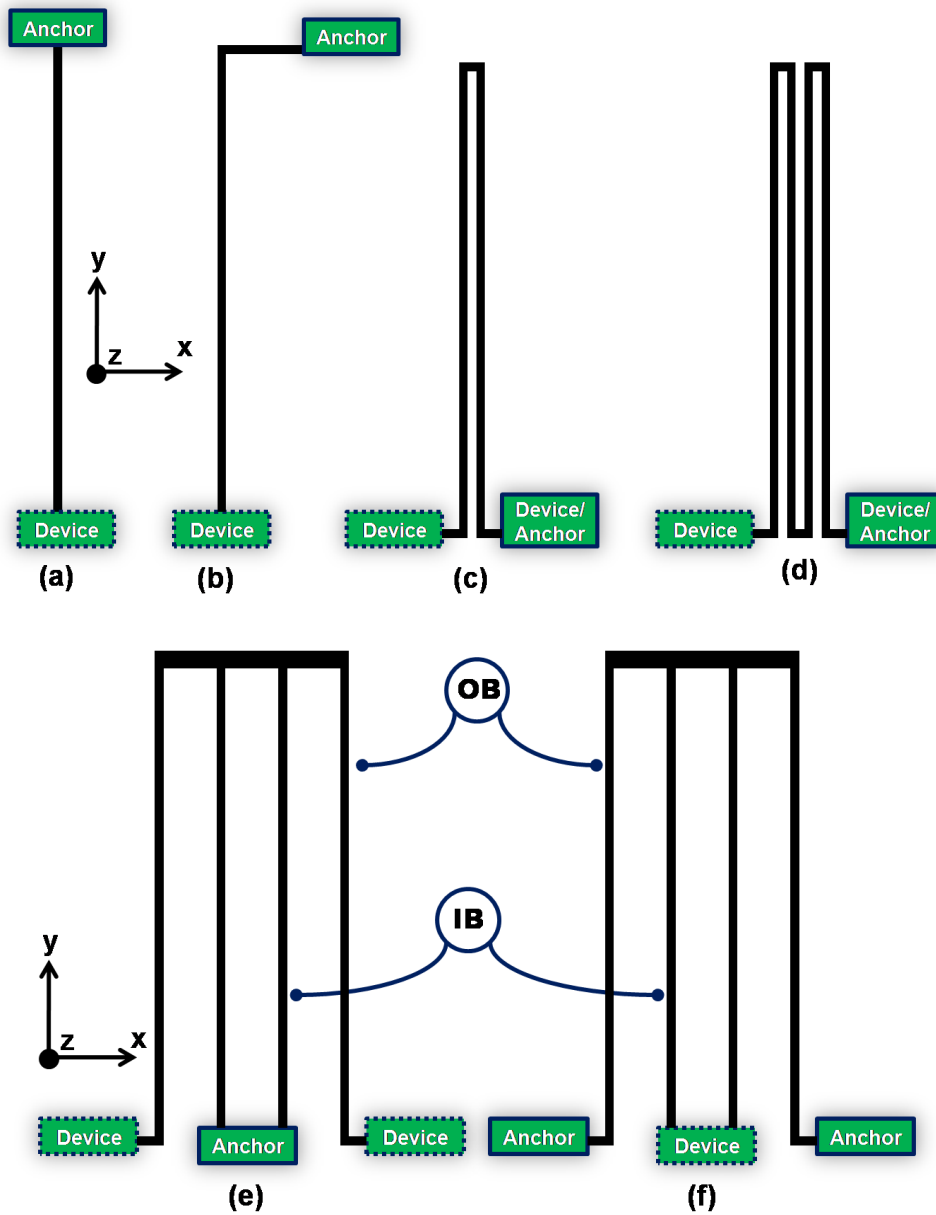
49

Figure 4.12: Different types of suspension: (a) straight beam, (b) crab-leg beam, (c) folded beam, (d) double-folded beams, (e) folded beams with inner fold, and (f) folded beams with outer fold. Here OB and IB indicate Outer Beam and Inner Beam respectively. Note that the spring structure shown in (f) is used for the resonator in this thesis.

where, k_f and k_{df} denote the stiffnesses of folded beams and double-folded beams respectively. Fig. 4.12(e) and (f) show two other types of configuration of double-folded beams. Here the beams are attached to a rigid truss and are folded either outward or inward. Please
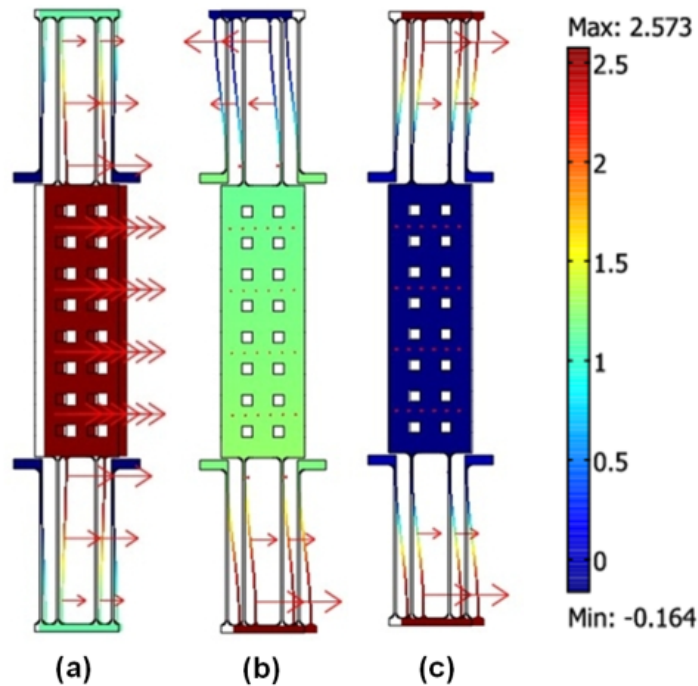
Figure 4.13: Modal analysis in Comsol: (a) first mode at 11511.95 Hz, (b) second mode at 67725.23 Hz, and (c) third mode at 70016.02 Hz. The bar on far-right represents normalized values with most positive value on top depicting the maximum value of displacement for a given mode. Size and number of the arrows are related to the values of displacement; maximum displacement of the mass in x-dir occurs in the first mode.

see Appendix C for the derivation of the spring constant for the folded beam pair shown in Fig. 4.12(f). The folded beam design reduces axial stress components present in a single beam and extends the stroke in the intended direction of motion. Each end of the folded beam pair (there would be a total of four pairs in a complete design) is free to expand and contract in all directions. A resonating mass is suspended by flexures on four sides; hence the total stiffness of the entire structure in a given direction can only be verified by running a modal analysis in FEA software. Fig. 4.13 shows the modal analysis with first three modes and associated vibrational frequencies. The fundamental mode is the obvious choice for the resonance. The truss reduces motion in the y-axis in this mode. The analysis of the other modes reveals that the frequencies corresponding to the other two modes are farther away from the fundamental frequency. These two frequencies are due to the torsional and lateral modes that can be present in the suspension beams (for a better estimate of the frequencies see Appendix B).

The long and narrow beams are terminated with fillets to minimize breakage as shown in Fig. 4.9. The design presented in this chapter is comprised of the folded beams with outer fold. The inner beams were designed to be slightly longer than the outer beams as shown in Fig. 4.9. This creates a ratio between the inner beams and outer beams and introduces an
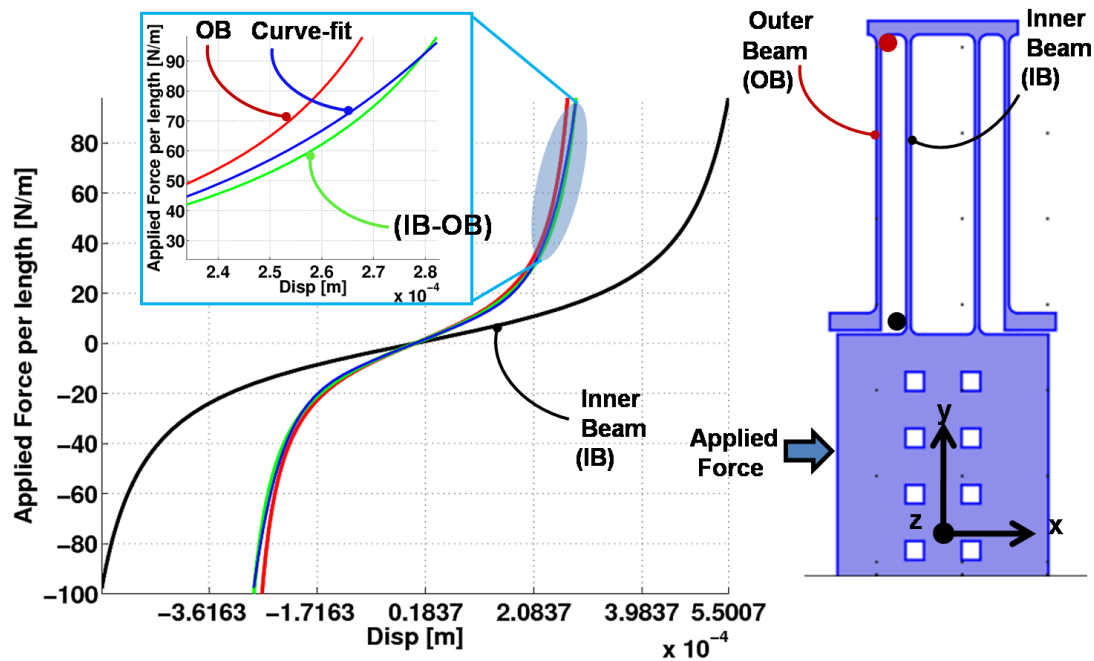
51

Figure 4.14: Effect of asymmetry 1 (Comsol): the force vs displacement profile curves for the inner and outer beams show large nonlinear stiffness when large force is present (note that the profile of the restoring force would be negative of this profile). The spring displacement is evaluated at the locations shown on the right. The inset shows three curves: outer beam stiffness, inner beam stiffness–outer beam stiffness (IB–OB), e.g. isolated inner beam stiffness, and curve-fitted data of IB–OB. From the curve-fitted data, the linear stiffness can be approximated as 52 N/m and cubic stiffness as 1×10^8 N/m^3 for the isolated inner beam.

asymmetry. With L_{OB} = 306 μm and L_{IB} = 336 μm, $k_{OB}/k_{IB} = L_{IB}^3/L_{OB}^3 = 1.32$. Also note the difference between the distance between the two beam pairs and the distance between two beams within a given pair. Fig. 4.14 shows the simulation of the displacement at key locations in the suspension beams while applying and increasing/decreasing the force adiabatically on the left boundary of the mass. Here it can be seen that the inner beam exhibits linear behavior over a large displacement range and has a smaller spring constant. Beyond this range, the inner beam shows nonlinearity. The outer beam also exhibits substantial nonlinearity when driven by a large force as it causes large deformation and it hardens more than the inner beam. Note that this simulation indicates the hard-spring effect in both the beams. Here the difference between the inner beam stiffness and outer beam stiffness is taken to compare the mismatch between the two beams as if they were uncoupled. It is clear that the outer beam shows more hardening than the isolated inner beam. The isolated stiffness of the inner beam is curve-fitted to extract the stiffness values. The approximate linear stiffnesses are 25 N/m and 52 N/m for the coupled inner beam and isolated inner beam, respectively. Based on the isolated inner beam data, the nonlinear spring constant is 1×10^8 N/m^3. Note that this simulation is based on static displacement and does not accurately predict the dy-
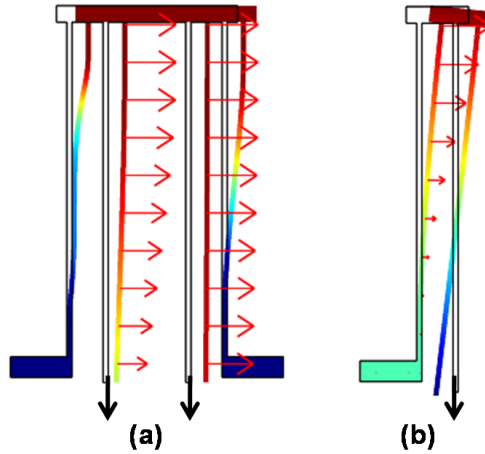
Figure 4.15: Effect of asymmetry 2 (Comsol): (a) in the presence of severe axial load, the outer beams also show large deformation and (b) truss can develop a moment. The black arrows indicate the boundaries at which the force was applied.

namic behavior. Please refer to Appendix B for the simulation of the dynamic response of the resonator based on these values.

Fig. 4.15 shows the effect of axial loading and reduced axial stiffness for the asymmetric flexures. After applying a very large load at the indicated location in Fig. 4.15(a), the outer beams can also deform, harden and contribute to the overall nonlinear restoring force. As seen in Fig. 4.15(b) partially rigid truss can develop a moment due to axial loading. These simulations mimic the movement of the structure due to severe axial loading at peak resonance. Another set of simulations exemplify the pronounced effect of axial loading as shown in Fig. 4.16. Here von Mises stress is the equivalent tensile stress under multi axial loading conditions. Fig. 4.16(a) shows the von Mises stress values at three different points in the inner and outer beams for the asymmetric design. Similarly Fig. 4.16(b) shows the stress values for the symmetric design with equi-distance and equi-height beams. The circles show the key points which can be evaluated to assess the stress conditions. At large values of the applied force it can be seen that the stress values at two key points exhibit a substantial difference in the asymmetric design than the symmetric design. When such a structure is driven with large force causing large deformation at peak resonance, it can exhibit a strong nonlinear behavior.

Normally the folded-beam pair is used to relieve the residual stress and axial loading that occurs in the design with single beams. The spring design that utilizes single, thin and long beams is prone to more axial loading. As shown in Fig. 4.7 such a beam tends to stiffen under large deformation. In this type of design, after releasing the device, the single beam expands and its length increases in order to relieve the average residual stress. However the stress gradient still remains. This gradient (assuming compressive stress) induces a moment and the beam bends (curls up) in order to relieve this stress gradient. The benefit of the folded-beam structure is that the truss can move in y-dir as the beams expand to relieve the residual

53
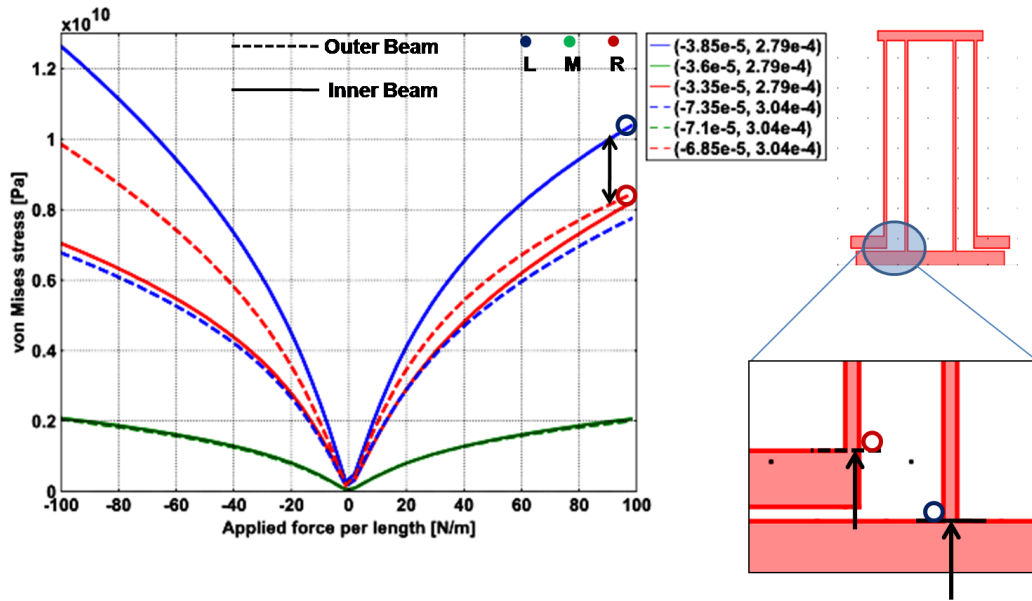
(a) von Mises stress evaluation for the asymmetric design
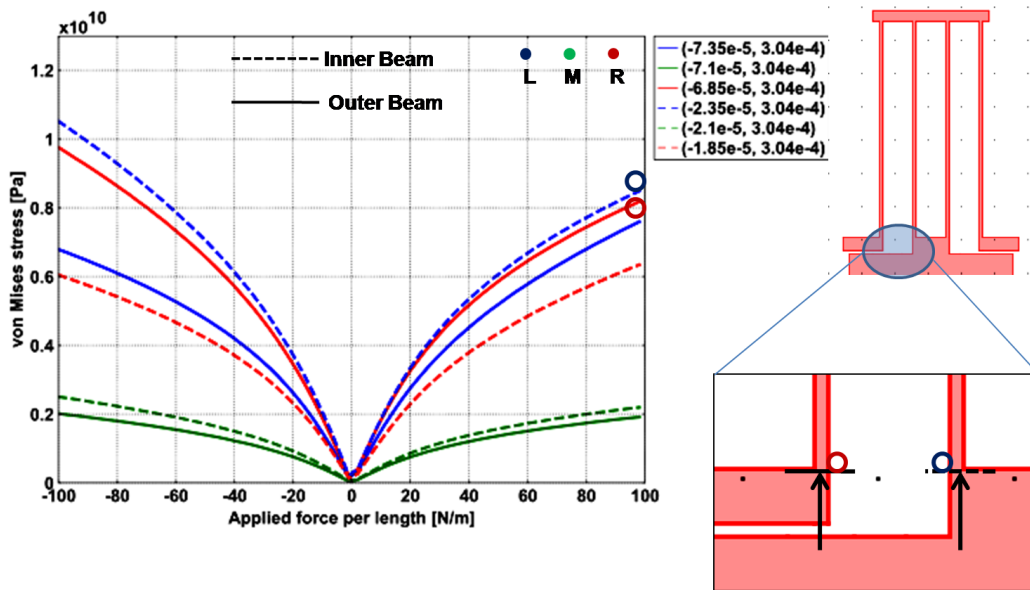
(b) von Mises stress evaluation for the symmetric design

Figure 4.16: von Mises stress simulation for two different designs (Comsol): (a) the simulation study of the three major points in the current design and (b) in the symmetric design. Note that the region, where the beams' neutral axes stretch, are analyzed. In the case of the asymmetric design, the simulations show a substantial gap in the stress values for the inner and outer beam when the applied force is very large. In the case of the symmetric design, the outer and inner beams contract and expand uniformly and the gap in the stress values is minimal.
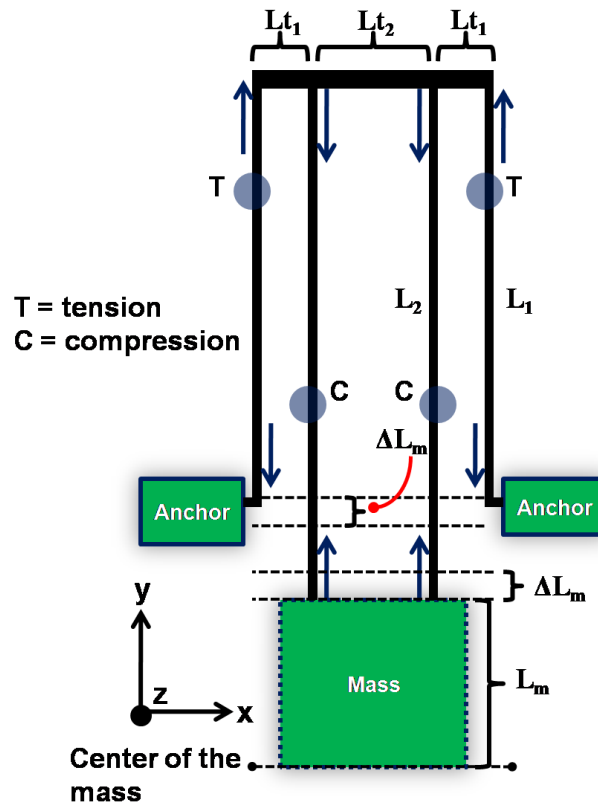
Figure 4.17: Designed beams under axial loading: here the outer beam and inner beam lengths are L_1 and L_2, respectively. If we assume that a compressive axial stress is present in the inner beams during *motion*, they contract given that the truss is somewhat compliant. Consequently the outer beams expand to relieve the additional stress experienced by the structure. Here ΔL_m is the change in the length of the inner beams where L_m is the distance between the tip of the inner beams and the center of the mass.

stress after releasing the device [56]. In the design presented in this thesis, the mismatch between the lengths of the outer and the inner beams creates a mismatch in the stress that is experienced by the structure during actuation. These details are discussed next.

As shown in Fig. 4.7 when the beam is bent during actuation, it experiences axial stress due to the average residual stress in the beam. Let's assume that a large compressive axial stress is present on the inner beams. The change in the length of the inner beams, which is denoted by ΔL_m in Fig. 4.17 where L_m is equal to the distance between the tip of the inner beams and the center of the mass. Let stress per lateral area be $\sigma = E\epsilon$, where E = Young's modulus and ϵ = strain in the beam. Let the strain due to the change in L_m be ϵ_m and the total

beam strain be ϵ_b which can be derived as,

$$\epsilon_m = \frac{\Delta L_m}{L_m}, \tag{4.4a}$$

$$\epsilon_b = \frac{\Delta L_2}{L_2} = \frac{\Delta L_m}{L_2} = \frac{\epsilon_m L_m}{L_2}. \tag{4.4b}$$

Now the stress force S_2 in the inner beams can be derived as,

$$\sigma_b = E\epsilon_b = E\frac{\epsilon_m L_m}{L_2}, \tag{4.5a}$$

$$S_2 = \sigma_b wh = \left(E\frac{\epsilon_m L_m}{L_2}\right)wh. \tag{4.5b}$$

The stress force S_2 contributes to the linear elastic restoring force and hardens the beam when it goes through large deformation. As seen in Fig. 4.17 the outer beams stretch accordingly to relieve this additional stress force experienced by the inner beams. In a symmetric design, e.g. $L_{t1} = L_{t2}$ and $L_1 = L_2$, the outer beams expand by the same length. If the truss is not fully compliant, then the expansion can be even less than ΔL_m in the outer beams. Additionally $L_1 < L_2$ and hence from Eq. 4.5, $\sigma_1 > \sigma_2$. And so it is obvious that the tensile stress S_1 would be more than the compressive stress S_2. Due to these reasons the expansion/contraction experienced by the outer beam is not fully matched by the contraction/expansion experienced by the inner beam. And so the outer beams would harden more than the inner beams for the same range of displacement as shown in Fig. 4.14. The overall restoring force profile, given that the beam is driven symmetrically, then shows cubic nonlinear stiffness as result of the hardening of the beams as seen in Fig. 4.14.

4.4 Summary

In this chapter the design process of a nonlinear MEMS resonator was discussed. First the basics of microfabrication were discussed and the major steps of the fabrication process were summarized. Next the nonlinearity in MEMS was explained and the basis of nonlinearity on the material deformation was explicated. Next the design of the MEMS resonators used in this research was discussed. Based on the designed comb-drive, the simulation results of the electrostatic actuation generating the time-varying electrostatic force were presented. Different types of the suspension springs were shown. An occurrence of nonlinearity in this design was shown and the causes of nonlinearity were elaborated.

Chapter 5

Simulation Study of Coupled Nonlinear MEMS Resonators

In this chapter, a unidirectionally coupled system consisting of the individual resonators mentioned in the previous chapter is investigated. The local bifurcations of the coupled system are analyzed. Here the behavior of the coupled system according to the change in the coupling parameter and the excitation force is targeted. Phenomena such as the quasiperiodic oscillations and the synchronization are shown.

5.1 Coupling Topology

Many types of inter-element coupling is possible. For a closed-loop system of coupled system, two primary types of inter-element coupling can be visualized: (1) bidirectional and (2) unidirectional. Furthermore, in the case of the unidirectional coupling, two types of coupling topologies are possible: a) diffusive and b) direct [31]. A diffusive coupling is defined by a coupling related to the difference between the displacement variables. For example, diffusive coupling occurs when a coupling bar is placed between the resonators. On the other hand in the case of the direct coupling, only the previous element (or the next element if the direction of coupling is reversed) produces the coupling term for a given element in the coupled system as shown in Fig. 5.1. From the perspective of design, a tunable coupling parameter is important in that it provides more flexibility. As an example, this type of coupling can be implemented by placing current-to-voltage converters, op-amp gain stage, and op-amp buffers between the resonators. The gain of an amplifier with high bandwidth can be easily tuned so that the total coupling strength between the resonating elements is changed linearly. Given that the buffers have a high input impedance and low output impedance, the flow of the motional current is always forward, i.e. from a given resonating element to the next resonating element. Consequently this implementation creates a direct, linear, and unidirectional coupling scheme between the individual elements. Note that this coupling topology and its proposed implementation simplify the problem of the coupled system significantly. The dynamics of a single resonator (see Eq. 3.14) in the coupled system with
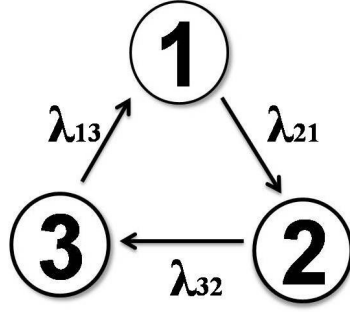
Figure 5.1: Unidirectional coupling scheme in a ring of coupled resonators.

direct coupling from the neighboring element can be described as

$$x_j'' + \delta x_j' + x_j + \beta x_j^3 = \epsilon \cos(\omega \tau) + \lambda_{jk} x_k, \tag{5.1}$$

where x_j denotes the displacement variable of the single resonator in the coupled system and λ_{jk} is the coupling strength with k denoting the index of the previous element as is shown in Fig. 5.1. Here j = (1,2,3) corresponds to k = (3,1,2). To reduce the complexity and the number of parameters of the coupled system, it is assumed that (a) the coupling strength is identical between the elements, i.e. $\lambda_{21} = \lambda_{32} = \lambda_{13} = \lambda$, (b) the number of elements = 3, and (c) all other parameters are identical. The parameter space now contains three tunable variables: coupling strength λ, excitation amplitude ϵ, and excitation frequency ω.

5.2 Autonomous System ($\epsilon = 0$)

Here the coupled system without any excitation force is considered. Fig. 5.2 shows one parameter bifurcation diagram for x_1 as λ is varied. As shown in Fig. 5.2, while sweeping the coupling strength λ from right to left, the equilibrium point $x_1 = x_2 = x_3 = 0$ looses its stability by going through a supercritical Hopf Bifurcation (HB) at a critical value of $\lambda_c = -4.04 \times 10^{-3}$ [43]. Another bifurcation point is marked as Neimark-Sacker (NS) where quasiperiodic cycles appear. The above simulation was performed by integrating Eq. 5.1 using 4th order Runge-Kutta method. For a thorough analytical derivation, the reader is referred to [57]. Next we focus on the stability analysis.

5.2.1 Stability of the Equilibrium

Stability of the synchronous equilibrium was verified by plotting Asymptotic Continuous Spectrum (ACS) curves along with discrete eigenvalues for each resonator [7]. Fig. 5.3(a) shows one set of the complex conjugate eigenvalues for different λ values. The ACS curves shown in Fig. 5.3(a) represent a continuous set of eigenvalues for each λ with discrete eigenvalues of each resonator shown as big dots on these curves (please see Appendix A). For
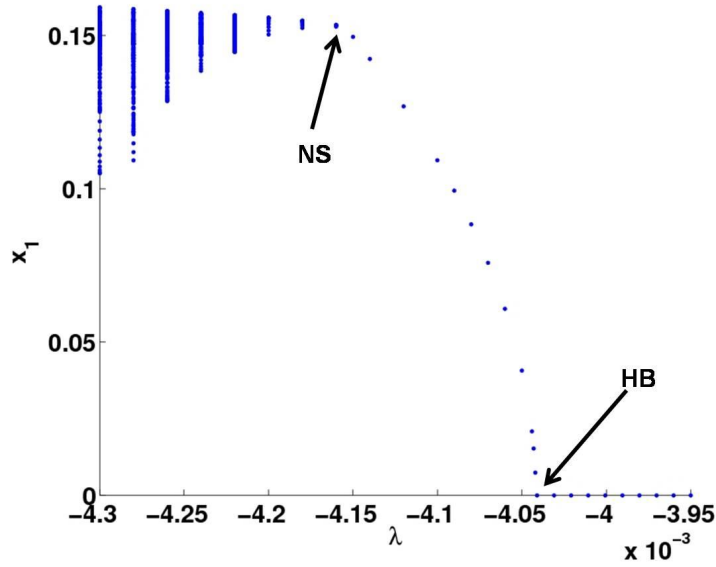
58

Figure 5.2: One parameter bifurcation diagram for x_1 with λ as the bifurcation parameter obtained numerically by integrating Eq. 5.1: Hopf Bifurcation (HB) occurs at a critical value of $\lambda = -4.04 \times 10^{-3}$. Periodic oscillations continue until another bifurcation point at $\lambda = -4.15 \times 10^{-3}$, where quasiperiodic oscillations appear through Neimark-Sacker (NS) bifurcation.

$\lambda > \lambda_c$ all of the eigenvalues stay within left-hand plane. For $\lambda < \lambda_c$, one of the eigenvalues crosses into the right-hand plane. As shown in Fig. 5.3(b), the critical value of λ_c can also be confirmed by evaluating the real part of eigenvalues while sweeping λ values. Periodic rotating waves appear at a critical value of λ for which the frequency of the oscillation was observed as 1.008. Fig. 5.4(a) shows the time-series of the coupled system at $\lambda = -4.08 \times 10^{-3}$ (after the critical value). A single oscillation frequency can be confirmed from the power spectrum shown in Fig. 5.4(b). As seen from Fig. 5.4c, the phase-space encloses a circle. The phase difference is also evident from the Poincaré section shown in Fig. 5.4d. Stability check done by evaluating eigenvalues of the system on the linearized Poincaré map indicates that two complex conjugate pairs stay within the unit-circle while the complex conjugate pair for the third solution stays around 1 (see section 5.2.2 for the method used in stability check). Further reducing in the bifurcation parameter increases both the frequency and the amplitude of the oscillations as shown in Fig. 5.2. These periodic cycles are stable up to $\lambda = -4.15 \times 10^{-3}$, where the system goes through a secondary Hopf bifurcation. At this point one of the complex conjugate pair exits the unit-circle indicating that system goes through Neimark-Sacker (NS) bifurcation as marked in Figs. 5.2 [43]. Fig. 5.5 shows the state of the system when λ is changed to -4.28×10^{-3}. As shown in Fig. 5.5(a), the original phase-locked state between the three oscillators is now destroyed and the system shows amplitude-modulated periodic cycles. Frequencies other than the original oscillatory
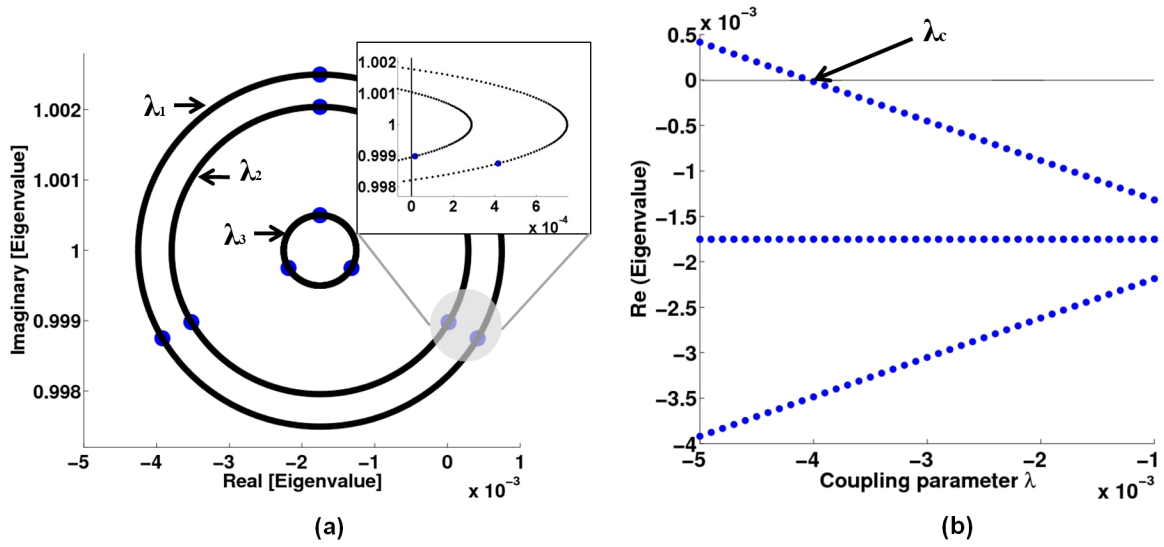
Figure 5.3: Stability of the equilibrium: (a) Asymptotic Continuous Spectrum (ACS) curves for $\lambda = \lambda_1 = -1 \times 10^{-3}$, $\lambda = \lambda_2 = -4.08 \times 10^{-3}$, and $\lambda = \lambda_3 = -5 \times 10^{-3}$. Inset shows the zoomed view of one of the eigenvalues for λ_2 and λ_3. (b) Real part of eigenvalues vs. λ with λ_c as marked.

frequency arise as seen from the power spectrum in Fig. 5.5(b). Note that the third harmonic components also begin to rise for $\lambda = -4.28 \times 10^{-3}$. The phase-space now evolves into a torus as seen in Fig. 5.5c. Individual oscillators follow a closed loop on the Poincaré section as seen in Fig. 5.5d. Further decreasing the coupling parameter causes the system to undergo global symmetry-breaking bifurcations in a sequence resulting in multiple tori. Poincaré section generated for the values of λ in the multiple tori region shows a closed ring containing the three individual oscillator paths shown in Fig. 5.5d. The behavior shown for negative λ was also observed for a positive change in λ with the critical value $\lambda_c = 4.04 \times 10^{-3}$. Note that in all the simulations random nonidentical initial conditions were used. Indeed this is similar to the actual devices in which noise in the electronics and variation in the fabrication process make the initial positions of the three resonators nonidentical. Identical initial conditions can cause oscillation death in this system.

5.2.2 Stability of the Periodic Solution

In this section, the technique used to determine the stability of periodic solution for both the autonomous system and the nonautonomous system (discussed in section 5.3) is briefly described. A detailed discussion can be found in [43]. Let the coupled system with λ be represented by one dimensional set of equations in the matrix form as,

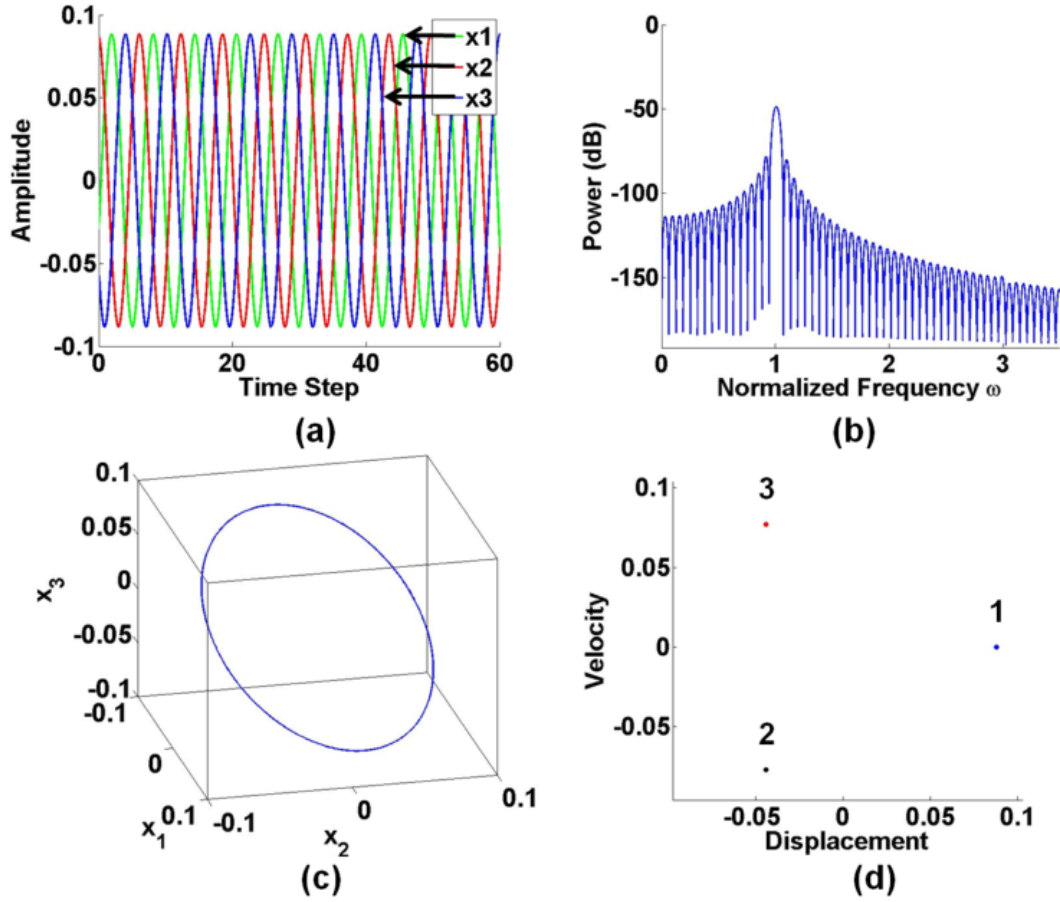$$\dot{\mathbf{y}} = \mathbf{f}(\mathbf{y}, \lambda), \tag{5.2}$$

60

Figure 5.4: Simulation of coupled system for $\lambda = -4.08 \times 10^{-3}$ and $\epsilon = 0$: (a) Time-series for x_1, x_2, x_3, (b) Power spectrum for x_1, (c) Phase-space for x_1, x_2, x_3, and (d) Poincaré section with $(\dot{x}_1, x_1)$, $(\dot{x}_2, x_2)$, and $(\dot{x}_3, x_3)$.

where $\mathbf{y} = (x_1, \dot{x}_1, x_2, \dot{x}_2, x_3, \dot{x}_3)^T$. Let $\mathbf{y}(t)$ be the periodic orbit with period T_o. Let $\mathbf{q}^*$ be the fixed point at which the periodic orbit $\mathbf{y}(t)$ intersects the Poincaré map $\mathbf{P}$. Linearization of $\mathbf{P}$ at $\mathbf{q}^*$ leads to a linear map:

$$\eta_{k+1} = D[\mathbf{P}(\mathbf{q}^*)]\eta_k, \tag{5.3}$$

where η is a small perturbation around the fixed point $\mathbf{q}^*$. The eigenvalues of the Jacobian $D[\mathbf{P}(\mathbf{q}^*)]$ correspond to Floquet multipliers of the periodic orbit $\mathbf{y}(t)$. Floquet multipliers are the eigenvalues of the monodromy matrix $\mathbf{M}$, where $\mathbf{M} = \partial \mathbf{P}(\mathbf{q}^*)/\partial \mathbf{q}$. In order to find the monodromy matrix $\mathbf{M}$, let $\mathbf{M} = \mathbf{\Phi}(T_o)$, where $\mathbf{\Phi}(T_o)$ is the solution of the variational matrix $\mathbf{\Phi}(t)$ at $t = T_o$. Then it follows that integrating the combined system as,

$$\begin{pmatrix} \dot{\mathbf{y}} \\ \dot{\mathbf{\Phi}} \end{pmatrix} = \begin{pmatrix} \mathbf{f}(\mathbf{y}, \lambda) \\ \mathbf{f}(\mathbf{y}, \lambda)\mathbf{\Phi} \end{pmatrix}, \tag{5.4}$$
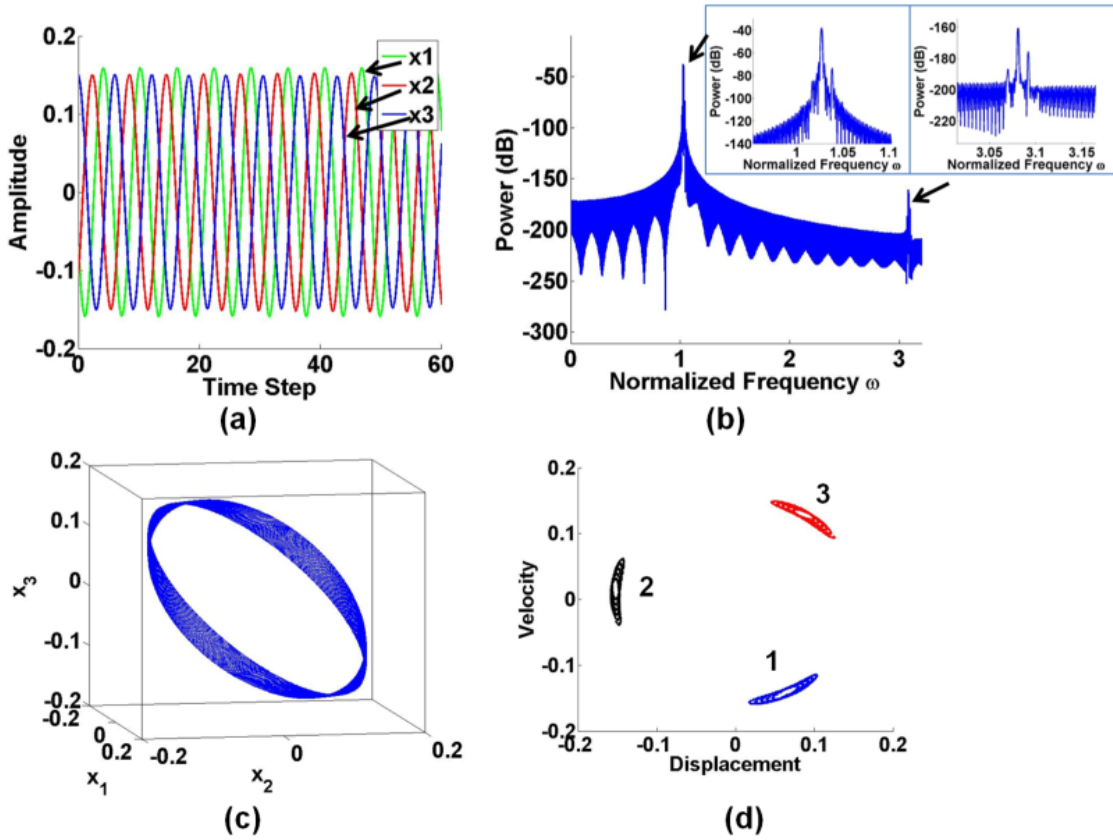
Figure 5.5: Simulation of coupled system for $\lambda = -4.28 \times 10^{-3}$ and $\epsilon = 0$. (a) Time-series for x_1, x_2, x_3, (b) Power spectrum for x_1 and the zoomed view around fundamental frequency and its third harmonic, (c) Phase-space for x_1, x_2, x_3, and (d) Poincaré section with $(\dot{x}_1, x_1)$, $(\dot{x}_2, x_2)$, and $(\dot{x}_3, x_3)$.

with initial conditions $\begin{pmatrix} \mathbf{y(0)} \\ \mathbf{\Phi(0)} \end{pmatrix} = \begin{pmatrix} \mathbf{q^*} \\ \mathbf{I} \end{pmatrix}$ until $t = T_o$ gives us the monodromy matrix. If the eigenvalues of the mondromy matrix are located inside the unit-circle (e.g. modulus of the complex eigenvalue is less than 1) then the periodic orbit is considered to be stable. By examining the values of the Floquet multipliers corresponding to the unstable solution, the bifurcation can be classified as: (a) Saddle-Node or Pitchfork if $|\rho| = 1$, (b) Neimark-Sacker if $\mathfrak{I}(\rho) \neq 0$, where $\mathfrak{I}$ denotes imaginary part, and (c) Period-doubling if $|\rho| = -1$ [43] [58]. As is shown in Fig. 5.6(a) for $\lambda = -4.08 \times 10^{-3}$, one set of eigenvalues stays at 1, for which the eigenvectors are tangent to the periodic orbit through the Poincaré section, indicating neutrally stable perturbation [43]. The other Floquet multipliers stay inside the unit-circle indicating stable periodic solution. As shown in Fig. 5.6(b) for $\lambda = -4.28 \times 10^{-3}$, one pair of Floquet multipliers exits the unit circle indicating unstable periodic solution. It is interesting to note that for $\lambda = -4.28 \times 10^{-3}$ a third eigenvalue is located outside the unit-circle on the real axis. While decreasing the λ past the NS point marked on Fig. 5.2, the system seems
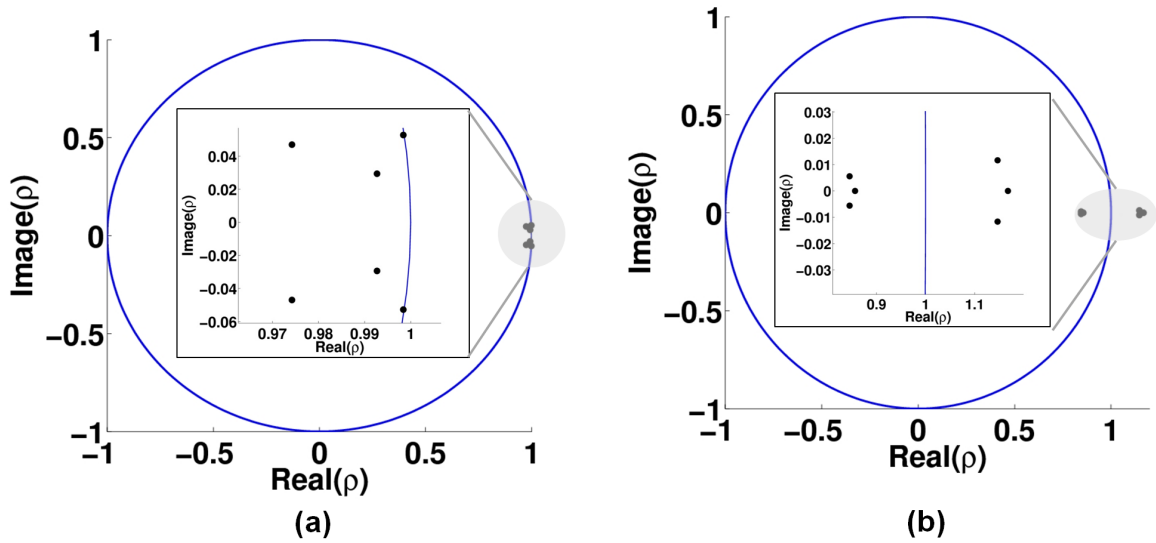
Figure 5.6: Floquet multipliers of the autonomous system for two different values of λ: (a) $\lambda = -4.08 \times 10^{-3}$; one complex conjugate pair stays at 1 making the system neutrally stable. The rest of the multipliers are located inside the unit-circle. (b) $\lambda = -4.28 \times 10^{-3}$; the complex conjugate pair is located outside the unit-circle indicating that the system has gone through Neimark-Sacker (NS) bifurcation. The third eigenvalue outside the unit-circle indicates that system has gone through a Saddle-Node (or Pitchfork) bifurcation as well.

to have gone through a Saddle-Node (or Pitchfork) bifurcation along with Neimark-Sacker bifurcation.

5.3 Nonautonomous System ($\epsilon \neq 0$)

With a nonzero ϵ, the state of the coupled system changes drastically. As shown in Eq. 5.1, the excitation force is applied identically to all three resonators. Fig. 5.7 shows the synchronization regions for $\lambda = -4.08 \times 10^{-3}$ with the detuning effects around $\omega = 1$ and $\omega = 3$.

5.3.1 1:1 Sync

Recall that ω is the ratio of the excitation frequency and the natural frequency of the coupled system which depends on the coupling strength. The simulations show that inside the Arnold tongue where ω is around 1, the individual resonators are fully entrained to the excitation frequency. For lower ω values, 1:1 region shows bending which indicates that higher order nonlinear terms are present due to mixing from subharmonic regions (e.g. 3:1 region). Outside the Arnold tongues, the coupled system shows almost periodic oscillations
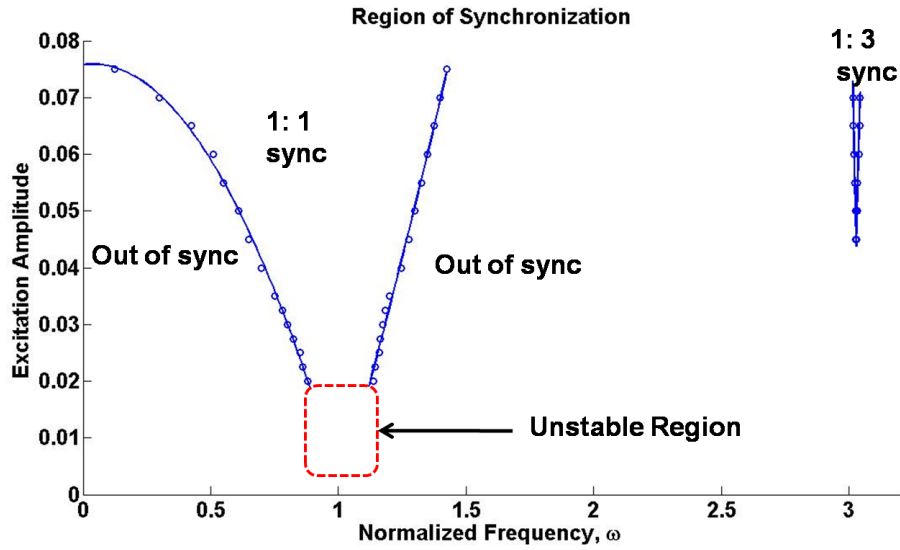
Figure 5.7: Regions of synchronization for $\lambda = -4.08 \times 10^{-3}$ around $\omega = 1$ and $\omega = 3$. Here circles represent numerically obtained boundary and the solid line is the fitted curve.

near the boundaries and quasiperiodic oscillations away from the boundaries. With a high δ (damping constant) and low ϵ, 1:1 sync region can have a closed curve just above the area marked with red square in Fig. 5.7. However for the value of δ used in this study, no synchronization was observed in this area hence the open region. This region shows unstable responses due to the simultaneous effects of damping, coupling strength, and the excitation force. For an example, for $\epsilon = 0.001$ and $\omega = 1.05$, the system looses its original synchronized state as seen in Fig. 5.8(a) and the interaction of the three oscillators results in the rise of the third harmonic components as seen in Fig. 5.8(b). Also note that amplitude level of the third harmonic continues to rise with multiple frequency components around it for $\epsilon \geqslant 0.001$. Increasing ϵ shows that stable periodic oscillations begin to appear at a higher value as shown in Figs. 5.9(a) and 5.9(b). While increasing values of ϵ the system first goes through a Saddle-Node (or Pitchfork) bifurcation at $\epsilon = 0.0031$. Local stability analysis shows that one complex conjugate pair leaves the unit-circle indicating Neimark-Sacker bifurcation as seen in Fig. 5.10(a). These differences indicate a qualitative change in the behavior at low ϵ. Fig. 5.10(b) shows Floquet multipliers during ω sweep at $\epsilon = 0.035$ for two values: $\omega = 0.5$ and $\omega = 1.9$. The system goes through Torus (NS) bifurcation at these detuned values of ω. At $\lambda = -4.28 \times 10^{-3}$ it was observed that originally unstable system (see Fig. 5.5) stabilizes in the presence of excitation force; the coupled system shows many spectrum components until ϵ is sufficiently high at which full entrainment occurs.
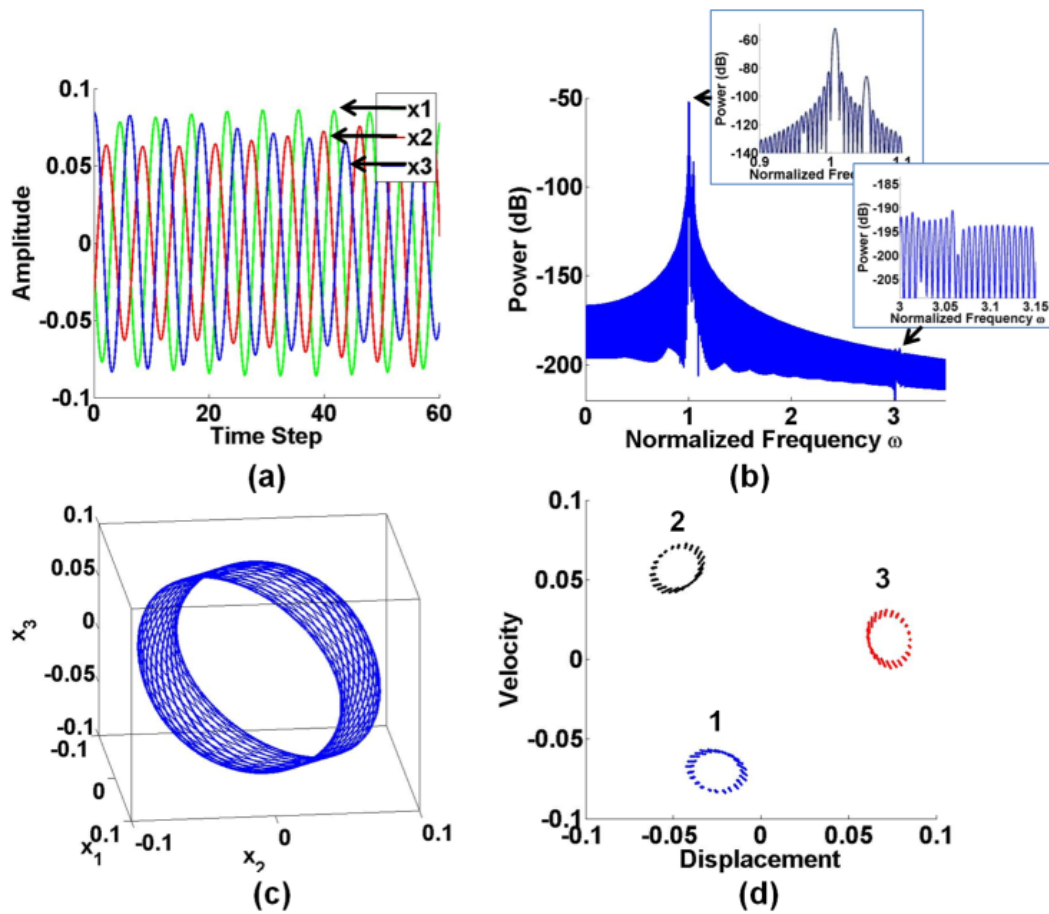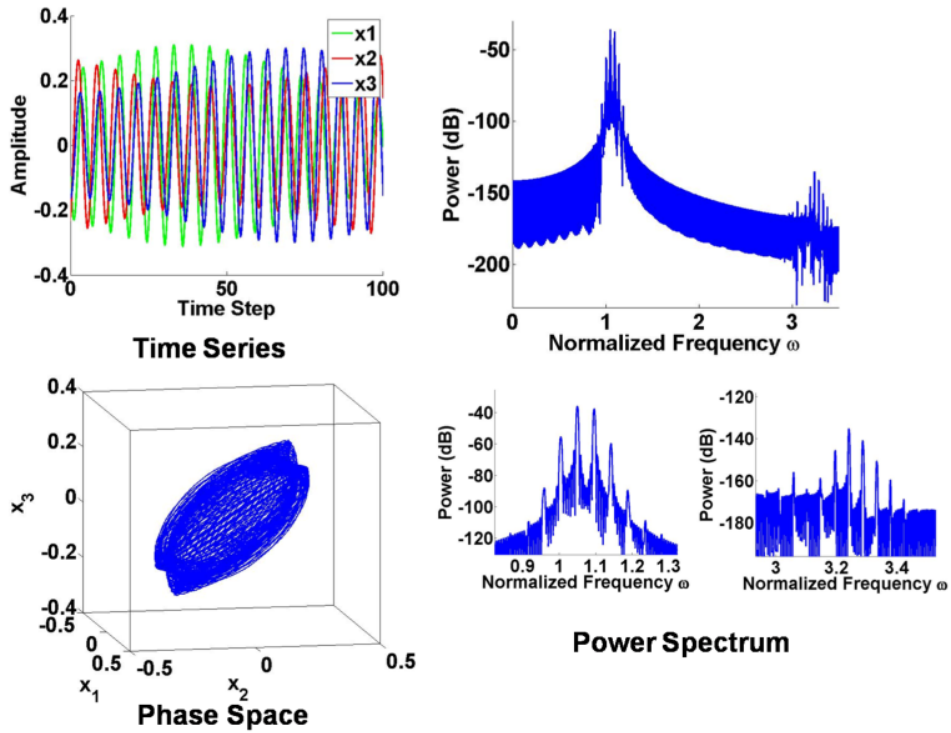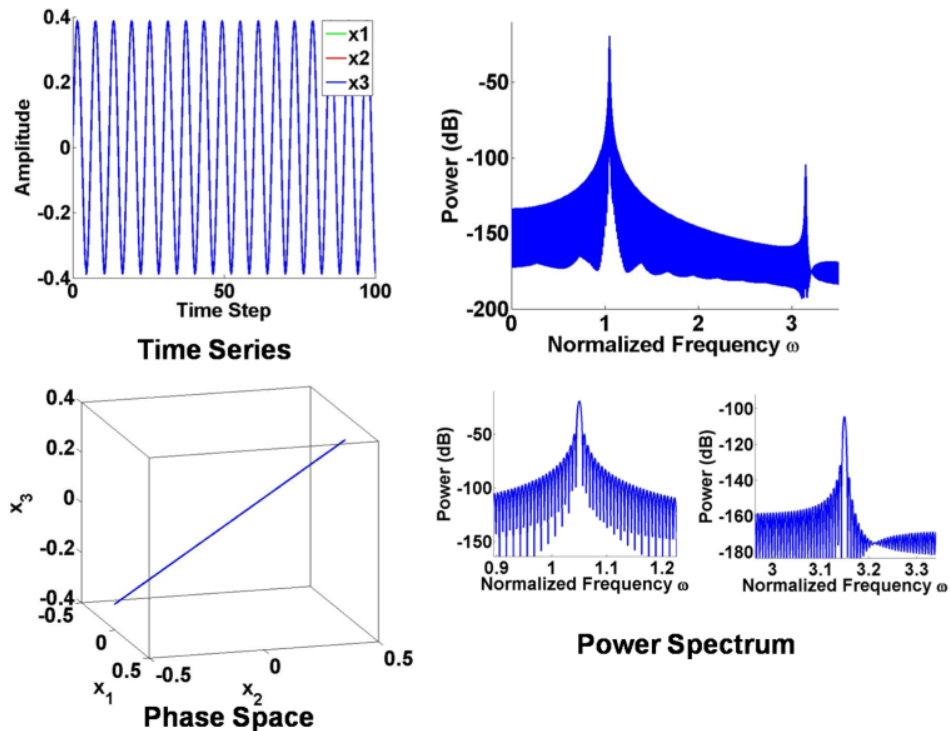
Figure 5.8: Simulation of coupled system for $\lambda = -4.08 \times 10^{-3}$, $\epsilon = 0.001$, and $\omega = 1.05$: (a) Time-series for x_1, x_2, x_3, (b) Power spectrum for x_1 and the zoomed view around fundamental frequency and its third harmonic, (c) Phase-space for x_1, x_2, x_3, and (d) Poincaré section with $(\dot{x}_1, x_1)$, $(\dot{x}_2, x_2)$, and $(\dot{x}_3, x_3)$.

5.3.2   1:3 Sync

Albeit of having a narrow region around $\omega = 3$, the coupled system shows $2\pi/3$ phase-locked state similar to Fig. 5.4. Here the frequencies of the individual oscillators are locked at 1/3rd of the excitation frequency as shown in Fig. 5.11. Close to this region (e.g. around $\omega = 3.15$) the coupled system shows a full entrainment to the excitation frequency as shown in Fig. 5.12 as the value of ϵ is raised from 0.1 to 2. The 1:3 sync region also shows an open area below $\epsilon = 0.04$ where the oscillations are too unstable to be synchronized at lower values of ϵ and the oscillations display a transitory behavior between almost periodic to periodic at higher values of ϵ until the 1:3 synchronization occurs.

(a) $\lambda = -4.08 \times 10^{-3}$, $\boldsymbol{\epsilon = 0.01}$, and $\omega = 1.05$

(b) $\lambda = -4.08 \times 10^{-3}$, $\boldsymbol{\epsilon = 0.1}$, and $\omega = 1.05$

Figure 5.9: Simulation of coupled system for $\lambda = -4.08 \times 10^{-3}$, $\omega = 1.05$ while varing ϵ: (a) $\epsilon = 0.01$ and (b) $\epsilon = 0.1$. In both the figures, time-series for x_1, x_2, x_3, power spectrum for x_1 and the zoomed view around the fundamental and the third harmonic, and phase-space for x_1, x_2, x_3 are shown.
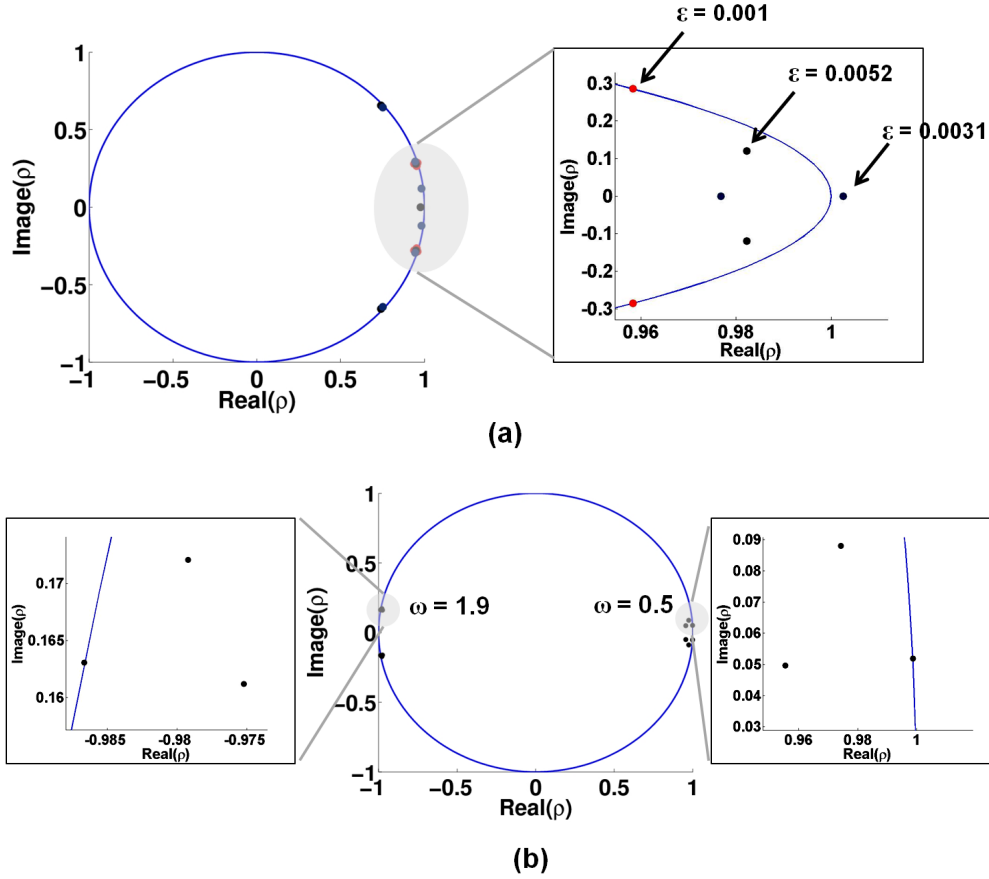
66

Figure 5.10: Floquet multipliers in two sweep directions around 1:1 sync region shown in Fig. 5.7: (a) $\epsilon = 0.001, 0.0031, 0.0052$ at $\omega = 1.05$. While sweeping ϵ from low to high, at $\epsilon = 0.001$ the system goes through Neimark-Sacker (NS) bifurcation, at $\epsilon = 0.0031$ the system goes through Saddle-Node (SN) bifurcation, and at $\epsilon = 0.0052$ the system shows almost-periodic oscillations. From this point as ϵ is increased all the multipliers stay inside the unit-circle and the system eventually shows periodic oscillations. (b) $\omega = 0.5$ and $\omega = 1.9$ at $\epsilon = 0.035$. As ω is swept from the center of 1:1 sync region past the left boundary and the right boundary, one complex-conjugate pair moves out of the unit-circle indicating NS bifurcation at $\omega = 0.5$ and at $\omega = 1.9$ respectively.

5.3.3 Effect of Damping

As shown previously, the sync region remains open at lower values of ϵ. To substantiate the effects of damping in this region, a separate set of simulations were undertaken to comprehend the sensitivity of the coupled system. After changing δ to 0.01 and making appropriate changes in the other parameters, a different set of sync regions were found following the same procedure shown in the previous section. The 1:1 region is shown in Fig. 5.13(a) and 1:3 region is shown in Fig. 5.13(b). As seen from Fig. 5.13(a) the 1:1 sync
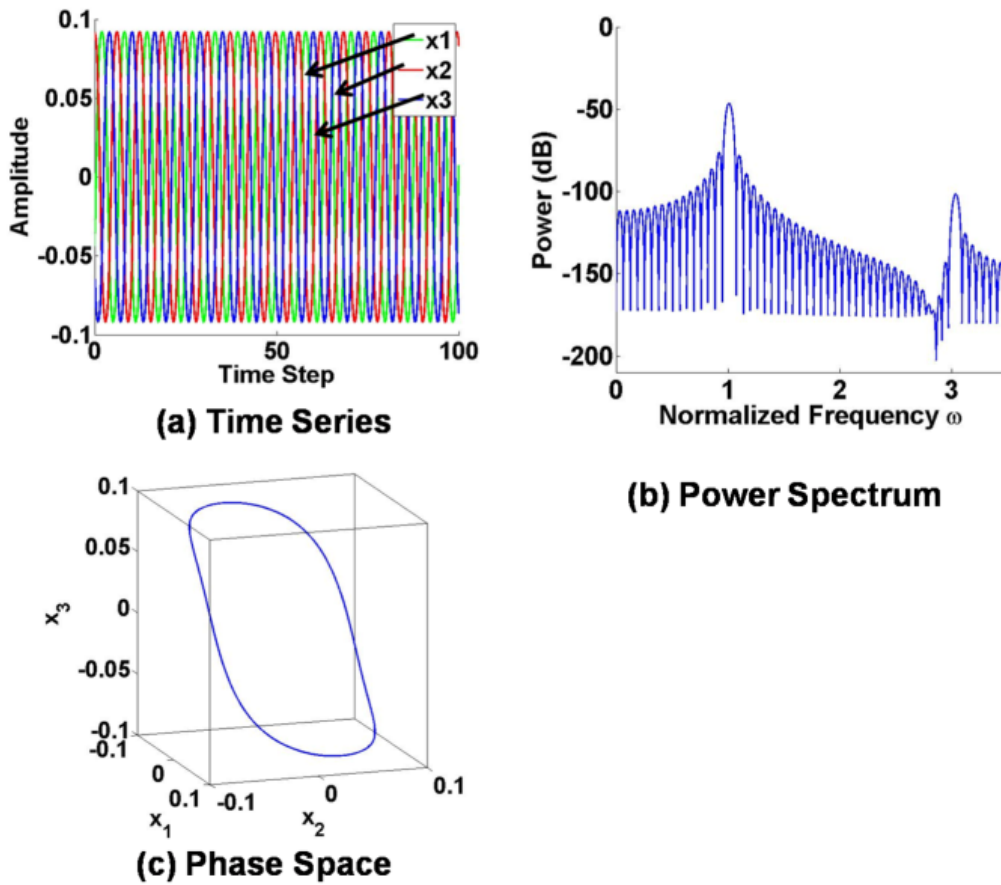
Figure 5.11: Simulation of coupled system for $\lambda = -4.08 \times 10^{-3}$, $\epsilon = 0.05$, and $\omega = 3.03$: (a) Time-series for x_1, x_2, x_3, (b) Power spectrum for x_1 and the zoomed view around the fundamental and the third harmonic, and (c) Phase-space for x_1, x_2, x_3.

region shows an enclosure at the lower values of ϵ. The effect of other possible sync regions and nonlinearity can be seen at the left boundary in Fig. 5.13(b) where the coupled system exhibits almost periodic to periodic behavior near this boundary.
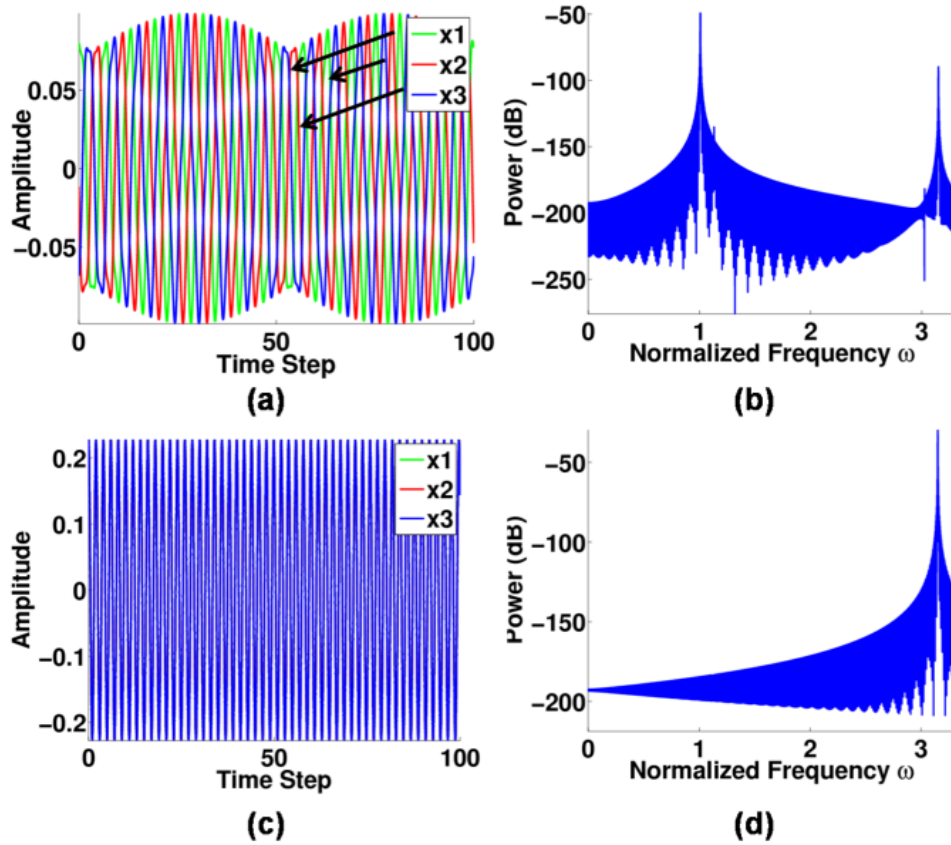
Figure 5.12: Simulation of coupled system for $\lambda = -4.08 \times 10^{-3}$ and $\omega = 3.15$: (a) and (c) show the time-series for x_1, x_2, x_3 at $\epsilon = 0.1$ and 2 respectively. Here (b) and (d) show the associated power spectra for x_1 and the zoomed view around the fundamental frequency and the third harmonic.
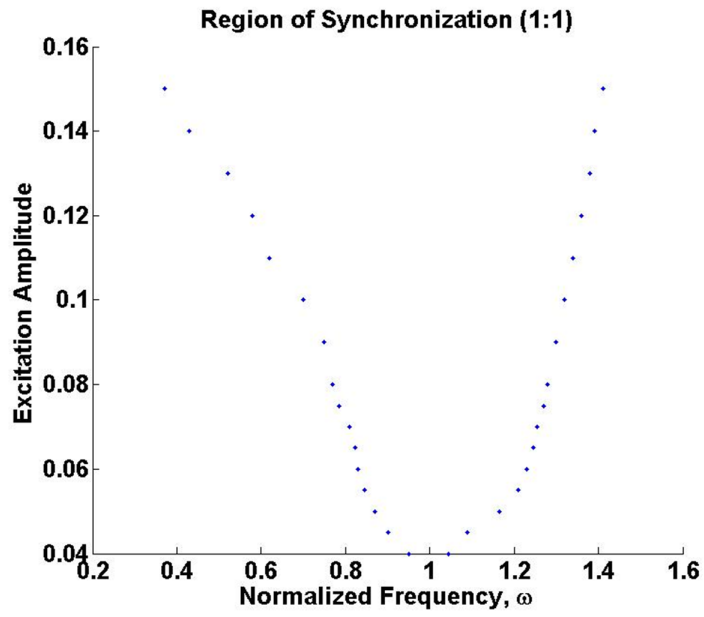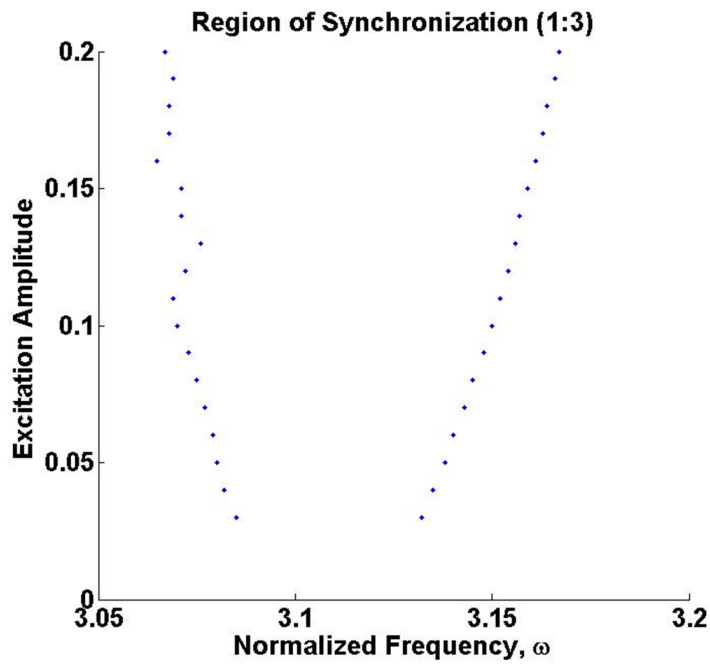
Figure 5.13: Sync regions obtained for $\delta = 0.01$ and $\lambda = 0.012$: (a) 1:1 sync region and (b) 1:3 sync region

5.4   Discussion

The system shown in Eq. 5.1 has a rotational symmetry described by cyclic group $\mathbf{Z_3}$ with permutation $(x_1, x_2, x_3) \mapsto (x_3, x_2, x_1)$ [59]. The change in the coupling strength of rotationally symmetric system results in the solutions that have spatio-temporal symmetry [7]. Group theory combined with equivalent Hopf bifurcation theory can describe four possible states of phase-locking behavior in a ring of three coupled oscillators: (a) completely synchronized state, (b) one third of a cycle out-of-phase with each other, (c) two synchronized to each other with third resonator with unrelated phase, or (d) two out of synchrony and the other at twice the frequency [3]. These states describe the generic behavior of the coupled system and therefore it was not possible to observe all four states for the coupled system presented in this study.

5.4.1   Autonomous System

In section 5.2 it was shown that, after going through the Hopf bifurcation, all periodic solutions of a single resonator within the coupled system maintain a fixed phase difference with the neighboring element. Generally in a ring of n-coupled elements (unidirectionally or bidirectionally coupled), the system exhibits $2\pi/n$ phase difference between neighboring elements for odd n [8] [60]. Similarly in this system with n=3, $2\pi/3$ phase difference appears for all stable periodic cycles. Past a specific value of λ, the symmetry between the three oscillators in a phase-locked state breaks and the system goes through a secondary Hopf bifurcation leading to a torus without the spatio-temporal symmetry as seen in Fig. 5.5c. Decreasing the value of λ from this point onwards causes the coupled system to go through a sequence of symmetry breaking bifurcations as indicated in Fig. 5.2. It was observed during the simulations that these bifurcations lead to multiple tori with each bifurcation adding another fundamental frequency till the trajectories of three elements envelope each another by surrounding the individual loops charted by each element (shown in Fig. 5.5d). This suggests that as more frequencies are added, the coupled system becomes more unstable. Note that this change occurs in a narrow range of the coupling parameter.

5.4.2   Nonautonomous System

From Fig. 5.5 we can see that at a specific value of the coupling strength, the coupled system with symmetry-breaking bifurcations shows the 1/3 subharmonic oscillations accompanied by the quasiperiodic oscillations. It is possible for such a system in a priori oscillatory state to be synchronized at an excitation frequency exactly 3 times the oscillation frequency [8] [58]. This and other types of behavior observed in this system in the presence of the excitation force creates three distinct states : (a) unstable, (b) fully entrained to the excitation frequency, and (c) phase-locked and synchronized at a ratio of the excitation frequency. At a slightly detuned excitation frequency and at a low value of excitation amplitude, in the region shown as the red square in Fig. 5.7, the coupled system in a priori oscillatory state breaks the symmetry as shown in Fig. 5.8. The phase difference between individual

elements and the excitation force does not remain constant which makes the system unstable. While increasing the excitation amplitude value from low to high at $\omega = 1.05$, local stability analysis shown in Fig. 5.10(a), indicates that the system goes through an interesting series of bifurcations; from Torus (NS) bifurcation to Saddle-Node (or Pitchfork) bifurcation which leads to almost-periodic oscillations. In this region damping can be the prominent cause of such behavior. The following was observed while adiabatically increasing ϵ from 0.001 to 0.01 in this region. At $\epsilon = 0.001$, the largest pair of the multipliers stays outside the unit-circle. Increasing ϵ from here the largest pair of eigenvalues moves inside the unit-circle. After increasing ϵ from here the largest pair meets at the real axis and then they move in opposite direction on the real axis; one of them eventually crosses the unit-circle. While increasing ϵ from here the largest pair shows transitory behavior such as moving inside the unit-circle and moving out of the unit-circle on the real axis. Further increasing ϵ makes the pair move inside the unit-circle. Similar behavior was observed for $\delta = 0.01$ with an appropriate change in the other parameters as shown in section 5.3.3. Therefore we can attribute this behavior to damping before verifying it experimentally. An increment in the excitation amplitude overcomes the effect of damping and this results in periodic oscillations which are fully frequency-locked at the excitation frequency. Similar behavior occurs around 1:3 sync region at a low excitation amplitude. In all of the above states the interaction between the detuned individual resonators causes third harmonic components to rise. Note that the system still maintains its original frequency of oscillations. As noted before increasing the value of excitation amplitude causes the system to synchronize in 1:1 and 1:3 sync regions shown in Fig. 5.7. Here at higher excitation amplitude and at frequency outside the sync regions but close to the boundaries, the oscillations were observed to be almost periodic. While detuning the frequency slightly away from the boundaries, state (c) described in the beginning of section 5.4[1] was observed. Detuning the frequency farther away from the boundaries causes the coupled system to go through symmetry breaking bifurcations leading to quasiperiodic oscillations. Local stability check for the frequency values away from the boundary confirms this phenomena as is shown in Fig. 5.10(b). These simulations show how the coupled system reacts while changing the excitation amplitude and detuning the excitation frequency; these two factors govern how the system, in a priori oscillatory state for a given λ, can be eventually synchronized. Simulations performed in the region of parameter space where λ is below the critical coupling strength indicate that the system can start oscillations only in the presence of the excitation signal; this case is similar to the case of uncoupled individual resonators. In this study individual MEMS resonators with identical natural frequencies were considered. It is possible for resonators on different chip dies or on the same chip die to have nonidentical natural frequencies due to the variation of the mass caused during the fabrication. It was observed in the simulation that even after slightly detuning the natural frequencies of the resonators the coupled system synchronizes in the presence of the excitation force. The fully synchronized state of the coupled system shown in Fig. 5.7 is then similar to the injection-locking of oscillators with different natural frequencies by an external force [14]. The multitude of properties discussed above indicate that the present

---

[1] Two resonators synchronize with each other while the third resonator exhibits an unrelated phase.

system of coupled nonlinear resonators can be used as a sensor depending on the applications. These include a MEMS implementation of multifrequency synthesis shown in [10], drive axis implementation of coupled gyro system analyzed in [24], and implementation of a sensing element to detect an excitation force with a dependence on the *frequency* and the *damping*.

5.5 Summary

In this chapter the simulation study of a unidirectional coupled system of resonators was presented. It was shown by numerical methods that the coupled system can oscillate without an excitation signal at a specific value of the coupling strength and can also exhibit quasiperiodic cycles with a change in the coupling strength. Adding an external force to the coupled system in a priori oscillatory state changes the dynamics significantly. Phase-locked and frequency-locked states of the coupled system were also discussed. It is concluded from the local bifurcation analysis that the coupled system has a strong potential to be used as a sensor depending on the application due to a dependence on the coupling strength, the damping, and the excitation force amplitude and frequency.

Chapter 6

Characterization of Nonlinear MEMS Resonators

In this chapter the experimental results of the individual nonlinear resonator and the coupled system are presented.

6.1 Resonance Characteristics

There are many methods for electrostatically actuating MEMS device. The single resonator can be actuated by applying an ac excitation voltage with a dc bias between the mass and either of the electrodes. Typically the motional current, which is proportional to the change in the capacitance between the movable comb fingers and the fixed comb fingers, is measured. Measurements were performed on Agilent 4294A impedance analyzer using the test setup shown in Fig. 6.1(a). Using the capacitive bridge technique, the impedance of the DUT is measured by calculating the ratio between the voltage across the DUT and the current across it. This ratio consists of magnitude and phase [61]. Here the left electrode was connected to the high port, the device (anchor pad) was connected to the low port of the impedance analyzer, and the right electrode was connected to ground. For all the measurements shown in the subsequent sections, the data contains the real part and the imaginary part of the complex impedance. By selecting this option impedance analyzer calculates an equivalent series resistance as the real part and equivalent series reactance as the imaginary part. From the equivalent circuit model of a resonator it can be observed that the real part contains a purely mechanical term and an offset added by purely capacitive term, whereas the imaginary part contains purely capacitive terms (see Appendix B). Thus the mechanical and the electrical parameters of the device can be quickly determined from the real part and the imaginary part, respectively.

The resonators were excited with the bias of 20 V and the ac amplitude of 25 mV and the pressure was set to 30 Pa. Table 6.1 summarizes the resonance characteristics. Group I comprised of the resonators that were chosen from three separate dies (referred to as Res B, Res D and Res E from here on). Taking the resonant frequency of Res E as the center, the
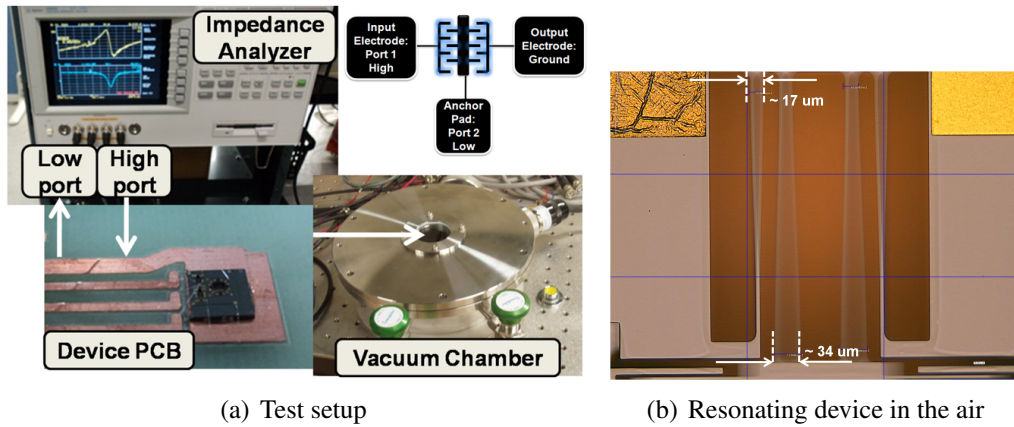
(a) Test setup

(b) Resonating device in the air

Figure 6.1: Single resonator exeepriments: (a) shows the test setup used for the results shown in sections 6.1 and 6.2. Here the top right corner shows how the device was actuated. The captured motion of one of the devices at its resonant frequency is shown in (b). Note the unequal displacement values for the inner and the outer beams.

variation in the other resonant frequencies was calculated as 0.27% for Res B and 1.69% for Res D. From –3 dB bandwidth points around the resonant frequency, Q was calculated as 2955 for Res B, 4440 for Res D, and 2861 for Res E. Group II comprised of the three resonators that were selected from a single die (referred to as Res 1, Res 2 and Res 3 from here on). Taking the resonant frequency of Res 3 as the center, the variation in the other resonant frequencies was calculated as 0.47% for Res 1 and 0.08% for Res 2. Q was calculated as 4640 for Res 1, 5540 for Res 2, and 4026 for Res 3. Based on these results it can concluded that the matching for resonators on the same die is better than that of resonators on the separate dies. Note that the amplitude level of Res 1 at the resonant frequency was observed to be substantially higher than those of Res 2 and Res 3 whereas Res 2 exhibited the highest Q. These variations can be due to the change in the effective mass during the fabrication. The causes of variation in the mass include different doping angle, debris deposited during fabrication and die separation, minute cracks, and/or change in parasitic capacitance of bonding wires and the circuit board. Q factors can vary according to the position of the resonator on the die or the fabrication lot making it more or less robust to the dicing and cutting of the

Table 6.1: Comparison of Resonators in Group I and Group II

	Group I (Separate Dies)			Group II (Single Die)		
	Res B	Res D	Res E	Res 1	Res 2	Res 3
Resonant frequency (kHz)	8.274	8.436	8.296	8.816	8.865	8.858
Q factor	2955	4440	2861	4640	5540	4026
Peak amplitude level based on impedance (dB)	56.21	56.83	55.25	68.58	52.14	53.72

dies, a variation in ohmic resistance between electrodes, and the parasitic capacitances. Also note that minor variations in the pressure inside the vacuum chamber were observed during the experiments.

6.2 Hysteresis Characteristics

In this section, the nonlinear resonance characteristics of the resonators in Group I and Group II are described.

To begin with, many different resonators on separate dies from Group I were characterized in the air. All of these resonators were tested at a high bias and the maximum allowable
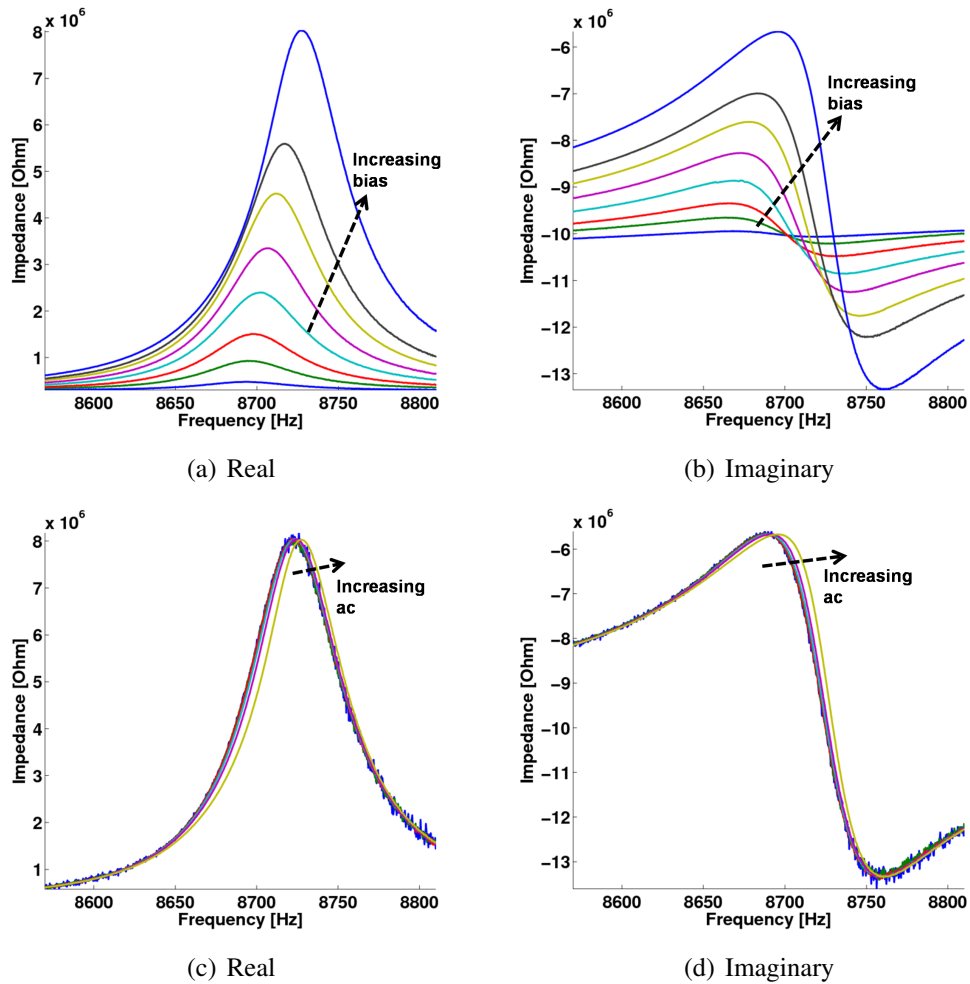

(a) Real

(b) Imaginary

(c) Real

(d) Imaginary

Figure 6.2: Upsweep frequency response curves for Res A (Group I) in the air: (a) and (b) show the effect of bias sweep at (12.9V, 24.02V, 33.32V, 44.03V, 53.6V, 63.4V, 71.5V, 87V) with constant ac amplitude of 1V. Here (c) and (d) show the effect of ac sweep at (50mV, 100mV, 200mV, 400mV, 600mV, 1V) at constant bias of 87V.

ac amplitude of 1 V to determine their nonlinear behavior and to analyze the hysteresis characteristics during the upsweep and the downsweep of the frequency. Fig. 6.2(a) shows the frequency response curves of Res A (from Group I) under different excitation scenarios during the upsweep. Here Figs. 6.2(a) and 6.2(b) show the resonator response in the *air* while varying the bias from 12.9 V to 87 V with constant ac amplitude of 1 V. It is clear from the shift in the resonant frequency that the resonator exhibits the hard-spring effect. This effect is diminished when the ac amplitude is varied from 50 mV to 1 V at constant bias of 87 V as seen in Figs. 6.2(c) and 6.2(d). The hard-spring effect was observed to be more pronounced in the vacuum. In the vacuum, the slide-film damping between the fingers [19] and the overall motional resistance against the air molecules is lowered which results in a high Q factor. High Q factor and an addition of the third-order vibrations pull frequency response to the right as the springs harden. Fig. 6.3 depicts a typical frequency response that was observed during the upsweep and the downsweep of the frequency where the pressure, the ac amplitude and the bias values were set to 30 Pa, 105 mV, 20 V, respectively. Ringing effect was observed during the upsweep and the downsweep of the frequency where the vibration amplitude jumps down and up, respectively. This effect can be attributed to two factors: (1) a low damping effect in the vacuum and (2) the sensitivity of the instrument. For example, the resonator shows lower ringing when the bandwidth of the instrument is lowered. Additionally a longer dwell time at each frequency point helps stabilize the device and thereby reduces the ringing effect (see Fig. 1.1(b)). Note that for the remainder of this chapter, the jump-down and jump-up frequency points define the hysteresis window. Within the hysteresis window the resonator exhibits two vibrational amplitudes at a single frequency. Outside of the window, the resonator exhibits one stable vibrational amplitude. This indicates that the resonator has gone through the saddle-node bifurcation [43].
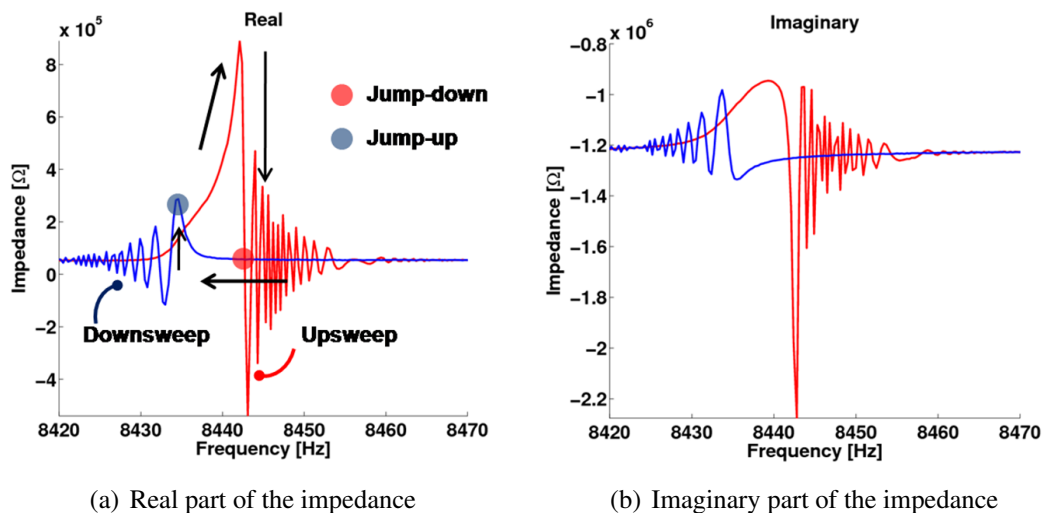

(a) Real part of the impedance

(b) Imaginary part of the impedance

Figure 6.3: Frequency response of Res D (Group I) during upsweep and downsweep: (a) real part and (b) imaginary part. The excitation conditions were set as ac excitation amplitude = 105 mV and bias = 20 V at pressure = 30 Pa.
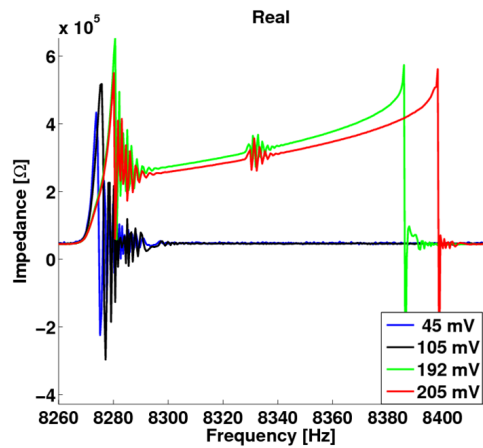
6.2.1 Resonator Group I: Separate Dies

In the subsequent sections, the effects of varying the ac voltage, the bias voltage and the pressure for the resonators on three separate dies are described.
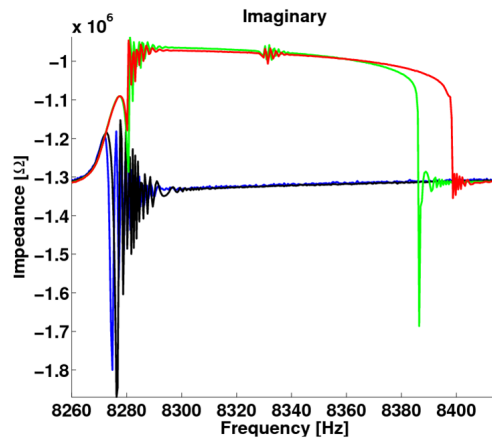
Ac Voltage

Fig. 6.4 shows the response of the resonators Res B, Res D and Res E while varying the excitation amplitude and keeping the pressure and the bias constant at 30 Pa and 20 V, respectively. For the purpose of clarity, the downsweep responses are not shown. However it was observed that less than 5 Hz variation existed during the downsweep in all three resonators . As shown in Fig. 6.4, the resonators show a typical hard-spring response up to a certain value of the excitation amplitude after which the response extends to a higher value of frequency. As shown in Fig. 6.4 the approximate values of the ac excitation amplitude at which the extension occurs are 192 mV for Res B, 147 mV for Res D, and 170 mV for Res E. The frequency at which the extension in a given resonator occurs at higher excitation amplitudes is nearly identical. For example, this frequency is about 8445 Hz at 147 mV and 205 mV in the case of Res D as shown in the inset in Fig. 6.4(c). Another important observation is that during the upsweep Res B and Res E show slight ringing in the middle of the curve as shown in Fig. 6.4(a) and Fig. 6.4(e) respectively. The resonators seem to have gone through more bifurcations which help continue the upsweep response. After continuing the vibration this way, the springs can maintain a stable vibration up to only a certain frequency, after which it drops to a lower value such that the restoring force in the springs can maintain an equilibrium with the excitation force. It was observed that Res D exhibits the largest hysteresis window at 205 mV. In the case of the extended hysteresis it is worthy to note that the imaginary part of Res D (Fig. 6.4(d)) shows nearly constant capacitive impedance. This is more or less true for the other two resonators as well. This characteristic can be extremely beneficial when the resonator is required to have nearly zero or a minimal variation within a specific band of excitation frequency. This indicates robustness against the variation in the vibration frequency that can occur due to the noise. Also note that within the extended hysteresis region the coexistence of two vibrational amplitudes indicates a better control and predictability for switching the resonator between the two states. However the mechanism for the extended hysteresis (see section 6.3) depends on the interplay between outer beam and inner beam which needs to be carefully controlled. This feature is crucial in facilitating multiple bifurcations in the resonator and thereby extending the response. It is worthy to note that by increasing ac voltage, the folded beam pairs exhibit large displacement which leads to large deformation as the beams harden. Hence the overall nonlinear spring constant increases when ac voltage is increased and as a result the responses *do not overlap* before the extended region for small values of ac voltage.
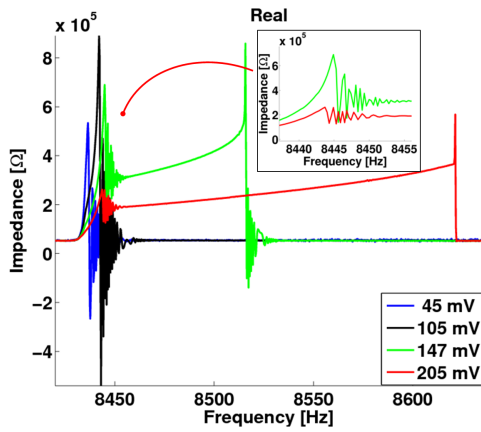
Bias Voltage

Fig. 6.5 shows the effects of changing the bias during the upsweep of frequency. Note that the imaginary parts are omitted. The values of the ac excitation amplitude and the
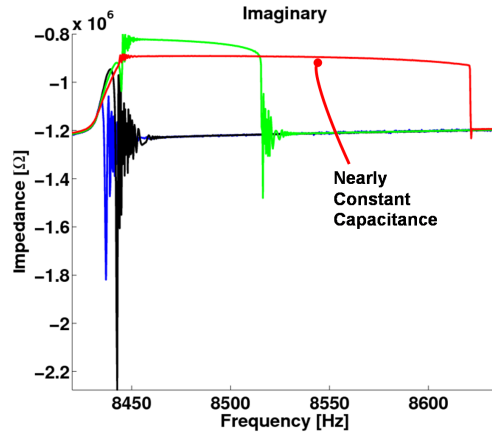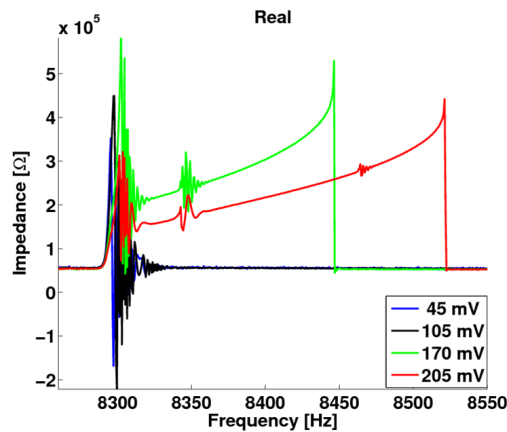
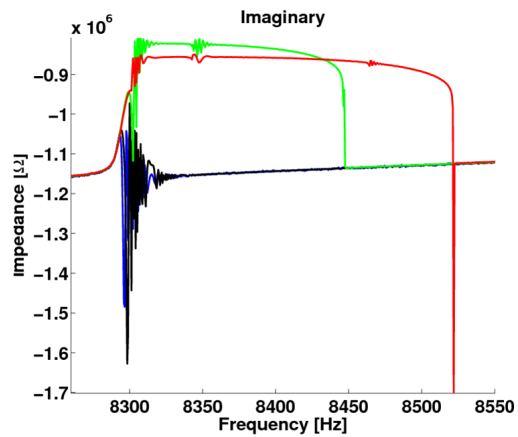Figure 6.4: Real (left column) and imaginary (right column) parts of the resonator response during the upsweep of frequency at bias = 20 V and pressure = 30 Pa. (a)-(b): Res B with the ac amplitude sweep at [45 mV, 105 mV, 192 mV, 205 mV], (c)-(d): Res D with the ac amplitude sweep at [45 mV, 105 mV, 147 mV, 205 mV], and (e)-(f): Res E with the ac amplitude sweep at [45 mV, 105 mV, 170 mV, 205 mV]. Note that downsweep of the frequency is not shown for clarity.

pressure are kept constant at 205 mV and 30 Pa, respectively. The behavior shown in Fig. 6.5 is qualitatively similar to that of the responses shown in the previous section. Here the electrostatic force increases significantly while incrementing the bias voltage. This is due to an increase in the steady-state capacitance between the comb fingers. The resonators display the nonlinear resonance at a low bias value. Also it is important to note that the extension of the hysteresis depends more on the bias voltage than the ac excitation amplitude. For example, a high ac excitation amplitude with a low bias does not always induce the extended hysteresis. As mentioned in the previous section, the frequency at which the extension occurs was observed to be identical while increasing the bias value. The bias values at which the extension occurs are 14.7 V for Res B, 13.5 V for Res D, and 16.2 V for Res E. Notice that for all three resonators, an increase in the bias value yields a higher amplitude and they *overlap*
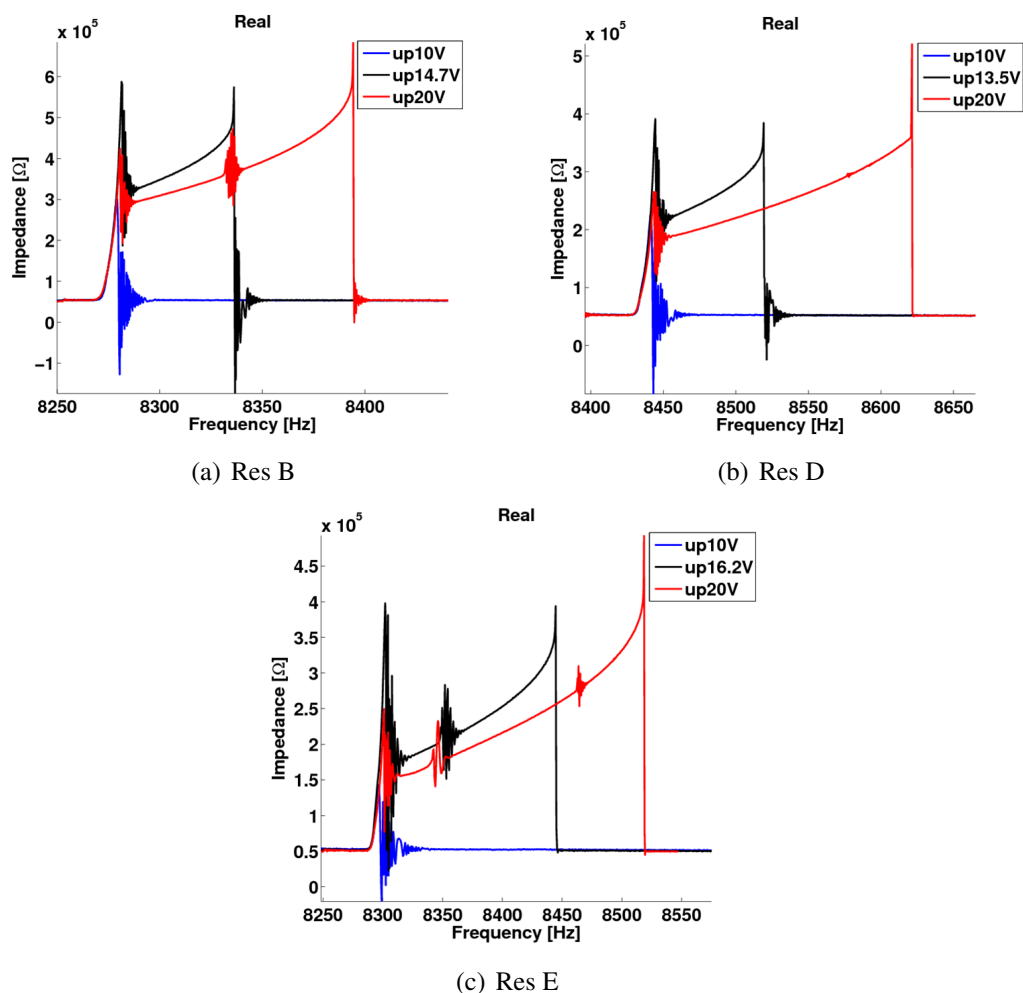

(a) Res B

(b) Res D

(c) Res E

Figure 6.5: Real part of the frequency response curves with ac excitation amplitude = 205 mV and pressure = 30 Pa: (a) Res B with bias values = [10 V, 14.7 V, 20 V], (b) Res D with bias values = [10 V, 13.5 V, 20 V], and (c) Res E with bias values = [10 V, 16.2 V, 20 V]. Downsweep is omitted for clarity.

each other until a specific bias value at which the extension occurs. This is not necessarily true when increasing the ac voltage as seen in Figs. 6.4(a), 6.4(c), 6.4(e) where the response shifts slightly to the right before the ensuing extension occurs. The effect of increasing bias is that it changes the equilibrium position of the resonator around which the folded beam pairs resonate in the presence of the ac voltage. Hence the change in dc does not significant increase the overall nonlinear spring constant which results in *overlapping* of the frequency response in the lower frequency range. The change the nonlinear stiffness is only prominent at a large dc leading to the extended response for an identical value of ac voltage.

Hysteresis Window

Fig. 6.6 refers to the hysteresis window calculated from the jump points during the upsweep and the downsweep for Res B as an example. Fig. 6.6(a) illustrates the change in the hysteresis window when the ac excitation voltage is varied at constant bias of 20 V and Fig. 6.6(b) illustrates the change in the hysteresis window when the bias is varied at constant ac excitation voltage of 205 mV. The pressure was kept constant at 30 Pa. For the measurements shown in Fig. 6.6(a), the maximum excitation amplitude was chosen as 305 mV so that the device can still exhibit extended hysteresis. Above this value the hysteresis window stays constant. As seen from Fig. 6.6 the device starts to exhibit the nonlinear resonance at a low excitation value. As the excitation voltage is increased the device shows a drastic change in the hysteresis window. As shown in Fig. 6.4(a) 6.4(c) 6.4(e), changing the ac excitation amplitude extends the hysteresis window but lowers the vibrational amplitude in all resonators. The oscillation phenomenon depending on time (e.g. ringing), which may be induced by the possible interaction between the outer and inner beams, continue adiabatically

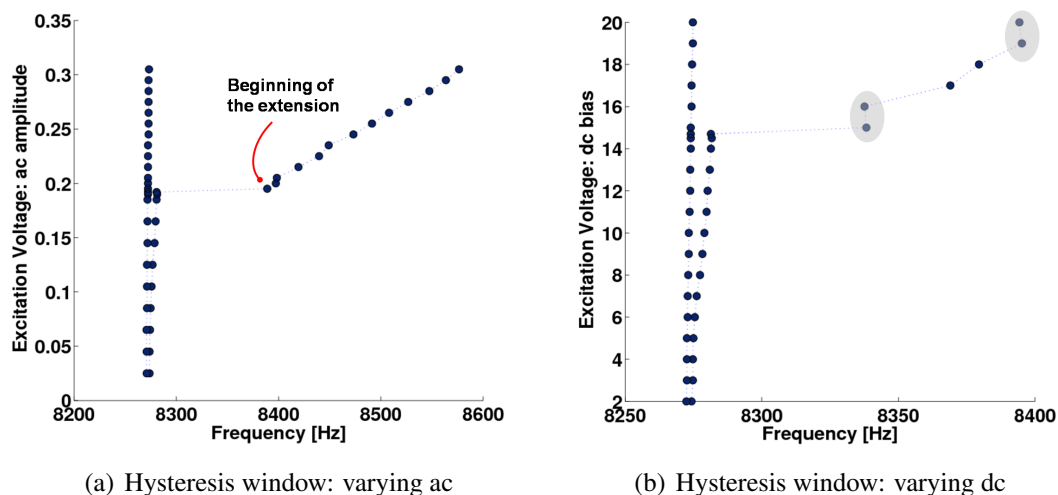(a) Hysteresis window: varying ac (b) Hysteresis window: varying dc

Figure 6.6: Hysteresis windows for Res B: (a) varying ac excitation amplitude with bias = 20 V and (b) varying bias with ac excitation amplitude = 205 mV. The ovals show constant amplitude points. Left forks represent jump points during downsweep and right forks represent jump points during upsweep. Here bias = 20 V and pressure = 30 Pa.

while changing the ac excitation amplitude and as a result the hysteresis windows widen. However this is not necessarily true while changing the bias as seen in Fig. 6.6(b). It was observed that after engaging into the extended mode, the vibrational amplitude: (a) increases with an increase in bias and (b) stays almost constant at a few frequency points as shown in Fig. 6.6(b). This behavior is typical in all the resonators and markedly shows the effect of varying the bias on the nonlinear resonance. One possible reason for this disparate behavior can be that an increase in the bias increases the steady-state capacitance between the comb fingers. Consequently the qualitative behavior of the device can change due to the nonlinear resonance dependence on the bias.

Pressure

Pressure affects the molecular resonance in the material and as a result the motional resistance exhibited by the device increases with an increase in the pressure. For example, the experiments conducted on a device in the air showed only the linear resonance due to high damping. Bias > 60 V and ac amplitude = 1 V were required to produce any motion in the device. In air the device was not tested at an excitation value higher than the above value lest it may break. Hence a clear nonlinear resonance and extension of the hysteresis were not observed. However in the vacuum starting at 100 Pa, the devices exhibited a distinct nonlinear resonance similar to the one shown in previous sections due to the low damping. To compare the influence of pressure and the damping, devices were tested at 50 Pa, 30 Pa and 15 Pa. Fig. 6.7 shows the upsweep response of Res E with ac excitation amplitude = 205 mV at bias = 20 V while varying the pressure. Here it can be seen that at all pressure values, the nonlinear resonance occurs at approximately the same frequency point. The circled numbers in the Fig. 6.7(a) mark the ringing behavior at approximately the same frequency points. This type

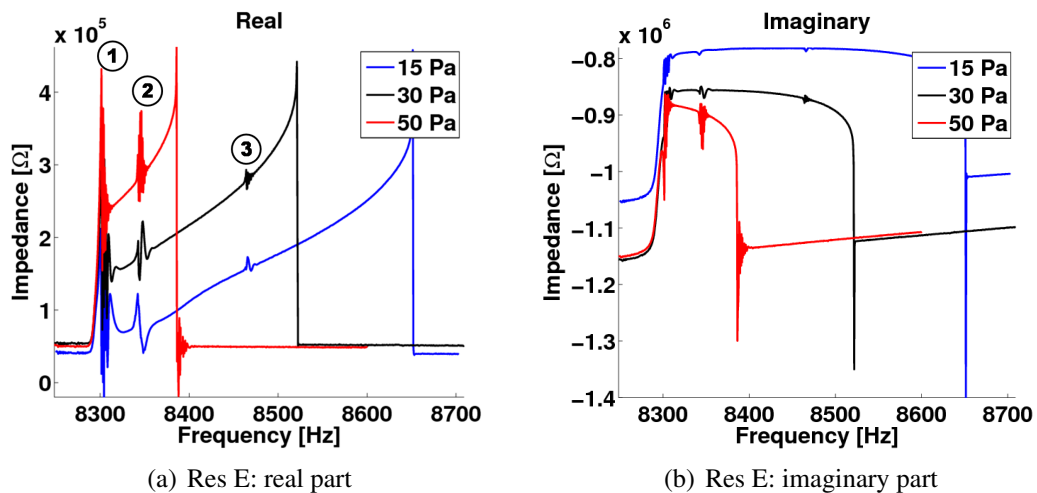(a) Res E: real part   (b) Res E: imaginary part

Figure 6.7: Effects of varying pressure from 15 Pa to 30 Pa to 50 Pa for Res E with ac excitation amplitude = 205 mV and bias = 20 V: (a) real part and (b) imaginary part. Multiple extension points were observed which are marked as (1),(2), and (3) in (a).

of ringing within the extended region was observed more or less in all three resonators. Note that this behavior may have been induced by additional bifurcations. The mechanism behind these bifurcations can be attributed to the interaction of the outer beams with the inner beams thereby sustaining the vibrations. Fig. 6.7(a) also shows that the width of the upsweep region increases with a decrease in pressure mainly due to an increase in the motional capacitance between the comb fingers. As pressure decreases from 50 Pa to 15 Pa, the amplitude of the vibrations also decreases as seen in Fig. 6.7(a). As the pressure is decreased the imaginary impedance level increases (it becomes more positive and the absolute imaginary impedance level decreases) due to an increase in the steady-state capacitance. For example, the values of capacitance derived from the imaginary impedance are 21.65 pF at 50 Pa, 22.35 pF at 30 Pa, and 24 pF at 15 Pa around the excitation frequency of 8.312 kHz. The increase in capacitance is due to a decrease in the damping effect. Here a higher damping effect relates to a higher dispersion of the energy between the comb fingers. Also note that at 15 Pa the imaginary curve shows almost constant impedance which is on par with the results shown in Figs. 6.4(b), 6.4(d), 6.4(f). The capacitance derived from the imaginary impedance for Res E at 15 Pa is plotted in Fig. 6.8(a). The deviation of capacitance values between 8.312 kHz and 8.479 kHz from the maximum capacitance in this range is shown in Fig. 6.8(b). Here we can see that the absolute deviation is around 1.2% neglecting the jumps at the extension points. Finally it is important to note that while varying the pressure, the temperature change inside the chamber was not monitored or considered. Temperature can affect the molecular resistance and the damping such that some of the qualitative behavior may change.

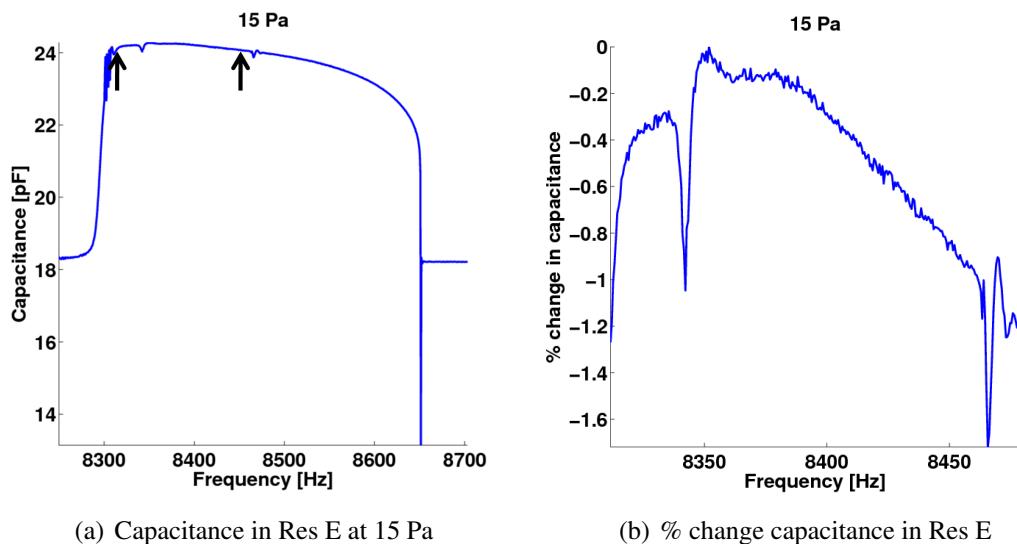(a) Capacitance in Res E at 15 Pa   (b) % change capacitance in Res E

Figure 6.8: Capacitance in Res E for the excitation conditions shown in Fig. 6.7 at 15 Pa: (a) capacitance versus frequency and (b) % change in capacitance from the maximum capacitance between the range shown by the arrows in (a).
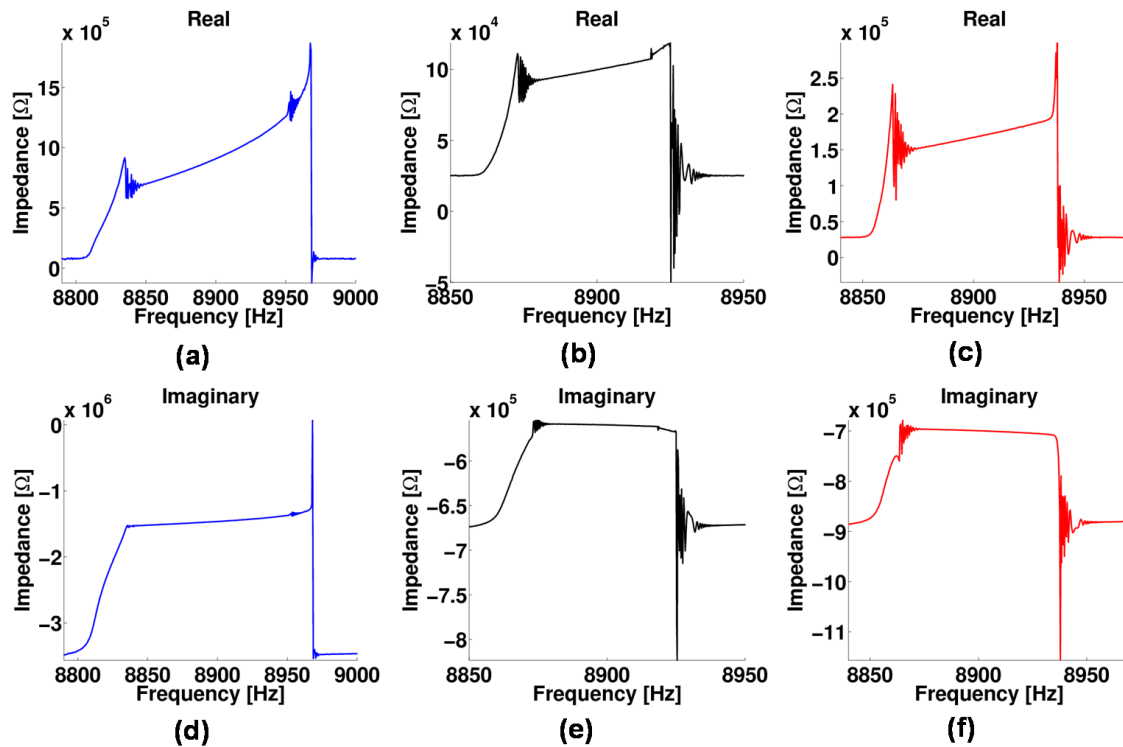
Figure 6.9: Comparison of the frequency responses of the three resonators on a single die with ac excitation amplitude = 205 mV, bias = 20 V, pressure = 30 Pa: (a), (b), and (c) are the real parts pertaining to Res 1, Res 2, Res 3 respectively whereas (d), (e), and (f) are the imaginary parts pertaining to Res 1, Res 2, Res 3 respectively. Note that the downsweep response is not shown for clarity.

6.2.2   Resonator Group II: Single Die

As discussed before the three resonators on a single die provided a better matching. Their resonant frequencies were observed to be closer to each other than those of the resonators in Group I. The behavior exhibited by the devices from Group II, while varying the excitation voltages and pressure, is qualitatively similar to the ones from Group I. Here in Fig. 6.9(a)–(c), the real parts of the response generated during the upsweep by the three resonators on a single die are shown for a comparison. The imaginary parts of the responses are shown in Fig. 6.9(d)–(f). Note that the amplitude levels of all three resonators are different with that of Res 2 being the smallest. As seen from Figs. 6.9(a) and (d), Res 1 shows substantially higher vibration than the other two resonators. This discrepancy was also observed on other test dies at the same location.
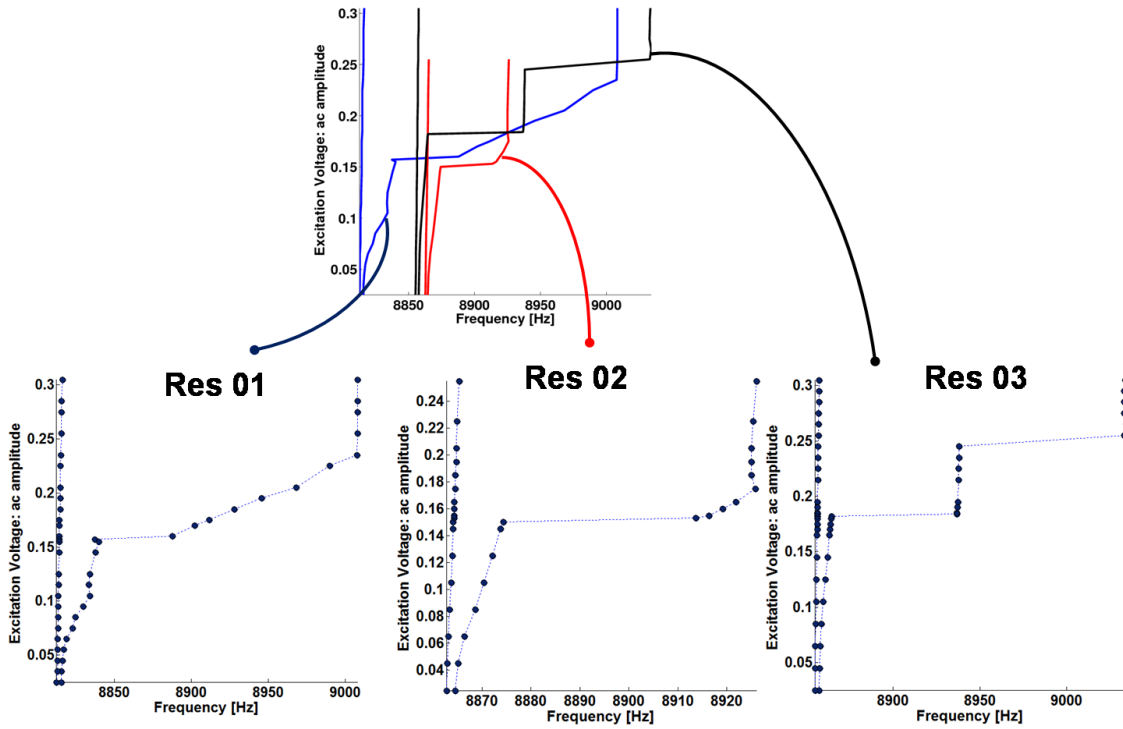
Figure 6.10: Comparison of the hysteresis window of the three resonators on a single die with varying ac excitation amplitude. Left forks represent jump-down points during downsweep and right forks represent jump-up points during upsweep. Here bias = 20 V and pressure = 30 Pa.

Change in ac Voltage

As shown in Fig. 6.9, the resonators show a typical hard spring response up to a certain value of the excitation amplitude. After that the response extends to a higher frequency as shown in Fig. 6.9. The frequency at which the extension in a given resonator occurs while sweeping the ac voltage was observed to be nearly identical as discussed in the previous sections.

Figure 6.10 shows the comparison of the hysteresis window while sweeping the ac excitation voltage. Here it can be seen that Res 2 shows the smallest window whereas Res 1 exhibits the largest window almost covering the other two resonator windows. The transition to the extended hysteresis in all three resonators is clear. Also note that at high enough ac excitation voltages, the windows stay nearly constant. This is particularly evident in the upper right side of the right forks for the three resonators. These values of ac excitation voltage seem to be the limit after which the amplitude of the vibrations stay nearly constant. By this comparison the characterization of the individual resonators is comprehensive and now they can be utilized in the coupled system and can be evaluated under varying ac excitation amplitude and excitation frequency (see section 6.4).
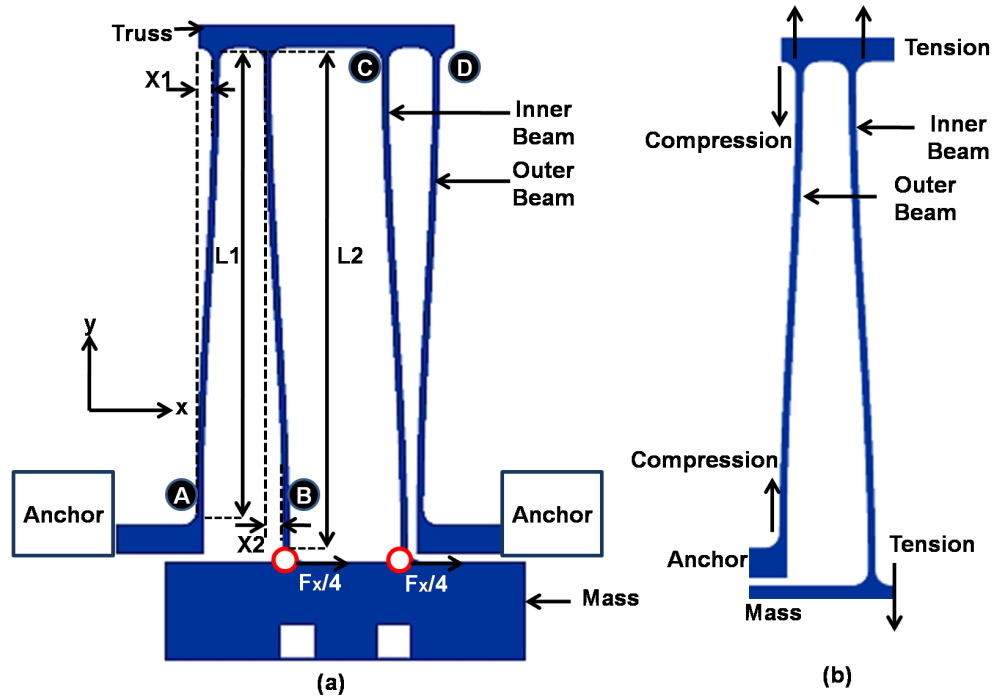
Figure 6.11: Mechanism for the hard-spring effect and extension of hysteresis: (a) outer beams are stiffer than inner beams due to L1<L2 which makes the displacements X1 and X2 different at peak resonance. Also note the differences between distances A–B and C–D, and (b) compressive stress on the outer beam and the tensile stress in the inner beam are not matched (see Ch. 4: section 4.3.3.

6.3   Mechanism for the Extended Nonlinear Resonance

The causes of the nonlinear behavior shown in the above sections are as follows. The inner beams shown in Fig. 6.11(a) develop higher modes of vibration due to a large compressive force experienced during the peak resonance to maintain an equilibrium; the truss can only partially remove the high tensile force present during peak resonance. This can cause the hard-spring effect. The ratio of the outer beam spring constant to the inner beam spring constant is 1.32. Because the outer beams are stiffer than the inner beams, they tend to compress less while being displaced during the peak resonance as discussed in Chapter 4. This type of nonuniform stress distribution can add to the hardening of the springs. Also note that in a symmetrical set of folded flexures containing four inner-outer beam pairs, the force applied to each inner-outer beam pair is $F_x/4$, where F_x is the total applied force on the mass. Here the inequality in the stiffnesses exists which makes the *restoring force* in a given inner-outer beam pair unequal during peak resonance displacement. This causes an asymmetric expansion and contraction of the folded beams which creates unequal displacements denoted by A-B and C-D in Fig. 6.11(a). All these conditions can cause the mass to sustain the vibrations as the frequency is swept past the resonant frequency and as a result

the extension of hysteresis can occur.

6.3.1 Folded Beam Pair as Coupled Oscillators

As shown earlier, when a single resonator is excited by an ac voltage with large bias, it exhibits hard-spring effect and hysteresis as the excitation frequency is swept. If the actuation occurs only in one direction, e.g. only through the parallel plate capacitance with dc bias, then the restoring force can be represented as $F_r(x) = k_1 x + k_2 x^2 + k_3 x^3 + O(x^4)$. However if the structure moves symmetrically in both x_+ and x_- direction in the presence of the ac excitation voltage, then we can assume that $F_r(-x) = -F_r(x)$. Therefore the restoring force contains only the odd order terms, hence $F_r(x) = k_1 x + k_3 x^3 + O(x^5)$. For simplicity, let the restoring force be $F_r(x) = k_1 x + k_3 x^3$ for the dynamic response generated in the presence of the ac excitation voltage. Now we focus on the effect of the cubic nonlinearity.

A MEMS resonator can be modeled as R-L-C circuit [62] where R represents the damping, L represents the mass, and C represents the spring constant. Appendix C shows the method by which the linear response of the resonator can be modeled by deriving the electrical equivalent circuit and then curve-fitting it to the measured data based on the model parameters. However this method is inadequate for modeling the nonlinear response due to the multiple bifurcations observed in the experiments. An elaborate model consisting of electrical equivalent circuit components, that can predict the nonlinear response, involves the displacement as the controlling voltage and several voltage controlled current sources as was
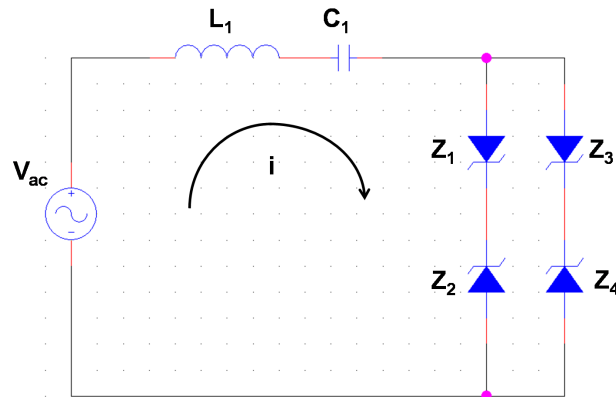

Figure 6.12: Experimental circuit to assess the hard-spring effect: inductor represents the mass and the capacitor represents the spring constant. Here the resistor from R-L-C circuit is removed to obtain better Q in the air. The nonlinear portion of the circuit is built from two pairs of Zener diodes in parallel. Each pair contains 15 V Zener diodes connected back-to-back in the clipper mode. Having two diode pairs increases the nonlinear effect as was observed in the experiment. Here $L_1 = 20\ \mu$H and $C_1 = 0.1\ \mu$F. The circuit was connected to the impedance analyzer which measures the current i after applying the voltage V_{ac} at different frequencies.

shown in [63]. A different approach involves a quantitative match between the simulation and the experimental results [12]. Here a plausible explanation of the extended behavior is provided by performing the experiments on Duffing type electronic circuit. Fig. 6.12 shows the circuit used for investigation of the nonlinear behavior. This circuit represents the MEMS resonator without the resistor because the experiments on this circuit were conducted in the air to increase the overall Q. The nonlinear Duffing-like behavior can be emulated by connecting two back-to-back pairs of Zener diodes and thus creating symmetric I-V characteristics. Having one diode pair is sufficient however it was observed that two pairs enhance the nonlinear effect.

Fig. 6.13(a) shows the frequency response curves of the circuit shown in Fig. 6.12. The amplitude of the excitation voltage is swept as 20 mV, 50 mV, 100 mV, 150 mV and 200 mV which eventually results in Duffing-like hard-spring behavior. These experimental results show that this circuit is a good candidate for conducting further experiments to simulate the behavior of the MEMS resonator which also shows hard-spring response as shown in Fig. 6.13(b).

Coupled Response

The folded-beam pair used in the MEMS resonator can be visualized as two coupled oscillators such as the one shown in Fig. 6.12. The coupled system of L-C-Diode oscillators is shown in Fig. 6.14. Here a series R_c and L_c were used as the coupling circuit where R_c represents the damping between the two resonating beams and L_c represents a portion of the truss.

The discrepancy in the lengths of the beams would result in different resonant frequencies if the oscillators were to be uncoupled. This behavior is shown in Fig. 6.15(a) which depicts the uncoupled frequency response of the two oscillators. The component values are identical; however the variation/tolerance in the individual components results in different resonant frequencies. This behavior emulates the uncoupled folded-beam pair with unequal lengths which can be modeled as two uncoupled oscillators. After being connected via the coupling circuit, the coupled system consisting of the L-C-Diode oscillators can emulate the folded-beam pair as shown in Fig. 6.15(b). The coupled system of two oscillators shows the in-phase peak and the out-of-phase peak as expected. The second peak was observed to be substantially smaller than the first peak for smaller values of R_c and L_c. After increasing L_c, the energy of the coupled system shifts to the peak on the right. Here the resistance R_c (damping) is also changed to examine its effect. As R_c increases from 384 Ω to 893 Ω, the first peak dampens and connects with the second peak; the imaginary portion of the response shows that these peaks also merge with each other. This behavior is qualitatively similar to the extended responses of the MEMS resonator shown in the previous sections. The ringing is negligible around jump down and jump up points in the coupled system of L-C-Diode oscillators compared to the MEMS resonator as seen in Fig. 6.13. This is because the electrical circuit experiments were conducted in the air which increases overall damping and because the coupling resistance is higher which dampens the unstable vibrations.

From these experiments it can be seen that two factors, the mass of the truss (coupling
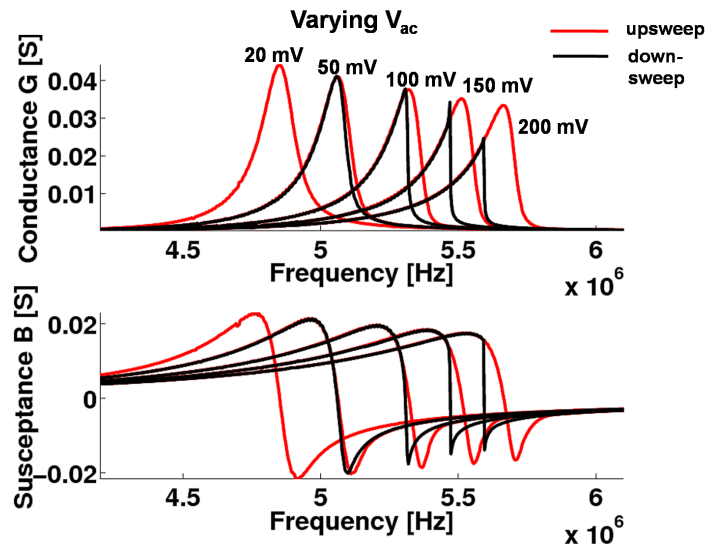
(a) Measured response of electronic Duffing circuit
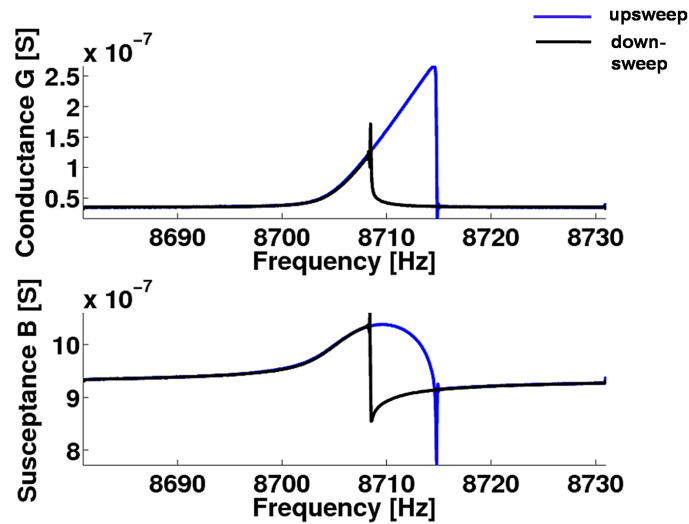
(b) Measured response of MEMs resonator

Figure 6.13: Comparison of the nonlinear resonance of the experimental electronic circuit with MEMS resonator: (a) the measured frequency response of the circuit shown in Fig. 6.12: here the conductance and susceptance curves are shown to emulate the nonlinear behavior exhibited by the circuit. As the voltage V_{ac} is swept, the circuit shows an increment in the peak frequency and the behavior is similar to Duffing effect. The hard-spring behavior is evident and a sizable hysteresis can be observed at 200 mV. (b) The measured frequency response of a MEMS resonator at $V_{ac} = 105$ mV, $V_{dc} = 20$ V, and pressure $= 50$ Pa: note the qualitative match between (a) and (b) at large ac voltage.
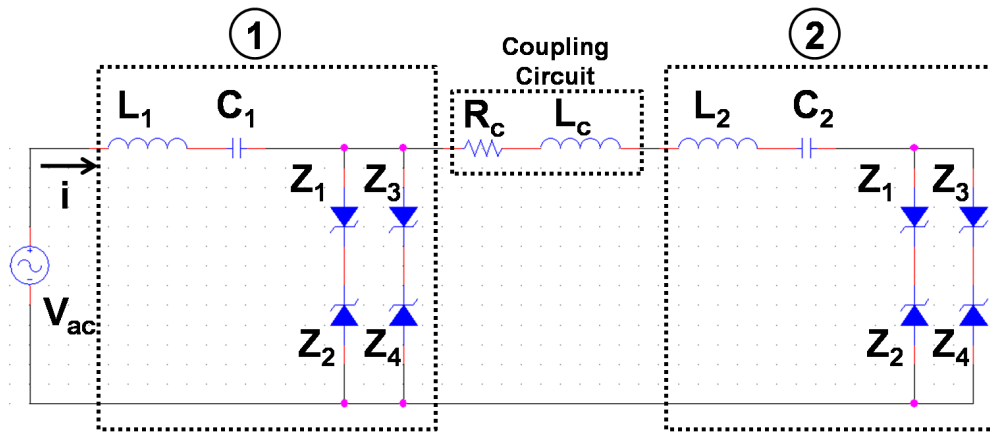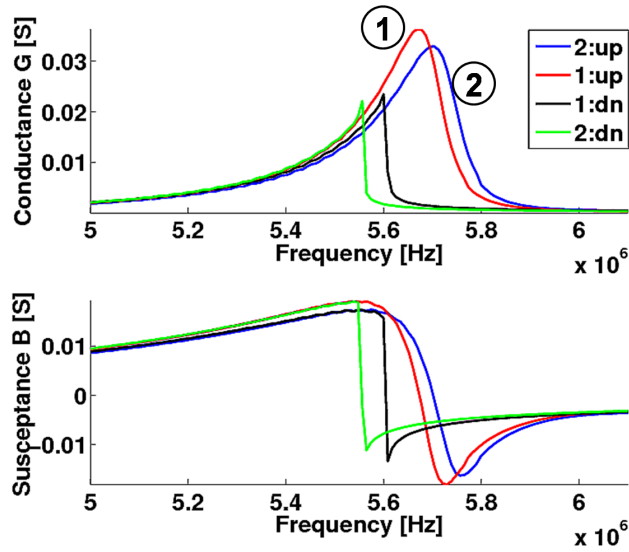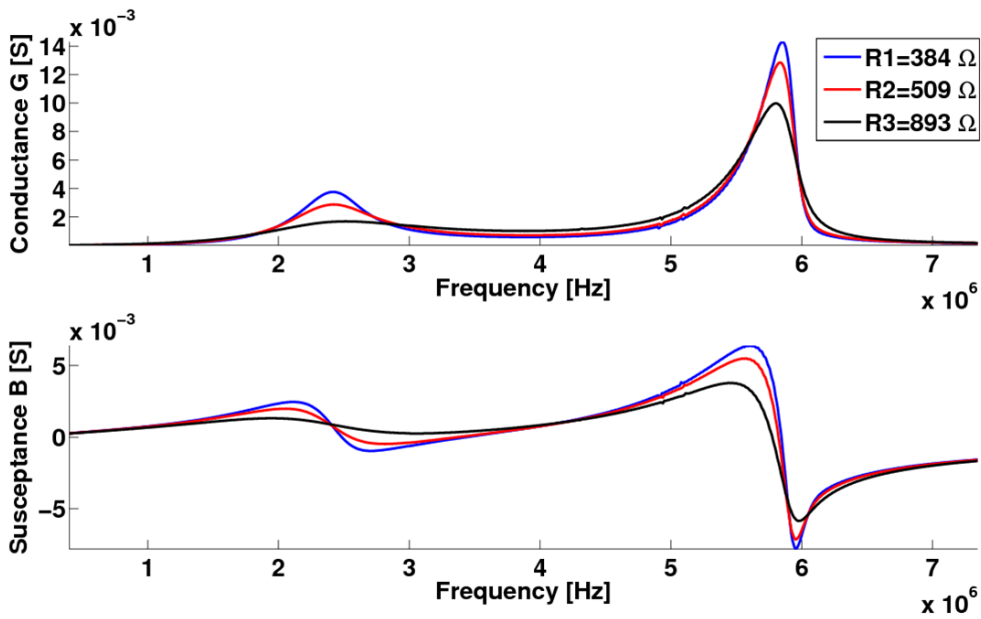
Figure 6.14: Coupled system of the L-C-Diode oscillators: here the L-C-Diode oscillators denoted by 1 and 2 represent the inner beam and the outer beam, respectively. The coupling circuit includes R_c and L_c as these components represent the damping and the connecting truss between the beams, respectively.

inductance) and the damping between the beams (coupling resistance), affect the coupled response. When the movement of the truss is small, it acts as a rigid beam which makes the inner and outer beams move perfectly in-phase with each other. However with large velocity of the truss, the inner and outer beams become weakly coupled by the truss since the dynamic equilibrium of the truss relative to the mass changes. As a result the moving truss makes the beams move slightly out-of-phase with each other. Additionally when the structure moves at its resonant frequency the inner beams come closer the outer beams and thus the damping is increased.

As noted in Ch. 4, large force leads to large deformation which results in a given beam (inner or outer) being axially loaded and being hardened. Because of the unequal lengths, the outer beams harden more than inner beams in the same displacement range. As seen in the previous sections, a typical hard-spring response is seen for a small value of excitation voltage. Ringing always occurs at SN bifurcation points during the upsweep and downsweep which are indicated in Fig. 6.16(a) as ④ and ⑤, respectively. As noted before ringing can be reduced by increasing the dwell time at each frequency and by increasing damping; ringing is the primary indicator of the instability in the structure. For small values of the excitation voltage, the tension and the compression of the beams is matched (e.g. when the inner beam expands, the corresponding section of the outer beam compresses and vice versa). The result of the combined interaction of the beams makes the frequency response lean to the right as is shown in Fig. 6.16(a) in region I due to mismatch in the compression and tension of the beams as indicated in Fig. 6.16(b). Also in region I, around to the frequency point where the peak amplitude occurs, the damping between the beams increases with large displacement as they come close to each other (see Appendix B). Even though the analogy between the folded-beam pair and coupled Duffing oscillators holds true in all three regions shown in Fig. 6.16(a), the effect of coupling between the two beams is not so prominent

(a) Uncoupled response

(b) Coupled response

Figure 6.15: The measured frequency responses of the L-C-Diode oscillators: (a) if the coupling is removed then the uncoupled response shows two distinct resonant frequencies. This behavior emulates the uncoupled folded-beam pair with unequal lengths. (b) The coupled responses of the two oscillators connected as in Fig. 6.14 are shown: the in-phase resonant peak and out-of-phase resonant peaks merge if the damping, e.g. the value of R_c is increased. This behavior is qualitatively similar to the extended response of the MEMS resonator shown in the previous sections. Note that $L_c = 60\ \mu H$.
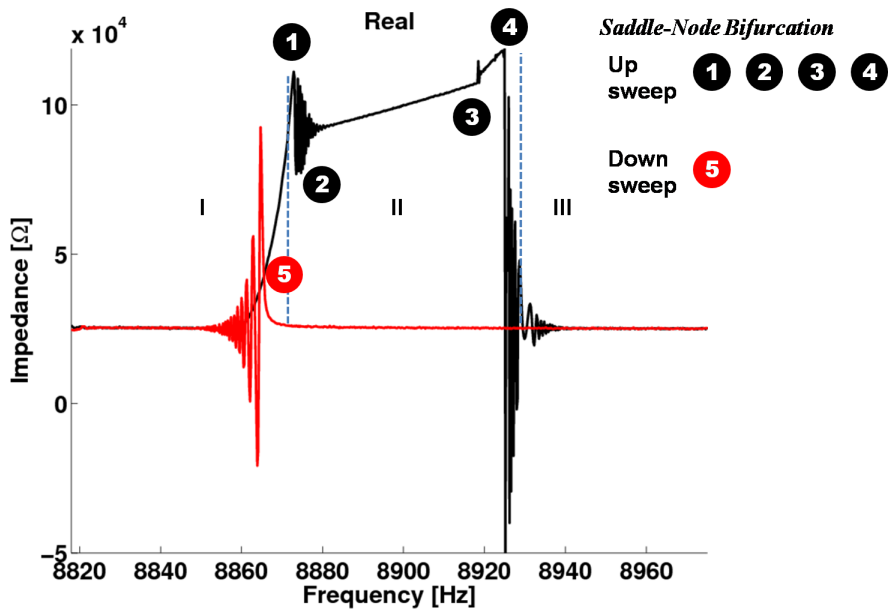
(a) Extended response and multiple bifurcation points
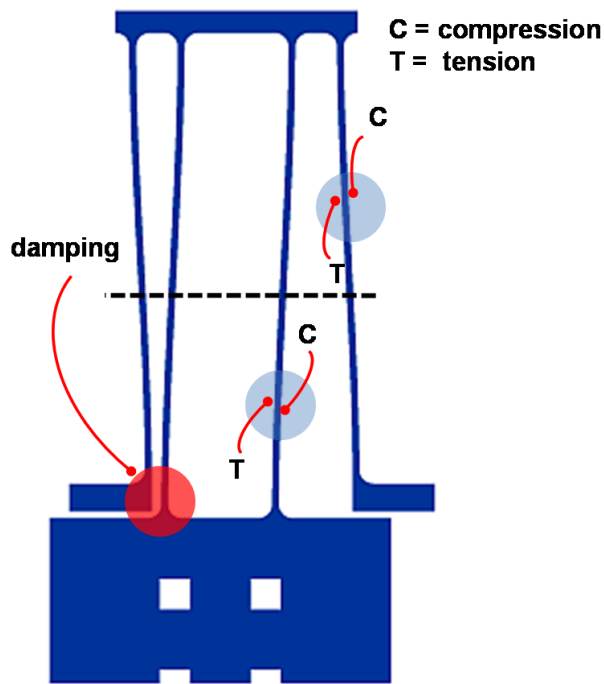
(b) Damping and tension/compression effect in the folded beam pair

Figure 6.16: Extended hard-spring behavior of Res 2: a) frequency response at $V_{ac} = 205$ mV, $V_{dc} = 20$ V and pressure = 30 Pa. Here the locations where Saddle-Node (SN) bifurcations which lead to stable periodic response are marked by numbers. Note that one SN point is observed during the downsweep whereas multiple SN points can be seen during the upsweep. Region I, II, III are classified as pre-extended region, extended region, and post-extended region, respectively. (b) Large deformation of beams due to large force (Comsol): damping between the beams and tension/compression in the beams due to the large deformation are shown (see Appendix B for the picture of the device during motion).

for small displacements in Region I or III. After reaching the peak amplitude at ①, the amplitude drops at the subsequent frequency point as expected and the resonator exhibits *ringing*; however the increased damping between the beams reduces ringing which helps stabilize the beams and after going through ② the resonator enters region II as shown in Fig. 6.16(a). Within region II, the folded-beam structure behaves as the coupled oscillator system as the movement of the truss increases (L_c in Fig. 6.14 increases) and as a result the out-of-phase peak develops. Note that ③ is also created due to overall instability of the structure in region II. Finally ④ is reached as the dynamic equilibrium point; here the interplay between the restoring force, damping and the applied force reaches maximum stable vibration after which the resonator enters region III. Note that as the frequency is swept, the stable and unstable equilibria (periodic cycles) collide at each of the SN points after which the resonator exhibits a stable equilibrium (periodic cycle). After each SN point the resonator markedly shows a *ringing* response which leads to some stable behavior.

In summary, the following occurs within the extended region: a) damping between the beams increases which makes the outer beams resonate slightly out-of-phase than the inner beams, b) the outer beams harden more than the inner beams, and c) truss becomes compliant due to the mismatch in the compression and tension cycle within the inner beams and the outer beams as shown in Fig. 6.16(b). Also note that the symmetric placement of the four folded-beam pair can be slightly asymmetric due to the variation of the beam width and thickness during the fabrication. The combination of all of the above factors extends the frequency response.

Noise

The noise in MEMs devices can be classified in many categories including mechanical-thermal noise (see Appendix A), Brownian noise, flicker ($1/f$) noise, and white Gaussian noise [64]. $1/f$-type noises, which result in spreading of the frequency-spectrum for a given frequency, originate mainly from the motional resistance in the MEMS device whereas white Guassian noise can be attributed to the electronics used for excitation and detection [11]. The effect of the noise on the hysteresis was observed to be two-fold: (1) variation in the resonant frequency and (2) shrinkage of the window. Moreover, higher noise levels tend to affect the resonant frequency such that minor variations from one reading to the next can occur. These variations can cause the hysteresis to be unclear if the SNR is very low. For example, both the jump-down and jump-up points can be indistinguishable. At high SNR, smaller ambient perturbations and/or other electronics related jitters can shift the jump-up and jump-down points and as a result the hysteresis window can shrink. For example, the frequency-sweep experiments were also conducted by a function generator and the current was extracted by the current-to-voltage converters and the amplifiers. These experiments showed a significant effect of the noise from the electronics and the improper grounding on the bifurcation points. Hence it is crucial to design a good PCB and use different ranges of by-pass capacitors to filter out the power-supply noise.
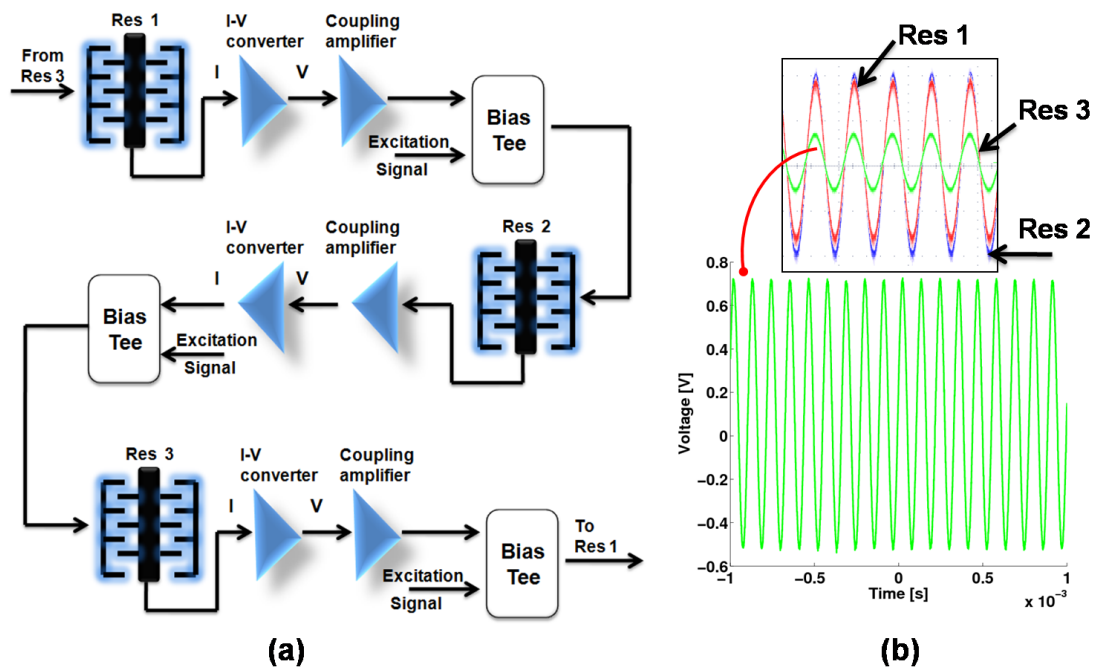
Figure 6.17: Test setup and in-phase vibrations: (a) the block diagram of the coupling circuit used in the experiments and (b) the emergent in-phase vibrations without the ac excitation signal.

6.4 Ring of Coupled Nonlinear MEMS Resonators

The coupled experiment was performed by using the resonators in Group II. The test die was attached by a non-conductive epoxy in the center of the device PCB and devices were wire-bonded to the pcb traces using gold wires with 1 mil (~25 μm) diameter. As mentioned before, one of the electrodes was grounded and the excitation signal was connected to the other electrode. The motional current produced by the device was read off the anchor pad. The substrate, the pcb, and the vacuum chamber were also grounded to reduce parasitic capacitances. The experiments were conducted on a motion resistant test-bench to dampen the ambient vibrations. The three resonators on a single die were coupled together by discrete electronics such that they form a closed-loop system, i.e. 1→2→3→1.

6.4.1 In Phase Vibrations

In this section, in-phase vibrations produced by the coupled system are discussed.

Autonomous System (No Ac Excitation Signal)

In this experiment the devices were biased using a dc power supply. As mentioned in Chapter 3, the bias plays a role of shifting the equilibrium position of the resonator. If a

resonator is in steady-state and the bias is applied suddenly, the resonator changes its steady-state or the equilibrium value (in the single well potential) after some transient behavior induced by the noise in the circuit. Hence without the bias the initial positions of the resonators are identical before applying an excitation signal [1]. Additionally it is important to note that the electrostatic force can not be induced without the bias. As a result the springs can not go through large deformation when driven by a time-varying excitation signal. Therefore the nonlinear vibrations, which play a crucial role in the emergence of oscillations due to the synchronization of the resonators, are also absent. For this reason the self-sustained oscillations are not induced and/or maintained without the bias. Therefore the initial positions of the resonators are changed by applying the bias; the bias induces nonlinearity in the presence of an excitation signal. As shown in Fig. 6.17(a) the output of a given resonator was fed to current-to-voltage (I-V) converter which was connected to an amplifier with a variable gain (labeled as the 'coupling amplifier'). Thus the coupling amplifier can tune the overall coupling strength between the resonators. The output of the coupling amplifier was then connected to the next element in the ring (see Appendix B for the circuit diagram). Next a bias of 20 V was applied simultaneously. After that the resonators were self-excited by adjusting the gains of the coupling amplifiers. The inherent noise vibrations in the circuit components act as the excitation signals to the resonators. The noise induced vibrations are amplified by the coupling amplifiers. In this way the noise is fed from the one element to the next element in the loop and thus each element drives the other element with this noise. As the noise in the system traverses around the loop, the resonators start to vibrate first arbitrarily and then by responding to the mechanism of self-organized synchronization induced by the coupling strengths past the critical values. Eventually at a sufficiently large vibration the resonators fully synchronize with each other, as a result as the signal-to-noise ratio gets higher, and the stable sinusoidal vibrations emerge depending on the coupling strengths that were set.

Similarly the experiment was reversed and verified by first setting the coupling strengths to the critical values and then applying the bias. It should be noted that if the bias is turned off after the stable vibrations have emerged, then the oscillations eventually diminish. This observation points to the importance of the nonlinear vibrations that can lead to the synchronization of the resonators such that self-sustained oscillations are created and maintained. Fig. 6.17(b) shows the full grown vibrations of Res 3. Here the shared frequency of oscillation is approximately 9 kHz and the amplitude levels are 2.12 V for Res 1, 0.68 for Res 2, and 1.86 V for Res 3. It was observed that for all possible combinations of the coupling strengths that produce the stable vibrations, two of the resonators exhibit nearly identical amplitude levels while the third resonator would stay at about half of their levels. This can be due to mismatch in the resonators and/or the interface electronics used for coupling. Also note that the difference in the coupling strengths can also produce asymmetric vibrations between the resonators which affect the amplitude levels. In addition to that the in-phase vibrations can be attributed to strong coupling between the resonators. The frequency and the amplitude of the vibrations increase as the coupling strengths are carefully matched and increased. While tuning the coupling strengths, a narrow range of frequencies was observed in which sta-

---

[1] Here we assume that the fabrication process has no/very little effect on the initial positions of the resonators.
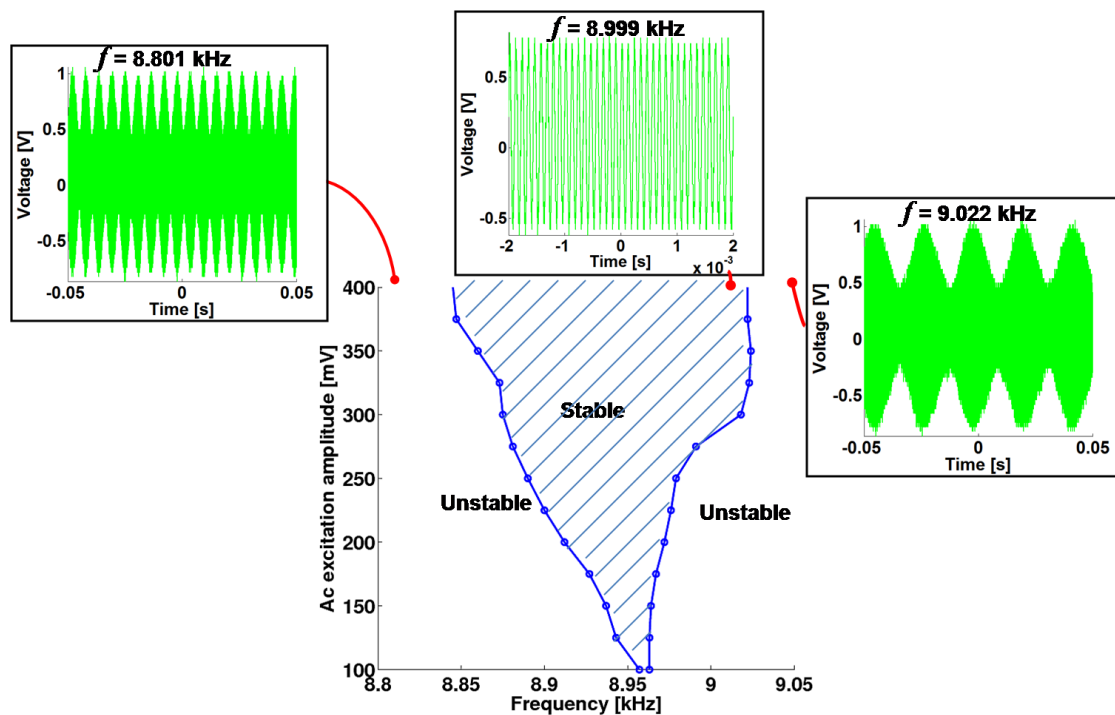
96

Figure 6.18: The coupled system with a priori in-phase vibrations in the presence of ac excitation signal: region of synchronization is shown where x-axis denotes the frequency of the excitation signal and y-axis denotes the peak-to-peak voltage level of excitation signal. Outside of the sync region, the oscillations are quasiperiodic as shown in the insets.

ble vibrations occur. Other combinations of the coupling produce unstable (quasiperiodic) vibrations.

Synchronization with the ac Excitation Signal

In this experiment, the ac excitation with bias was applied to the input ports of the coupled system via a bias-tee network. The 1:1 region of synchronization is shown in Fig. 6.18, inside which the frequency of the coupled system was observed to be the same as the excitation frequency. Unstable (quasiperiodic) oscillations were observed outside of the boundaries. It was observed that the region of synchronization can shrink, widen, or shift by changing coupling strengths which effect the self-excited frequencies and the amplitude levels. The influence of large nonlinearity is also evident by the curved boundaries. Below 100 mV, the vibrations were observed to be unstable with significant quasiperiodicity. It is possible for this region to be closed depending on damping and the noise in the circuit. For example, at the pressure of 15 Pa the same coupled system shows a wider area below 100 mV (see Appendix B).
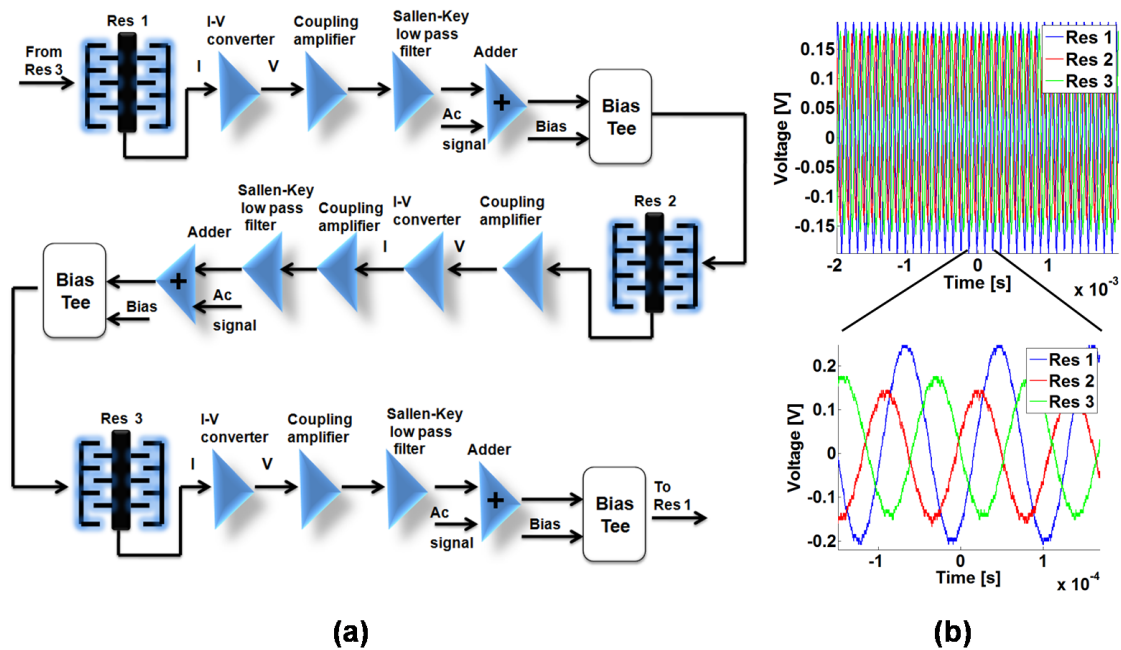
Figure 6.19: Test setup and out-of-phase vibrations: (a) the block diagram of the coupling circuit used in the experiments and (b) the emergent out-of-phase oscillations. The frequency of self-excited oscillations is 8.991 kHz with the test conditions bias=20 V and pressure=30 Pa.

6.4.2 Out of Phase Vibrations

For this experiment, the coupling circuit shown Fig. 6.17(a) was improved by adding an RC low pass stage followed a 2-pole Sallen-Key low pass filter with a cutoff frequency around 15 kHz and with a sharp roll-off [65]. As shown in Fig. 6.19(a), the filter was followed by an adder circuit with a gain stage in order to add the ac excitation signal to the given resonator signal. The adder circuit was followed by the bias-tee network where the combined signals were added to the bias voltage (see Appendix B for the circuit diagram). For the autonomous system only the bias voltage was applied. For all the experiments discussed in this section the gain of the coupling amplifier was fixed and only the gain of the adder circuit was changed in order to change the coupling strength. Out of phase oscillations emerge as the couplings strengths are changed to a specific ratio. The amplitude levels are 0.256 V for Res 1, 0.152 V for Res 2, and 0.184 V for Res 3 and the oscillation frequency is 8.991 kHz. The out-of-phase vibrations exhibit nearly $2\pi/3$ phase difference with each other as seen in Fig. 6.19(b). However this state of the coupled system proved to be difficult to synchronize in the presence of the excitation signal. An another pattern of out-of-phase vibrations with nearly identical amplitude levels was obtained by a slight change in the coupling ratio as shown in Fig. 6.20(a). The amplitude levels are 0.58 V for Res 1, 0.64 V for Res 2, and 0.58 V for Res 3 and the oscillation frequency is 8.664 kHz. Fig. 6.20(b) shows the associated re-
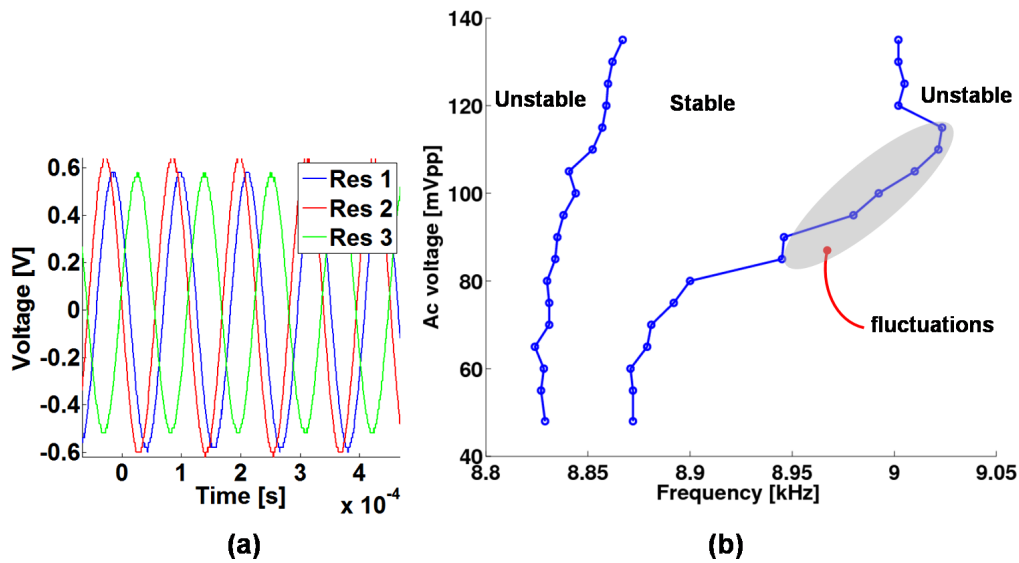
Figure 6.20: The coupled system with out-of-phase vibration at nearly identical amplitude levels: (a) the self-excited oscillations and (b) the region of synchronization. The frequency of self-excited oscillations=8.864 kHz with the test conditions bias=20 V and pressure=100 Pa.

gion of synchronization in the presence of the excitation signal. Note that the pressure level was dropped to 100 Pa for these experiments; the emergent oscillations were observed to be similar to the ones at 30 Pa. Here the left boundary was easier to obtain whereas the oscillations showed rapid fluctuations around the right boundary. This behavior can be attributed to the mismatch between the resonators and their relative engagement/disengagement of the extended hard-spring behavior shown in Fig. 6.10.

In an another experiment the out-of-phase a priori vibrations shown in the previous section were changed to the quasiperiodic (unstable) vibrations by changing the coupling strengths. It was observed that in the presence of excitation signal with at a substantial amplitude, this state of the coupled system also synchronizes to the excitation frequency as shown in Fig. 6.21. However a full region of synchronization was difficult to obtain for this type of oscillations due to the excessive instability present in the autonomous system with this set of coupling strengths.

Finally it should be noted that the simulation study (see Chapter 5) showed that the coupled system should be able to exhibit self-excited oscillations with $2\pi/3$ phase difference when the coupling strength exceeds a critical value. In the presence of the excitation signal it can exhibit 1:1 sync region and a very narrow 1: 3 sync region. The qualitative behavior of the 1:1 sync region in the simulations and the experiments was observed to be similar. However 1:3 sync region was not observed in the experiments. Here it is important to note that the coupling strengths needed to be modified independently in the experiments and that they were not identical to each other. As a result 1:3 sync region can completely vanish or
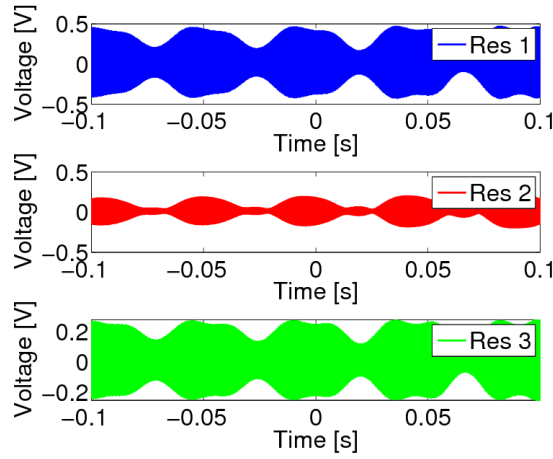
(a) f = 8.89 kHz
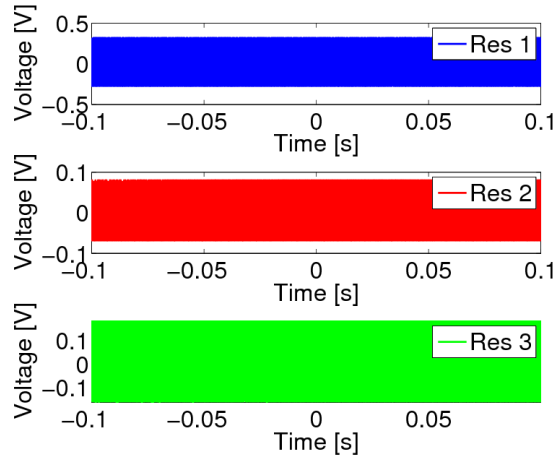
(b) f = 8.906 kHz
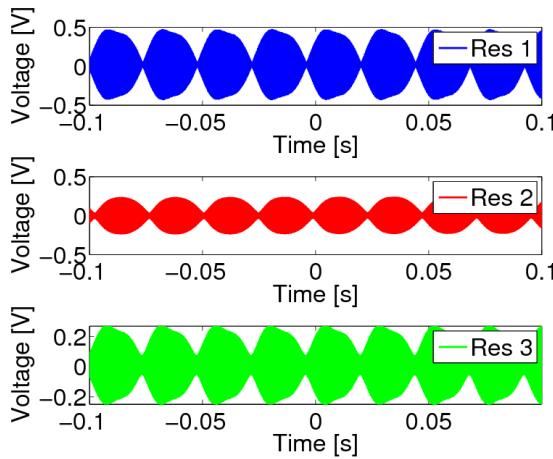
(c) f = 8.949 kHz

Figure 6.21: Synchronization of a priori quasiperiodic oscillations: (a) out-of-sync at f = 8.90 kHz, (b) in-sync at f = 8.906 kHz, and (c) out-of-sync at f = 8.949 kHz. Here f denotes the excitation frequency.

can be extremely narrow. Hence it would be difficult to detect it in the experiments.

6.5 Observations

In this section, the observations based on the experimental results shown in this chapter are elucidated. To begin with, a better control of the extended response is needed. If properly controlled, the extended response can increase the robustness of the coupled system. Possible solutions include symmetric spring design with the usage of stopper mechanism (e.g. pegs) in order to control the length of the outer beams while actuating the stopper mechanism with dc voltage. Another important aspect is the matching between the resonators on single die which can be improved by Monte Carlo simulation[2]. The coupled system can be used to detect mechanical excitation and its effect on region of synchronization can be analyzed in a similar manner as the ac excitation.

Around the boundaries of the sync region, the system is very sensitive and shows a rapid transition from unstable to stable vibrations. This property can be useful as the coupled system can be used in self-excited and forced mode as the inertial sensors to increase sensitivity and robustness in the presence of noise. Additionally the application of coupled system as inertial sensor is attractive because the sync region shows sensitivity with respect to the coupling strength (e.g. shrinking or widening of the sync region). Effects of damping include closed or wider regions for low excitation amplitude; this property of the system can be used for pressure sensing. In the self-excited mode, th frequency range can be changed by varying the coupling strength. The frequency range can be increased with better control of the extended behavior and the system can be used for frequency synthesis.

6.6 Summary

In this chapter, the characterization results of the nonlinear MEMS resonators was presented. First the resonance characteristics of resonators on separate dies and on single die were shown. Next the hysteresis characteristics of different resonators from separate dies and from single die were shown under varying excitation conditions. It was discovered that for this particular design of the resonator, an extension of hysteresis occurs under specific excitation conditions. It was shown that the hysteresis can be effectively tuned by varying the ac voltage, dc bias and pressure. Next the mechanism behind the hysteresis and the nonlinear behavior were briefly discussed. Furthermore the effect of nonlinearity was analyzed by conducting experiments on the coupled system of L-C-Diode resonators. The results showed a qualitative match with the extended hard-spring behavior of the MEMS resonator.

The latter part of the chapter was devoted to the experimental results of the coupled nonlinear MEMS resonators in a ring formation. The in-phase and the out-of phase vibrations of the coupled system were presented and the regions of synchronization were shown.

---

[2] The effect of manufacturing variability such as film thickness or the beam width can be analyzed using Monte Carlo simulation by randomly sampling each variable and by combining their statistical distribution [19].

The experimental study shown in this chapter indicates that the coupled system has a strong potential as a sensor depending on the applications.

Chapter 7

Conclusions and Future Work

This research was aimed at the synthesis of design, analysis, and characterization of non-linear MEMS resonators in the coupled system. The dynamics of both the single nonlinear MEMS resonator and the coupled system of nonlinear MEMS resonators were investigated. In the following sections, the conclusions of this study are presented and the course of the future work is discussed.

7.1   Conclusions

As shown in this study the single nonlinear resonator exhibited the hard-spring response. Under specific excitation conditions it showed an extension of the hysteresis during the up-sweep and the downsweep of the excitation frequency. The extension of the hysteresis and thus an enlargement of a usable amplitude and bandwidth were observed in all the resonators. This extension can be tuned by changing the excitation voltage. Furthermore a unidirection-ally coupled system that consists of these nonlinear resonators was characterized and it was shown that this system can oscillate at a certain value of the coupling strength. A change in the coupling strength produced a change in the oscillation frequency and the amplitude of the autonomous system. It can also exhibit quasiperiodic oscillations depending on the coupling strength. The autonomous system exhibited in-phase vibrations and out-of-phase vibrations depending on the coupling circuit and the combination of the coupling strengths. Characterization of the coupled system in the presence of the excitation force showed that the coupled system can be fully synchronized to the excitation frequency in a priori in-phase and out-of-phase oscillatory state. A priori quasiperiodic oscillations can also be synchro-nized to the excitation frequency. It was shown that the changes in the excitation voltage affect the frequency response significantly. Sensitivity with regards to the coupling strength, excitation frequency, excitation amplitude and pressure was demonstrated. Thus the coupled system shown in this study can be used as a sensor.
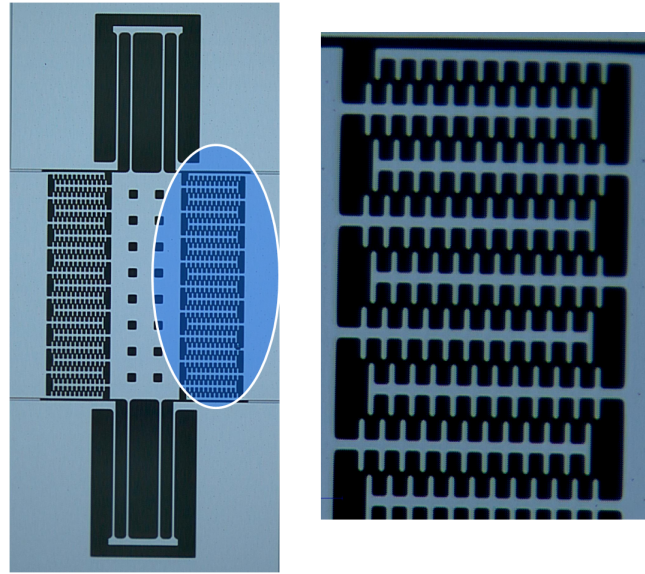
Figure 7.1: A different MEMS resonator fabricated in SOIMUMPs process: the noninterdigitated comb fingers induce the parametric resonance by modifying the linear and nonlinear spring constants with the time-dependent restoring force terms [16]. The dimensions of the flexure and the mass are identical to the resonator shown in the previous chapters. Here both the excitation and the detection are parametric and identical.

7.2 Future Work

This section entails the potential application areas in which the coupled system can be employed.

7.2.1 Coupled Integrated MEMS

The coupled system described in this thesis was realized by connecting discrete MEMS devices to each other via discrete electronics. However a better and reliable approach would be to combine the MEMS devices and the interface electronics on a single substrate [44]. The matching issues discussed in the previous chapters can be addressed better in an integrated process. Also note that the miniaturization of the electronics allows a larger system to be realized by combining MEMS and CMOS devices on single substrate.

7.2.2 Parametric Resonance in Coupled Micromechanical Resonators

The study shown in this thesis can be complimented by exploring the parametric resonance in the nonlinear MEMS resonators. Utilizing the parametric resonance, a unidirectionally coupled system can be constructed by discrete electronics. Major tasks of the study in this type of coupled system can include an analytical study of the governing dynamics dictated by nonlinear Mathieu's equation (see Appendix A), the numerical simulations, and

finally an experimental characterization. A candidate device in which the electrostatic force produces time dependent restoring force terms is shown in Fig. 7.1. The cause of such phenomena is due to the noninterdigitated comb-drives [16]. At high bias and ac excitation voltage, the preliminary experiments show soft-spring behavior for this type of device. Furthermore, such a device can be driven stochastically (e.g. to imitate the noise and the ambient vibrations) to harness energy by utilizing a large bandwidth [66].

7.2.3 Coupled MEMS Gyroscopes

The utility of the coupled MEMS resonators in a ring can also be demonstrated as the x-axis implementation of coupled gyroscopes in a ring. This research has many prospects such as the Coupled Inertial Navigation System (CINS) mentioned in [24]. This in-depth study has shown that the dynamics of the individual gyroscopes can be synchronized to each other depending on the coupling strength. Here the coupled system has been shown to minimize the effects of noise thereby minimizing the phase drift in the gyroscopes. A robust inertial rate sensor system can be constructed on a single substrate following the approach mentioned earlier. A candidate gyroscope device that has been modified from the single resonator is shown in Fig. 7.2.

7.2.4 Energy Harvesting using Coupled Nonlinear MEMS Resonators

A 1-DOF device can be utilized to explore the benefits of energy harvesting. It has been shown that the nonlinear resonating devices can broaden the frequency range allowing robustness against frequency variation and thereby increasing the power output [55]. The resonator shown in this research is a good candidate because of the extended hard-spring behavior. A 2-DOF device modified from the design of the gyroscope shown previously can also be utilized. In either the 1-DOF device or the 2-DOF device, having a control over the extended hard-spring behavior is imperative. Additionally the design can be carefully implemented to allow either the soft-spring or the hard-spring behavior depending on a minimum number of control parameters is also beneficial. Next, this combined design can be assessed to investigate the energy harvesting properties. As a first step this can be accomplished by using PZT-thin film resonators to mimic the ambient vibrations. The next obvious step would be to couple such devices in a ring to assess their synchronization properties.

7.2.5 Higher Order Coupled MEMS Resonators

Given the maturation of the design of the individual resonator and the successful miniaturization of the coupled system on a single substrate, the coupled MEMS resonators can be utilized in a higher order system. Fig. 7.3(a) shows the design concept by defining the inter-element coupling between the individual resonators as the base level. Multiple single chips can now be coupled together in the same fashion which defines the top level as seen in Fig. 7.3(b). The benefits of this type of system can only be investigated by carrying out a detailed analysis and characterization.
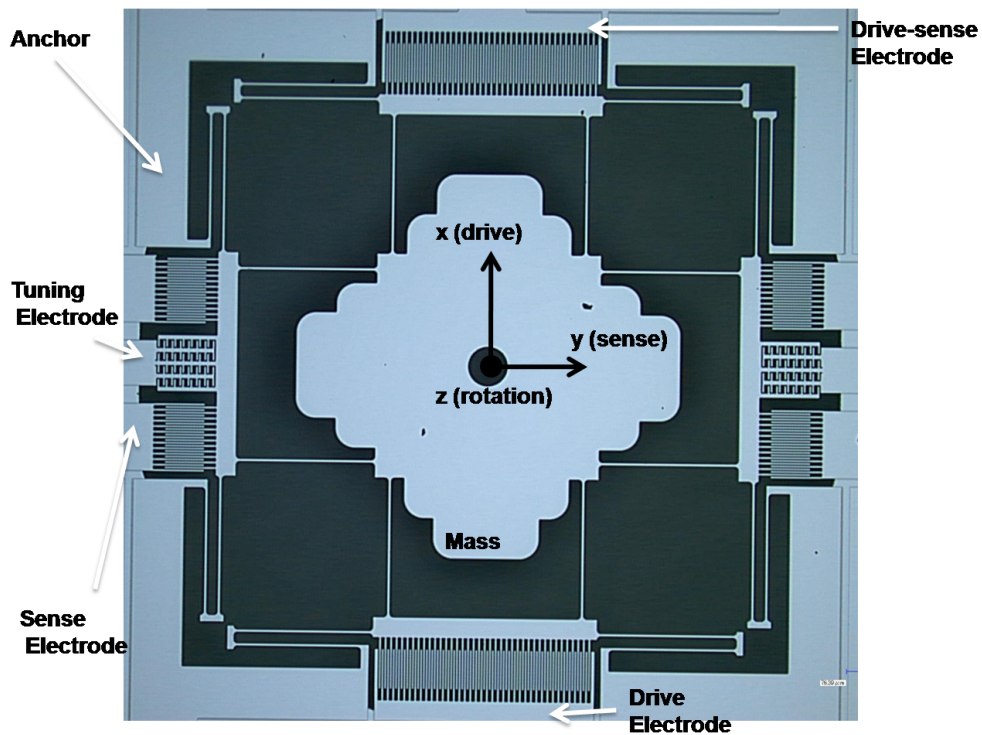
Figure 7.2: A micro gyroscope based on the modified design of the nonlinear resonator shown in the previous chapters: Here the mass is increased to restrict the resonance frequency below 5 kHz. The thin suspension flexures and support beams can be vibrated with nonlinear resonance.

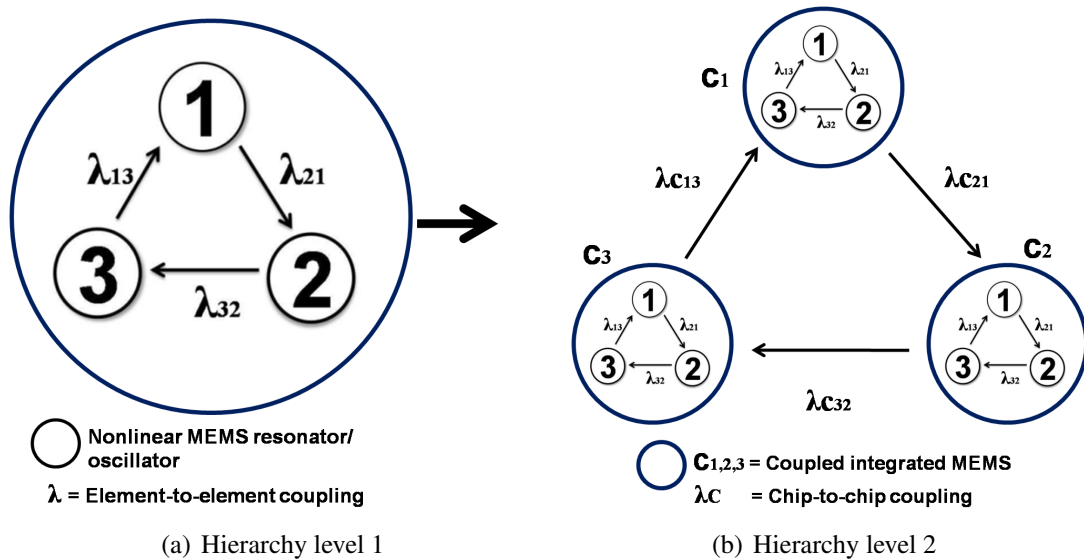(a) Hierarchy level 1

(b) Hierarchy level 2

Figure 7.3: Design concept with multiple coupled integrated MEMS: (a) inter-device coupling defines the base level within a single integrated MEMS chip. (b) inter-chip coupling defines the top level of the coupled integrated MEMS on a single PCB.

Appendices

Appendix A

Chapter 5

Stability of Equilibrium

The stability of the equilibrium can be established by the method of Asymptotic Continuous Spectrum (ACS) as mentioned in [7, 67]. Fig. 1 depicts the unidirectionally coupled system as was shown in Chapter 5. To begin with a given resonator within the coupled
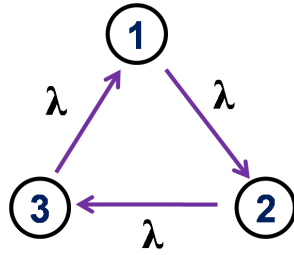

Figure 1: Unidirectionally coupled system shown in Ch.5 with λ as the element to element coupling strength.

system can be represented by a system of one dimensional nonlinear equations as,

$$x'_j = y_j \tag{1a}$$
$$y'_j = -\delta y_j - x_j - \beta x_j^3 + \lambda x_{j-1}, \tag{1b}$$

where x_j and x_{j-1} are the displacement variables of the given element and the previous element respectively, δ = damping constant, and β = nonlinear stiffness.

Eq. 1 can be represented in vector form as,

$$\begin{bmatrix} x'_j \\ y'_j \end{bmatrix} = \begin{bmatrix} 0 & 1 \\ -1 & -\alpha \end{bmatrix} \begin{bmatrix} x_j \\ y_j \end{bmatrix} + \begin{bmatrix} 0 & 0 \\ -x_j^3 & 0 \end{bmatrix} + \begin{bmatrix} 0 & 0 \\ \lambda & 0 \end{bmatrix} \begin{bmatrix} x_{j-1} \\ y_{j-1} \end{bmatrix} \tag{2}$$

The above equation can be represented in a rotation-symmetric form as,

$$z'_j = \mathbf{A}z_j + \mathbf{b} + \mathbf{H}z_{j-1}, \tag{3}$$

where,

$$\mathbf{A} = \begin{bmatrix} 0 & 1 \\ -1 & -\alpha \end{bmatrix}, \mathbf{b} = \begin{bmatrix} 0 & 0 \\ -x_j^3 & 0 \end{bmatrix}, \mathbf{H} = \begin{bmatrix} 0 & 0 \\ \lambda & 0 \end{bmatrix}$$

Now let

$$\mathbf{z} = \begin{bmatrix} z_1 \\ z_2 \\ z_3 \end{bmatrix}, \mathbf{I} = \begin{bmatrix} 1 & 0 & 0 \\ 0 & 1 & 0 \\ 0 & 0 & 1 \end{bmatrix}, \mathbf{B} = \begin{bmatrix} \begin{bmatrix} 0 & 0 \\ -x_1^3 & 0 \end{bmatrix} & 0_{2\times2} & 0_{2\times2} \\ 0_{2\times2} & \begin{bmatrix} 0 & 0 \\ -x_2^3 & 0 \end{bmatrix} & 0_{2\times2} \\ 0_{2\times2} & 0_{2\times2} & \begin{bmatrix} 0 & 0 \\ -x_3^3 & 0 \end{bmatrix} \end{bmatrix}, \mathbf{G} = \begin{bmatrix} 0 & 0 & 1 \\ 1 & 0 & 0 \\ 0 & 1 & 0 \end{bmatrix}.$$

Where $\mathbf{G}$ is the connectivity matrix of the coupled system. Now the coupled system can be represented in the tensor product form as[1]

$$\mathbf{z}' = (\mathbf{I} \otimes \mathbf{A})\mathbf{z} + \mathbf{B} + (\mathbf{G} \otimes \mathbf{H})\mathbf{z}, \tag{4}$$

Equilibrium Point

We are interested in checking the stability of the equilibrium point, $\mathbf{z} = [0_{2\times1}, 0_{2\times1}, 0_{2\times1}]^T$. After linearizing the system in Eq. 4 around the equilibrium point we arrive at,

$$d\mathbf{z}' = (\mathbf{I} \otimes \mathbf{A} + \mathbf{G} \otimes \mathbf{H})d\mathbf{z}, \tag{5}$$

where $d\mathbf{z} = [dz_1, dz_2, dz_3]^T$. After block-diagonalizing Eq. 5 we obtain to N = 3 independent systems of resonators,

$$\psi' = (\mathbf{A} + \gamma_j \mathbf{H})\psi_j, j = 1, 2, 3. \tag{6}$$

Where $\gamma_j = e^{i2\pi j/N}$ = eigenvalues of $\mathbf{G}$. The associated family of characteristic equations is,

$$\det(\mathbf{M} - e\mathbf{I}) = 0, \tag{7}$$

where $\mathbf{M} = \mathbf{A} + \gamma_j \mathbf{H}$ and $\mathbf{e} = [e_1, e_2]^T$ = eigenvectors for the given j. With these equations in place, we can determine the eigenvectors for each j from $\mathbf{M}$. For the discrete family of resonators, e.g. N = 3, we denote $\mathbf{M_d}$. Similarly we can derive the continuous family of resonators, e.g. N = very large number, by replacing γ_j in Eq. 6 with $e^{i\phi}$. We can visualize the eigenvalues γ_j as discrete points on the closed curves $\mathbf{e}(\phi)$, where $0 \le \phi \le 2\pi$, which are called the *Asymptotic Continuous Spectrum* curves. For the continuous family, we denote $\mathbf{M_c}$. Then it follows that,

$$\mathbf{M_d} = \begin{bmatrix} 0 & 1 \\ -1 + \lambda e^{i2\pi j/N} & -\alpha \end{bmatrix}, \mathbf{M_c} = \begin{bmatrix} 0 & 1 \\ -1 + \lambda e^{i2\phi} & -\alpha \end{bmatrix}.$$

Where $j = (1, 2, 3)$, $N = 3$, and $\phi \in [0, 2\pi]$.

---

[1]Example: if $a_{2x2} = \begin{bmatrix} a_{11} & a_{12} \\ a_{21} & a_{22} \end{bmatrix}$ and $b_{2x2} = \begin{bmatrix} b_{11} & b_{12} \\ b_{21} & b_{22} \end{bmatrix}$ then

$$a \otimes b = \begin{bmatrix} a_{11}\begin{bmatrix} b_{11} & b_{12} \\ b_{21} & b_{22} \end{bmatrix} & a_{12}\begin{bmatrix} b_{11} & b_{12} \\ b_{21} & b_{22} \end{bmatrix} \\ a_{21}\begin{bmatrix} b_{11} & b_{12} \\ b_{21} & b_{22} \end{bmatrix} & a_{22}\begin{bmatrix} b_{11} & b_{12} \\ b_{21} & b_{22} \end{bmatrix} \end{bmatrix} = \begin{bmatrix} a_{11}b_{11} & a_{11}b_{12} & a_{12}b_{11} & a_{12}b_{12} \\ a_{11}b_{21} & a_{11}b_{22} & a_{12}b_{21} & a_{12}b_{22} \\ a_{21}b_{11} & a_{21}b_{12} & a_{22}b_{11} & a_{22}b_{12} \\ a_{21}b_{21} & a_{21}b_{22} & a_{22}b_{21} & a_{22}b_{22} \end{bmatrix}$$

Coupled Resonators: Analytical Solution

The dynamics of a single resonator in the coupled system with direct-coupling from the neighboring element can be described in the dimensionless form as,

$$
\begin{aligned}
x_1'' + \delta x_1' + x_1 + \beta x_1^3 &= \epsilon \cos(\omega\tau) + \lambda_{13} x_3, \\
x_2'' + \delta x_2' + x_2 + \beta x_2^3 &= \epsilon \cos(\omega\tau) + \lambda_{21} x_1, \\
x_3'' + \delta x_3' + x_3 + \beta x_3^3 &= \epsilon \cos(\omega\tau) + \lambda_{32} x_2.
\end{aligned}
\tag{8}
$$

Applying *method of averaging* on Eq. 8 yields,

$$
\begin{aligned}
\dot{r}_1 &= \tfrac{1}{2\omega}[-\omega\delta r_1 - F\sin\theta_1 + \lambda r_3 \sin(\theta_3 - \theta_1)] \\
\dot{\theta}_1 r_1 &= \tfrac{1}{2\omega}[-(\omega^2 - 1)r_1 + \tfrac{3}{4}\beta r_1^3 - F\cos\theta_1 - \lambda r_3 \cos(\theta_3 - \theta_1)] \\
\dot{r}_2 &= \tfrac{1}{2\omega}[-\omega\delta r_2 - F\sin\theta_2 + \lambda r_1 \sin(\theta_1 - \theta_2)] \\
\dot{\theta}_2 r_2 &= \tfrac{1}{2\omega}[-(\omega^2 - 1)r_2 + \tfrac{3}{4}\beta r_2^3 - F\cos\theta_2 - \lambda r_1 \cos(\theta_1 - \theta_2)] \\
\dot{r}_3 &= \tfrac{1}{2\omega}[-\omega\delta r_3 - F\sin\theta_3 + \lambda r_2 \sin(\theta_2 - \theta_3)] \\
\dot{\theta}_3 r_3 &= \tfrac{1}{2\omega}[-(\omega^2 - 1)r_3 + \tfrac{3}{4}\beta r_3^3 - F\cos\theta_3 - \lambda r_2 \cos(\theta_2 - \theta_3)]
\end{aligned}
\tag{9}
$$

Where (r_1, r_2, r_3) and $(\theta_1, \theta_2, \theta_3)$ denote amplitude and phase of the system respectively.

Chapter 6

Mechanical-Thermal Noise

Noise has its origin in the dissipation of energy [68]. Here the noise is discussed as the thermal (Johnson-Nyquist) noise in MEMS originating from the thermal agitation of electrons or temperature induced fluctuations in the carrier (free electron) density in the material [64]. Assume that the transduction factor η converts the electrostatic energy into mechanical energy as $\eta = (\partial C/\partial x)V_{dc}$, where C is the parallel-plate capacitance of the device, x is the displacement, and V_{dc} is the excitation voltage. Then the dynamics of a MEMS resonator can be described by the electrical equivalent circuit when it is excited by a thermal noise voltage source v_n as [12],

$$
L_m \frac{di_n}{dt} + R_m i_n + \frac{1}{C_m} \int i_n \, dt = v_n.
\tag{10}
$$

Where, $L_m = \dfrac{m}{\eta^2}$, $R_m = \dfrac{c}{\eta^2}$, and $C_m = \dfrac{\eta^2}{k_1}$. Here m denotes the resonator mass, c denotes the damping factor, and k_1 denotes the linear spring constant. The variable i_n denotes the motional current through the circuit shown in Fig. 2. Applying Laplace transform with $s = j\omega$, the Eq. 10 becomes,

$$
sL_m I_n + R_m I_n + \frac{1}{sC_m} I_n = V_n.
\tag{11}
$$

The absolute value of the mean square current can be shown as,

$$
\bar{I}_n^2 = \frac{\bar{V}_n^2}{R_m^2 + \left(\omega L_m - \dfrac{1}{\omega C_m}\right)^2}.
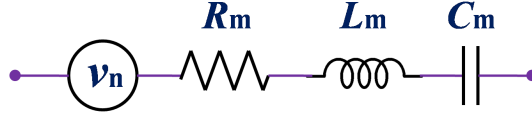\tag{12}
$$

Figure 2: MEMS resonator replaced with the electrical equivalent circuit: here R_m represents the damping loss, L_m represents the resonator mass, and C_m represents the spring. v_n is the thermal noise source.

With $\omega_o = 1/\sqrt{L_m C_m}$ and $Q = \omega_o L_m/R_m$, the above equation becomes,

$$\bar{I}_n^2 = \frac{\bar{V}_n^2}{R_m^2(1 + Q^2(\omega/\omega_o - \omega_o/\omega))}. \tag{13}$$

The energy change and the total energy stored in the inductor in a given frequency interval df can be described as [68], $dE = \frac{1}{2}L_m\bar{I}_n^2 df$ and $E = \frac{1}{2}L_m\int_0^\infty \bar{I}_n^2 \, df$, respectively.

After substituting Eq. 13 in the expression of the total energy, using $Q = L_m/(2\pi R_m)$ and rewriting it in terms of f, we arrive at the following equation,

$$E = \frac{\bar{V}_n^2}{4\pi R_m} \int_0^\infty \frac{Q}{1 + Q^2(f' - 1/f')^2} \, df'. \tag{14}$$

Where, $f' = f/f_o$. Evaluation of this expression by substituting $f' = e^a$ for $a \in [0, \infty]$ gives $E = \frac{\bar{V}_n^2}{8R_m}$ [68]. Next we can equate the thermal energy $\frac{1}{2}k_B T$ with the above and find the thermal noise voltage as,

$$E = \frac{\bar{V}_n^2}{8R_m} = \frac{1}{2}k_B T, \tag{15a}$$

$$\bar{V}_n^2 = 4k_B T R_m. \tag{15b}$$

Where, k_B denotes Boltzmann's constant and T denotes the temperature.

Note that with k_B as 1.38×10^{-23} J/K, T in K and R_m in Ω, the voltage $\bar{V}_n = \sqrt{4k_B T R_m}$ has the unit of nV/$\sqrt{Hz}$.

For a given bandwidth Δf, the rms voltage can be written as

$$V_n = \sqrt{4k_B T R_m \Delta f}. \tag{16}$$

Note that the above noise voltage is based entirely on the motional resistance which is related to the damping factor. Other noise sources can be present in the MEMS including the actuation and sensing electronics as well as the instruments used for the measurements. The cumulative effect of the other noise sources may be quite large.

Chapter 7

Parametric Resonance

Suppose that the parametrically excited resonator shown in Chapter 7, moves primarily in x direction, and other modes of vibration do not affect the motion in x direction. With $V_{in} = (V_{dc} + V_{ac} \cos(\omega_d t))^{1/2}$, we can write the dynamics of this resonator by using the nonlinear Mathieu's equation, which has been simulated numerically and verified experimentally in [69–71], as follows,

$$m\ddot{x} + c\dot{x} + k_1 x + k_3 x^3 = -(r_1 x + r_3 x^3)V_{in}^2 , \qquad (17a)$$

$$m\ddot{x} + c\dot{x} + \left(k_1 + r_1 V_{dc} + r_1 V_{ac} \cos(\omega_d t)\right)x + \left(k_3 + r_3 V_{dc} + r_3 V_{ac} \cos(\omega_d t)\right)x^3 = 0 . \qquad (17b)$$

Where m = mass, c = damping parameter, ω_d = excitation frequency, V_{dc} and V_{ac} = dc and ac voltages respectively, k_1, k_3 = linear and nonlinear mechanical stiffnesses respectively, r_1 and r_3 = linear and nonlinear *electrostatic* stiffnesses respectively.

If we let $2\tau = \omega_d t$, then the dimensionless form of the above equation can be written as,

$$x'' + \epsilon\alpha x' + \left(\delta + 2\epsilon \cos(2\tau)\right)x + \epsilon\left(a + 2b \cos(2\tau)\right)x^3 = 0. \qquad (18)$$

Where, $''$ and $'$ are derivatives with respect to dimensionless time τ. The rest of the parameters are,

$$\alpha = \frac{c}{r_1 V_{ac}}, \qquad \delta = \frac{(k_1 + r_1 V_{dc})}{m\omega_d^2/4}, \qquad \epsilon = \frac{2r_1 V_{ac}}{m\omega_d^2}, \qquad a = \frac{2(k_3 + r_3 V_{dc})}{r_1 V_{ac}}, \qquad b = \frac{r_3}{r_1}.$$

The transition curves can be obtained from the $\epsilon - \delta$ parameter space by using ϵ as the perturbation parameter and expanding ϵ to the 1st order in Eq. 18 [72] .

Appendix B

Chapter 3

Damping

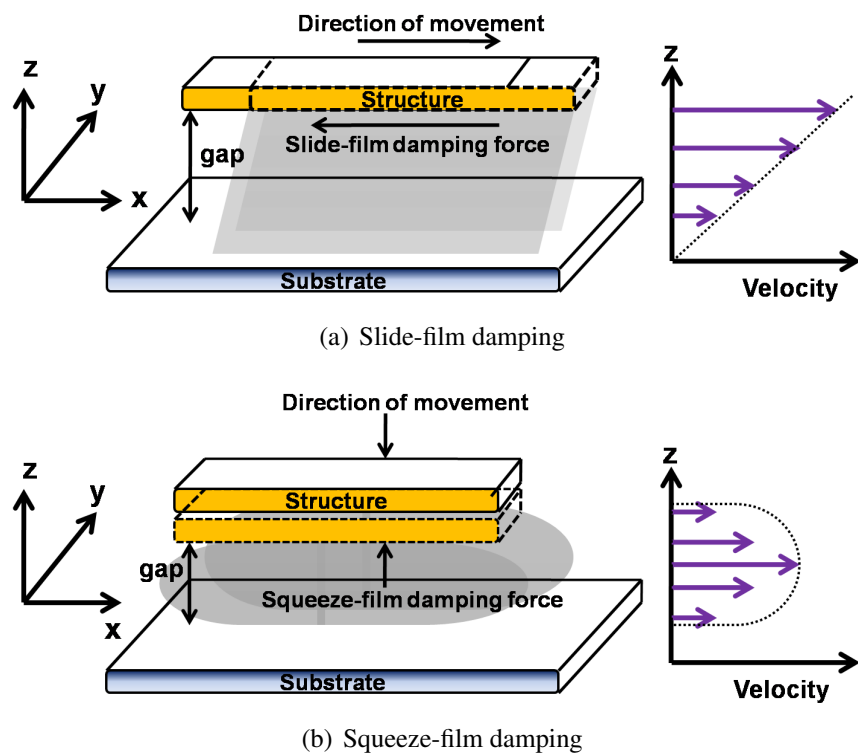(a) Slide-film damping

(b) Squeeze-film damping

Figure 3: Major types of damping encountered in MEMS: (a) slide-film damping or Couette-flow damping as the two plates move past each other and its velocity profile. (b) squeeze-film damping as the two plates move towards each other and its velocity profile.
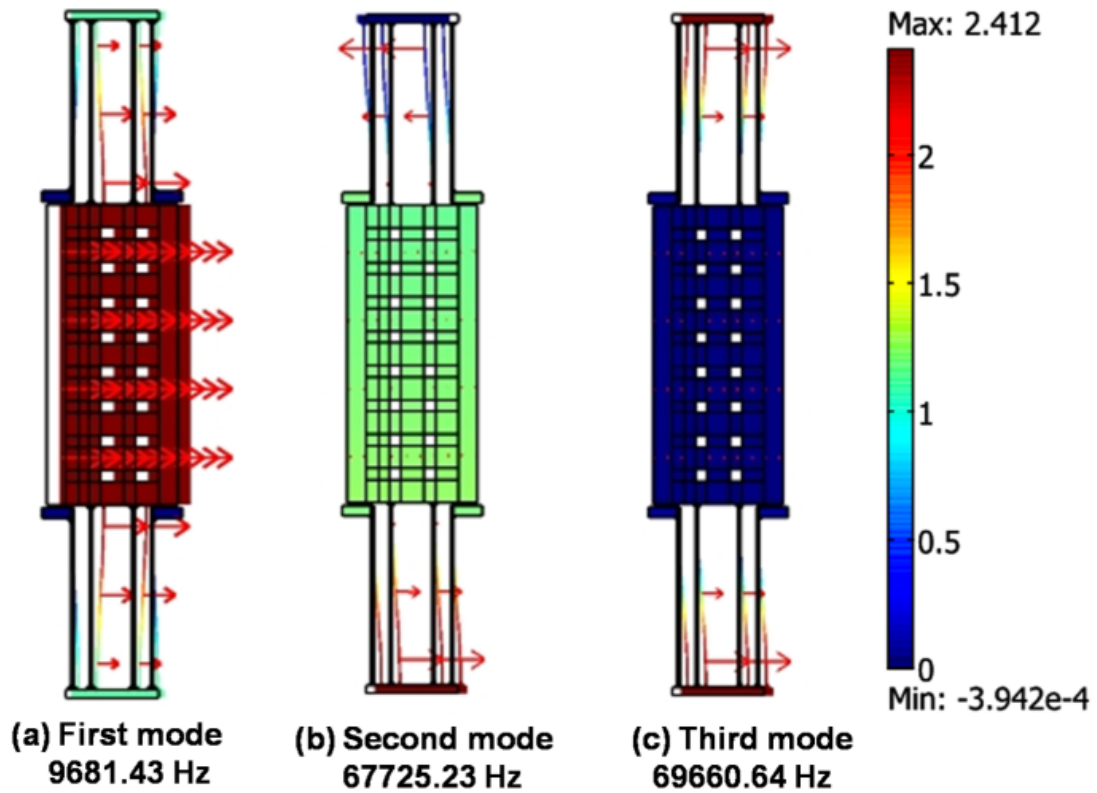
Chapter 4

Accurate modal analysis

(a) First mode
9681.43 Hz

(b) Second mode
67725.23 Hz

(c) Third mode
69660.64 Hz

Figure 4: Modal analysis in Comsol: (a) first mode at 9681.46 Hz, (b) second mode at 67602.35 Hz, and (c) third mode at 69660.78 Hz. The bar on far-right represents normalized values with most positive value on top depicting the maximum value of displacement for a given mode. Size and number of the arrows are related to the values of displacement; maximum displacement of the mass in x-dir occurs in the first mode. Here an accurate estimate of the modes is made by replacing the comb-fingers on either sides with an equivalent mass.
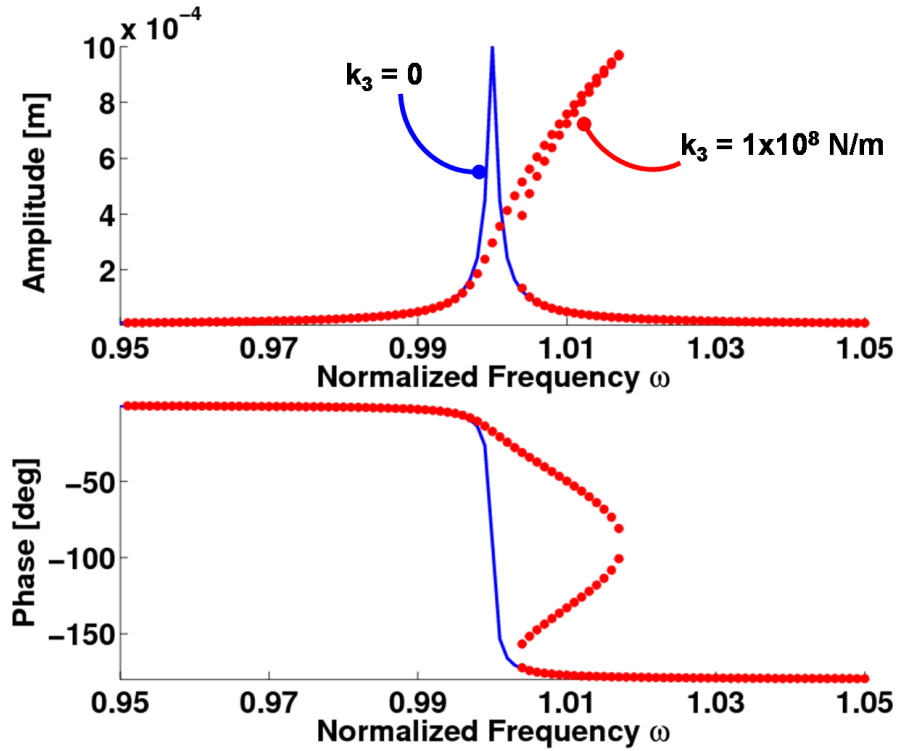
Figure 5: Dynamic response of the resonator with the stiffness values extracted from the curve-fitted data in Fig. 4.14: here Eq. 3.14 is used for which the corresponding constants shown in Eq. 3.13 are: $m = 8.115 \times 10^{-9}$ kg (effective mass as calculated in Appendix C), $k_1 = 52$ N/m, $k_3 = 1 \times 10^8$ N/m^3, $Q = 3000$ and hence $c = 1.36 \times 10^{-6}$ Ns/m, $A_d = 2.053 \times 10^{-4}$ N. Note that the amplitude of displacement shown in this simulation depends entirely A_d and Q factor; therefore it may not accurately represent the actual dynamical displacement in the experiments.

Chapter 6

Parasitics and Frequency Response

From Fig. 6(b), after deriving the equation for the transfer function and then dividing the equation into the real and imaginary parts, we arrive at,
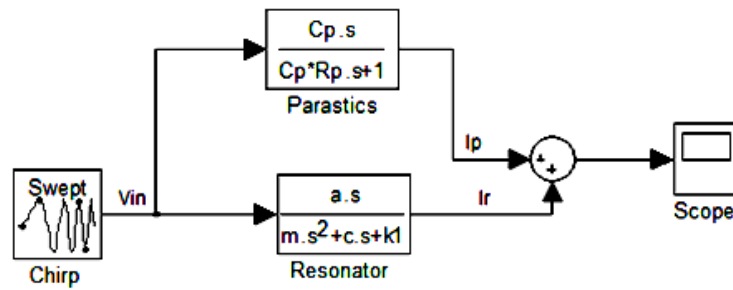
$$Re = K\left(\frac{ac\omega^2}{(k_1 - m\omega^2)^2 + c^2\omega^2} + \frac{R_p C_p^2 \omega^2}{(R_p C_p \omega)^2 + 1}\right), \tag{19a}$$

$$Im = K\left(\frac{a(k_1 - m\omega^2)\omega}{(k_1 - m\omega^2)^2 + c^2\omega^2} + \frac{C_p \omega}{(R_p C_p \omega)^2 + 1}\right). \tag{19b}$$

Where K = amplifier gain, k_1 = linear spring stiffness, c = damping coefficient, m = mass, ω = excitation frequency, and $a = \dfrac{1}{2}\dfrac{\partial C_x}{\partial x}V_{dc}$ = transduction factor that converts electrostatic potential energy into mechanical energy. Note that in the above equations $C_p = C_{p1} + C_{p2}$. If
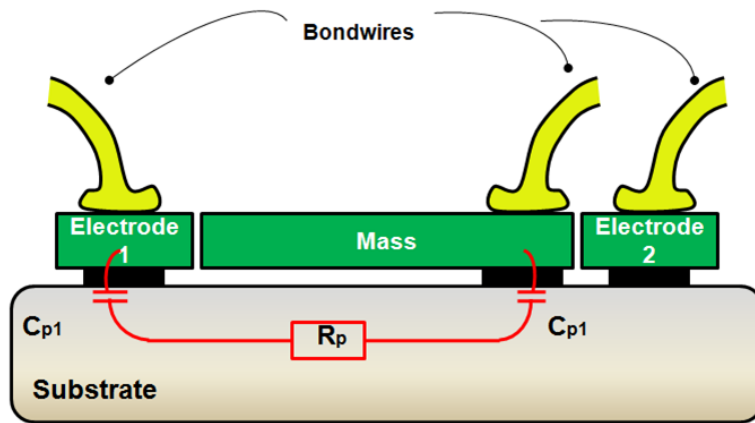
(a) Parasitics present in MEMS device

(b) Transfer function with parasitics

Figure 6: (a) Typical parasitics present in MEMS device. Here C_{p1} and C_{p2} are the parasitic capacitances between the electrodes and the substrate and R_p is the parasitic resistance present in the substrate. (b) Simulink model that represents the mechanical system of resonators and the parasitic effects [40].

the substrate is grounded then $R_p = 0$ in the above equations; this indicates that the real part of the response would contain purely mechanical terms whereas the imaginary part would be offset by $C_p\omega$.
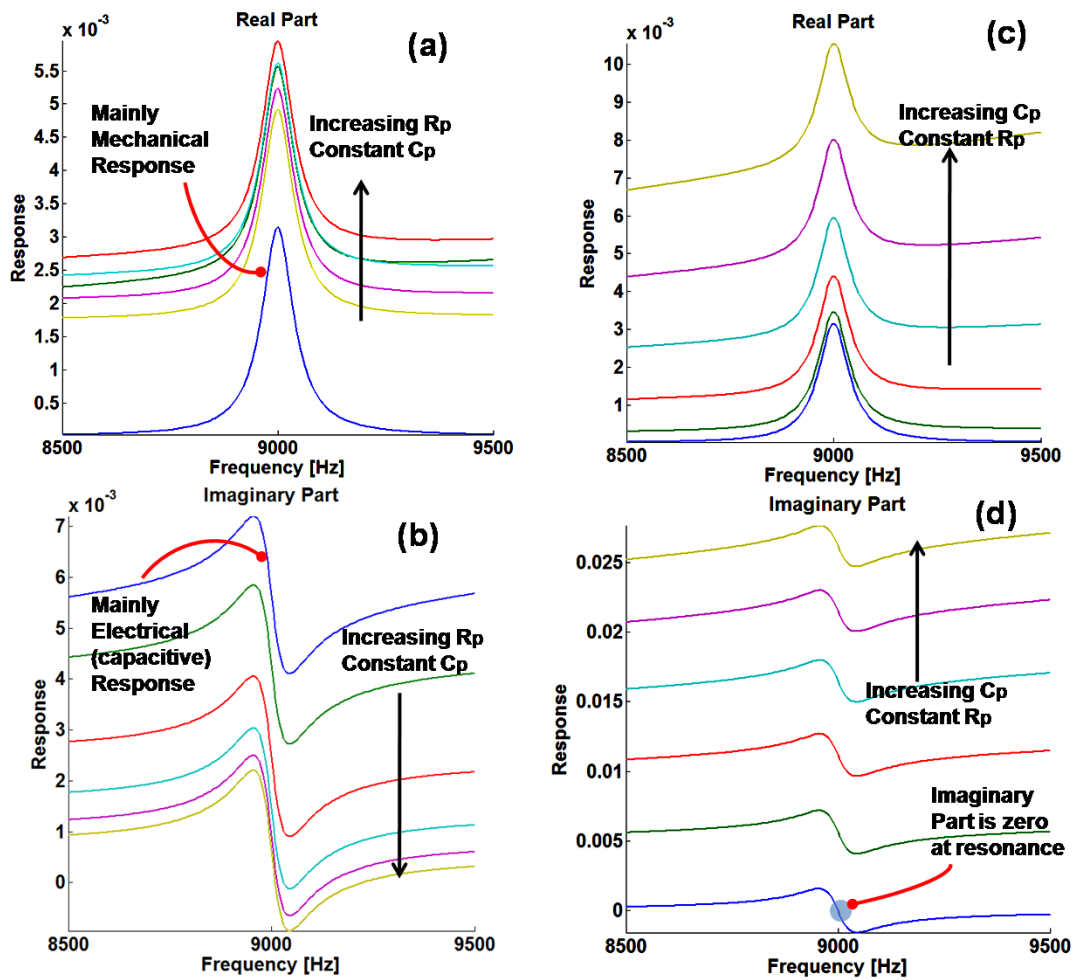
Figure 7: Effects of parasitics on the frequency response curves: (a) and (b) show the real and imaginary response curves respectively for R_p = (0, 100, 200, 300, 400, 500) Ω and C_p = 0.1 μF. Note that the change in R_p and C_p are in the opposite directions. (c) and (d) show the real and imaginary response curves respectively for R_p=10 Ω and C_p = (0.1, 0.2, 0.3, 0.4, 0.5) μF. Here it can be seen that increasing C_p causes the real part of the response to shift up and then skew to the left. The effect of increasing C_p on the imaginary part of the curve is obvious as it is the major contributor. In (c) and (d) for C_p = 0.1 μF, the peak occurs in the real part where the imaginary part is zero. This is the natural frequency of the resonator. This is particularly useful when determining the other variables in the model. Some or all of the above effects are visible in the experiments.

Design of Coupled Resonators

In Figs. 8 and 9 various coupling topologies for the resonators fabricated in PolyMUMPs and SOIMUMPs are shown.
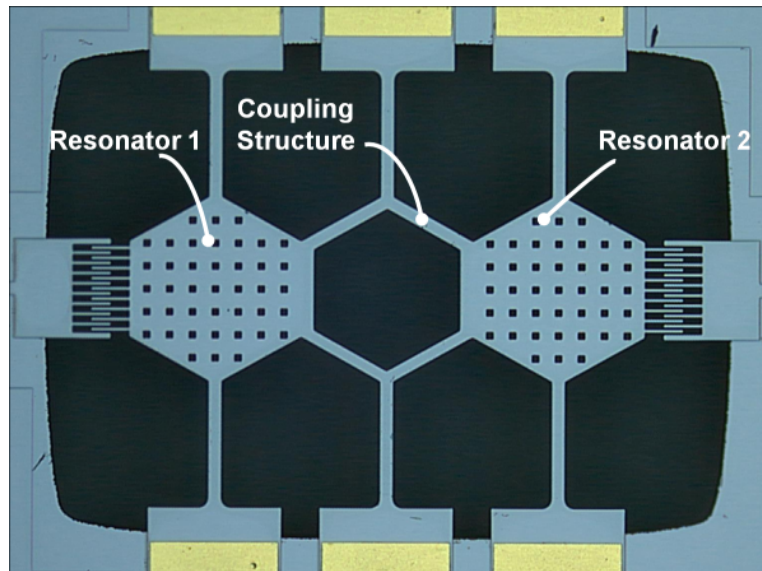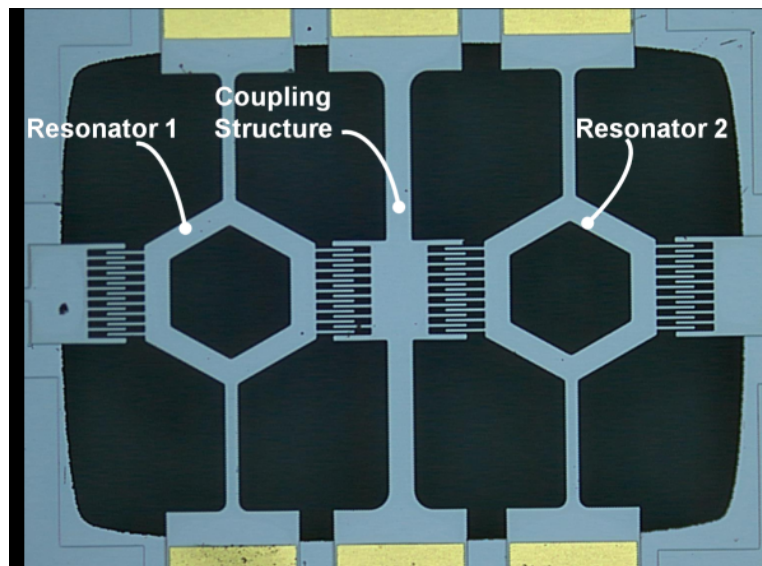
119
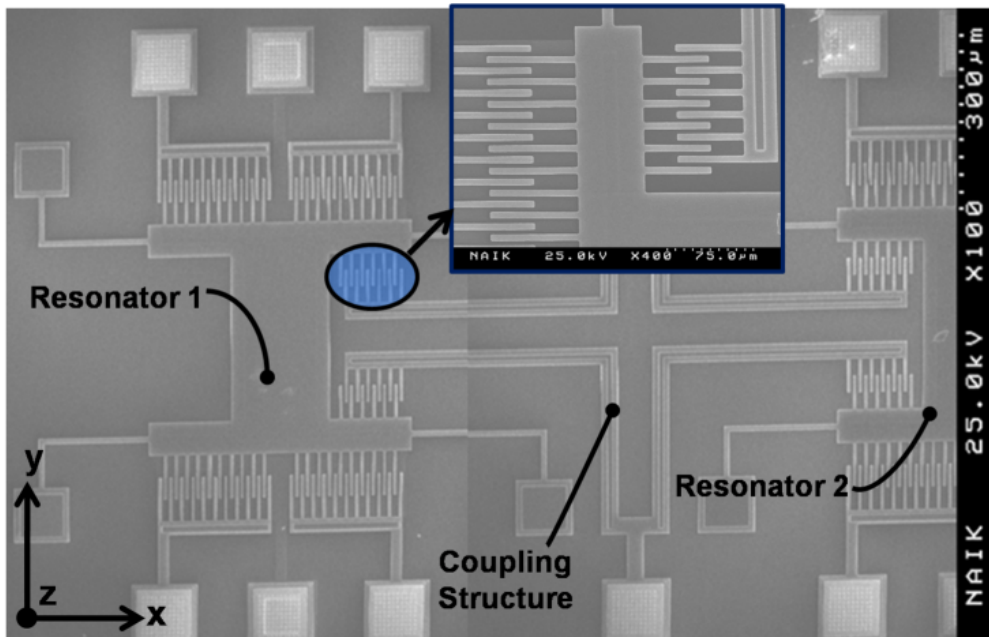
(a) Coupled resonators 01
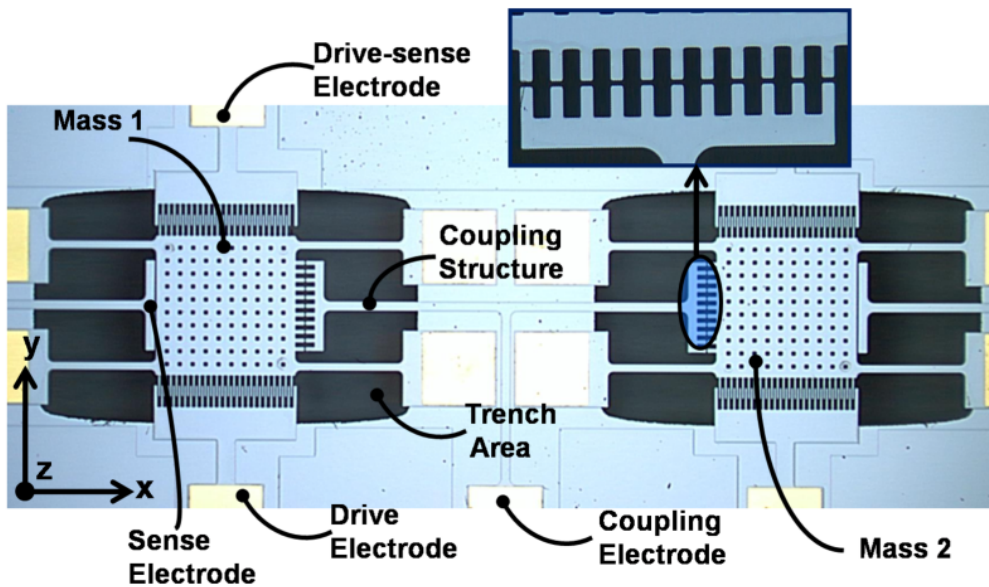
(b) Coupled resonators 02

Figure 8: (a) Coupled resonators 01: The devices were fabricated in PolyMUMPs. The resonators are suspended by crab-leg flexures and connected to each other by harmonically coupled fixed structure with *interdigitated* comb fingers. The idea then would be to bias the two resonators and the coupling structure at the same level. Next both the resonators would be excited individually by an ac voltage. Resonating structures can then interact with each other capacitively. Here the coupling would be bidirectional. (b) Coupled resonators 02: The devices were fabricated in SOIMUMPs. The resonators are suspended by straight beam flexures and connected to each other by parametrically coupled fixed structure with *noninterdigitated* comb fingers. The excitation and coupling strategies are similar (a).

120

(a) Coupled resonators 03

(b) Coupled resonators 04

Figure 9: (a) Coupled resonators 03: The devices were fabricated in SOIMUMPs. The resonators are suspended by straight beam flexures. A hexagonal ring was used as the mass. The resonators were connected to each other by another hexagonal ring. The idea then would be to bias the two resonators and the coupling structure at the same level. Next both the resonators would be excited individually by an ac voltage. Resonating structures can then interact with each other mechanically. Here the coupling would be bidirectional. (b) Coupled resonators 04: The devices were fabricated in SOIMUMPs. The excitation strategy is similar to (a). Here the interaction takes place through harmonically coupled comb drive which would be biased at the same level. Note the similarity with the coupling in Fig. 8(a).
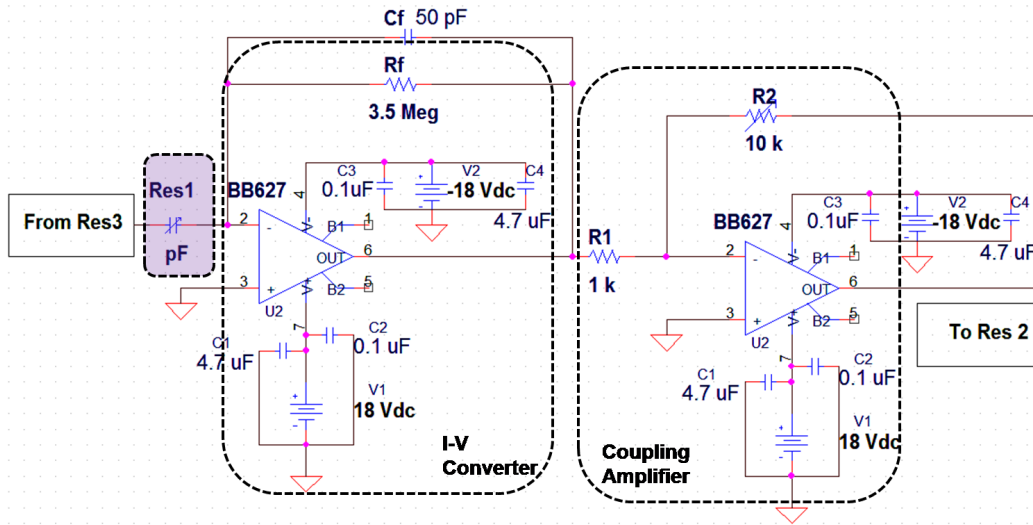
Experiments

Figure 10: Circuit used for Res 1 to obtain the in-phase vibrations: here the output of resonator was biased and coupled via bias-tee (not shown). The feedback capacitor C_f converts the velocity current output into the displacement current. Note that for nonautonomous experiment the bias-tee circuit was slightly modified.
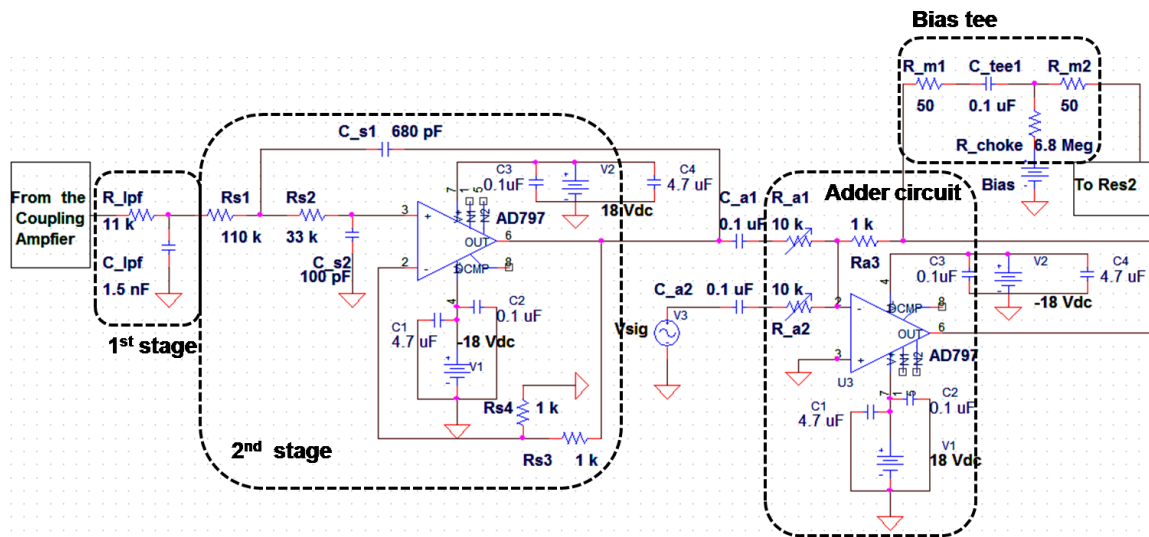

Figure 11: Circuit used for Res1 to obtain the out-of-phase vibrations: here the output of the coupling amplifier shown in Fig. 10 goes into the first stage (RC) of the low pass filter, which is followed by the second stage (2-pole Sallen-Key filter). Next the signal is passed through dc-blocking capacitor and added to the ac excitation voltage using the adder circuit. Next, the combined signal is connected to bias tee circuit where the bias is added; the biased signal is then connected to the input of the next resonator. Note that for the autonomous experiment, V_{sig} was not connected.
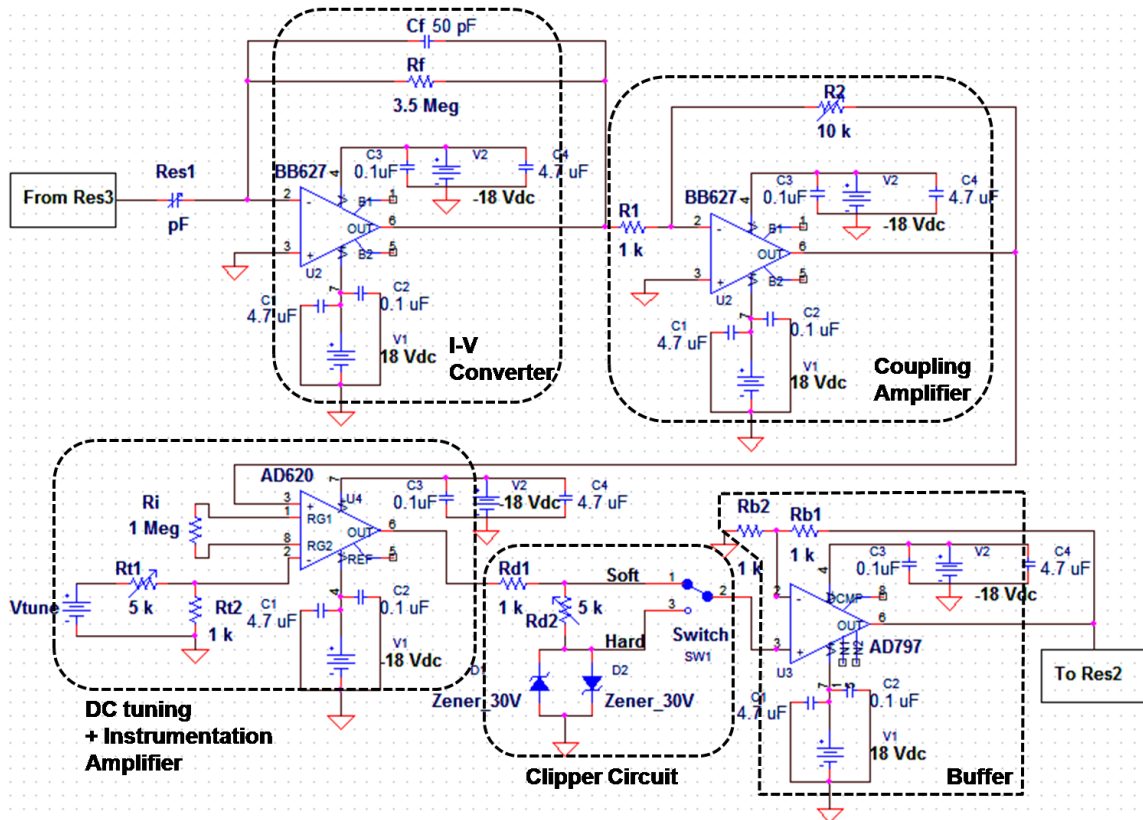
Figure 12: Circuit for Res 1 with *optional* signal processing circuits: the top half of the circuit is same as Fig. 10. The instrumental amplifier balances dc gain and can reduce it to zero if necessary. This is followed by the clipper circuit with 30 V zener diodes to clip the amplitude if it exceeds +/–1.4 V. The clipper circuit can generate hard and soft clipped voltages with more or less harmonics respectively; i.e. in the hard clipped response the voltage is more squarish than the soft clipped response. This circuit is followed by the buffer circuit, the output of which then goes to the input of the next resonator. Note that this circuit has diodes as the additional nonlinear elements and therefore it was not utilized in all of the experiments.
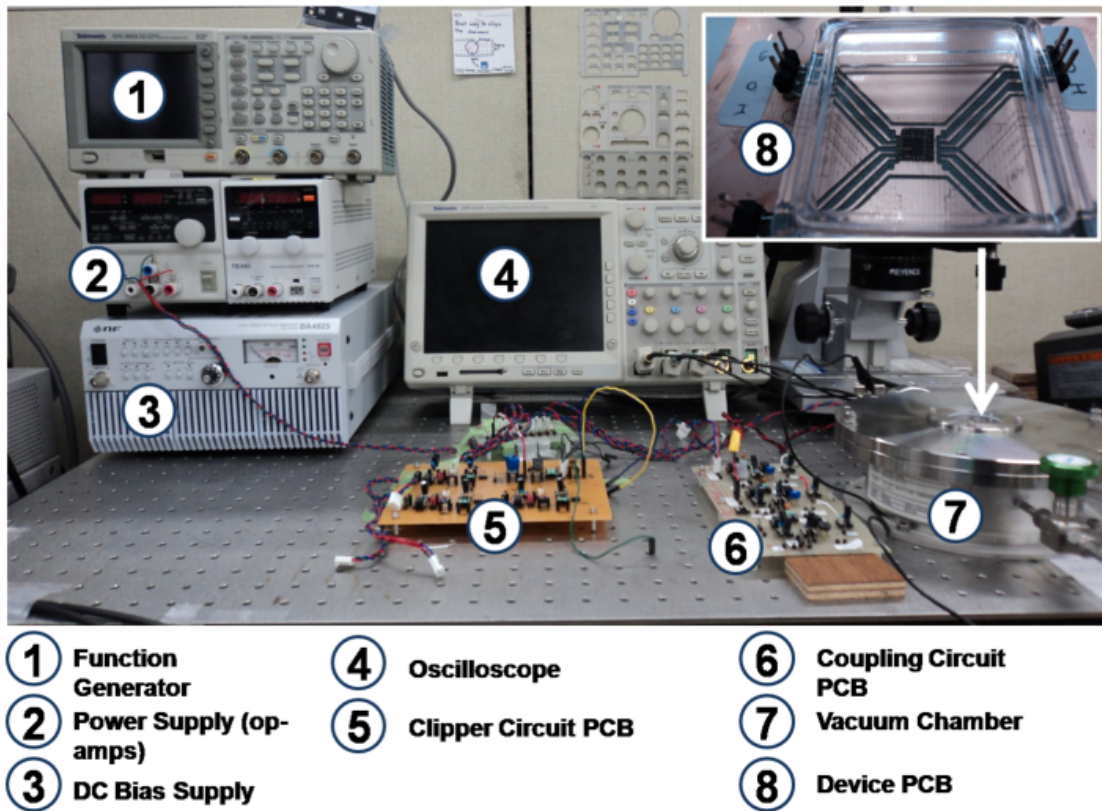
123

Figure 13: The test setup with necessary instruments and parts used in the coupled experiment. Inset shows the device PCB with die in the center.
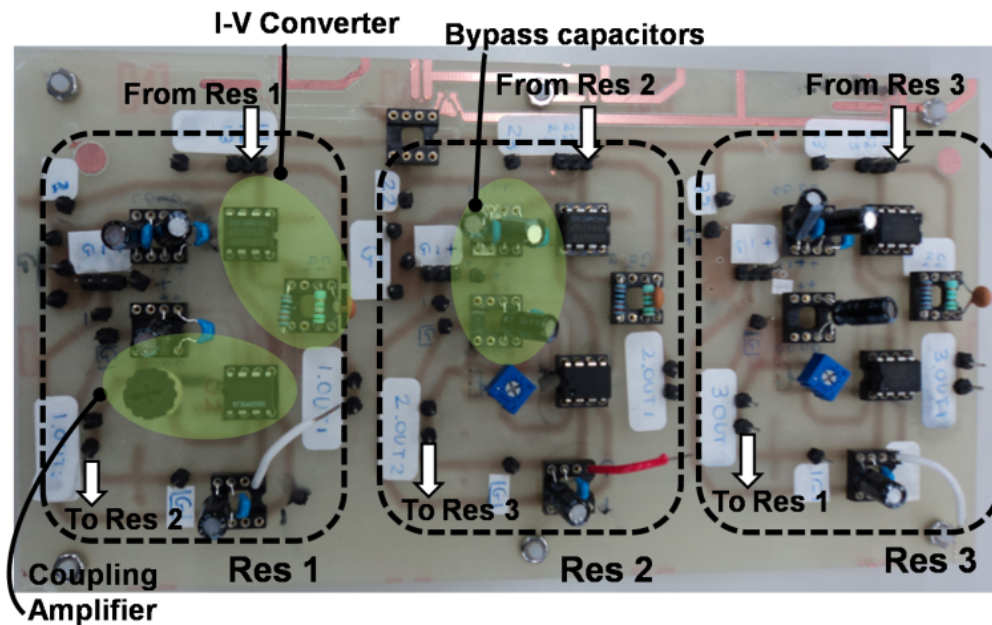
(a) Top side of the coupled board
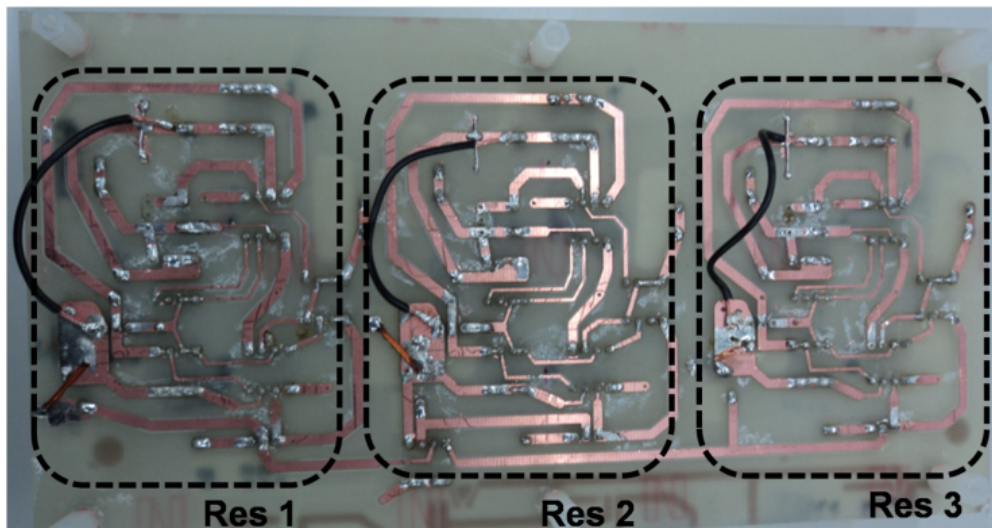
(b) Bottom side of the coupled board

Figure 14: Pictures of the assembled board (Coupling Circuit PCB in Fig. 13) for the coupled experiment: (a) top side of the board. The output of the given resonator was connected to the input of the I-V converter. I-V converter was then connected to the coupling amplifier. The output of the coupling amplifier would then connect to the input of the next resonator in the ring. (b) Bottom side of the board. The extra copper was removed to reduce the parasitic effects and the noise generated by the floating metal.
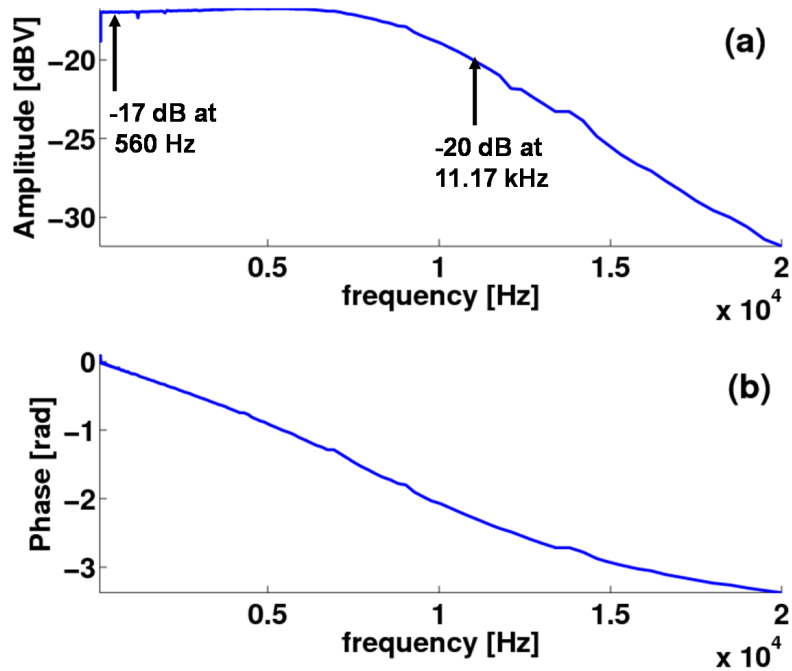
Figure 15: Frequency response of the 3-pole low pass filter measured on the lockin amplifier NF Electronic Instruments 5610B: (a) amplitude and (b) phase. Note that the cutoff frequency at –3dB point is about 11.17 kHz.
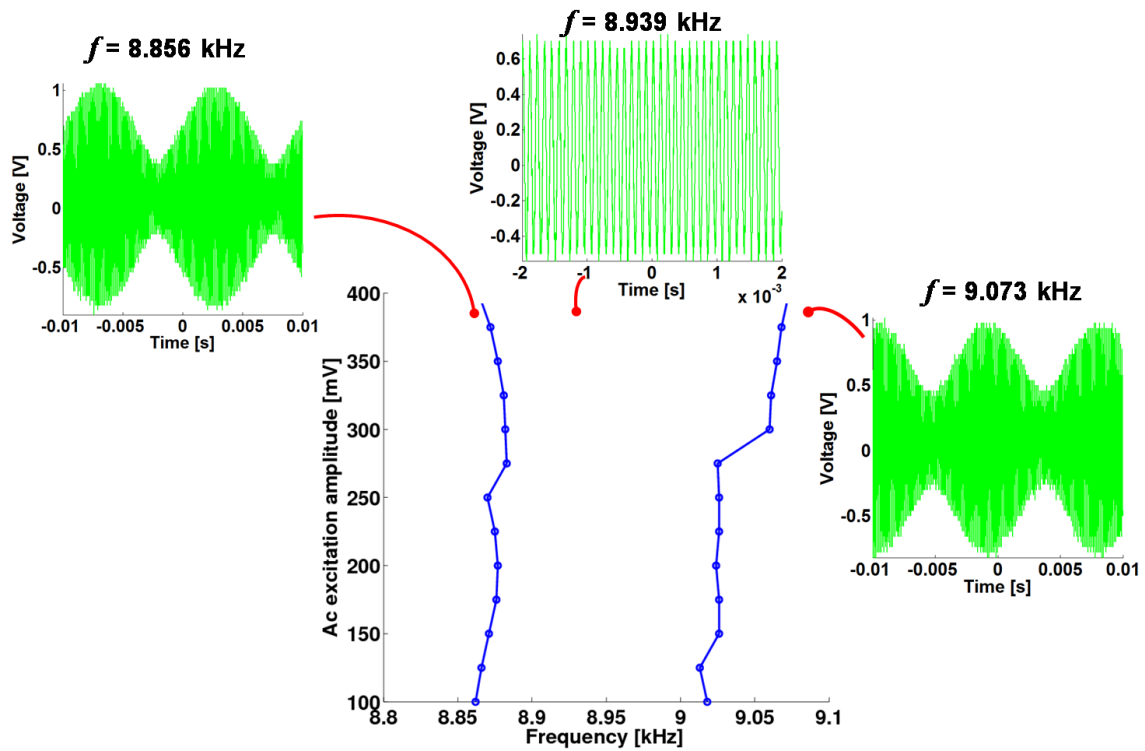
Figure 16: Synchronization of the in-phase vibrations with pressure = 15 Pa: here the test setup is same as in Fig. 6.17 with pressure = 30 Pa. Note that the behavior is qualitatively similar to the region of synchronization shown in Fig. 6.18. However for low damping the sync region widens and stays open for low values of ac excitation amplitude. Also note that the synchronization is not robust around the boundaries. Because of low damping the perturbed vibrations do not settle quickly into a steady-state.

127
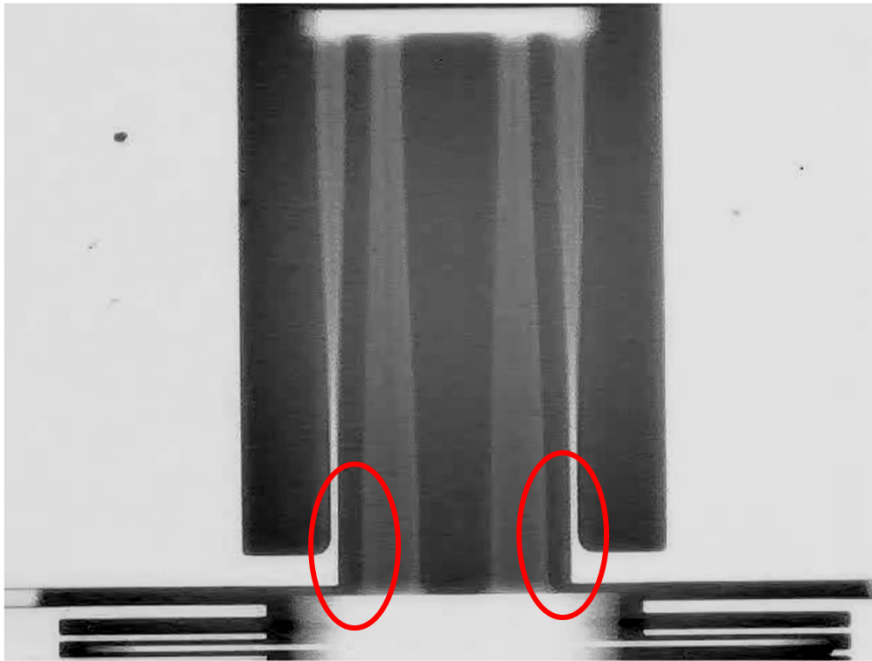
Figure 17: Picture of the device during peak resonance in the extended region: excitation conditions are V_{dc} = 20V, V_{ac} = 305 mV, and pressure = 30 Pa. Note the proximity of the inner and outer beams indicated by the ovals which results in an increase in the damping effect.

Appendix C

In this appendix, the model of the resonator based on the experimental methods and the characterization results is developed.

Effective Mass

The key parameter in the model is the effective mass of the resonator. In this section the method that was used to determine the effective mass is described.

As shown in Fig. 18(a), the lengths of the outer beam and the inner beam are denoted as L_1 and L_2, respectively. The maximum distance traveled from the equilibrium by the outer beam and the inner beam are denoted as x_1 and x_2, respectively. Due to the four fold symmetry in the resonator, we only need to analyze one forth of the folded flexures with $F_e/4$ as the applied force, where F_e is the electrostatic force generated between the fixed and the movable combs in the x direction. First we assume that this force acts as a point load at the tip of the inner beam. As shown in Fig. 18(b), the force applied to the outer beam is slightly less than the inner beam. However if the truss is rigid in x direction then the force applied on the inner beam and the outer beam can be assumed to identical.

Folded Flexures

Figure 19(a) shows one of the four beam pairs with the appropriate moments created by the force and the inner beam. Fig. 19(b) shows that each of the beams can be broken into two segments of fixed-free beams. Next we focus on the derivation of the spring constant of a single fixed-free beam in order to find the spring constants of the inner beam and the outer beam.

Fixed-free Beam

The moment created by the force in the beam is countered by the beam moment as shown in Fig. 19(a). The beam deflects in x direction as the central axis of the beam stretches in the y direction; this deflection can be described from the curvature of the stretched beam. The curvature, denoted by κ, can be found as $\kappa = 1/R$, where R is the radius of the central axis of the deformed beam with length L. Note that this is only true for small angle deflections. The curvature of the central axis is $1/R = \mathrm{d}^2x/\mathrm{d}^2y = -M_x/(EI_x)$ and the beam moment
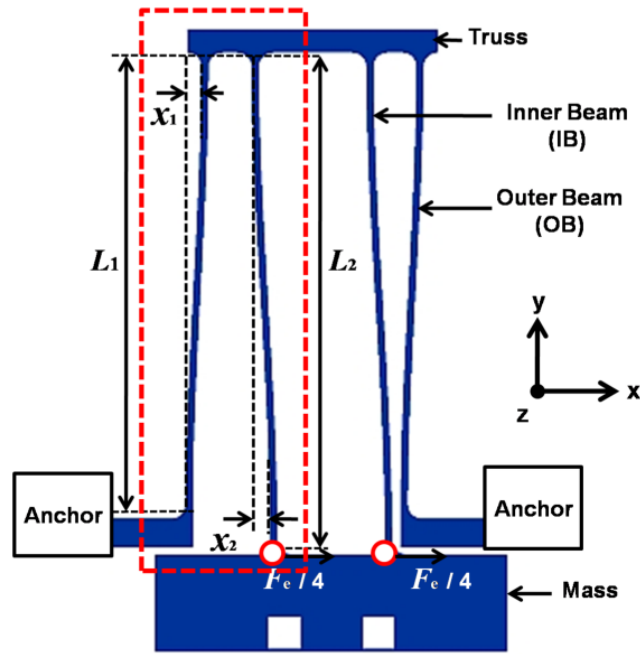
(a) Folded flexure of the resonator
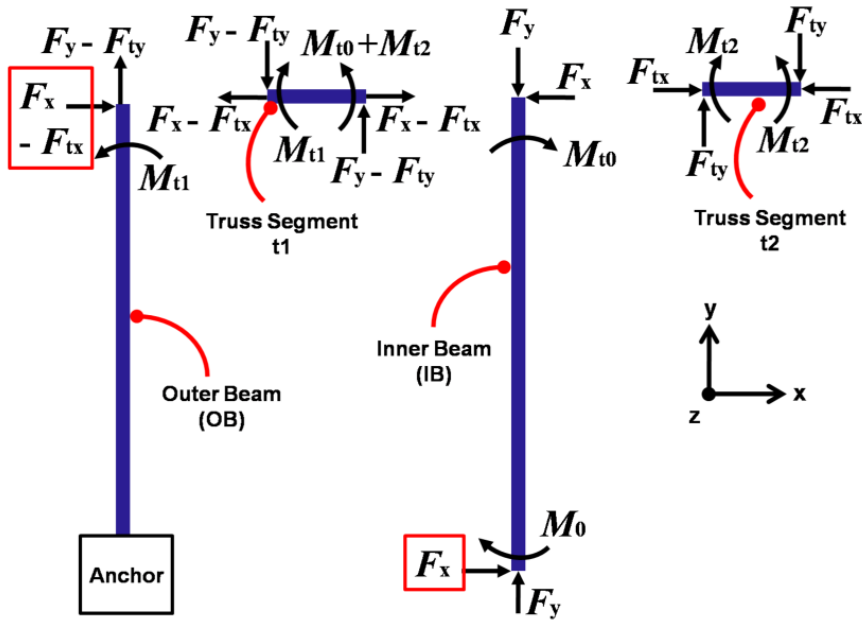
(b) Free body diagram of the folded flexure

Figure 18: Forces and moments present in the folded flexure: (a) the folded beams are shown with the pertinent parameters used in the analysis of effective mass. Here $F_e/4$ is the electrostatic force applied at the tip of the inner beam in the x-dir. The area marked in red square is used for the free body diagram. (b) Free body diagram of the folded flexure shows forces acting on different segments. Note that $F_x = F_e/4$ from (a). It is worthy to note that the force impinging on the outer beam in the x-dir is less than on the inner beam. However if the truss is assumed to be rigid in the x direction then we can ignore the correction F_{tx} given $F_x \gg F_{tx}$. This implies that the forces acting at the tip on the inner and outer beam are identical.
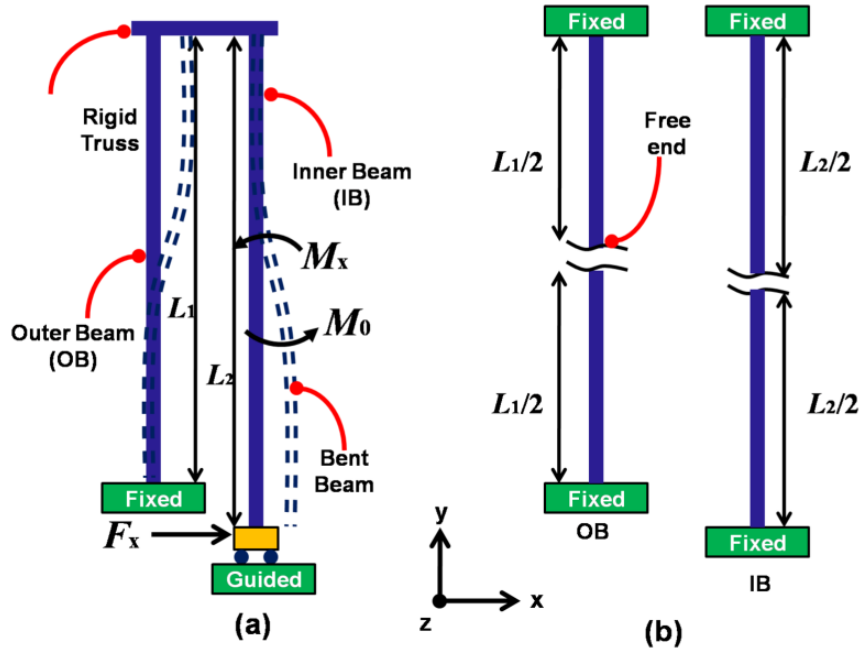
130

Figure 19: Fixed-guided beam pair as a parallel combination of fixed-free beams: (a) the beam pair consists of the inner beam and the outer beam with the pertinent lengths and the deformations as shown. Here $F_x = F_e/4$ is the force applied at the tip of the inner beam. This force creates a moment M_o which is countered by the beam moment in x direction as M_x in the middle section where it bends in order to create equilibrium hence $M_x = -M_o$. (b) Each of the beams can be broken into the segments with equal lengths. Each segment can be viewed as the fixed-free beam. For a given beam within the pair, the spring constant is the parallel combination of stiffnesses of the two segments. Consequently the spring constant for the pair is the parallel combination of the stiffnesses of the inner beam and the outer beam.

$M_x = -M_o = -F_x(L-y)$ [56]. Here x and y are the beam displacements in x and y directions, respectively. E is the Young's modulus and I_x is the second moment of the cross sectional area of the beam. Then it follows that the deflection x due to the force F_x at the tip of the beam can be found as,

$$
\begin{aligned}
\frac{\mathrm{d}^2 x}{\mathrm{d}^2 y} &= -\frac{M_x}{EI_x} = \frac{F_x}{EI_x}(L-y), \\
\implies \int \frac{\mathrm{d}^2 x}{\mathrm{d}^2 y} &= \frac{\mathrm{d}x}{\mathrm{d}y} = \frac{F_x}{EI_x}\left(Ly - \frac{1}{2}y^2\right).
\end{aligned}
$$

$$
\begin{aligned}
\implies x &= \frac{F_x}{EI_x}\int_0^L \left(Ly - \frac{1}{2}y^2\right)\mathrm{d}y, \\
&= \frac{F_x}{EI_x}\frac{L^3}{3}.
\end{aligned} \tag{20}
$$

131

Hence the spring constant in x direction is,

$$\frac{F_x}{x} = \frac{3EI_x}{L^3} = \frac{3E}{L^3}\frac{1}{12}hw^3$$

$$k_x = \frac{1}{4}Eh\left(\frac{w}{L}\right)^3. \tag{21}$$

Where w is the width of the beam. Note that the above equation pertains to the fixed-free beam of length L due to the point load of F_x. As shown in Fig. 19(b), a fixed-guided beam can be represented as a pair of fixed-free beams. From Eq. 21, each of the segments of the outer beam with the length $L_1/2$ and the inner beam with the length $L_2/2$ has the spring constants,

$$k_{o1} = 2Eh\left(\frac{W}{L_1}\right)^3, \ k_{o2} = 2Eh\left(\frac{W}{L_2}\right)^3. \tag{22}$$

Fixed-Guided Beam

It follows that the total spring constant of the fixed-guided beam is the parallel combination of the spring constants of the segments as the fixed-free beams, e.g. $k_1 = k_{o1} \parallel k_{o1}$ and $k_2 = k_{o2} \parallel k_{o2}$ and hence,

$$k_1 = Eh\left(\frac{W}{L_1}\right)^3, \ k_2 = Eh\left(\frac{W}{L_2}\right)^3. \tag{23}$$

It is also evident that the equivalent spring constant of the given beam pair, k_p, is also the parallel combination of k_1 and k_2,

$$
\begin{aligned}
k_p &= k_1 \parallel k_2 = \left(\frac{1}{k_1} + \frac{1}{k_2}\right)^{-1}, \\
&= \frac{EhW^3}{L_1^3 + L_2^3} = \frac{EhW^3}{L_2^3}\left(\frac{r}{r+1}\right), \ r = \left(\frac{L_2}{L_1}\right)^3.
\end{aligned}
\tag{24}
$$

Note that the above equation pertains to the point load F_x. For a given beam pair, the equivalent spring constant due to the force $F_x = F_e/4$ (see Fig. 18(a)) is found as,

$$k_c = \frac{F_e/4}{x} = 4k_p = \frac{4EhW^3}{L_2^3}\left(\frac{r}{r+1}\right). \tag{25}$$

Note that the above equation is applicable to the beams in a given pair with identical width of W with nonidentical lengths[2].

---

[2] For the beams with identical lengths $l = L_1 = L_2$ and widths W, $k_c = 2EhW^3/l^3$. With identical lengths but non-identical widths with the width ratio as $r = W_2/W_1$, $k_c = 4Eh(W_2/l)^3/(r+1)$.

Referring back to Fig. 18(a) and equating the applied force with the restoring forces in the inner and outer beam pair leads to,

$$F_e/4 \;=\; k_1 x_1 = k_2 x_2,$$

$$\frac{k_1}{k_2} \;=\; \frac{x_2}{x_1},$$

$$\frac{x_2}{x_1} \;=\; \left(\frac{L_2}{L_1}\right)^3 = r \approx 1.325. \tag{26}$$

From the layout, the lengths of the outer beam and the inner beam are determined as $L_1 \approx 305.5\ \mu m$ and $L_2 \approx 335.5\ \mu m$, respectively. In Eq. 26 the ratio r is determined after excluding the fillet lengths. However depending on the fabrication and the movement of the structure during the peak displacement at the resonance frequency, the fillet lengths may also need to be included.

Let the displacement of the center of the mass be $x_c = x_1 + x_2$. Then it follows from Eq. 26 that $x_1 = \left(\dfrac{1}{1+r}\right) x_c$ and $x_2 = \left(\dfrac{r}{1+r}\right) x_c$.

Potential and Kinetic Energies of the Beam Pair

In this section the Raleigh-Ritz method is used to find the effective mass at the *resonant frequency* of the entire structure [20]. Let the displacement of the mass be denoted as $x(t) = x_c \cos(\omega t)$, when the time-varying electrostatic force is applied due to the mass. Let the kinetic energy of the effective mass be denoted by $K(t)$ and the potential energy of the effective mass be denoted by $T(t)$, which is equal to the work done by the applied force. The maximum energy expressions and their relationship at the peak displacement can be derived as,

$$T(t) = \frac{1}{2} k_c x(t)^2, \tag{27a}$$

$$T_{\max} = \frac{1}{2} k_c x_c^2, \tag{27b}$$

$$K(t) = \frac{1}{2} M_{\mathrm{eff}} v(t)^2, \; v(t) = \frac{\mathrm{d}x(t)}{\mathrm{d}t}, \tag{27c}$$

$$K_{\max} = \frac{1}{2} M_{\mathrm{eff}} \omega_o^2 x_c^2, \tag{27d}$$

$$T_{\max} = K_{\max}. \tag{27e}$$

Where k_c is the stiffness experienced by the center of the mass during the peak displacement x_c due to the bending of a given beam pair. Here ω_o is the resonant frequency of the structure and M_{eff} is the total effective mass of the resonator.

Potential Energy

Note that the maximum potential energy T_{max} is the total work done by the strained beams within a given pair as they are maximally deformed during the peak displacement. Therefore T_{max} depends on the displacement of a given beam pair assuming that all four beam pairs deform identically. Now T_{max} can be found by substituting Eq. 25 into Eq. 27(b),

$$T_{max} = \frac{1}{2}\left[\frac{4EhW^3}{L_2^3}\left(\frac{r}{r+1}\right)x_c^2\right]. \tag{28}$$

Kinetic Energy

The peak deflection of the outer beam as a function of y over the entire length can be expressed as [20],

$$x_{OB}(y) = \frac{F_e}{4EhW^3}\left(3L_1y^2 - 2y^3\right); 0 \le y \le L_1. \tag{29}$$

Evaluating $x_{OB}(y)$ at L_1 leads to the expression of $x_{OB}(y)$ in terms of x_c as,

$$x_{OB}(L_1) = x_1 = \left(\frac{1}{1+r}\right)x_c = \frac{F_e}{4EhW^3}L_1^3,$$

$$\implies \left(\frac{1}{1+r}\right)x_c/L_1^3 = \frac{F_e}{4EhW^3},$$

$$\implies x_{OB}(y) = \left(\frac{x_c}{1+r}\right)\left[3\left(\frac{y}{L_1}\right)^2 - 2\left(\frac{y}{L_1}\right)^3\right]. \tag{30}$$

From the velocity at the resonant frequency ω_o and Eq. 30, the expression of the kinetic energy of the outer beam is derived as,

$$v_{OB}(y) = \left(\frac{x_c}{1+r}\right)\left[3\left(\frac{y}{L_1}\right)^2 - 2\left(\frac{y}{L_1}\right)^3\right]\omega_o,$$

$$K_{OB} = \frac{1}{2}\int_0^{L_1}\left(\frac{x_c}{1+r}\right)^2\left[3\left(\frac{y}{L_1}\right)^2 - 2\left(\frac{y}{L_1}\right)^3\right]^2\omega_o^2\,dM_{OB}. \tag{31}$$

Where, M_{OB} is the mass of an outer beam. Assuming that the beam is made of uniform material, $dM_{OB}/M_{OB} = dy/L_1$ and hence $dM_{OB} = \dfrac{M_{OB}}{L_1}dy$. After substituting dM_{OB} into Eq. 31, we obtain

$$K_{OB} = \frac{1}{2}\left(\frac{M_{OB}x_c^2\omega_o^2}{L_1(1+r)^2}\right)\int_0^{L_1}\left[3\left(\frac{y}{L_1}\right)^2 - 2\left(\frac{y}{L_1}\right)^3\right]^2 dy,$$

$$K_{OB} = \frac{1}{2}\left(\frac{0.371M_{OB}}{(1+r)^2}\right)x_c^2\omega_o^2. \tag{32}$$

Consequently the total kinetic energy of the four outer beams in the entire structure is found as,

$$K_{\text{OB}} = \frac{1}{2}\left(\frac{1.486}{(1+r)^2}\right)M_{\text{OB}}x_c^2\omega_o^2.\tag{33}$$

The deflection of the inner beams $x_{\text{IB}}(y)$ depends on x_c. The peak deflection of the inner beam as a function of y over the entire length can be expressed in a similar manner as the outer beam as follows,

$$\begin{aligned}x_{\text{IB}}(y) &= x_c - x_2\left[3\left(\frac{y}{L_2}\right)^2 - 2\left(\frac{y}{L_2}\right)^3\right],\\ &= x_c\left(1 - \frac{r}{r+1}\right)\left[3\left(\frac{y}{L_2}\right)^2 - 2\left(\frac{y}{L_2}\right)^3\right].\end{aligned}\tag{34}$$

After going through the derivation as shown previously, the kinetic energy of the all four inner beams in the entire structure is found as,

$$K_{\text{IB}} = \frac{1}{2}\left[4\left(1 + 0.371\left(\frac{r}{r+1}\right)^2 - \left(\frac{r}{r+1}\right)\right)\right]M_{\text{IB}}x_c^2\omega_o^2.\tag{35}$$

Where, M_{IB} is the mass of an inner beam.

Let the velocity of the truss be denoted as v_{TR} at the resonant frequency. The truss velocity depends on the x_2 since the truss is connected to the mass via the inner beam. Recognizing that $v_{\text{TR}} = \omega_o x_2 = \omega_o\left(\frac{r}{r+1}\right)x_c$, the kinetic energy of the two trusses in the structure is,

$$K_{\text{TR}} = \frac{1}{2}\left[2\left(\frac{r}{r+1}\right)^2\right]M_{\text{TR}}x_c^2\omega_o^2.\tag{36}$$

Where, M_{TR} is the mass of a single truss. Now the maximum total kinetic energy of the entire structure K_{max} can be written as,

$$K_{\text{max}} = \frac{1}{2}\left(\omega_o x_c\right)^2\left[M_c + 2\left(\frac{r}{r+1}\right)^2 M_{\text{TR}} + 4\left(1 + 0.371\left(\frac{r}{r+1}\right)^2 - \left(\frac{r}{r+1}\right)\right)M_{\text{IB}} + \left(\frac{1.486}{(1+r)^2}\right)M_{\text{OB}}\right].\tag{37}$$

Where, M_c is the mass of the perforated plate plus the mass of the fillets. From Eq. 37, it is clear that the effective mass of the structure at the peak displacement is,

$$M_{\text{eff}} = \left[M_c + 2\left(\frac{r}{r+1}\right)^2 M_{\text{TR}} + 4\left(1 + 0.371\left(\frac{r}{r+1}\right)^2 - \left(\frac{r}{r+1}\right)\right)M_{\text{IB}} + \left(\frac{1.486}{(1+r)^2}\right)M_{\text{OB}}\right].\tag{38}$$

Substituting Eq. 28 and Eq. 37 into Eq. 27(e) gives us the expression for the resonant frequency of the structure as,

Method	Design Type		
	No Fillets	Fillets (lengths omitted)	Fillets (half of the lengths included)
Analytical	$f_o = 9.173$ kHz $M_{eff} = 8.09 \times 10^{-9}$ kg	$f_o = 10.01$ kHz $M_{eff} = 8.108 \times 10^{-9}$ kg	$\mathbf{f_o = 9.566}$ **kHz** $\mathbf{M_{eff} = 8.115 \times 10^{-9}}$ **kg**
Comsol	$f_o = 9.039$ kHz	$f_o = 9.681$ kHz (Appendix B)	$f_o = 9.681$ kHz (Appendix B)

$$\omega_o = \sqrt{\frac{4Eh(W/L_2)^3[r/(r+1)]}{M_{eff}}}. \tag{39}$$

Table 1 shows the comparison of the resonant frequency calculated from Eq. 39 and the simulations performed in Comsol. The table enlists two different designs based on inclusion or exclusion of the fillets. It can be seen from the first column that without the fillets, the analytical result matches the simulation result very well. For the design with the fillets, half of the fillet lengths should be included in order to match the analytical result to the simulation result. Hence the value of M_{eff} in bold is used in the calculations and simulations shown in the subsequent sections.
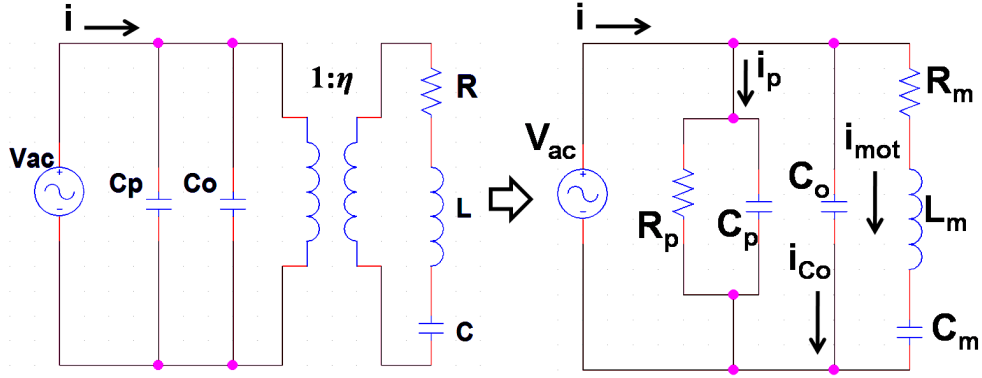
Electrical Equivalent Circuit

Figure 20(a) shows the resonator as the spring-mass-damper system and its electrical equivalent circuit. Here the spring is represented by capacitance $C = 1/k_1$, the damping coefficient is represented by resistance $R = b$, and the resonator mass is represented by inductance $L = M_{eff}$. The force applied to the resonator appears as the voltage across the series combination $R - L - C$. Since k_1 is the effective spring constant of the system (denoted as k_c in the previous section), the resonant frequency is simply $\omega_o = 1/\sqrt{LC}$. The current i flows in the circuit shown in Fig. 20(a) when the resonator is charged with q after connecting a voltage source between the fixed electrode and the resonator mass. Hence,

$$\begin{aligned} i &= \frac{dq}{dt}, \\ &= \frac{d(CV)}{dt}, \\ &= C_o\frac{dV}{dt} + V\frac{dC}{dt}, \\ &= i_{C_o} + i_{mot}. \end{aligned} \tag{40}$$

Where i_{C_o} is the displacement current as it is based on the displacement of the 'gap-closing' capacitor. i_{mot} is the velocity current or the motional current as it is based on the motion due
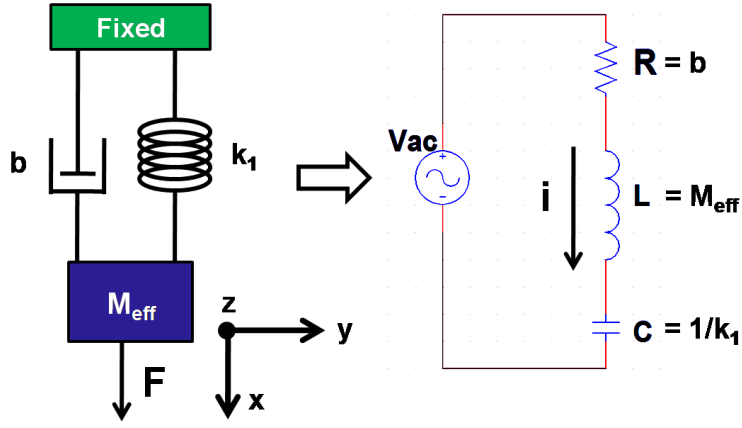
(a) Spring-mass-damper system and its electrical equivalent circuit

(b) Modified electrical equivalent circuit with parasitics

Figure 20: Electrical equivalent circuit: (a) a MEMS resonator can be represented as the spring-mass-damper system with spring constant as k_1 in x-direction, damping coefficient as b, resonator mass as M_{eff}, and electrostatic force F acting on this mass in the x-direction. Each of the elements can then be represented electrically by the transformation $1/k_1 \rightarrow C$, $b \rightarrow R$, and $M_{eff} \rightarrow L$ [62]. (b) Electrical equivalent circuit is modified to include the affects of electrostatic actuation and the transduction factor η that converts the electrostatic energy into mechanical energy. Resistor R_p and capacitor C_p are included to denote the parasitic effects. Additionally the circuit also includes static capacitance C_o when the bias is present. Note that $R_m = b/\eta^2$, $L_m = M_{eff}/\eta^2$, and $C_m = \eta^2/k_1$.

to the capacitance that varies with time. Here the static capacitance C_o can be found as,

$$C_o = 2N\epsilon_o h(s + x_o)/g, \tag{41a}$$

$$x_o = \left(\frac{1}{2} \frac{\partial C_o}{\partial x_o} V_{dc}^2 \right)/k_1. \tag{41b}$$

Where $\epsilon_o = 8.85 \times 10^{-12}$ is the vacuum permittivity, h and g are the height of the device and the gap between the comb fingers, respectively. Here x_o is the static displacement due to the bias V_{dc}.

Let the total actuation voltage be $V(t) = V_{dc} + V_{ac} \cos(\omega_d t)$, where ω_d is the excitation frequency. Note that the electrostatic force is $F_e = \frac{1}{2} \frac{\partial C}{\partial x} V(t)^2$. Ignoring the higher order frequency term and the dc term, and keeping only the harmonic term, the electrostatic force is simply,

$$
\begin{aligned}
F_e &= \left(\frac{\partial C}{\partial x} V_{dc} \right) V_{ac} \cos(\omega_d t), \\
&= \eta V_{ac} \cos(\omega_d t).
\end{aligned}
\tag{42}
$$

Where $\eta = \left(\frac{\partial C}{\partial x} \right) V_{dc}$ is the transduction factor as it converts the electrostatic energy into the mechanical energy. In this design the resonator transduction is achieved by capacitive actuation. Therefore for a set of N movable comb fingers placed between fixed comb fingers, the transduction factor is,

$$
\eta = \left(\frac{2N\epsilon_o h}{g} \right) V_{dc}.
\tag{43}
$$

Now the motional current i_{mot} can be derived as,

$$
\begin{aligned}
i_{mot} &= V_{dc} \frac{dC}{dt}, \\
&= V_{dc} \frac{\partial C}{\partial x} \frac{\partial x}{\partial t}, \\
&= \eta \frac{dx}{dt}.
\end{aligned}
\tag{44}
$$

Let $V_1 = V_{ac} \cos(\omega_d t)$. Then it follows that the displacement current i_{C_o} is,

$$
i_{C_o} = C_o \frac{dV_1}{dt}.
\tag{45}
$$

The dynamics of the system shown in Fig. 20(a) can be described as,

$$
\begin{aligned}
M_{eff} \frac{d^2 x}{dt^2} + b \frac{dx}{dt} + k_1 x &= F_e, \\
\frac{M_{eff}}{\eta} \frac{di_{mot}}{dt} + \frac{b}{\eta} i_{mot} + \frac{k_1}{\eta} \int i_{mot}\, dt &= \eta V_1, \\
\frac{M_{eff}}{\eta^2} \frac{di_{mot}}{dt} + \frac{b}{\eta^2} i_{mot} + \frac{k_1}{\eta^2} \int i_{mot}\, dt &= V_1, \\
L_m \frac{di_{mot}}{dt} + R_m i_{mot} + \frac{1}{C_m} \int i_{mot}\, dt &= V_1.
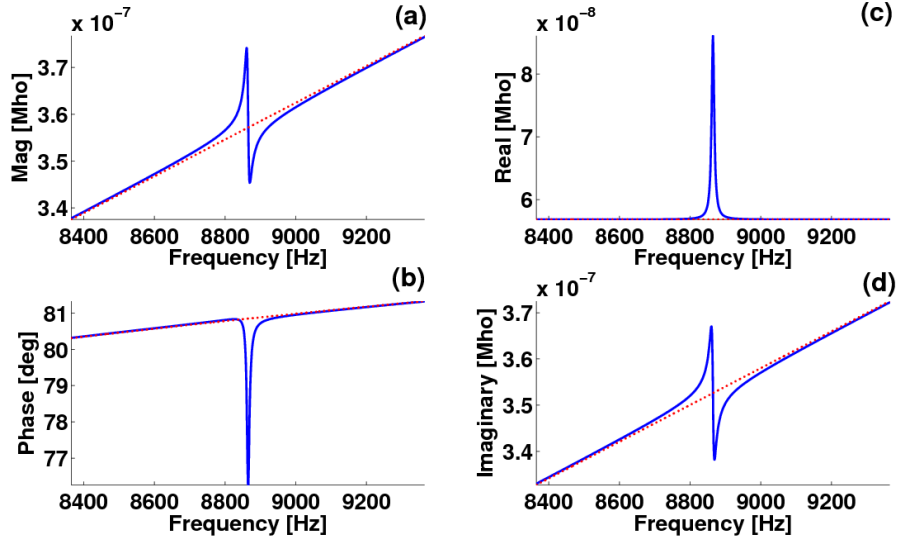\end{aligned}
\tag{46}
$$

Figure 21: Admittance plots simulated from Eq. 47(a) for $Q = 600$: (a) and (b) show the magnitude and phase parts whereas (c) and (d) show the real and imaginary parts. Note that slope of the line shown in red is based on $Y_{\text{elec}} = R_p^{-1} + \omega_d(C_o + C_p)$. Here $V_{\text{dc}} = 20$ V, $C_o = 0.58$ pF, $R_p = 17.6$ MΩ, and $C_p = 5.8$ pF. Also note that the mean of the real part of the admittance shown in (c) depends on R_p.

Where $R_m = b/\eta^2$, $L_m = M_{\text{eff}}/\eta^2$, and $C_m = \eta^2/k_1$.

Eq. 46 represents the dynamics of the resonator in in terms of its electrical equivalent circuit with current i_{mot}. Additionally the resonator also exhibits i_{C_o} through C_o when an voltage with the bias is applied. By adding the parasitic effects as R_p and C_p, all the elements are incorporated in the resonator model as shown in Fig. 20(b). After going through the derivation, the admittance of the circuit is,

$$Y = \left(R_p^{-1} + j\omega_d C_p\right) + \left(j\omega_d C_o\right) + \left(\frac{j\omega_d C_m}{1 - (\omega_d/\omega_o)^2 + j\omega_d R_m C_m}\right), \qquad (47a)$$

$$Y = \left(R_p^{-1} + j\omega_d C_p\right) + \left(j\omega_d C_o\right) + \left(\frac{j\omega_d C_m}{1 - (\omega_d/\omega_o)^2 + j\omega_d/(Q\omega_o)}\right). \qquad (47b)$$

Where the quality factor $Q = \dfrac{\omega_o L_m}{R_m}$ and the resonant frequency $\omega_o = \dfrac{1}{\sqrt{L_m C_m}}$.

Based on the admittance, the electrical equivalent impedance can be calculated simply as $Z = 1/Y$ and hence,

$$Z = \left[\left(R_p^{-1} + (j\omega_d C_p)^{-1}\right) + \left(j\omega_d C_o\right)^{-1} + \left(R_m + j\left(\frac{(\omega_d/\omega_o)^2 - 1}{\omega_d C_m}\right)\right)\right]^{-1}. \qquad (48)$$

Figs. 21 and 22 show the admittance and impedance plots simulated from Eq. 47(a) and
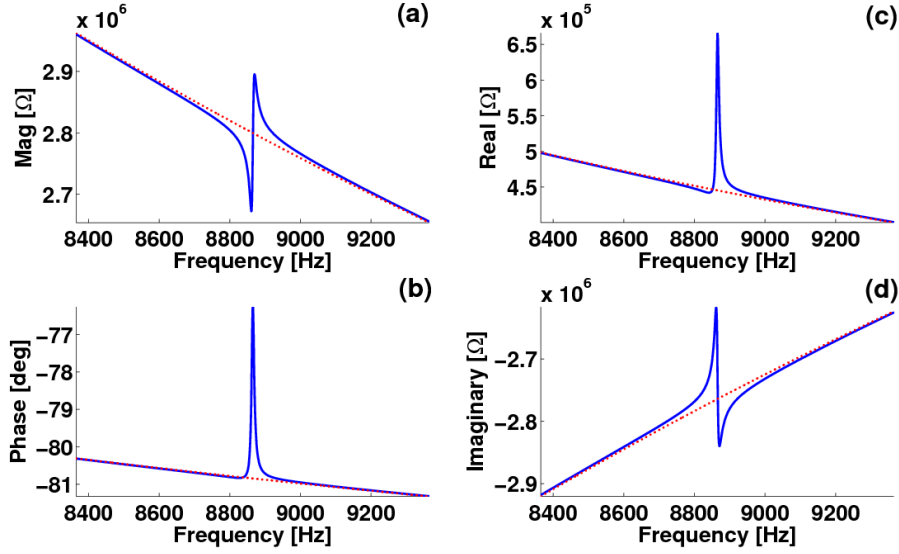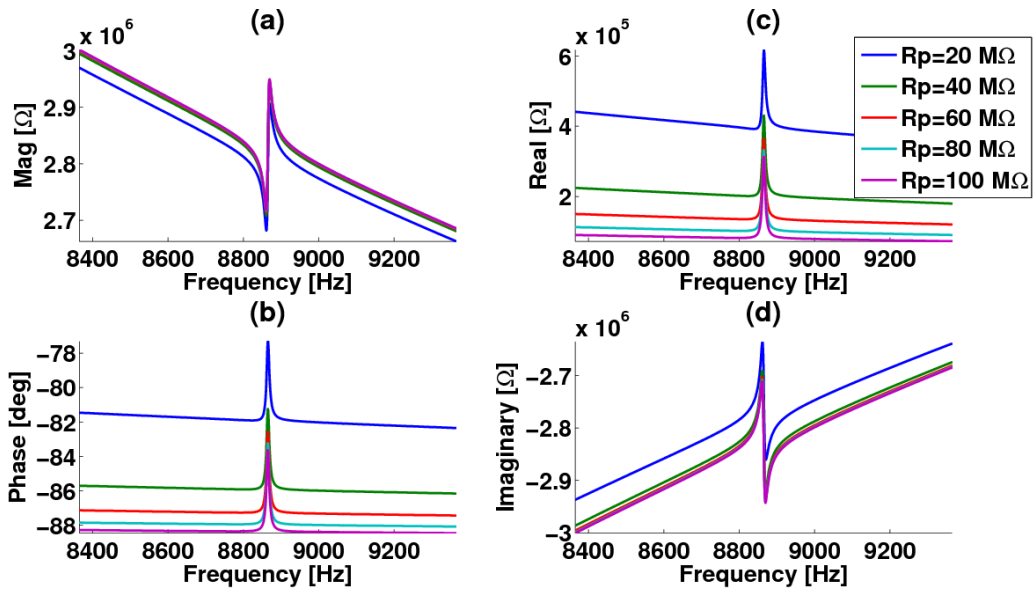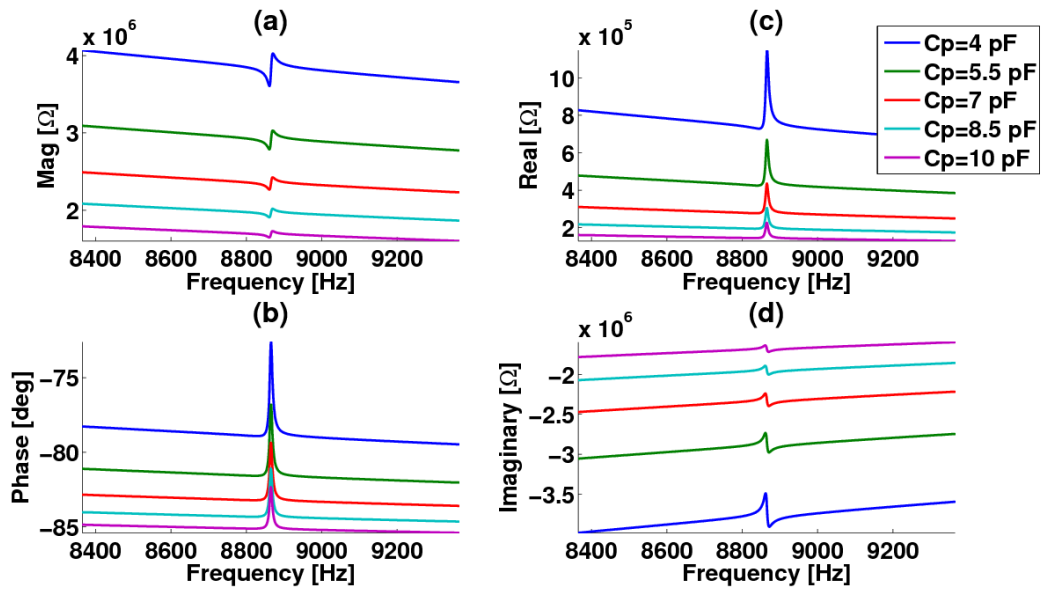
Figure 22: Impedance plots simulated from Eq. 48 for $Q = 600$: (a) and (b) show the magnitude and phase parts whereas (c) and (d) show the real and imaginary parts. Note that slope of the line shown in red is based on $Z_{\text{elec}} = (R_p^{-1} + \omega_d(C_o + C_p))^{-1}$. Parameter values are same as in Fig. 21.

Eq. 48, respectively. Here the effects of the parasitics are evident from the skewed responses in the magnitude and the imaginary plots. R_p affects the resistance as it decides the offset from zero in the real part of the response. The responses shown in Fig. 22 match the experimental results without any nonlinear effects. Note that in the experimental results shown in Ch. 6, the response is multiplied by some gain set by the amplifiers in the instrument. Also note that this model is based entirely on the actuation and detection method used in the experiments. The model may differ depending whether one port or two ports are used for the actuation and the detection [73, 74]. Expectedly, the peaks of the curves shown in Figs. 21 and 22 lower and flatten as the Q factor lowers as was observed in the simulations. Note that an accurate model should include the source resistance ($\sim 50\ \Omega$) and bondwire inductances. Source resistance is very small compared to the parasitic resistance used in the simulations and R_m. A single gold bondwire with $\sim 25\ \mu m$ diameter and ~ 2 mm length has very small inductance (~ 0.5 nH) [75] and negligible impedance at the operational frequency. Therefore the effect of the bondwires and the source resistance is neglected in the model. The model should be improved if device is packaged and has many bondwires and package parasitics. These factors can influence the characteristics of the model significantly. The affects of parasitics is portrayed in Fig. 23. As shown in Fig. 23(a), the slope of the real part decreases after increasing R_p. Likewise as the capacitance C_p increases, the real part of the curve decreases and the peak of both the real part and the imaginary part flattens as shown in Fig. 23(b). It is obvious that C_p has greater influence and can diminish the resonance curve if it is not minimized by either grounding the substrate and other unused ports or by using the die directly

(a) Effect of increasing R_p

(b) Effect of increasing C_p

Figure 23: Effects of increasing parasitics on the impedance simulated from Eq. 48 for $Q = 1000$: (a) $C_p = 5.76$ pF and $R_p = [20$ MΩ, 40 MΩ, 60 MΩ, 80 MΩ, 100 MΩ$]$ and (b) $R_p = 20$ MΩ and $C_p = [4$ pF, 5.5 pF, 7 pF, 8.5 pF, 10 pF$]$.
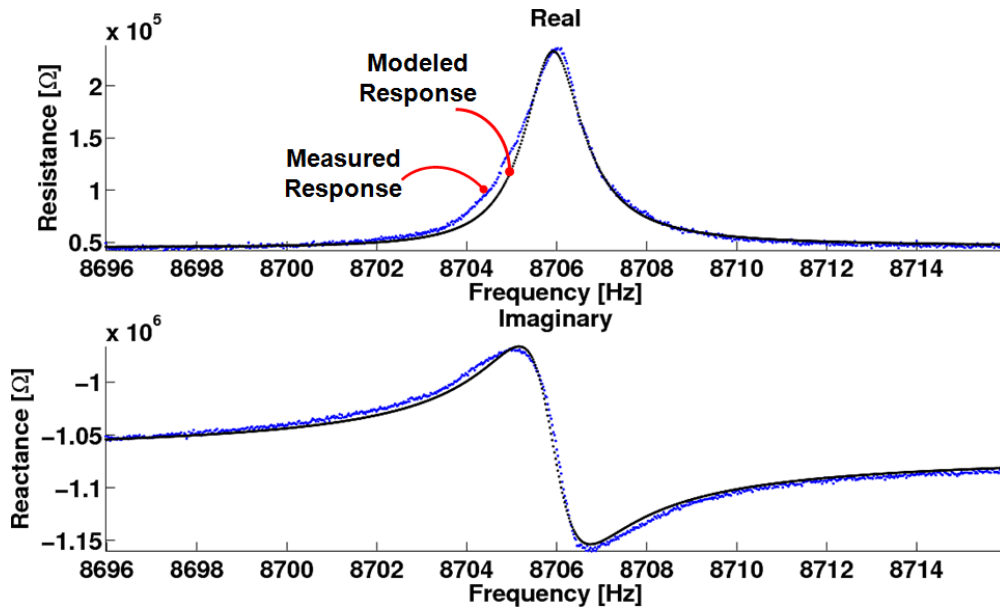
Figure 24: Comparison of the measured data and modelled data: the model in Eq. 48, which was shown in Fig. 20(b), is used for the data collected on Impedance Analyzer 4294A . Here V_{dc} = 20V, V_{ac} = 20 mV, and pressure = 50 Pa. The extracted parameters are listed in Table 2.

on the pcb instead of packaging it.

Fig. 24 shows the comparison of the measured data for one of the resonators and the data based on the model shown in Fig. 20 and Eq. 48. The modelled data shows a good match. The extracted parameters are shown in Table 2.

Table 2: Extracted parameters

Parameter	Value
Q	5550
f_o	8705.75 Hz
k_1	24.28 N/m
η	0.115 µN/V
C_o	0.576 fF
R_m	6.042 MΩ
L_m	613.08 kH
C_m	545.14 aF
R_p	25 MΩ
C_p	16.51 pF

Bibliography

[1] A. Partridge and J. McDonald, "Mems to replace quartz oscillators as frequency sources," *NASA technical brief (June Issue)*, vol. 30, no. 6, 2006.

[2] L. Yan, M. Wu, and W. C. Tang, "A 1.14 ghz piezoelectrically transduced disk resonator," *18th IEEE Int. Conf. on MEMS*, vol. 30, pp. 203–206, 2005.

[3] S. H. Strogatz, *Nonlinear Dynamics and Chaos: With Applications to Physics, Biology, Chemistry, and Engineering*. Reading: Addison-Wesley, 1994.

[4] K. Kaneko and I. Tsuda, *Complex systems: chaos and beyond*. Berlin: Springer-Verlag, 2000.

[5] K. Kaneko and I. Tsuda, *Theory and applications of coupled map lattices*. New York: John Wiley and Sons, 1993.

[6] E. Sanchez and M. Matias, "Experimental observation of a periodic rotating wave in rings of unidirectionally coupled analog lorenz oscillators," *Physical Review E*, vol. 57, no. 5, pp. 6184–6186, 1998.

[7] P. Perlikowski, S. Yanchuk, M. Wolfrum, A. Stefanski, P. Mosilek, and T. Kapitaniak, "Routes to complex dynamics in a ring of unidirectionally coupled systems," *Chaos*, vol. 20, no. 2, pp. 013111.1–013111.10, 2010.

[8] V. In, A. R. Bulsara, A. Palacios, P. Longhini, A. Kho, and J. D. Neff, "Coupling-induced oscillations in overdamped bistable systems," *Physical Review E*, vol. 68, no. 4, pp. 045102.1–045102.4, 2003.

[9] V. In, P. Longhini, N. Liu, A. Kho, J. D. Neff, A. Palacios, and A. R. Bulsara, "A bistable microelectronic circuit for sensing extremely low electric field," *Journal of Applied Physics*, vol. 107, pp. 014506.1–014506.8, 2010.

[10] A. Palacios, R. Carretero-Gonzlez, P. Longhini, and N. Renz, "Multifrequency synthesis using two coupled nonlinear oscillator arrays," *Physical Review E*, vol. 72, no. 2, pp. 026211.1–026211.9, 2005.

[11] V. Kaajakari, T. Mattila, A. Oja, and H. Seppa, "Nonlinear limits for single-crystal silicon microresonators," *Journal of MEMS*, vol. 13, no. 5, pp. 715–724, 2004.

[12] R. M. C. Mestrom, R. H. B. Fey, J. T. M. van Beek, K. L. Phan, and H. Nijmeijer, "Modelling the dynamics of a mems resoantor: Simulations and experiments," *Sensors and Actuators A*, vol. 142, no. 1, pp. 306–315, 2008.

[13] C. T. C. Nguyen and R. T. Howe, "An integrated cmos micromechanical resonator high-q oscillator," *IEEE Journal of Solid-state circuits*, vol. 34, no. 4, pp. 440–455, 1999.

[14] S. Beeby, *MEMS Mechanical Sensors*. Norwood: Artech House Publishers, second ed., 2004.

[15] Y. C. Wang, S. G. Adams, and J. S. Thorp, "Chaos in mems, parameter estimation and its potential application," *IEEE Transactions on Circuits and Systems–I: Fundamental Theory and Applicaitons*, vol. 45, no. 10, pp. 1013–1020, 1998.

[16] B. E. DeMartini, H. E. Butterfield, J. Moehlis, and K. L. Turner, "Chaos for a micro-electromechanical oscillator governed by the nonlinear mathieu equation," *Journal of MicroElectroMechanical Systems*, vol. 16, no. 6, pp. 1314–1323, 2007.

[17] L. A. Oropeza-Ramos, C. B. Burgner, and K. L. Turner, "Robust micro-rate sensor actuated by parametric resonance," *Sensors and Actuators A*, vol. 152, pp. 80–87, 2009.

[18] F. Hoppensteadt and E. Izhikevich, "Synchronization of mems resonators and mechanical neurocomputing," *IEEE transactions on circuits and systems*, vol. 48, no. 2, pp. 133–138, 2001.

[19] C. Acar and A. Shkel, *MEMS Vibratory Gyroscopes*. New York: Springer Science+Business Media, 2009.

[20] K. Wang and C. Nguyen, "High-order micromechanical electronic filters," *IEEE International Micro Electro Mechanical Systems Workshop*, pp. 25–30, 1997.

[21] V. Chivukula and J. Rhoads, "Microelectromechanical bandpass filters based on cyclic coupling architectures," *Journal of Sound and Vibration*, vol. 329, pp. 4313–4332, 2010.

[22] S. Shim, M. Imboden, and P. Mohanty, "Synchronized oscillation in coupled nanomechanical oscillators," *Science*, vol. 316, pp. 95–99, 2007.

[23] E. Buks and M. Roukes, "Electrically tunable collective response in a coupled micromechanical array," *Journal of MicroElectroMechanical Systems*, vol. 11, no. 6, pp. 802–807, 2002.

[24] H. Vu, A. Palacios, V. In, P. Longhini, and J. D. Neff, "Two-time scale analysis of a ring of coupled vibratory gyroscopes," *Physical Review E*, vol. 81, no. 3, pp. 031108.1–031108.14, 2010.

[25] S. D. Sarma, "Spintronics," *American Scientist*, vol. 89, pp. 516–523, 2001.

[26] F. Caruso, *Colloids and Colloid Assemblies: Synthesis, Modification, Organization and Utilization of Colloid Particles*. Weinheim: Wiley-VCH, 2004.

[27] N. Haramein and E. A. Rauscher, "The origion of spin: a consideration of torque and coriolis forces in einstein's field equations and grand unification theory," in *Proceedings of the Paris Symposium: Honoring the 83rd Birthday of Jean-Pierre Vigier*, 2005.

[28] L. M. Smith, "Nanostructures: The manifold faces of dna," *Nature*, vol. 440, pp. 283–284, 2006.

[29] C. Gershenson, *Design and Control of Self-organizing Systems*. Mexico: Coplt ArXives, 2007.

[30] A. T. Winfree, *The geometry of biological time*. New York: Springer-Verlag, 2001.

[31] A. Pikovsky, M. Rosenblum, and J. Kurths, *Synchronization: A Universal Concept in Nonlinear Sciences*. Cambridge University Press, 2001.

[32] S. Strogatz, *Sync: the emerging science of spontaneous order*. New York: Hyperion, 2003.

[33] S. Strogatz, "Spontaneous synchronization in nature," in *IEEE International Frequency Control Symposium*, 1997.

[34] G. M. Whitesides and B. Grzybowski, "Self-assembly at all scales," *Science*, vol. 295, pp. 2418–2421, 2002.

[35] J. Guckenheimer and P. Holmes, *Nonlinear Oscillations, Dynamical Systems, and Bifurcations of Vector Fields*. New York: Springer-Verlag, 1983.

[36] S. De and N. Aluru, "Complex nonlinear oscillations in electrostatically actuated microstructures," *Journal of MEMS*, vol. 15, no. 2, pp. 355–369, 2006.

[37] Y. Kuramoto, *Chemical Oscillations, Waves and Turbulence*. New York: Springer, 1984.

[38] P. Bhansali and J. Roychowdhury, "Injection locking analysis and simulation of weakly coupled oscillator networks," in *Advanced Simulation and Verification of Electronic and Biological Systems*, pp. 71–88, New York: Springer Science+Business Media, 2011.

[39] J. Rhoads, S. W. Shaw, and K. L. Turner, "Nonlinear dynamics and its applications in micro and nanoresonators," in *ASME Dynamic Systems and Control Conference*, October 2008.

[40] C. Acar, *Robust Micromachined Vibratory Gyroscopes*. Ph.D. thesis, UC Irvine, 2004.

[41] S. Vemuri, *Behavioral Modeling of Viscous Damping in MEMS*. M.S. thesis, Carnegie Mellon University, 2000.

[42] T. Parker and L. Chua, *Practical Numerical Algorithms For Chaotic Systems*. Springer-Verlag, 1989.

[43] R. Seydel, *Practical Bifurcation and Stability Analysis*. Springer-Verlag, 1994.

[44] TowerJazz, "Towerjazz mems foundry." `http://www.jazzsemi.com/pdf/MEMS-Overview-FINAL.pdf`.

[45] S. N. Labs, "Summit v overview." `http://www.mems.sandia.gov/tech-info/summit-v.html`.

[46] A. Cowen, G. Hames, D. Monk, S. Wilcenski, and B. Hardy, "Soimumps design handbook revision 6.0." MEMSCAP, Inc, 2009.

[47] R. K. Bansal, *Strength of Materials*. New Delhi: Laxmi Publications, 2010.

[48] H. Gercek, "Poisson's ratio values for rocks," *International Journal of Rock Mechanics and Mining Sciences*, vol. 44, no. 1, pp. 1–13, 2007.

[49] J. Carter, A. Cowen, B. Hardy, R. Mahadevan, M. Stonefield, and S. Wilcenski, "Polymumps design handbook revision 11.0." MEMSCAP, Inc, 2005.

[50] V. Kaajakari, "Silicon as an anisotropic mechanical material - a tutorial." `http://www.kaajakari.net/˜ville/research/tutorials/tutorials.shtml`.

[51] M. A. Hopcroft, W. D. Nix, and T. W. Kenny, "What is the young's modulus of silicon?," *Journal of Microelectromechanical Systems*, vol. 19, pp. 229–238, 2010.

[52] V. Kaajakari, T. Mattila, A. Lipsanen, and A. Oja, "Nonlinear mechanical effects in silicon longitudinal mode beam resonators," *Sensors and Actuators A: Physical*, vol. 120, no. 1, pp. 64–70, 2005.

[53] S. Huang and X. Zhang, "Gradient residual stress induced elastic deformation of multilayer mems structures," *Sensors and Actuators A: Physical*, vol. 134, pp. 177–185, 2007.

[54] Q. Jing, *Modeling and Simulation for Design of Suspended MEMS*. Ph.D. thesis, Carnegie Mellon University, 2003.

[55] D. Miki, M. Honzumi, Y. Suzuki, and N. Kasagi, "Large-amplitude mems electret generator with nonlinear spring," *23rd IEEE Int. Conf. Micro Electro Mechanical Systems*, pp. 176–179, 2010.

[56] C. T. C. Nguyen, "Introduction to mems design: Lecture notes." `http://inst.eecs.berkeley.edu/˜ee245/fa08/`, 2008.

[57] S. Naik, T. Hikihara, H. Vu, A. Palacios, V. In, and P. Longhini, "Local bifurcations of synchronization in self-excited and forced unidirectionally coupled micromechanical resonators," *Journal of Sound and Vibration (under review).*

[58] T. Hisakado, *Study on Bifurcation Phenomena in Three-Phase Circuit.* Ph.D. thesis, Kyoto University, 1997.

[59] M. Golubitsky and I. Stewart, *The Symmetry Perspective.* Birkhauser-Verlag, 2003.

[60] C. Laing, "Rotating waves in rings of coupled oscillators," *Dynamical Systems*, vol. 13, no. 4, pp. 305–318, 1998.

[61] Agilent, "4294a impedance analyzer service manual." `http://home.agilent.com`.

[62] V. Kaajakari, *Practical MEMS.* Las Vegas: Small Gear Publishing, 2009.

[63] T. Veijola, T. Mattila, O. Jaakkola, J. Kiihamaki, T. Lamminmaki, A. Oja, K. Ruoko-nen, H. Seppa, P. Seppala, and I. Tittonen, "Large-displacement modelling and simulation of micromechanical electrostatically driven resonators using the harmonic balance method," in *Microwave Symposium Digest., 2000 IEEE MTT-S International*, vol. 1, pp. 99–102, 2000.

[64] F. Mohd-Yasin, D. J. Nagel, and C. E. Korman, "Noise in mems," *Measurement Science and Technology*, vol. 21, pp. 012001–012023, 2010.

[65] R. Mancini, *Op amps for everyone: design reference.* Burlington: Elsevier, 2003.

[66] J. Moehlis, J. Rogers, B. DeMartini, and K. Turner, "Exploiting nonlinearity to provide broadband energy harvesting," in *Proceedings of the ASME 2009 Dynamic Systems and Control Conference*, October 2009.

[67] P. Perlikowski, S. Yanchuk, P. A. Tass, and O. V. Popovych, "Periodic patterns in a ring of delay-coupled oscillators," *Physical Review E*, vol. 82, pp. 036208.1–036208.12, 2010.

[68] V. Kaajakari, "Mems tutorial: mechanical noise in microelectromechanical systems." `http://www.kaajakari.net/~ville/research/tutorials/tutorials.shtml`.

[69] W. Zhang, R. Baskaran, and K. Turner, "Effect of cubic nonlinearity on auto-parametrically amplified resonant mems mass sensor," *Sensor and Actuators A: Physical*, vol. 102, no. 1, pp. 139–150, 2002.

[70] S. Adams, F. Bertsch, and N. MacDonald, "Independent tuning of linear and nonlinear stiffness coefficients," *Journal of MicroElectroMechanical Systems*, vol. 7, no. 2, pp. 172–180, 1998.

[71] K. Turner, S. Miller, P. Hartwell, N. M. andS. Strogatz, and S. Adams, "Five parametric resonances in a microelectromechanical system," *Nature*, vol. 396, no. 6707, pp. 149–152, 1998.

[72] R. H. Rand, "Lecture notes on nonlinear vibrations (version 52)." `http://www.tam.cornell.edu/randdocs/`, 2005.

[73] R. Legtenberg, A. W. Groeneveld, and M. Elwenspoek, "Comb-drive actuators for large displacements," *Journal of Micromech. Microeng*, vol. 6, pp. 320–329, 1996.

[74] H. Tilmans, "Equivalent circuit representation of electromechanical transducers: I. lumped-parameter systems," *Journal of Micromechanics and Microengineering*, vol. 6, no. 1, pp. 157–176, 1996.

[75] Amkor-Technology, "3d bondwire electrical modelling results." `http://ece.wpi.edu/analog/resources/1mil_bwire_RLC.pdf`, 2001.

[76] R. Hoyle, *Pattern Formation*. Cambridge: Cambridge University Press, 2006.

[77] M. Hamermesh, *Group Theory and Its Application to Physical Problems*. Reading: Addison-Wesley, 1964.

[78] M. Golubitsky and I. Steward, *The Symmetry Perspective*. Basel: Birkhauser-Verlag, 2002.

[79] M. Golubitsky and D. Schaeffer, *Singularities and Groups in Bifurcation Theory: Vol I*. New York: Springer-Verlag, 1985.

[80] M. Golubitsky, I. Stewart, and D. Schaeffer, *Singularities and Groups in Bifurcation Theory: Vol II*. New York: Springer-Verlag, 1988.

[81] G. Lodge, J. A. Walsh, and M. Kramer, "A trilinear three-body problem," *International Journal of Bifurcation and Chaos*, vol. 13, no. 8, pp. 2141–2155, 2003.

[82] J. Guckenheimer and P. J. Holmes, *Nonlinear Oscillations, Dynamical Systems and Bifurcations of Vector Fields*. New York: Springer-Verlag, 1983.

[83] S. Wiggins, *Introduction to Applied Nonlinear Dynamical Systems and Chaos*. New York: Springer-Verlag, 1990.

[84] B. Ermentrout, *Simulating, analyzing, and animating dynamical systems: a guide to XPPAUT for researchers and students*. Society for Industrial and Applied Mathematics, Philadelphia, 2002.

[85] G. K. Fedder, *Simulation of Microelectromechanical Systems*. PhD thesis, University of California at Berkeley, Berkeley, CA, USA, 1994.

[86] M. E. Inchiosa, V. In, A. R. Bulsara, K. Wiesenfeld, T. Heath, and M. H. Choi, "Stochastic dynamics in a two-dimensional oscillator near a saddle-node bifurcation," *Physical Review E*, vol. 63, no. 6, pp. 066114.1–066114.10, 2001.

[87] P. Longhini, *Nonlinear Dynamics Design and Operation of Advanced Magnetic Sensors*. Ph.D. thesis, San Diego State University, 2005.

[88] P. Longhini, A. L. de Escobar, F. Escobar, V. In, and A. Bulsara, "Novel coupling scheme for the dynamics of non-uniform coupled squid," *IEEE Transactions On Applied Superconductivity*, vol. 19, pp. 749–752, 2009.

[89] P. Longhini, S. Berggren, A. Palacios, V. In, and A. L. de Escobar, "Modeling non-locally coupled dc squid arrays," *IEEE Transactions On Applied Superconductivity*, vol. 21, no. 3, pp. 391–393, 2011.

[90] V. In, A. Kho, J. D. Neff, A. Palacios, P. Longhini, and B. Meadows, "Experimental observation of multifrequency patterns in arrays of coupled nonlinear oscillators," *Physical Review Letters*, vol. 91, no. 24, pp. 244101.1–244101.4, 2003.

[91] S. Naik and T. Hikihara, "Characterization of a mems resonator with extended hysteresis," *IEICE Electronics Express*, vol. 8, no. 5, pp. 291–298, 2011.

List of Publications

Journal articles

- S. Naik and T. Hikihara, "Characterization of a mems resonator with extended hysteresis," *IEICE Electronics Express*, vol. 8, no. 5, pp. 291–298, 2011.

- S. Naik, T. Hikihara, H. Vu, A. Palacios, V. In, P. and Longhini, "Local Bifurcations of Synchronization in Self-excited and Forced Unidirectionally Coupled Micromechanical Resonators," *Journal of Sound and Vibration*, (under review).

- S. Naik, T. Hikihara, H. Vu, A. Palacios, V. In, P. and Longhini, "Characterization of Synchronization in a Unidirectionally Coupled System of Nonlinear Micromechanical Resonators," *Sensors and Actuators A: Physical*, (under review).

International conference proceedings

- S. Naik and T. Hikihara, "Investigation of Nonlinearity in Coupled MEMS Gyroscopes," *2009 International Symposium on Nonlinear Theory and its Applications*, Sapporo, Japan, pp. 519–522, Oct. 2009.

Domestic conference proceedings and technical reports

- S. Naik and T. Hikihara, "Derivation of Dynamical Equations of Coupled MEMS Gyroscopes," *IEICE Technical Report: NLP 2008-152*, vol. 108, no. 477, pp. 7–12, The Consortium of Universities in Kyoto, Japan, March 10–11, 2009.

- S. Naik and T. Hikihara, "Numerical Study on the Quasi-periodic Behavior in Coupled MEMS Resonators," *IEICE Technical Report: NLP 2010-85*, vol. 110, no. 255, pp. 25–30, Osaka University, Osaka, Japan, Oct. 2010.